

Fakultät Mathematik und Naturwissenschaften
Technische Universität Dresden

**Growth of unsaturated, cyclic, and
polycyclic aromatic hydrocarbons:
Reactions under the conditions of the
interstellar medium**

von

Robert Barthel



2008

**Growth of unsaturated, cyclic, and polycyclic aromatic
hydrocarbons: Reactions under the conditions of the
interstellar medium**

DISSERTATION

zur Erlangung des akademischen Grades

Doctor rerum naturalium
(Dr. rer. nat.)

vorgelegt

der Fakultät Mathematik und Naturwissenschaften
der Technischen Universität Dresden

von

Dipl.-Chem. Robert Barthel
geboren in Pirna

Dresden 2008



1. Gutachter: Prof. Dr. Gotthard Seifert

2. Gutachter: Prof. Dr. Michael Schreiber

3. Gutachter: Prof. Dr. Christine Joblin

Eingereicht am: 09. Mai 2008

Verteidigt am: 02. Oktober 2008

Contents

Glossary	V
Introduction	1
1 Observation and chemistry modelling of interstellar hydrocarbons and PAHs	5
1.1 Astronomical observation aspects	5
1.1.1 Spectral evidences of hydrocarbons and PAHs in molecular clouds . . .	5
1.2 Proposed hydrocarbon and PAH hypothesis	7
1.2.1 Consequences of the hypothesis	8
1.3 Chemistry modelling of interstellar hydrocarbons and PAHs	8
1.3.1 Principal routes	8
1.3.2 Thermochemical formation route	9
1.3.3 Chemistry modelling by simulating chemical networks	10
1.3.4 Chemistry modelling of hydrocarbon formation and growth processes .	11
2 Computational methods	13
2.1 Structure of the reaction analysis	13
2.1.1 Chemical route analysis	14
2.2 Reaction kinetics and statistical rate theories	15
2.2.1 The effective ion-molecule rate coefficient k_{eff}	15
2.2.2 Phenomenological ion-molecule based capture rate coefficient	16
2.2.3 Molecular dynamics based capture rate coefficient	18
2.2.4 Isomerisation/dissociation coefficients - k_{x_i} , k_d	19
2.2.5 The radiative relaxation rate coefficients k_r	22
2.3 Thermodynamic equilibrium between products	23
2.3.1 Definition of the relative concentrations	24
2.4 Quantum chemistry methods	24
2.4.1 <i>Ab initio</i> methods	24
2.4.2 Density functional theory methods	25
2.4.3 Density-functional tight-binding method	26
2.5 Reaction minimum energy path and transition state search	30
2.5.1 NEB method	30

3	Methyne as precursor for interstellar ion-molecule reactions	33
3.1	Methyne in the ISM	33
3.2	Selected properties of methyne	34
3.3	Reactivity and regioselectivity of methyne	35
3.4	Hypothesis of reactions between interstellar CH and hydrocarbons	36
4	Methyne + hydrocarbon ions $C_xH_x^+$ ($x=2-6$)	39
4.1	Preview on the formation of benzene cation and tropylium	40
4.2	$C_2H_2 + CH^+$	42
4.2.1	DFTB based MD simulations	43
4.2.2	Product energetics	46
4.2.3	Reaction path analysis	47
4.3	$C_3H_3^+ + CH$	50
4.3.1	DFTB based MD simulations	50
4.3.2	Product energetics	53
4.3.3	Reaction path analysis	56
4.4	$C_5H_5^+ + CH$	59
4.4.1	DFTB based MD simulations	59
4.4.2	Product energetics	63
4.4.3	MEP analysis by the NEB method and TS reoptimisation	65
4.5	$C_6H_6^+ + CH$	70
4.5.1	DFTB based MD simulations	70
4.5.2	Product energetics	75
4.5.3	MEP analysis by the NEB method and TS reoptimisation	76
4.6	Summary and discussion	82
5	Methyne + hydrocarbon ions $C_xH_x^+$ ($x=5-10$)	87
5.1	DFTB-MD simulations	87
5.1.1	Production distribution	88
5.1.2	Production distribution based on the cross sections	90
5.1.3	Capture rate coefficients	91
5.2	Energetic considerations	92
5.2.1	Thermodynamic product stabilities	92
5.2.2	Reaction energies	92
5.2.3	Population distribution	94
5.3	MEP analysis by the NEB method and TS reoptimisation	95
5.3.1	Constriction	95
5.3.2	Thermal elimination of H_2	96
5.4	Summary	99

6	Methyne + hydrocarbon ions $C_xH_{x-2}^+$ ($x=10-13$)	101
6.1	Preview on the growth of PCHs and PAHs by CH	101
6.2	$C_{10}H_8^+ + CH$	103
6.2.1	DFTB based MD simulations	103
6.2.2	Product energetics	105
6.2.3	Reaction path analysis	108
6.3	$C_{11}H_9^+ + CH$	112
6.3.1	DFTB based MD simulations	112
6.3.2	Product energetics	116
6.3.3	Reaction path analysis	117
6.4	$C_{12}H_{10}^+/C_{13}H_{10}^+ + CH$	121
6.4.1	DFTB based MD simulations of $C_{12}H_{10}^+ + CH$	121
6.4.2	DFTB based MD simulations of $C_{13}H_{11}^+ + CH$	123
6.4.3	Product energetics	125
6.4.4	Reaction path analysis of selected mechanisms	125
6.5	Summary and discussion	129
7	Methyne + PAH ions $C_xH_{2/x}^+$ ($x=20, 24$)	133
7.1	$C_{20}H_{10}^+ + CH$	134
7.1.1	DFTB based MD simulations	134
7.1.2	Product energetics	136
7.1.3	Reaction path analysis	139
7.2	$C_{24}H_{12}^+ + CH$	141
7.2.1	DFTB based MD simulations	142
7.2.2	Product energetics	143
7.2.3	Reaction path analysis	144
7.3	Summary	146
8	Summary and conclusions	149
	Appendix A Calculated molecular and reaction data	153
A.1	Dipole moment and polarisability of various hydrocarbons	153
A.2	$C_4H_4^+ + CH$	156
	Appendix B Realisation of applied methods	161
B.1	MD simulation setup	161
B.2	Determination of k_f and σ_{MR} based on the MD simulations	166
B.3	Analysis of reaction channels by bond criteria and topology	166
B.4	NEB setup	168
	Appendix C Reference data	171
C.1	Interstellar medium and molecules	171
C.2	Spectroscopical data of interstellar molecules and particles	173

Appendix D Properties of the ISM	175
D.1 Phases of the ISM	175
D.2 Molecular clouds - the habitat of interstellar molecules	175
D.3 Diffuse and dark clouds	176
D.4 Bok globules and clumps	176
D.5 Composition of a molecular cloud	176
Appendix E Theoretical background	177
E.1 Reaction kinetics and statistical rate theories	177
E.2 Basis sets	180
E.3 Reaction minimum energy path and transition state search	181
Bibliography	185

Glossary

NOTATION	DESCRIPTION	PAGE
abbr.	Abbreviation	46
ADO	Average dipole orientation <i>theory</i>	13
b	Collision parameter	17
Bdz1	B3LYP/6-31G(d)	26
Bdz2	B3LYP/cc-pVDZ	26
Btz1	B3LYP/6-311G++(3df,3pd)	26
Btz2	B3LYP/cc-pVTZ	26
Btz3	B3LYP/aug-cc-pVTZ	26
CSE	Circumstellar envelope	1
CTST	Canonical transition state theory	16
$\Delta_{\text{R}}E$	Reaction energy	46
$\Delta_{\text{R}}G$	Free reaction enthalpy	54
$\Delta_{\text{R}}H_{0\text{K}}$	Molar reaction enthalpy at 0 Kelvin	46
$\Delta_{\text{R}}S$	Reaction entropy	54
DFT	Density functional theory	1
DFTB	Density functional tight binding	1
DIB	Diffuse interstellar band	6
exp	experimental	34
$f_{x\leftrightarrow y}$	Fraction of x transforming into y based on the rate coefficients	16
G3	Gaussian-3 <i>theory</i>	25
HAC	Hydrogenated amorphous carbon	6
Hdz1	HF/6-31G(d)	34
IC	Interstellar chemistry	1
IEB	Infrared emission band	1
IR	Infrared	1
ISM	Interstellar medium	1
k_{ADO}	<i>ADO theory-based</i> capture rate coefficient	16
k_{DC}	RRKM-based rate coefficient obtained by Direct count method	48
k_{L}	<i>Langevin theory-based</i> capture rate coefficient	16
$k_{\text{MD}}(T)$	Canonical MD-based capture rate coefficient	18

NOTATION	DESCRIPTION	PAGE
$k_{\text{MD}}(\varepsilon)$	Microcanonical MD-based capture rate coefficient	18
k_{m}	modified CTST-based rate coefficient	48
k_r	Radiative relaxation rate coefficient	22
k^{v}	RRKM-based rate coefficient only considering vibrational modes of the transition state	48
k^{vr}	RRKM-based rate coefficient considering vibrational and rotational modes of the transition state	48
k_{WR}	RRKM-based rate coefficient obtained by Whitten-Rabinovitch approximation	48
LUP	Locally updated planes (<i>algorithm</i>)	30
M1//M2	Single-point calculation by method M1 at the geometry obtained by M2	26
MD	Molecular dynamics	1
Mdz1	MP2/6-31G(d)	25
Mdz2	MP2/cc-pVDZ	25
MEP	Minimum energy path	1
Mtz2	MP2/cc-pVTZ	25
Mtz3	MP2/aug-cc-pVTZ	25
NEB	Nudged elastic band	1
P	Reaction probability	18
PAH	Polycyclic aromatic hydrocarbons	1
PCH	Polycyclic hydrocarbons	2
Pdz4	PW91/DZVP	26
PEdz4	PBE/DZVP	26
PES	Potential energy surface	1
PEtz4	PBE/TZVP	26
Ptz4	PW91/TZVP	26
Qdz1	QCISD(T)/6-31G(d)	34
$r_{x \leftrightarrow y}$	Ratio of the rate coefficients of isomerisation from x to y to isomerisation from y to x	48
RRKM	Rice-Ramsberger-Kassel-Marcus (<i>theory</i>)	16
$\sigma_{\text{R},i}$	Reaction cross section of channel i	18
SD	SCC-DFTB, self-consistent charge DFTB	29
TS	Transition state	29
UIR	Unidentified infrared (<i>band</i>)	7
UV	Ultraviolet	1
VIS	Visible	1
WR	Whitten-Rabinovitch (<i>approximation</i>)	20



Introduction

Hydrocarbons and polycyclic aromatic hydrocarbons (PAHs) have been long discussed as part of the interstellar medium (ISM) composition based on both theoretical and experimental data [1, 2, 3, 4, 5] as well as spectroscopical observations [6, 7]. Over 70% of the 140 interstellar molecules identified to date contain carbon and 15% of them are categorised as hydrocarbons [8] (Table C.1). The presence of mid-sized and large (more than 50 carbon atoms) entities in this environment is, therefore, very likely. Theoretical and experimental studies on the non-thermal interstellar emission features seem to point at molecules of the PAH type as carriers [9, 10, 11, 12]. Moreover, well known spectroscopic features such as the infrared (IR) emission bands (IEBs) and / or ultraviolet (UV) and visible (VIS) extinction features have been partially assigned to aromatic and aliphatic moieties also in hydrocarbons [13, 14, 15] supporting the PAH presence in the ISM (the so-called PAH hypothesis).

The behaviour of hydrocarbons and PAHs in the ISM and their influence on its temperature, opacity and chemistry have been investigated for several decades. In particular, interstellar chemistry (IC) modelling based on the presence of different classes of particles has been effectively used to provide information on the chemical evolution of the molecular abundances [16, 17], and to explain the relation between carbon containing molecules and grains [18]. However, while the IC of small molecules has been extensively studied and detailed reaction mechanisms and rate coefficients have been provided [19, 20, 21, 22], the study of growth mechanisms for large hydrocarbons and PAHs has been restricted to circumstellar envelopes (CSEs) [3, 21, 23]. Moreover, although laboratory approaches have compared the formation of the large hydrocarbons and PAHs in the CSE with the processes occurring during hydrocarbon combustion or pyrolysis, the exact formation mechanisms in the ISM are still poorly understood [24, 25].

The aim of this work is to provide a detailed study of formation and growing mechanisms concerning hydrocarbons and PAHs with 2–24 carbon atoms under the conditions of the dense ISM. In these particular environments, the high molecular densities and ionisation rates allow the restriction of the chemical routes to only thermochemical gas-phase reactions between ions and molecules, thus simplifying the computational study.

Theoretical chemistry provides a large variety of methods for the determination of the thermodynamics and dynamical aspects of a chemical reaction such as molecular dynamics (MD), statistical rate theories, and minimum energy path (MEP) analysis. In each case, the electronic structure is required, which can be provided by quantum chemical methods. The quality of the system in terms of accuracy is defined by the approximation of the underneath

lying quantum mechanics. The goals are, therefore, to reach the highest accuracy and to be comparable with experiments. However, the computational cost of using accurate quantum chemical methods such as *ab initio* methods scales exponentially with system size. Different approaches such as density functional theory (DFT) based methods allow the access to larger systems since the scaling of computational costs with system size is smaller. The simulation of molecular dynamics of chemical reactions considering random initial conditions, the variation of collision energies and other collision parameters in order to sample the reaction potential energy surface (PES) and product distributions requires several hundred trajectories. This is beyond the scope of DFT and *ab initio* methods in the case of midsized to large systems. On the other hand, a sufficient approach can be given by approximate DFT methods such as the density functional tight binding (DFTB) [26, 27]. So far, adiabatic quasi-classical molecular dynamics based on DFTB methods have been applied to reaction dynamics and property analysis [28, 29, 30, 31]. For the analysis of the chemical reactions in this work, *ab initio*, DFT and DFTB method(s) are combined and complementarily used. DFTB based MD simulations are applied to provide a qualitative sampling of the reaction potential energy surface. Resulting trajectories serve to initialise the minimum energy path optimisation at the DFT level of theory using the nudged elastic band (NEB) method. Additionally, resulting products and transition states are refined using DFT and *ab initio* methods to provide thermodynamic quantities and reaction rate coefficients. Through extensive MD simulations, the selection of particular reactions paths is based on reaction probability weighting rather than on empirical weighting.

Among the possible hydrocarbon and PAH precursors, methyne (CH) is chosen based on its known reactivity in laboratory and planetary atmosphere chemistry [32, 33, 34, 35]. The study of CH based reactions is carried out as follows:

- In Chapter 1, the observational and growing aspects of interstellar hydrocarbons and PAHs are given. The approach to hydrocarbon and PAH formation based on gas-phase ion-molecule reactions is derived.
- The computational methods used for the reaction analysis, i. e., the determination of capture rate coefficients, product distributions, thermodynamic and molecular quantities, and isomerisation rate coefficients, are described in Chapter 2.
- In Chapter 3, the reactivity and regioselectivity of methyne as well as its role in ion-molecule reactions are presented.
- In Chapter 4, the reaction mechanisms of CH based chain growth and cyclisation are studied through reactions between methyne and non-cyclic hydrocarbons $C_xH_x^+$ with the dimension $x = 2-6$.
- The reaction mechanisms of CH based ring size growth, the rearrangements resulting in an additional ring unit, and the mechanisms for possible hydrogen elimination are discussed in terms of the reactions between methyne and monocyclic hydrocarbons $C_xH_x^+$ with the dimension $x = 5-10$ (Chapter 5) as well as between methyne and bicyclic hydrocarbons C_xH_{x-2} with $x = 10-13$ (Chapter 6).

-
- In Chapter 7, the reaction mechanisms of CH addition into large polycyclic hydrocarbons and the aspects of the steric hindrance of polycyclic hydrocarbons (PCHs) related with ring extension are studied through reactions between methyne and polycyclic aromatic hydrocarbons $C_xH_{x/2}$ with $x = 20, 24$.

A summary of the most relevant results, the astrophysical impact of the studied reactions, and some conclusions are given in Chapter 8.

Supplementary results, detailed descriptions and additional data are given in the appendices. Appendix A contains computed dipole moments and polarisabilities of selected hydrocarbons which have been used to determine ion-molecule capture rates as described in Chapter 4. Moreover, Appendix A contains selected data of chemical reactions which are not described in detail in Chapter 4. Technical setups are presented in Appendix B. This appendix contains the MD simulation setup for the derivation of the reaction cross sections and capture rate coefficients as well as the NEB setup. Supplementary reference data are provided in Appendix C. A summary of the physical and chemical composition of the ISM is provided in Appendix D. Theoretical aspects of the statistical rate theories, and reaction path methods are described in Appendix E.

1 Observation and chemistry modelling of interstellar hydrocarbons and PAHs

Space is big. Really big. You just won't believe how vastly hugely mindbogglingly big it is.

THE HITCHHIKERS'S GUIDE TO THE GALAXY

In this chapter, spectral observations and theoretical and experimental aspects concerning hydrocarbons and PAHs are summarised. Note that only (unsaturated) hydrocarbons are considered. These refer to C_xH_y with $x \geq y$ and to different constitutional structures such as non-, mono-, di-, tri- and polycyclic. Based on their structural and electronic relations to PAHs, which originate from sp^2 -hybridised carbon, these hydrocarbons are included into the PAH hypothesis. Moreover, polycyclic hydrocarbons (PCHs) consisting of hexagonal moieties can be defined as supersaturated or superdehydrogenated PAHs.

The reviewed issues concerning the identification of PAHs and hydrocarbons and the chemistry of the PAH and hydrocarbons are also provided in this chapter. The description of proper PAH formation routes in the ISM is important in order to support the PAH hypothesis. The study of the formation of PAH and hydrocarbons under the conditions of the ISM is discussed. The chapter is completed by the derivation of the formation routes for the PAHs and hydrocarbons based on the aspects of the interstellar chemistry models. It includes the evaluation of potential precursors for the formation of PAHs and hydrocarbons.

1.1 Astronomical observation aspects

The physical and chemical characteristics of interstellar medium are given in Appendix D.

1.1.1 Spectral evidences of hydrocarbons and PAHs in molecular clouds

The reported spectral identification and evidences of hydrocarbons can be divided into molecular lines and bands, emission and absorption, stellar and non-stellar, and wavelengths such as radio, infrared (IR), visible (VIS) and ultraviolet (UV).

1.1.1.1 Evidences based on molecular lines

Sharp and resolved molecular lines are observed in regions of the ISM and MCs with lowest densities, such as diffuse clouds.

Molecular lines at UV/VIS wavelength

The observation of this feature is restricted to small di- and triatomic hydrocarbons. They are difficult to track since they coincide with broad absorption bands of the ISM which originate from other molecules and particles. The methyne molecule, CH, was identified based on observed transitions at 315 and 430 nanometre (nm^{†1}) [32]. Another observed transitions have been allowed to identify CH⁺ (423 nm) and C₂ (876 nm) [32].

Molecular lines at millimetre wavelength

Observed transitions in the millimetre and sub-millimetre wavelength originate from rotational transitions of polar molecules. In the case of simple structures, e. g. linear molecules which correspond to rigid rotors, the unambiguous identification of hydrocarbons was reported. Most of the hydrocarbons in the list of identified interstellar molecules (Table C.1) are of such structure. This includes polyenenitriles (cyanopolyenes) HC_{2n+1}N, polyacetylenes HC_{2n}H, carbon chain radicals C_nH and cumulene carbenes H₂C_n [36, 37, 38, 39].

1.1.1.2 Evidence based on molecular bands

Molecular bands originate from vibrational, vibrational-rotational and electronic transitions.

Absorption bands in stellar spectra

More than 200 characteristic interstellar absorption bands, also referred as diffuse interstellar bands (DIBs), between the optical and NIR region between 200 and 1300 nm are enlisted. They can be separated from stellar absorption bands by their non-correlation to star movement, but correlation with interstellar reddening [40]. The spatial resolution of the strength of the DIBs indicates that the carriers are concentrated at edges of dense molecular clouds [41]. The diversity of the DIBs indicates the presense of several class of carriers.

Based on laboratory and theoretical investigations, assignments of particular DIBs can be made to PAHs and their cations [1, 2, 42, 43, 44], hydrocarbon chains [45], carbon chains [46, 47, 48], solid carbon [49, 50] and fullerenes [51, 52, 53]. However, no assignment was obtained to date.

Absorption bands of non-stellar spectra in the IR region

Absorption bands in the region of the IR wavelength can be observed by many astronomical objects such as the Galactic centre [13] or the Taurus dark clouds [54]. The IR absorption bands originate from vibrational transitions in molecules or solids. In the case absorption bands correlate with the general extinction, it is supposed that the carriers are more of solid character rather than small molecules. In the range of 2500 nm up to 10000 nm (4000-1000 cm⁻¹), distinctive vibration modes with high optical depth are identified. Bands in the range of 3330 nm (3000 cm⁻¹) to 3570 nm (2800 cm⁻¹) are commonly assigned to CH vibration modes [13, 14, 15]. Depending on the co-existences of other absorption bands, these interstellar CH vibration modes have been proposed to originate from aliphatic hydrocarbons [14] (indicated by the subfeatures at 3380 and 3420 nm which correspond to the symmetric C-H stretching frequencies of -CH₃ and -CH₂- groups), from hydrogenated

^{†1} Length in nanometre, 1 nm = 1·10⁻⁹ m

amorphous carbon (HAC) [55], from irradiated ice grain mantles composed of H₂O, CO and hydrocarbons [54], and from PAHs [56].

Emission bands

Strong emission features dominate the mid-IR region between 3 and 13 μm [57] all over the galaxy. These features originate from molecules and very small solids. Their ambiguous character have named them unidentified IR bands (UIRs), infrared emission bands (IEBs) or infrared emission features (IEFs). The origin of the bands are the external (UV-radiated) parts of the MCs and the diffuse ISM [58, 59]. These bands do not stem from thermal emissions. The origin of these emission features is supposed to be a combined UV/VIS pumped electronic excitation and de-excitation by IR fluorescence [9, 10]. Considering the range of emission, this phenomenon requires hot and therefore very particles. Observed emission bands in the range of 3.3×10^{-6} to 11.3×10^{-6} m are commonly assigned to CH stretching, CC stretching and CH out-of-plane bending modes of sp²-hybridised carbon-containing carriers [5, 10, 15, 18, 60, 61]. Due to the possible relation with aromatic hydrocarbon structures [6, 62, 63, 64, 65, 66], these bands have been also named aromatic IR bands (AIBs).

1.2 Proposed hydrocarbon^{†2} and PAH hypothesis [59, 67, 68]

The reported results from observations of astronomical environments have shown that in a few cases the unambiguous identification of molecules is possible. These molecules are mostly polar and/or small. However, observed spectra of absorption/emission bands in the IR and UV/VIS wavelengths are difficult to match with particular molecules. Observed bands represent the spatial superposition of each present carrier. Similar functional moieties of different chemical compounds and coinciding bands complicate the assignment to interstellar bands.

Analysis of the observations combined with, in particular, theoretical and experimental studies favour PAHs and hydrocarbons and have allowed to formulate a hypothesis. which is also referred to as the PAH model. What supports the hypothesis?

1. CARBON ABUNDANCE AND CHEMICAL DIVERSITY:

Carbon reaches together with oxygen the highest abundance after hydrogen and helium; C/H = 140–350 ppm [69, 70]. Moreover, carbon provides a large diversity to chemical constitution of molecules and solids. Therefore, multiple spectral features could be explained mostly by this element source.

2. PHOTOPHYSICS:

Theoretical and experimental studies of the photophysical properties of PAH and hydrocarbons indicate a match with the required structural photostability, UV extinction features [1, 2, 43], and the IR emission features (sequential UV-pumping and IR fluorescence) [4, 9, 10, 71, 72, 73, 74, 75] of the interstellar carrier. The global heating in

^{†2}The hypothesis is commonly only referred to PAHs. As pointed out at the beginning of Chapter 1 all unsaturated hydrocarbons considered in this work are included in this hypothesis due to structural and electronic relations to the PAHs.

the ISM by photo-electric effects is also provided by the characteristics of the PAHs and large hydrocarbons [76].

1.2.1 Consequences of the hypothesis

Average size of proposed molecules

Based on comparison of interstellar UV extinction features with those of small PAHs [77], the size of PAHs was found to be restricted to large PAH of 30 atoms and more in order to match these extinction features.

Abundance of proposed molecules

According to the PAH hypothesis and the ratio of near-IR attributed to PAH and far-IR emission attributed to dust [5, 9, 10], the total abundance of PAHs in diffuse ISM has been estimated to be in the range of 3×10^{-7} to 5×10^{-5} per H atom, i. e., up to 20% of elemental carbon is related to PAHs. It would make the PAHs the second most abundant carbon species after CO.

Chemistry of proposed molecules

The formation of PAHs and hydrocarbons, that produce the reported features, has to correspond with the observed and evaluated conditions of the ISM [10]. Moreover, proposed PAHs and HCs should be related with observed appearance of interstellar grains [56]. This would be the case of carbon based grains.

1.3 Chemistry modelling of interstellar hydrocarbons and PAHs

1.3.1 Principal routes

Circumstellar versus interstellar route

Two different sources for the origin of PAHs and hydrocarbons have been considered: The direct formation of hydrocarbons and PAHs in the ISM, i. e., a route at ultra-low temperature and density, and / or the formation in the circumstellar envelopes (CSEs), i. e., hot and dense areas around stars that massively eject carbon.

CSEs of carbon-rich giants^{†3} are characterised by carbon outflows of about $3 M_{\odot} \text{ kpc}^{-2} \text{ Myear}^{-1}$ [5] which is equal to about $3300 \text{ Carbon particles} \cdot \text{m}^{-2} \cdot \text{s}^{-1}$. The temperatures and densities in these outflows rise up to 1000 K and 10^{-10} to $10^{-6} \text{ atm}^{\dagger4}$, which is a magnitude of 3 to 7 higher than of densities observed in MCs. These conditions are suitable to propose PAH and hydrocarbon formation mechanisms based on pyrolysis and combustion processes [21]. Formed PAHs and hydrocarbons are supposed to enrich the ISM by migration and distribution based on stellar winds. Additional formation during migration could be possible in the hot expanding gas of supernovae [79].

The direct production of hydrocarbons and PAHs in the ISM is expected from different mechanisms. The possible formation / growth mechanisms will be addressed in this work.

^{†3}Late evolutionary phase of stars with initial 0.5 to 5 solar masses characterised by enhanced carbon/oxygen ratio ($\text{C/O} > 1$) [78].

^{†4}Pressure in atmosphere units (1 atm=101.325 kPa)

Formation / growth versus shattering / dissociation route in the ISM

The shattering of carbon grains by grain-grain collisions is supposed to lead to PAH and hydrocarbons of different sizes [80]. Based on the structure of MCs, the photodissociation of larger particles and grains is expected to be concentrated at the outer parts, e.g. at the edges to stars with strong radiation fields.

Inside MCs, the dominant formation pathway is supposed to shift from photochemical to thermochemical mechanisms due to increasing radiation shielding.

1.3.2 Thermochemical formation route

The thermochemical formation routes in the cold phase of the ISM is restricted to specific types of reactions as given in Table 1.1. The low density and temperature only permits reactions between ions and neutrals that are effectively barrierless, exothermic and binary^{†5}. Without any kind of collisional activation, initial reaction barriers inhibit any formation / growth reaction in the ISM.

Table 1.1: Photo- and thermochemical gas phase reactions of the ISM and typical rates adopted from [5].

<i>chemical</i>	formula	rate
dissociative recombination	$A^+ + e \rightarrow C + D$	$10^{-7} \text{ cm}^3\text{s}^{-1}$
ion-molecule	$A^+ + B \rightarrow AB^{+\ddagger} \rightarrow C^+ + D$	$10^{-9} \text{ cm}^3\text{s}^{-1}$
associative detachment	$A^- + B \rightarrow AB + e$	$10^{-9} \text{ cm}^3\text{s}^{-1}$
charge transfer	$A^+ + B \rightarrow A + B^+$	$10^{-9} \text{ cm}^3\text{s}^{-1}$
neutral-neutral ^a	$A + B \rightarrow AB^{\ddagger} \rightarrow C + D$	$10^{-11} \text{ cm}^3\text{s}^{-1}$
<i>photo-induced</i>		
photodissociation	$AB^{(0/+)} + h\nu \rightarrow A^{(0/+)} + B$	10^{-9} s^{-1}

^arestricted to exothermic and barrierless types, i. e., radical-radical

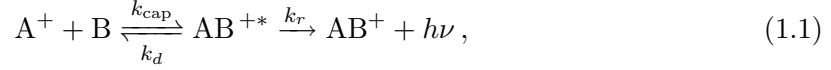
1.3.2.1 Ion-molecule reactions in the ISM

Early developments of chemical models of formation and depletion of small interstellar molecules have been based on ion-molecule reactions [19, 21, 22, 81, 82, 83, 84, 85]. Characterised by the highest reaction rates and based on sufficient ionisation of the ISM, the ion-molecule reactions have been considered to be substantial to the interstellar chemistry [19, 86]. The investigations of this work will be, therefore, addressed to ion-molecule reactions in order to determine the possibility of a thermochemical formation of hydrocarbons and PAHs in the dense and UV-radiation-shielded parts of the ISM.

At the collision, each ion-molecule type reaction is determined by a local minimum of the potential energy. Under energy conservation, the excess energy is dissipated into the molecular system. It leads to electronically, vibrationally and rotationally activated products species. The deactivation is restricted to radiative processes. Ion-molecule reactions that include

^{†5}Binary reactions are restricted to two-body collisions.

radiative deactivation^{†6} are defined as follows [87, 88]:



where k_{cap} represents the association rate constant, k_d is the redissociation rate constant, and k_r corresponds to the radiative emission rate constant. A defined, effective bimolecular rate constant k_{eff} for the loss of coreactants ($-d[A^+]/dt$) or gain of products ($d[AB^+]/dt$) is given by the relation [88, 89]:

$$k_{\text{eff}} = \frac{k_{\text{cap}} \cdot k_r}{k_d + k_r}, \quad \begin{matrix} k_d \gg k_r \\ \simeq \end{matrix} \frac{k_{\text{cap}} \cdot k_r}{k_d}, \quad \begin{matrix} k_d \ll k_r \\ \simeq \end{matrix} k_{\text{cap}}. \quad (1.2)$$

The ion-molecule reaction scheme addressed in this work has been extended since large-sized reactants and products permit multiple isomerisation steps before radiative deactivation (compare Section 2.2.1).

Source of ionisation

The impact of the ion-molecule reactions in the ISM depends on the degree of ionisation of the ISM, which is provided by the cosmic ray^{†7} (CR) and UV radiation of stars. Since the ISM is dominated by hydrogen, mostly hydrogen is ionised by CR. It transfers the ionisation to other molecular species by charge-transfer reactions. or by protonation [86]. The protonation agents H_3^+ is formed by



In diffuse clouds under high stellar radiation fields large molecules, grains, and atoms in particular contribute significantly by photoionisation to the degree of ISM ionisation.

The concept of ion-molecule reactions in UV-radiation shielded parts of the MC is considered to be possible. The cosmic ray rate is supposed to be attenuated by interstellar dust. The ionisation rates of H_2 and H are evaluated with 2.3 times and 1.1 times the primary cosmic-ray ionisation rate ζ_{CR} which decreases from $2 \times 10^{-16} \text{ s}^{-1}$ in diffuse clouds to $3 \times 10^{-17} \text{ s}^{-1}$ in dense clouds [5].

1.3.3 Chemistry modelling by simulating chemical networks

A consequent, next step in the study of interstellar chemical reactions is to retrieve chemical abundances of particular molecules and compound classes in order to compare with observation and to verify the applied model. This has been achieved by the formulation of chemical networks, which basically combine the individually investigated types of interstellar reactions in the set of equations:

$$\frac{dn_i}{dt} = \underbrace{\sum_{j,k} k_{jk} n_j n_k + \sum_j k_j n_j}_{\text{formation}} - n_i \times \underbrace{\left(\sum_j k_{i'j'} n_j + \sum_j k_{j'} \right)}_{\text{depletion}}. \quad (1.4)$$

^{†6}also referred to as ion-molecule radiative association (IMRA) reactions

^{†7}Mostly relativistic protons, He (10%) and electrons (1%) with energies of over 100 MeV per particle.

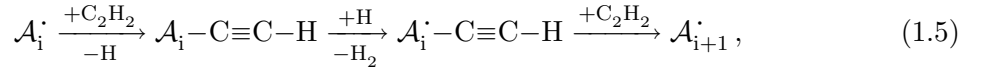
The abundance of each molecule i is determined by considering a set of reactions forming i and destroying i . The type of considered reactions is extendable, in Eq. (1.4) bimolecular (i. e., collision) and unimolecular (i. e., isomerisation) reactions are given.

1.3.3.1 Developments

The modelling of chemical networks in interstellar clouds considering the gas-phase reactions of small molecules have been reported in [19, 83, 84]. Over 130 species and 4000 reactions were used to evaluate chemical abundances with an evolution of 10^{15} seconds. The chemical networks have been extended to include grain-surface reactions [90, 91, 92] in order to improve results in grain-rich environments such as hot cores in MCs. Considered reaction rate coefficients have been enlisted in the UMIST database [93, 94] and the OSU database [95].

1.3.4 Chemistry modelling of hydrocarbon formation and growth processes

Chemistry modelling of hydrocarbon and PAH chemistry for different environments, such as CSEs [3, 96, 97, 98] and dense clouds [22, 25, 99], have been reported. The proposed chemistry of hydrocarbons in CSEs considers mechanisms that relate to soot formation of low-pressure acetylenic combustion and pyrolysis processes [21, 96, 100]. Here, polycyclic hydrocarbons are supposed to grow by an alternating hydrogen abstraction (creation of radicals) and acetylene addition mechanism (HACA) [96, 101]:



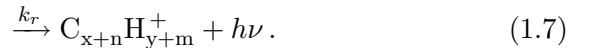
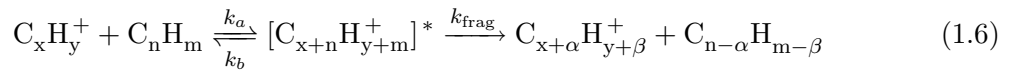
where \mathcal{A} represents the polycyclic hydrocarbon structure with i rings. A similar reaction mechanism has been proposed for polycyclic hydrocarbon cations \mathcal{A}^+ .

Several chemistry models have been set up that evaluate the abundance of large and complex hydrocarbons including PAHs [24, 25]. Unknown rate coefficients and mechanisms for the formation of large hydrocarbons have been simply estimated and averaged by commonly known characteristics of ion-molecule reactions. This means that individual growth mechanisms have been omitted. However, the results indicate that large hydrocarbon structures in the dense clouds in a time of several millions years can be formed.

A detail mechanism for the formation and growth of hydrocarbons and PAHs will be addressed in this work.

1.3.4.1 Considerations on growth of PCH and PAH ions in this work

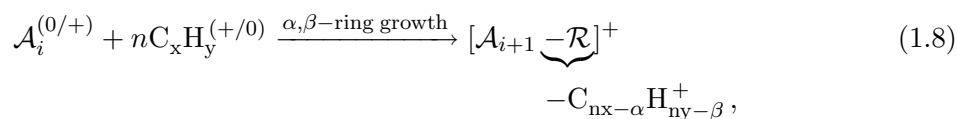
Based on provided concepts for thermochemical reaction in the ISM, the generic ion-molecule growth reaction of hydrocarbons is formulated as follows:



It includes two relaxation routes: fragmentation with rates k_{frag} and radiation with rates k_r .

Schematics of ring growth

The generic ring growth of PCHs and PAHs has been derived as follows:



where \mathcal{A} represents the parent structure of i rings. The n times addition or insertion of a small hydrocarbon precursor provides the formation of an additional ring. \mathcal{R} denotes the carbon and hydrogen excess, which is not required for the new ring of α carbons and β hydrogens. Based on Eq. (1.8) several types of ring growth depending on the structure of the parent structure are depicted in Figure 1.1.

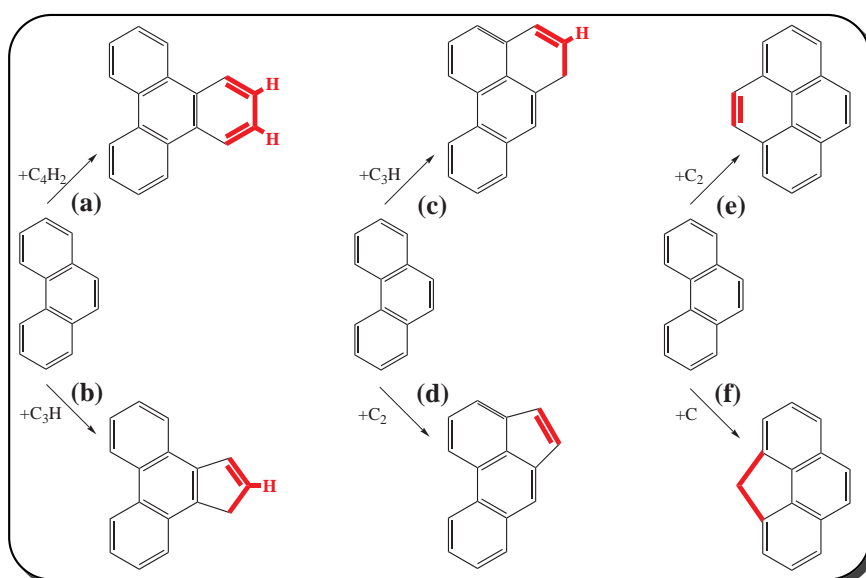


Figure 1.1: Schematic growth of PAHs by hexagons (upper part) and pentagons (lower part), for increasing number of inserted carbon atoms from left to right. The inserted groups are highlighted in the reaction products.

Suitable precursors

The ideal precursors of the PAH growth are C_4H_2 , C_3H and C_2 (Figure 1.1). In the case of an isotropic growth of PAHs, only the C_3H precursors would be required. It corresponds exactly to average amount of carbons and hydrogen per each ring added. However, the observed C_3H abundance as given in Table C.2 is about 2 order of magnitudes below other molecules such as C_2H , CH and C_2 . Among these three precursors, C_2 produces in average a hydrogen deficiencies that would create dehydrogenated PAH structures. The molecules C_2H and CH produce superhydrogenated PAHs.

CH precursor

Based on Figure 1.1, the ring addition by CH addition and insertion produces an excess of two hydrogens. The possibility of the dissociation of these two hydrogens in order to transform the PCH into a PAH structure, will be studied and discussed in this work.

2 Computational methods

A good decision is based on knowledge and not on numbers.

PLATO

In this chapter, the computational methods applied for the characterisation of the chemical reactions are presented. The structuring of the reaction analysis is given in the first section. The following sections deal with:

- Rate theory (Section 2.2), in order to calculate capture rate coefficients based on the *Langevin* model and average dipole orientation (ADO) model, and MD simulation based σ_R , $k_{MD}(\varepsilon)$ and $k_{MD}(T)$ values. The MD based values are derived by the application of a statistical framework. This statistical framework also establishes the determination of the product distribution.
- The details of the thermodynamic equilibrium calculation between products is represented in Section 2.3. It allows to compute a static, barrier-free product distribution and its dependence on temperature. It is based on the molecular properties derived by
- quantum theory methods (Section 2.4). *Ab initio* and DFT methods are enlisted which have been used for the calculation of molecular properties and for the reaction path optimisation. The second part deals with conceptual details of the DFTB method which has been applied to compute molecular dynamics (MD) trajectories.
- The nudged elastic band (NEB) method is described in Section 2.5. This kind of reaction path optimisation method requires energies and forces provided by quantum theory methods.

2.1 Structure of the reaction analysis

In order to study formation processes containing multiple chemical reactions, it is necessary to probe chemical reactions for its potential contribution to the formation process. In the case of this work, the potential of a reaction is evaluated by its impact under ultra-low temperatures (cf. ISM conditions). This can be achieved by MD simulations applying very low collision velocities. If applied in a framework of statistical rate theories, MD simulations provide characteristic reaction parameters. Therefore, the analysis of the chemical reactions is divided in this work into a hierarchic order:

1. MD simulations that provide product branching, reaction probabilities and principal mechanisms.
2. Reaction path analysis in order to study / evaluate low temperature mechanisms.
3. Product property analysis; molecular quantities are used to evaluate thermodynamic stability and thermodynamic product branching. Note that the harmonic (normal-mode) frequencies are retrieved from 2nd derivatives of the electronic energy with respect to the Cartesian nuclear coordinates.

This division has been established by a workflow scheme (Figure 2.1). The precise and

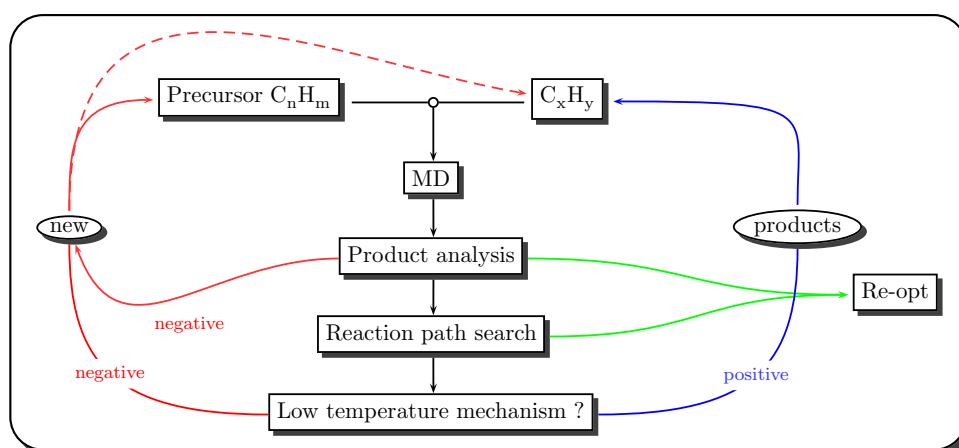


Figure 2.1: Applied workflow scheme of the chemical reaction analysis. The “reuse” of products as reactants in the next cycle of the chemical reaction analysis is depending on the pass of different criteria.

numerically effective sampling of the reaction by the DFTB-MD simulations allows to select or discard any further calculations. Although the precision of the MD simulation results are below of *ab initio* methods, the combination with statistics in terms of random based variable MD initialisation will provide probability weighted reaction routes. These routes are not empirically or manually selected. In contrast, the application of *ab initio* methods to chemical reactions requires a preselection of a single aspect, e. g. rearrangement of a bonding, due to the high computational effort. This preselection is often based on empirical decision or experimental results.

2.1.1 Chemical route analysis

A chemical route such as chain or ring growth is defined as a sequence of single chemical reactions where products are the reactants of the successive reaction. The chemical route analysis basically follows the outcome of each studied reaction. From each reaction the two or three most promising product molecules are considered in the successive reaction analysis as reactants. The selection of products is based on their formation quantities of the actual reaction and their thermodynamic stabilities. By this procedure, the chemical route analysis mimics the actual chemical evolution of a particular molecule.

2.2 Reaction kinetics and statistical rate theories

The rate coefficient k is an attribute of chemical reaction dynamics. It represents the coefficient in the differential equation:

$$\frac{d[X]}{dt} = k[X], \quad (2.1)$$

where $[X]$ is a molecular quantity proportional to the number of elementary entities. The rate coefficient k is determined based on theoretical approaches of reaction kinetics and statistical rate theories.

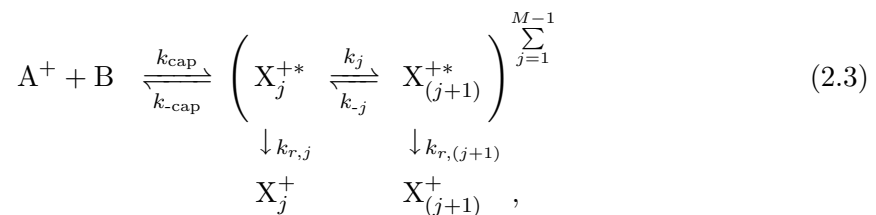
2.2.1 The effective ion-molecule rate coefficient k_{eff}

In the case of complex reaction dynamics that consists of N elementary mechanisms, the rate coefficient k in Eq. (2.1) can be expressed as a function of the rate coefficients of its elementary mechanisms k_i .

$$k = k(k_1, \dots, k_N) \equiv k_{\text{eff}}. \quad (2.2)$$

Each elementary mechanism rate coefficient k_i is additionally a function of energy ε , e. g. in the microcanonical representation of the system, or a function of temperature T , e. g. in the canonical representation of the reaction system. The complex rate coefficient k is also referred to as the effective rate coefficient k_{eff} if it describes the complete reaction.

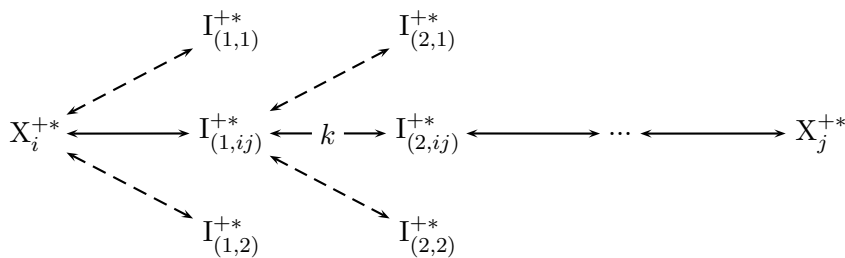
In the case of the ion-molecule reaction as given Eq. (1.1), which are analysed in this work, the effective rate coefficient is given by the relation of Eq. (1.2). Since the radiative ion-molecule based reaction of complex hydrocarbon reactants can involve M intermediate X_j , the chemical equation Eq. (1.1) is extended to the relation:



where k_{cap} is the bimolecular capture rate coefficient, $k_{\text{-cap}}$ represents the backward process of the capture, $k_{r,j}$ is the radiative deactivation rate coefficient, and k_j the forward and k_{-j} the backward isomerisation processes. For each structure in Eq. (2.3) the effective rate coefficient can be derived.

2.2.1.1 Estimation of k_{eff} for isomerisation process between X_i^{+*} and X_j^{+*}

The effective rate coefficient for the isomerisation of the energised product i (X_i^{+*}) to the energised product j (X_j^{+*}) via N intermediates $\text{I}_{(m,ij)}^{+*}$:



is estimated in this work by the relation:

$$k_{\text{eff}}(X_i^{+*} \rightarrow X_j^{+*}) = \min\{k^{\text{forw}}\} \times \prod_{m=1}^N f_{m,i \leftrightarrow j}. \quad (2.4)$$

The term $\min\{k^{\text{forw}}\}$ represents the minimum of all elementary rate coefficient among all directly involved isomerisation process in forward direction from X_i^{+*} to X_j^{+*} . However, each intermediate $I_{(m,i \leftrightarrow j)}^{+*}$ is considered to possess the possibility to decay in multiple intermediates including its origin and its successor on the pathway to X_j^{+*} . This means that from each intermediate only a fraction contributes to the isomerisation path X_i^{+*} to X_j^{+*} . In terms of quantification, this fraction can be defined as follows:

$$f_{m,i \leftrightarrow j} = \frac{k_{m,i \leftrightarrow j}^{\text{forw}}}{\sum k_m}, \quad (2.5)$$

where $k_{m,i \leftrightarrow j}^{\text{forw}}$ is the specified rate coefficient for the isomerisation of the intermediate $I_{(m,i \leftrightarrow j)}^{+*}$ to its successor on the pathway from X_i^{+*} to X_j^{+*} and $\sum k_m$ represents the sum of all possible isomerisation rates of $I_{(m,i \leftrightarrow j)}^{+*}$.

2.2.1.2 Determination of elementary rate coefficients

Each elementary rate coefficient will be calculated by different methods and theories in this work:

1. capture rate coefficients by the *Langevin* and *average dipole orientation* (ADO) model, and by applied statistics on MD simulations,
2. isomerisation rates by the *Rice-Ramsberger-Kassel-Marcus* (RRKM) theory and *canonical transition state theory* (CTST), and
3. radiative deactivation rates by evaluation of density of states and probability of a spontaneous emission.

2.2.2 Phenomenological ion-molecule based capture rate coefficient $k_{\text{cap}}^{\text{P}}$

The capture rate coefficient $k_{\text{cap}}^{\text{P}}$ of each model, k_{L} for *Langevin* and $k_{\text{ADO}}(T)$ for ADO, are based on the description of collisions between particles without structure in an attractive potential (Section E.1.1).

2.2.2.1 The Langevin model [82, 102]

The most simple capture model for ion-molecule reactions, which is also referred as the *Langevin* model, reduces the attractive interaction between the ion and the neutral to ion-induced dipole interactions:

$$V(R) = -\frac{q^2\alpha}{2R^4}, \quad (2.6)$$

where q is the point charge of the ion and α represents the point polarisability^{†1} of the neutral molecule. The reactivity probability is reduced to the step function P (Eq. (E.3)) for which the probability is unity at collision parameters $b < b_{\text{crit}}$. The critical collision parameter b_{crit} is defined as the maximal value for which collisions are reactive. At this specific state the captured reactants are orbiting each other [82].

Based on the potential in Eq. (2.6), the reaction cross section expressed by the critical collision parameter b_{crit} can be derived to the relation as follows:

$$\sigma(\varepsilon_{\text{coll}}) = \pi b_{\text{crit}}^2(\varepsilon_{\text{coll}}) \equiv \sigma_{\text{L}}(\varepsilon_{\text{coll}}) = \pi q \left(\frac{2\alpha}{\varepsilon_{\text{coll}}} \right)^{1/2}. \quad (2.7)$$

The capture cross section in Eq. (2.7) is inverse proportional to the relative collision velocity of reactants v_{coll} ^{†2}. As the result, the microcanonical capture rate coefficient $k_{\text{L}}(v) = v_{\text{coll}}\sigma_{\text{L}}(v)$ is independent of the velocity.

The corresponding thermal, i. e., canonical, rate coefficient $k_{\text{L}}(T)$ is derived by thermal averaging of the collision velocities applying the *Maxwell-Boltzmann* distribution. It follows:

$$k_{\text{L}}(T) = 2\pi q \left(\frac{\alpha}{\mu} \right)^{1/2}, \quad (2.8)$$

where μ is the reduced mass of the collision system, α the point polarisability, and q the charge. The thermal rate coefficient $k_{\text{L}}(T)$ is, therefore, independent of the temperature.

2.2.2.2 Dipole extended Langevin model

In the case of polar molecules the attractive interactions in the ion-molecule collisions are increased by the ion-permanent dipole potential V_{IPD} :

$$V_{\text{IPD}}(r, \theta) = -\frac{\mu_{\text{D}}q}{r^2} \cos \theta, \quad (2.9)$$

where μ_{D} is the permanent dipole moment of the molecule and θ is the angle between the dipole and the line of centres of the collision.

From the new effective potential $V'_{\text{eff}} = V_{\text{eff}} + V_{\text{IPD}}(r, \theta)$ the microcanonical rate coefficient has been derived to the relation [103]:

$$k(v_{\text{coll}}) = \pi \left[\left(\frac{4q^2\alpha}{\mu} \right)^{1/2} + \frac{2q\mu_{\text{D}}}{\mu v_{\text{coll}}} \right]. \quad (2.10)$$

^{†1}The point polarisability is given by the calculation of the isotropic polarisability of a molecule.

^{†2} $\varepsilon_{\text{coll}} = 0.5\mu \cdot v_{\text{coll}}^2$

Note that the v_{coll} corresponds to the relative velocity at infinite separation and the orientation of the dipole to the ion corresponds to $\theta = 0^\circ$. Based on Eq. (2.10), the thermal, i. e., canonical, rate coefficient $k(T)$ becomes [104]:

$$k(T) = \frac{2\pi q}{\mu^{1/2}} \left[\alpha^{1/2} + \mu_D \left(\frac{2}{\pi k_B T} \right)^{1/2} \right]. \quad (2.11)$$

Based on experimental results, the canonical rate coefficients by Eq. (2.11) have been reported to be too high [105]. Similar to the thermal averaging of velocities, a thermally averaged orientation of dipoles has been introduced [106, 107] in order to improve $k(T)$ values. This average dipole orientation (ADO) model introduces to the second term in the Eq. (2.11) a factor C_1 which is a function of the polarisability, the permanent dipole, and the temperature. This factor varies between 0 and 1:

$$k_{\text{ADO}}(T) = \frac{2\pi q}{\mu^{1/2}} \left[\alpha^{1/2} + C_1(\mu_D, \alpha) \mu_D \left(\frac{2}{\pi k_B T} \right)^{1/2} \right]. \quad (2.12)$$

The values of factor C_1 are evaluated according the parameterisation given in reference [107].

2.2.2.3 Disadvantages

The insufficient description of the short-range potentials and the disjoint and averaged reaction probability functions are the major limitations of the methods described above. Improvements are established by molecular dynamics based on quantum chemical theory as described in the following subsections.

2.2.3 Molecular dynamics based capture rate coefficient $k_{\text{cap}}^{\text{MD}}$

Based on the trajectories of molecular dynamics simulations, the microcanonical and canonical capture rate coefficients, $k_{\text{MD}}(\varepsilon)$ and $k_{\text{MD}}(T)$, are evaluated from counting statistics (Section E.1.2), i. e., reaction probability statistics P , and corresponding reaction cross sections σ_{R} .

The theoretical and technical realisation of the MD simulations are given in Section 2.4.3.1 and Section B.1. The technical determination of $k_{\text{MD}}(\varepsilon_{\text{coll}})$ and $k_{\text{MD}}(T)$ is given in Section B.2.

2.2.3.1 Determination of reaction cross section

The reaction cross section $\sigma_{\text{R},j}$ of the product j is determined by the relation:

$$\sigma_{\text{R},j}(\varepsilon_{\text{coll}}) \equiv \sigma_{\text{R},i_0 \rightarrow \{j\}}(\varepsilon_{\text{coll}}) = 2\pi \int_0^{b_{\text{max}}(\varepsilon)} P_{i_0 \rightarrow \{j\}}(\varepsilon_{\text{coll}}, b) b db. \quad (2.13)$$

The initial states α of the reactant pair i are, however, not averaged in this work according their statistical weights p_α . The MD simulations and corresponding counting statistics are reduced to the initial state of “frozen” reactants i_0 , i. e., without any non-fixed energy.

This reduction is considered to be sufficient since under the physical conditions of the ISM mostly low-level vibrational-rotational states of the reactant pair are occupied. These states combine a weight close to unity. In this work, these were approximated by i_0 , which in turn is approximately equal to the the initial state averaged reaction cross section $\sigma_{\text{R},\bar{i}\rightarrow\{j\}}$:

$$\sigma_{\text{R},i_0\rightarrow\{j\}}(\varepsilon_{\text{coll}}) \approx \sigma_{\text{R},\bar{i}\rightarrow\{j\}}(\varepsilon_{\text{coll}}). \quad (2.14)$$

This approximation is also supported by the fact that the investigated ion-molecule reactions have high non-collisional energy impact on their products, which exceeds the difference between the averaged initial state and the zero initial state $\varepsilon_{\text{rct}} \gg \Delta(\varepsilon_{\bar{i}} - \varepsilon_{i_0})$, thus negating any individual effect of a particular low-level state occupation on cross sections.

2.2.3.2 Determination of microcanonical capture rate coefficient $k_{\text{MD}}(\varepsilon_{\text{coll}})$

The non-state correlating microcanonical capture rate coefficient $k_{\text{MD}}(\varepsilon_{\text{coll}})$ is determined by the relation:

$$k_{\text{MD}}(\varepsilon_{\text{coll}}) = \sqrt{\frac{2\varepsilon_{\text{coll}}}{\mu}} \times \sum_j \sigma_{\text{R},i_0\rightarrow\{j\}}(\varepsilon_{\text{coll}}). \quad (2.15)$$

The summation of reaction cross sections over all products and intermediates defines the effective capture cross section where reaction probabilities and steric factors are determined by quantum chemical methods.

2.2.3.3 Determination of canonical capture rate coefficient $k_{\text{MD}}(T)$

The non-state correlating canonical capture rate coefficient $k_{\text{MD}}(\varepsilon_{\text{coll}})$ is defined by thermal averaging of the collision velocities and corresponding cross sections based on the *Maxwell-Boltzmann* distribution:

$$k_{\text{MD}}(T) = \sqrt{\frac{8}{\pi\mu k_{\text{B}}^3 T^3}} \int_0^\infty \varepsilon_{\text{coll}} e^{-\varepsilon_{\text{coll}}/k_{\text{B}}T} \times \left(\sum_j \sigma_{\text{R},i_0\rightarrow\{j\}}(\varepsilon_{\text{coll}}) \right) d\varepsilon_{\text{coll}}. \quad (2.16)$$

2.2.4 Isomerisation/dissociation rate coefficients - k_{x_i} , k_d

The unimolecular rate coefficients of isomerisation processes k_{x_i} and of dissociation / fragmentation processes k_d are evaluated by the *Rice-Ramsberger-Kassel-Marcus* (RRKM) theory (Section 2.2.4.1) and the *canonical transition state theory* (CTST) (Section 2.2.4.2). Molecular parameters such as harmonic frequencies and potential energies are obtained by DFT and *ab initio* calculations (Section 2.4).

2.2.4.1 Isomerisation rate coefficients evaluated by the RRKM theory

Determination of $\mathcal{W}(E)$ and $\rho(E)$ by direct counting of the quantum states

The simplest method known for the determination of the molecular quantum state sum $\mathcal{W}(E)$ and density $\rho(E)$ is the direct counting of all molecular quantum states. In particular for

harmonic oscillators, the Beyer-Swinehart (BS) algorithm [108, 109] gives an exact determination of $\mathcal{W}(E)$ and $\rho(E)$. Since the frequency determination in this work is based on the harmonic approximation, the counting of vibrational states by BS algorithm is exact. The sum and density of states for a given non-fixed energy (which is within the method referred as E_{\max}) are given by the relations:

$$\mathcal{W}(E_{\max}) = \sum_j^{E_{\max}} \mathcal{S}(E_j), \quad \rho(E_{\max}) = \frac{\mathcal{S}(E_{\max})}{\Delta E}, \quad (2.17)$$

where the working procedure divides the given non-fixed energy ($\simeq E_{\max}$) into intervals of grain size ΔE and counts all states within one interval j , i. e., $\mathcal{S}(E_j)$.

The summation up to E_{\max} gives the total sum \mathcal{W} . The division of number of state of the last interval ($\mathcal{S}(E_{\max})$) by the grain size results in the density of states at E_{\max} .

Rotors and anharmonicity of oscillators are not considered by the direct counting of the states within this work, but can be treated by the modification of the BS algorithm, i. e., the Stein-Rabinovitch (SR) algorithm [109].

The discontinuity in \mathcal{W} at low non-fixed energies may lead to zero density of states (compare diagrams within reference [110]). Therefore, an approximation of the density of states, which provides a continuous function, is used.

Semiclassical approximation of vibrational states

The Whitten-Rabinovitch (WR) approximation of quantised vibrational states of harmonic oscillators is used to calculate $\mathcal{W}(E)$ and the continuous function $\rho(E)$. Detailed description of all the introduced parameters below-mentioned can be found in references [110, 111, 112]. The empirical parameter α is introduced to the semiclassical *Marcus-Rice* approximation [113] in order to fit the sum of states \mathcal{W}_{WR} to \mathcal{W} of the direct counting:

$$W_{\text{WR}}(E_{\text{vib}}) = \frac{(E_{\text{vib}} - \alpha E_{\text{zpv}})^s}{\Gamma(s+1) \prod_i^s h \nu_i}, \quad \text{with} \quad \alpha = 1 - \beta_{\text{R}} \omega\left(\frac{E_{\text{vib}}}{E_{\text{zpv}}} = E_{\text{red}}\right) \quad (2.18)$$

$$\beta_{\text{R}} = \frac{(s-1)}{s} \frac{\sum \nu_i^2}{(\sum \nu_i)^2}$$

$$\omega(E_{\text{red}}) = \begin{cases} (5.00E_{\text{red}} + 2.73\sqrt{E_{\text{red}}} + 3.51)^{-1} & \text{if } 1.0 > E_{\text{red}} > 0.1 \\ \exp(-2.4191 \sqrt[4]{E_{\text{red}}}) & \text{if } E_{\text{red}} > 8.0 \end{cases},$$

where s is the number of harmonic oscillators, E_{vib} is the non-fixed energy distributed in the vibrational modes, E_{zpv} is zero-point energy, and Γ is the gamma function. *Whitten et al.* found in the parameter α an analytical relation between the distribution of the molecular frequencies, expressed by β_{R} , and the reduced energy $E_{\text{red}} (= E_{\text{vib}}/E_{\text{zpv}})$ [111] given by the factor $\omega(E_{\text{red}})$ (compare equations (2.18)). The density of vibrational states $\rho_{\text{WR}}(E_{\text{vib}})$ is given by the relation:

$$\rho_{\text{WR}}(E_{\text{vib}}) = \frac{dW_{\text{WR}}(E_{\text{vib}})}{dE_{\text{vib}}} = \frac{(E_{\text{vib}} - \alpha E_{\text{zpv}})^{(s-1)}}{\Gamma(s) \prod_i^s h \nu_i} \left[1 - \beta_{\text{R}} \frac{d\omega}{dE_{\text{red}}} \right], \quad (2.19)$$

where $d\omega/dE_{\text{red}}$ represents the first derivatives of the analytical function ω with respect to the reduced energy.

Semiclassical approximation of combined vibrational-rotational states

The evaluation of the combined vibrational-rotational quantum state sums $\mathcal{W}(E_{\text{vr}})$ and density $\rho(E_{\text{vr}})$ is based on the Whitten-Rabinovitch approximation incorporating rotational states. Both $\mathcal{W}_{\text{WR}}(E_{\text{vr}})$ and $\rho_{\text{WR}}(E_{\text{vr}})$ are given by the relation [112, 114]:

$$\mathcal{W}_{\text{WR}}(E_{\text{vr}}) = \underbrace{\left(\frac{8\pi^2}{h^2}\right)^{\frac{1}{2}r} \prod_{j=1}^p \left\{ \Gamma\left(\frac{1}{2}d_j\right) \mathcal{I}_j^{\frac{1}{2}d_j} \right\}}_{\parallel} \times \frac{(E_{\text{vr}} - \alpha E_{\text{zpv}})^{(s+\frac{1}{2}r)}}{\Gamma(s+1+\frac{1}{2}r) \prod_i^s h \nu_i} \quad (2.20)$$

$$\rho_{\text{WR}}(E_{\text{vr}}) = q'_{\text{rot}} \times \frac{(E_{\text{vr}} - \alpha E_{\text{zpv}})^{(s-1+\frac{1}{2}r)}}{\Gamma(s+\frac{1}{2}r) \prod_i^s h \nu_i} \left[1 - \beta'_R \frac{d\omega}{dE_{\text{red}}} \right], \quad (2.21)$$

where r is the total number of rotors, p is the number of degenerated rotors, and d_j is the degeneracy of the j -th rotor. The parameter β'_R refers to β_R scaled by the factor $(s+0.5r)/s$. The prefactor q'_{rot} represents the contribution of the rotational states to the combined vibrational-rotational states and corresponds to the rotational partition function Q_{rot} reduced by the temperature, i. e., $q'_{\text{rot}} = Q_{\text{rot}}/(kT)^{\frac{1}{2}r}$.

2.2.4.2 Rate coefficients based on the CTST

The microcanonical rate coefficients based on the RRKM theory are compared with canonical rate coefficients based on the CTST. The derivation of the CTST rate coefficient can be found in references [115, 116]. The concepts of the transition state in the RRKM theory trace back to the CTST. Based on the equilibrium constant K^\ddagger between the educt molecule and transition state, the overall rate coefficient k_{CTST} is expressed in terms of the partition functions Q_i as:

$$k_{\text{CTST}}(T) = \frac{k_B T}{h} \frac{Q^\ddagger}{Q} e^{-E_0/k_B T}, \quad (2.22)$$

where the factor $k_B T/h$ represents the mode of the translational motion.

Definition of the temperature

For the transition from the microcanonical to the canonical treatment of the system, the temperature is evaluated by the given/calculated energy of collision/reaction process applying the equipartition theorem. In the case of given non-fixed energy E_{vr} , the temperature is determined by $T = 2E_{\text{vr}}/((3N-3)k_B)$ excluding the translational degrees of freedom.

Modification

In order to compensate the overestimation of CTST rate coefficients [110], a quasi-microcanonical version of Eq. (2.22) is **tested** in this work. The thermalised educt at the internal

temperature T_1 is considered to be in an adiabatic equilibrium with the thermalised transition state at the internal temperature T_2 . Both temperatures were determined by the equipartition theorem at which the total energy of both systems was kept equal. The new rate coefficient k_m is expressed by the relation:

$$k_m(T_1, T_2) = \frac{k_B \langle T_{1,2} \rangle Q^\ddagger(T_2)}{h Q(T_1)}, \quad (2.23)$$

where the temperature of the factor of the translational motion is averaged between T_1 and T_2 . The exponential factor of Eq. (2.22) is omitted, since it represents the energy level correction in the combined system of energetic states [117].

2.2.5 The radiative relaxation rate coefficients k_r

In environments of low density such as the ISM, the relaxation of molecules is restricted to non-collisional processes, i. e., radiative relaxation by photon emission. The radiative relaxation/decay rate coefficients k_r of energetically activated complexes $A^* \text{ }^\dagger 3$, corresponding to:



are evaluated by a statistical approach. The relaxation of the energised complex is determined by the calculated probability of the spontaneous transmission of a vibrational-rotational mode i from level n_i to level $n_i - 1$. This corresponds to an infrared photon emission. The determined values can be, therefore, considered as *infrared* radiative cooling rates.

2.2.5.1 General statistical approach

Under the consideration of normal mode oscillators, the overall radiative vibrational relaxation rate of a polyatomic molecule with the vibrational energy E_{vib} is given by the relation [118]:

$$k_r = \sum_i \sum_{n_i} P_{n_i}^{(i)}(E_{\text{vib}}) \mathcal{A}_{n_i \rightarrow n_i - 1}^{(i)} \approx \sum_i \sum_{n_i} P_{n_i}^{(i)}(E_{\text{vib}}) n_i \mathcal{A}_{1 \rightarrow 0}^{(i)}, \quad (2.25)$$

where $\mathcal{A}_{n_i \rightarrow n_i - 1}^{(i)}$ is the *Einstein* coefficient of the vibrational mode i undergoing a transmission from level n_i to level $n_i - 1$ weighted by the probability $P_{n_i}^{(i)}$ of the mode i being in level n_i . The summation over all modes i and energetically accessible quanta n_i results in k_r . Due to the harmonic oscillator approximation, the *Einstein* coefficients $\mathcal{A}_{n_i \rightarrow n_i - 1}^{(i)}$ can be approximated by their lowest occupation numbers as follows:

$$\mathcal{A}_{n_i \rightarrow n_i - 1}^{(i)} = n_i \mathcal{A}_{1 \rightarrow 0}^{(i)}. \quad (2.26)$$

Higher transition, i. e., $\mathcal{A}_{n_i \rightarrow n_i - 2}^{(i)}$, viz. “overtones”, and transitions of combined modes i and j , i. e., $\mathcal{A}_{n_i n_j \rightarrow n_i - 1, n_j - 1}^{(i,j)}$, are not considered. The rate coefficient obtained by Eq. (2.25) are

^{†3}The term “complex” refers to the a polyatomic compound with an internal energy above or near the dissociation limit.

referred to as “fundamental” since it considers only $n \rightarrow n - 1$ transitions. The detailed derivation of Eq. (2.25) including overtones and combined modes can be found in reference [118].

2.2.5.2 Determination of $\mathcal{A}_{1 \rightarrow 0}^{(i)}$

The *Einstein* coefficients $\mathcal{A}_{1 \rightarrow 0}^{(i)}$ are determined by the relation:

$$\mathcal{A}_{1 \rightarrow 0}^{(i)} = \frac{8\pi}{c} \nu_i^2 I_i, \quad (2.27)$$

where the infrared absorption intensities I_i are evaluated by the relation [119, 120]:

$$I_i = \frac{N_A \pi}{3c^2} \left[\left(\frac{\partial \mu_x}{\partial Q_i} \right)^2 + \left(\frac{\partial \mu_y}{\partial Q_i} \right)^2 + \left(\frac{\partial \mu_z}{\partial Q_i} \right)^2 \right], \quad (2.28)$$

i. e., by the derivation of the dipole moments μ .

2.2.5.3 Determination of $P_{n_i}^{(i)}$

The probabilities $P_{n_i}^{(i)}$ of the individual modes i being in the level n_i are given by the relation [118, 121]:

$$P_{n_i}^{(i)} = \frac{\rho'_{\text{vib}}(E_{\text{vib}} - n_i h \nu_i)}{\rho_{\text{vib}}(E_{\text{vib}})}, \quad (2.29)$$

where $\rho(E_{\text{vib}})$ is the density of vibrational states at the non-fixed energy E_{vib} , and $\rho'(E_{\text{vib}})$ is the density of vibrational states excluding mode i and n_i quanta.

2.2.5.4 Extension to vibrational-rotational states & WR approximation

The densities obtained by Eq. (2.29) are extended to vibrational-rotational states in order to account for the coupled vibrational and rotational states corresponding the total non-fixed energy E_{vr} in polyatomic molecules [88]. The determination of these densities is based on the *Whitten-Rabinovitch* approximation of vibrational-rotational states [114] (Section 2.2.4.1). The combination of Eq. (2.21) and Eq. (2.29) results in the relation:

$$P_{n_i}^{(i)} = \frac{(E_{\text{vr}} - n_i h \nu_i + a' E'_{\text{zpv}})^{(s+r/2-2)}}{(E_{\text{vr}} + a E_{\text{zpv}})^{(s+r/2-1)}} \left(s + \frac{r}{2} - 1 \right) h \nu_i \left[\frac{1 - \beta_{\text{R}} \left(\frac{\partial \omega}{\partial E'_{\text{Red}}} \right)}{1 - \beta_{\text{R}} \left(\frac{\partial \omega}{\partial E_{\text{Red}}} \right)} \right], \quad (2.30)$$

where the variables with the prime correspond to a system with $s - 1$ oscillators. The definition of each of these variables are described in Section 2.2.4.1.

2.3 Thermodynamic equilibrium between products

Based on Eq. (2.3), energised intermediates and products of ion-molecule reactions are considered to be in thermodynamic equilibrium. This approximation is applied in order to

evaluate the product distribution based on thermodynamics.

This procedure is established by evaluating the relative stability of each product based on the relative local minimum energies and the partition functions. The determination of the partition functions is based on the harmonic frequency analysis.

2.3.1 Definition of the relative concentrations

For the determination of the relative concentration several assumptions are established^{†4}. As a result, existing isomerisation barriers are ignored and do not effect the thermodynamic equilibrium.

The population of the state i by the composite product system is defined as [117]:

$$n_i = N \frac{e^{-\varepsilon_i/k_B T}}{q}, \quad (2.31)$$

where N is the total number of molecules and $q = \sum_j e^{-\varepsilon_j/k_B T}$ the total partition function. The total number of k product molecules is the sum of these populations taken over the states belonging to k :

$$N_k(T) = \frac{N}{q} \sum_k e^{-(\varepsilon_k + \Delta\varepsilon_{0,k})/k_B T} = \frac{N q_k}{q} \sum_k e^{-\Delta\varepsilon_{0,k}/k_B T}, \quad (2.32)$$

where $\Delta\varepsilon_k$ is the energy difference between ground state energy of product k and the lowest product ground state corrected by their zero-point energies ($\Delta\varepsilon_{0,k} = \Delta\varepsilon_{\text{tot},k} + \Delta\varepsilon_{\text{zpe},k}$). The fraction of a product $x_k(T)$ in the mixture is finally determined by [122, 123, 124]:

$$x_k(T) = \frac{N_k(T)}{\sum_m N_m(T)} = \frac{q_k(T) \cdot e^{-\Delta\varepsilon_{0,k}/k_B T}}{\sum_m q_m(T) \cdot e^{-\Delta\varepsilon_{0,m}/k_B T}} \quad \text{with } k = 1, \dots, m. \quad (2.33)$$

2.4 Quantum chemistry methods

The determination of thermodynamic and molecular quantities as well as energies and forces are based on the concepts of the quantum chemistry.

2.4.1 *Ab initio* methods

Within the reaction analysis approach of this work (Section 2.1), *ab initio* methods are considered as the last level of the analysis where thermodynamic and molecular quantities are refined in order to achieve high accuracy quantities. Despite the high level of accuracy, the high scaling of the computational costs to the molecular size in terms of atoms permits only selected molecular structures for the application to *ab initio* methods. The computation of molecular energies, geometries^{†5} and harmonic frequencies have been restricted to

^{†4}i) The energetic states of each product are combined together where ii) each energetic state is independent and iii) the energy redistribution is accessible to all energetic states and is considerably fast.

^{†5}The determination of the geometry is based on different iterative methods such as Berny [125], Fletcher-Powell, quasi-Newton algorithm for finding the local minimum.

Møller-Plesset perturbation methods and the G3 method, which represents composite *ab initio* methods. A comparison of *ab initio*-based quantities with methods of the DFT will be also given in this work.

Møller-Plesset perturbation methods

The two prevalent methods used in this work are the MP2 [126] and the MP4 (as part of the G3 method) [127, 128] theory as implemented in the Gaussian program package [119, 129, 130]. Both methods are characterised by the calculation of the correlation energy in terms of the perturbation theory [131]. In the notation of the perturbation theory, the MP2 and MP4 energies correspond to the second and fourth perturbation order.

The second order perturbative correlation covers about 80-90% of the electron correlation. MP4 improves only by a small fraction the MP2 correlation energy [127]. MP_x calculations scale as $\mathcal{O}(n^{x+3})$ which make high order MP_x methods very computational demanding.

In the present study, the MP2 method has been applied with different basis sets (Section E.2). For convenience, the combination of MP2 and the double-zeta *split-valence* basis set 6-31G(d) [132], i. e., MP2/6-31G(d), has been abbreviated Mdz1. Further combinations of MP2 with different correlation-consistent valence basis sets^{†6} cc-pVDZ, cc-pVTZ, and aug-cc-pVTZ [133] are denoted by Mdz2, Mtz2, and Mtz3.

Composite *ab initio* methods

Apart from MP2 calculations, composite *ab initio* methods have been employed in order to calculate thermodynamic quantities. These methods combine high levels^{†7} of theory and small basis sets with methods of lower levels of theory with larger basis sets. It results in quantities that can be related to the extrapolation to a high level of theory with a large basis set at reduced computational costs.

Gaussian- N methods are one of the most commonly used composite methods. In the Gaussian-1 method [134], the total electronic energy of Mdz1 optimised structures is extrapolated to the QCISD(T)/6-311+G**(2df) level of theory. QCISD(T) level of theory represents a configuration interaction method [131], which has been shown to reproduce well the full configuration interaction (FCI) near equilibrium geometries [135] The basis set 6-311+G**(2df) is a triple-zeta split-valence basis set with contributions of diffuse and polarisation functions.

Within this work, the Gaussian-3 (G3) [136] method has been employed to calculate such thermodynamic quantities as the molar and free molar enthalpies. The Gaussian-3 based calculation of corresponds to QCISD(T)/G3large level of theory. The G3large basis set represents a composite triple-zeta basis set that provides for hydrogen a 6-311+G(2p) basis set, for 1st row elements 6-311+G(2df), and 2nd row elements 6-311+G(3d2f).

2.4.2 Density functional theory methods

The class of density functional theory (DFT) methods represents another fundamental concept of the modern quantum theory. In this concept the electronic structures are described

^{†6}These basis sets are designed to converge systematically to the complete basis set (CBS)

^{†7}Within the *ab initio* methods, the term “level” also refers to the level of the electronic correlation correction.

by their densities. The scaling of the numerical effort with increasing molecular size is, therefore, lower than for *ab initio* methods.

Depending on the description of the exchange-correlation potential V_{xc} [137], DFT methods are highly suitable for the determination of relative energies and reaction barriers for midsized and large molecules [137]. Therefore, DFT methods have been employed extensively in this work.

Generalised gradient approximation methods

Generalised gradient approximation (GGA) methods improve the shortcomings of the LDA methods by the introduction of density gradients [137].

For the calculation of thermodynamic properties two GGA methods have been employed in this work - the PW91 [138, 139] and PBE [140] method. For both methods, the local spin density basis sets DZVP [141] and TZVP [141] have been used. The following abbreviations are introduced in this work:

- Ptz4 for PW91/TZVP and Pdz4 for PW91/DZVP
- PEtz4 for PBE/TZVP and PEDz4 for PBE/DZVP

Hybrid methods

Hybrid methods are based on the combination of DFT and HF concepts for the approximations of the exchange-correlation energy (E_{xc}) [137]. Hybrid methods use semiempirical parameters in order to weight components of the approximative E_{xc} expression. These parameters are obtained by fitting to different thermodynamic quantities of molecule test sets. Despite the difficulties in the physical justification of this procedure, hybrid methods are extensively used due to reduced errors by up to 50% in calculations such as of bond length and thermodynamic quantities compared to LDA and GGA methods [137].

Within this work, the B3LYP method [142, 143] has been employed in order to calculate different thermodynamic quantities. B3LYP has been also applied for the geometry and reaction path optimisation. Applied basis sets range from 6-31G(d) over 6-311++G(3df,3pd), cc-pVDZ, and cc-pVTZ to aug-cc-pVTZ; the corresponding abbreviations are Bdz1, Btz1, Bdz2, Btz2 and Btz3, respectively.

In order to reduce the computational effort, a combination of geometry optimisation at lower level with single-point energy calculation at higher level of quantum theory is introduced; the notation will be `methodsingle point//methodGeometry`. Within this work, the combination of single-point energies at Btz1 with the geometry of Bdz1, denoted as Btz1//Bdz1, has been commonly applied.

2.4.3 Density-functional tight-binding method

The calculation of energies and their 1st derivatives (forces) with the *ab initio* and DFT methods and approximations demands high computational efforts (due to the iterative solvation). Regarding a single structure, such computational efforts are acceptable. However, with the task of performing molecular dynamics simulations (Section 2.4.3.1), i. e., propagating a large reaction systems over a period of picoseconds, the computational effort effectively increases

by several thousand times compared to a generic single point calculation. Although DFT pseudopotentials^{†8} schemes give a computational improvement, application for this work’s MD simulation scheme is questionable.

In order to avoid iterative and integration algorithms, an approximative LCAO-DFT-LDA scheme, originally developed by Seifert and coworkers [144], is used. Its resulting scheme corresponds to non-orthogonal tight-binding methods [26, 27], hence it is referred to as non-orthogonal **DF**-based **TB** scheme. The parameterisation of *Hamiltonian* and overlap matrix elements is not empirical but obtained from SCF-LDA calculations. It makes the DFTB scheme superior to empirical TB schemes, since it is transferable to any element of the period table.

In this work, the `deMon` package [145], maintained by *T. Heine*, was applied to perform MD simulations based on the DFTB method. It has been extended by the implementation of the NEB method in order to calculate minimum energy paths (Section 2.5).

The approximation of the effective potential

The application of the LCAO approach, where a set of K known spatial functions are linearly combined in order to produce a set of K molecular orbitals ψ_i

$$\psi_i = \sum_{\mu=1}^K C_{\mu i} \phi_{\mu} \quad i = 1, 2, \dots, K, \quad (2.34)$$

allows the description of the *Kohn-Sham* orbitals by the nuclei-centred atomic basis functions $\phi(\vec{r} - \vec{R})$. The *Kohn-Sham* equations can be, therefore, transformed into a set of algebraic equations (secular equations):

$$\sum_{\nu} c_{\nu i} (H_{\mu\nu} - \varepsilon_i S_{\mu\nu}) = 0 \quad \forall \mu, i, \quad (2.35)$$

$$S_{\mu\nu} = \langle \phi_{\mu} | \phi_{\nu} \rangle, \\ H_{\mu\nu} = \langle \phi_{\mu} | \hat{T} + V_{\text{eff}}(\vec{r}) | \phi_{\nu} \rangle,$$

where $H_{\mu\nu}$ and $S_{\mu\nu}$ are the elements of the Hamiltonian and the overlap matrix. In order to achieve the computational favourable two-centre representation for $H_{\mu\nu}$, the non self-consistent, effective one-electron potential $V_{\text{eff}}(\vec{r})$ is approximated by a superposition of atomic effective potentials v_0^k

$$V_{\text{eff}}(\vec{r}) = \sum_k v_0^k(\vec{r}). \quad (2.36)$$

Consistent to the approximation of the effective potential, the matrix elements of the *Hamil-*

^{†8}Strongly localised electrons around nuclei are described together by one potential and are not anymore explicitly considered.

tonian are reduced to two-centre contributions.

$$H_{\mu\nu} = \begin{cases} \langle \phi_\mu | \hat{T} + v_0^\alpha(\vec{r}) + v_0^\beta(\vec{r}) | \phi_\nu \rangle & \text{if } \mu \in \alpha, \nu \in \beta, \alpha \neq \beta, \\ \varepsilon_\mu & \text{if } \mu = \nu, \\ 0 & \text{otherwise.} \end{cases} \quad (2.37)$$

The diagonal elements contain the energies of the free atoms to insure correct asymptotic behaviour of dissociations into atoms.

Since matrix elements depend only on interatomic distances, they need only to be calculated once for each kind of element pair. Effectively, the matrix elements are stored in advance which obsoletes integration and makes the DFTB method as fast as common TB methods.

The total energy

Considering the superposition of atomic effective potentials, the total energy of *Kohn-Sham* DFT is given by:

$$E[\rho] = \sum_i^{\text{occ}} \varepsilon_i - \frac{1}{2} \sum_{\alpha,\beta} \int V_{\text{eff}}^{(\alpha)}(\vec{r}) \rho^\beta(\vec{r}) d\vec{r} - \frac{1}{2} \sum_{\alpha,\beta} \int \frac{Z_\alpha \rho^\beta(\vec{r})}{|\vec{r} - \vec{R}_\alpha|} d\vec{r} \quad (2.38)$$

$$+ \frac{1}{2} \sum_{\alpha \geq \beta} \int V_{\text{xc}}[\rho^\alpha(\vec{r}), \rho^\alpha(\vec{r})] \rho^\beta(\vec{r}) d\vec{r} + \frac{1}{2} \sum_{\alpha \neq \beta} \frac{Z_\alpha Z_\beta}{|\vec{R}_\alpha - \vec{R}_\beta|}.$$

Except the 1st term (sum over eigenvalues), all term can consistently reduced to two-centre contribution and summarised in a single short-range repulsive potential [146, 147]:

$$E_{\text{tot}}[\rho] = \sum_i^{\text{occ}} \varepsilon_i + \sum_{\alpha \neq \beta} U_{\text{rep}}(|\vec{R}_\alpha - \vec{R}_\beta|), \quad (2.39)$$

which effectively corresponds to the TB scheme. This short-range potential is parameterised and determined by comparison between calculations of *ab initio* methods and the DFTB eigenvalues of appropriate reference systems (dimers, small molecules, bulk systems):

$$U_{\text{rep}}(R_{\alpha\beta}) = E_{\text{tot}}^{\text{LDA}}(R_{\alpha\beta}) - \sum_i n_i \varepsilon_i(R_{\alpha\beta}). \quad (2.40)$$

In practice, the repulsive potentials are fitted by minimisation procedures to spline or polynomial representations

$$U_{\text{rep}}(R_{\alpha\beta}) = \sum_m C_m (R_c - R_{\alpha\beta})^m, \quad \forall R_{\alpha\beta} < R_c. \quad (2.41)$$

Empirical dispersion augmentation

The asymptotic behaviour of the ion-molecule reactions is determined by long-range potentials emerging from interactions between ions and molecule (dipole, induced dipole) and dispersion forces. Within the DFT and DFTB, only ion-induced dipole interaction are considered, while further asymptotic potentials are omitted. The augmentation of dispersion

interaction to DFTB was reported by *Elstner et al.* [148, 149] and has been used in this work as provided by the *deMon* package [145]. To consider ion-permanent dipole interactions for the determination of MD based capture rate coefficients, an extrapolation has been introduced (Section 4.6).

The *London* dispersion interaction was introduced to the DFTB [148, 149] using:

$$E_{\text{disp}} = E_{\text{DFTB}} - \sum_{i,j} f(\vec{R}_{ij}) \frac{C_{ij}}{\vec{R}_{ij}^6}, \quad (2.42)$$

where $C_{\alpha\beta} = I_i\alpha_i I_j\alpha_j / (I_i + I_j)$ represent a coefficient calculated by the empirical ionisation potentials I and polarisabilities α of the atoms i and j . The damping function $f(\vec{R}_{\alpha\beta})$ guarantees that the dispersion interaction vanishes at short range distances.

A self-consistent scheme

In case of strongly polarising heteroatomic systems, redistribution of charges are of importance which, however, is not provided by the DFTB scheme. An added scheme of self-consistence to the DFTB is based on a self-consistent charge (SCC) correction [148]. The total energy is expanded by second-order *Coulomb* correction term

$$E_{\text{tot}}^{\text{SCC}}[\rho] = \sum_i^{\text{occ}} \varepsilon_i + \sum_{\alpha \neq \beta} U_{\text{rep}}(|\vec{R}_\alpha - \vec{R}_\beta|) + \frac{1}{2} \sum_{\alpha\beta} \Delta Q_\alpha \Delta Q_\beta \gamma_{\alpha\beta} (|\vec{R}_\alpha - \vec{R}_\beta|), \quad (2.43)$$

where Q_i denotes the charge centred at atom i and $\gamma_{\alpha\beta}$ represents a parameter which is related to the chemical hardness η_i [150].

In this work, thermodynamic quantities calculated by the SCC-DFTB are denoted by SD.

2.4.3.1 Molecular dynamics

Molecular dynamics (MD) simulation are based on an approximate approach of quantum molecular dynamics in order to study long simulation times and accumulate proper amount of trajectories for the statistics (Section 2.2.3). Therefore, the MD simulations are described by a coupled set of Newton-type equations.

$$m_j \ddot{\vec{R}}_\alpha = - \frac{\partial}{\partial \vec{R}_\alpha} E(\vec{R}_1, \dots, \vec{R}_M) = -F_\alpha. \quad (2.44)$$

The classical trajectories $\vec{R}_\alpha(t)$ are propagated by the quantum-mechanically calculated energies and forces acting on the M nuclei. Both energies (Eq. (2.38) and Eq. (2.42)) and forces are derived from the non-SCC DFTB method including *London* dispersion:

$$F_\alpha = \sum_i^{\text{occ}} \sum_{\mu\nu} c_{\mu i} c_{\nu i} \left[- \frac{\partial H_{\mu\nu}}{\partial \vec{R}_\alpha} + \varepsilon_i \frac{\partial S_{\mu\nu}}{\partial \vec{R}_\alpha} \right] + \sum_\beta \frac{\partial}{\partial \vec{R}_\alpha} U_{\text{rep}}(|\vec{R}_\alpha - \vec{R}_\beta|) + \frac{\partial}{\partial \vec{R}_\alpha} E_{\text{disp}}. \quad (2.45)$$

Unless stated differently, the set of motion equations were solved by the *Verlet* algorithm [151] and a time step of 10 a.u. (2.419×10^{-17} s).

2.5 Reaction minimum energy path and transition state search

Methods for the minimum energy path and transition state (TS) optimisation were applied in order to find transition states. Attributes and thermodynamic quantities of TS are required for different methods applied in this work, e.g. isomerisation rate coefficients evaluation (Section 2.2.4.1).

Initialisation

The initialisation of the minimum energy path (MEP) optimisation / search was based on the coordinates of MD trajectories. In the case, a proposed transition or rearrangement between two isomers was not observed by the MD simulations, manual or linear interpolation was used to initialise the MEP search.

Each initialisation was treated by the same combination of algorithms: First, the optimisation of the path by a chain-of-states method, i.e., in the case of this work by the nudged elastic band method (Section 2.5.1) which is a derivative of the double-ending or double-state methods. This chain-of-state method also allowed the generation of a path between two states if requested. And second, the reoptimisation/refinement of the transition states by a single-point or single-state method, i.e., by an eigenvalue follower algorithm.

2.5.1 Nudged elastic band (NEB) method [152, 153]

The nudged elastic band method was applied in order to optimise the given path of structures to the MEP. The NEB method represents reasonable modifications of the chain-of-state methods. It provides the possibility of parallelisation, the control of the distribution of points on the path, and a high numerical performance since 2nd derivatives are not needed. The optimised nudged elastic band represent a good approximation to the real minimum energy path.

2.5.1.1 Force concept of the elastic band

The nudged elastic band method combines the principles of an elastic band with the optimisation scheme according the *Locally Updated Planes* (LUP) [154, 155] algorithm. However, the combination of the true potential with the parabolic spring potential based on the Eq. (E.20) allows degradation of the band during the optimisation process. This means that the elastic band tends to corner-cutting of curved pathways and disproportion of the structures on the band (Figure 2.2b). The first effect originates from the spring force components perpendicular to the direction of the path; the second effect stems from the true force components parallel to the path which drags the structures on the band down towards the adjacent local minima.

The elimination of the degradation was achieved by the introduction of a force projection scheme [156]. Dividing the true and spring forces into parallel and perpendicular components (Figure 2.2a) relative to the path tangent, the perpendicular components of the spring forces and the parallel components of the true forces are projected out. The NEB forces F_i^{NEB}

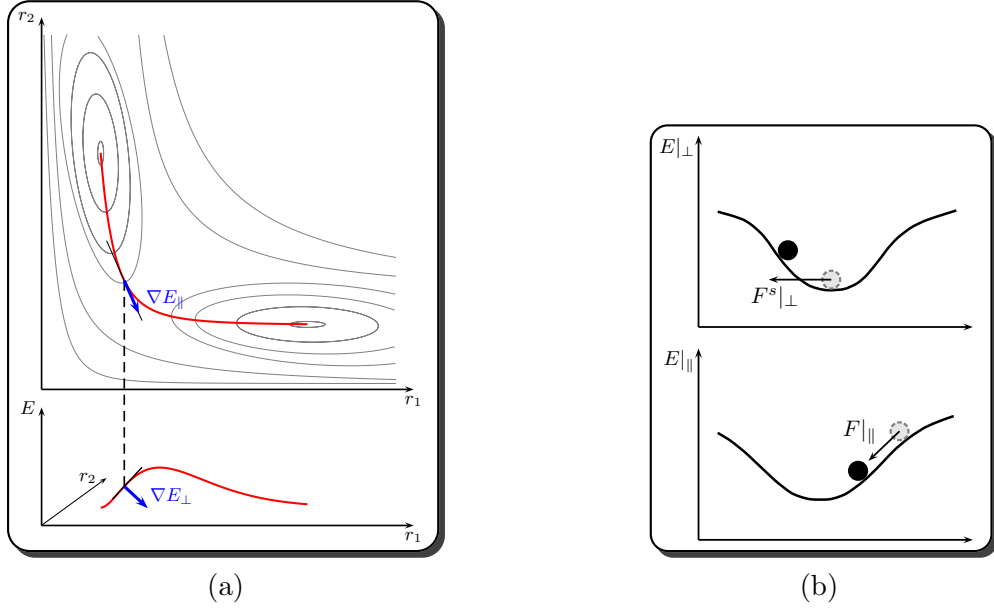


Figure 2.2: (a) Potential energy surface of an arbitrary reaction path projected by two representative reaction coordinates and the total energy: contour line diagram (top) and perpendicular to the top view (bottom). Picture (b) gives a cross-sectioned view along the minimum energy path with the corresponding E_{\perp} (top) and perpendicular to the minimum energy path with the corresponding E_{\parallel} (bottom). Due to the spring forces parallel to the band, corner-cutting of the band is observed. The true forces parallel to the band drag the structures to the local minimum.

acting on the structure i become:

$$F_i^{\text{NEB}} = F_i^s_{\parallel} + \nabla E(\vec{R}_i)|_{\perp}, \quad (2.46)$$

where the projected spring forces $F_i^s_{\parallel}$ and true forces $\nabla E(\vec{R}_i)|_{\perp}$ are determined by:

$$F_i^s_{\parallel} = K [(\vec{R}_{i+1} - \vec{R}_i) - (\vec{R}_i - \vec{R}_{i-1})] \frac{\tau_i}{|\tau_i|} \quad (2.47)$$

$$\nabla E(\vec{R}_i)|_{\perp} = \nabla E(\vec{R}_i) - \nabla E(\vec{R}_i) \frac{\tau_i}{|\tau_i|}. \quad (2.48)$$

Note that the quality of the elastic band, i. e., its minimisation, depends on the definition of the tangent.

2.5.1.2 Kinks on the elastic band

Based on the forces projection scheme (Eq. (2.46)), the minimisation of the elastic band has been observed to oscillate [156]. This means that the elastic band gets kinks which oscillate back and forth, especially at inflection points of the path. Kinks have been found to be a numerical misbehaviour caused by large parallel components of the forces over very small perpendicular components.

It was proposed to reduce the kinks by an appropriate definition of the tangent that gradually turns on the perpendicular component when the path becomes to kinky. A bisect definition for tangent τ_i and a switching function based on the angle between \vec{R}_{i+1} , \vec{R}_i and \vec{R}_{i-1} have been demonstrated [156]. Most recently, a reduction of kinks has been introduced by an

improved definition scheme of the tangents [157]:

$$\tau_i = \begin{cases} \tau_i^+ & \text{if } E_{i+1} > E_i > E_{i-1} \\ \tau_i^- & \text{if } E_{i+1} < E_i < E_{i-1} \\ \tau_i^+ \Delta E_i^{\max} + \tau_i^- \Delta E_i^{\min} & \text{if } E_{i+1} > E_{i-1} > E_i \\ \tau_i^+ \Delta E_i^{\min} + \tau_i^- \Delta E_i^{\max} & \text{if } E_{i-1} > E_{i+1} > E_i \\ \tau_i^+ \Delta E_i^{\max} + \tau_i^- \Delta E_i^{\min} & \text{if } E_i > E_{i+1} > E_{i-1} \\ \tau_i^+ \Delta E_i^{\min} + \tau_i^- \Delta E_i^{\max} & \text{if } E_i > E_{i-1} > E_{i+1} \\ \tau_i^+ / |\tau_i^+| + \tau_i^- / |\tau_i^-| & \text{else,} \end{cases} \quad (2.49)$$

where the tangents τ_i^+ and τ_i^- represent:

$$\tau_i^+ = \vec{R}_{i+1} - \vec{R}_i \quad \text{and} \quad \tau_i^- = \vec{R}_i - \vec{R}_{i-1}, \quad (2.50)$$

and ΔE_i^{\max} and ΔE_i^{\min} are estimated by:

$$\Delta E_i^{\max} = \max(|E_{i+1} - E_i|, |E_i - E_{i-1}|) \quad (2.51)$$

$$\Delta E_i^{\min} = \min(|E_{i+1} - E_i|, |E_i - E_{i-1}|). \quad (2.52)$$

The tangents of the first two cases in the equations (2.49) represent secants while in the residual cases they correspond to energy-weighted bisection. Equations (2.49) to (2.52) were applied in this work, since the approximation of the tangent by a bisection or a secant saves off the calculation of 1st derivatives. Moreover, a bisection setup also provides equal spaced point distribution in regions of large curvature.

2.5.1.3 Elaborations of the NEB method

Two elaborations of the NEB method were used in this work [157, 158]: First, the variable spring constant (VSC) and second, the climbing image (CI) algorithm. Both were applied to increase the density of structures around the transition state and to get a better approximation of the transition state. Details are given in Section B.4.1.

2.5.1.4 Optimisation of the nudged elastic band

The optimisation of the nudged elastic band was based on a quenched velocity Verlet algorithm [156] which is a derivative of the velocity Verlet algorithm [159]. The simple neglect of the velocities, i. e., the remove all the kinetic energy, in the time-domain based integration of the coordinates leads to the steepest-descent algorithm. It was proposed by Jónsson [156] that a partial quenching, i. e., zeroing, of the velocity components is more efficient. Keeping all velocity components parallel to the forces at the current step, accelerates the system towards the minimum. The established implementation corresponds, therefore, to:

$$\vec{u}^{\text{new}}(t) = \begin{cases} (\vec{u} \cdot \vec{F}) \vec{F} & \text{if } \vec{u} \cdot \vec{F} > 0 \\ 0 & \text{else.} \end{cases} \quad (2.53)$$

This procedure is equivalent to the increase of the timestep.

3 Methyne as precursor for interstellar ion-molecule reactions

All right ... all right ... but apart from better sanitation and medicine and education and irrigation and public health and roads and a freshwater system and baths and public order ... what have the Romans ever done for us?

MONTY PYTHON'S LIFE OF BRIAN

In this chapter, selected molecular properties and chemical reactivity of methyne^{†1} (CH) are presented. The reactivity and interstellar abundance suggest that methyne is a suitable precursor for the formation and growth of hydrocarbons and PAHs. Moreover, reports on reactions of surface-adsorbed hydrocarbons [160], studies of combustion processes [33] and reactions with neutral small hydrocarbons [34, 161, 162, 163] show that methyne might be involved in the combustion and in the planetary atmosphere chemistry. Methyne has been also found in expanding thermal plasma (ETP) of acetylene during vacuum-based deposition of hydrogenated amorphous carbon films [35, 164, 165].

Note that each molecule of significance will be abbreviated by a number **X**; starting with methyne by the number **1**.

3.1 Methyne in the ISM

The formation of hydrocarbons and PAHs by the reactions in Eq. (1.6) and Eq. (1.8) requires small precursor molecules with significant abundance (Section 1.3.4). Among the small known interstellar molecules, the methyne molecule is a good precursor candidate for the hydrocarbon growth because it is significantly abundant as given in Table C.2. The interstellar methyne molecules are supposed to be formed by gas-phase reactions in dark

^{†1}Alternative name according IUPAC: methylidyne

clouds as follows [166]:



and by photodissociation of CH_2 and CH_4 in diffuse clouds, i. e., under strong stellar radiation, as follows [166]:



A steady concentration of the CH molecule $n_{\text{CH}}/n_{\text{hydrogen}} = 10^{-8}$ - 10^{-7} is observed, which is, however, lower than the concentration of CO. CH depletion in interstellar/circumstellar environments is supposed to take place by ‘‘oxidation’’ [16]:



3.2 Selected properties of methyne

Properties of methyne obtained in this work such as ionisation energy, electron affinity^{†2}, dipole moment and polarisability are given in Table 3.1. More detailed studies of methyne concerning spectroscopical and electronic properties can be found elsewhere [167, 168, 169, 170].

Table 3.1: Ionisation energy (E_I) of $\text{X}^1\Sigma^+\text{CH}^+ \leftarrow \text{X}^2\Pi \text{CH}$, electron affinity (E_{ea}) of $\text{X}^2\Pi \text{CH} \leftarrow \text{X}^2\Sigma^-\text{CH}^-$, electric dipole moment (μ_D), and isotropic polarisability (α) of $\text{X}^2\Pi \text{CH}$ obtained by different methods applied in this work. Both, E_I and E_{ea} , were corrected by the zero-point vibrational energy. Experimental values of the carbon atom are given in the last column for comparison.

	SD	Ptz4	Btz3	Mtz3	G3	<i>exp.</i>	Carbon
E_I / eV	10.1014	11.0497	11.0160	10.6739	10.6395	10.64 [171] ^a	11.26 [172] ^a
E_{ea} / eV	0.2718	1.2343	1.3641	1.2618	1.1810	1.233 [167] ^b	1.262 [173] ^c
μ_D / D	–	1.5041	1.4571	1.6138	1.5582 ^d	1.46 [168]	–
$\alpha / a_{\text{bohr}}^3$	–	10.02	15.18	14.05	8.91 ^e	–	–

^aOptical spectroscopy

^bLaser photoelectron spectroscopy

^cLaser photodetachment

^dQdz1//Mdz1

^eHdz1

The electronic configuration of the CH ground state corresponds to $(1\sigma)^2(2\sigma)^2(3\sigma)^2(1\pi)^1$.

^{†2}Defined as $\text{X}^- \longrightarrow \text{X} + \text{e}^-$, i. e., positive values indicate an exothermic affinity.

The corresponding term symbol is denoted by $X^2\Pi$, which represents a doublet. The energy for the ionisation of CH from its ground state to the ground state of the corresponding CH^+ is 10.64 eV which is equal to the analysis by optical spectroscopy [171]. The results obtained in this work range from 10.1 to 11.05 eV. The smallest deviation is given by the G3 method; its value is identically to the experimental one. The largest deviation of 5.1% is found for the SD method. In the case of the electron affinity, the SD method underestimates the experimental value by more than a factor of four.

Dipole moment

The obtained dipole moment of methyne ranges from 1.457 to 1.614 Debye; the experimental value has been reported with 1.46 Debye [168]. In the case of ion-molecule reactions, the attractive long-range forces between any ion and methyne will be, therefore, determined by ion-induced dipole and ion-permanent dipole forces.

Comparison with carbon:

The ionisation potential and electron affinity of CH considerably agrees with those of the carbon atom as given in Table 3.1. Therefore, a similar behaviour in chemical reactions has been suggested [32].

Similarities to H_2 are not found, e.g. the ionisation potential of CH is evaluated to be at 15.4259 eV [174].

3.3 Reactivity and regioselectivity of methyne

The reactivity can be defined by different criteria such as rate coefficients or electronic / energetic stability. The evaluation by rate coefficients will be given below. Based on the ionisation potential and electron affinity, CH and the carbon atom (C) have closely related reactivities. The reactivity of CH estimated by energetic stability of the valence shell^{†3} indicates a high reactivity and electrophilicity since it possesses only 5 electrons in a valence shell with a maximum of 8. A higher electronic stability is achieved by acquiring up to 3 more electrons, e.g. in form of shared covalent bonds. It results in a high affinity for electrons which in return makes methyne highly reactive.

Average reaction energy gain forming 3 bonds

Taking into account the average bond energy ΔE_f of the carbon-carbon and carbon-hydrogen bonds (cf. Table 3.2), the average reaction energy for the formation of 3 covalent bonds ranges from 8.4 eV (in the case of a triple carbon bond) to 12.9 eV (in the case of three C–H bonds). The large gain of energy constitutes a high thermodynamic reactivity for methyne.

Regioselectivity

The regioselectivity in a reaction depends on the electronic properties of both reactants. The high reactivity and electrophilicity of methyne suggests that every position on the participating reactant can be attacked except for positions which are sterically hindered. In

^{†3}A filled valence shell is referred to the highest energetic stability.

Table 3.2: Average bond energy taken from [175]

bond	$\Delta E_f/\text{eV}$
C–C	3.59
C=C	6.42
C≡C	8.42
C–H	4.29

the case of equally distributed electron density of the participating reactant, the CH attack positions are suggested to be statistically distributed.

Omitting electronic excitation in this work

The obtained average reaction energy for the CH addition correlates with the energy for electronic excitation. This indicates a possible electronic excitation of product molecules formed by a CH addition reaction.

In this work, however, any electronic excitation has been explicitly not considered. The total amount of non-fixed energy has been assumed to be fast redistributed into vibrational and rotational modes which results in a highly vibrationally and rotationally activated product molecules.

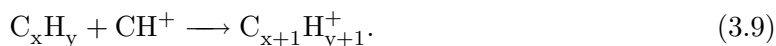
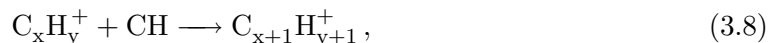
3.4 Hypothesis of reactions between interstellar CH and hydrocarbons

The high reactivity and abundance of CH, as stated above, allows to consider that interstellar methyne reacts with any present molecule including hydrocarbons. The amount of CH reacting with a specified molecule would not depend on its chemical nature but on its interstellar abundance. This indicates that potentially any interstellar hydrocarbon molecule can react with CH.

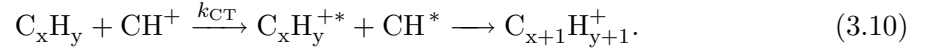
In the case that repeating cycles of reactions between CH and hydrocarbon molecules steadily increase the dimension of the hydrocarbons, the CH becomes a precursor for the hydrocarbon and PAH growth. Details of such CH based reaction routes will be presented in the chapters 4, 5, 6 and 7.

Aspects on the ground state of the ion-molecule reaction

In Section 2.2.3, the initialisation of any MD simulation in this work has been defined at the ground states of both reactants in randomised orientations. In the case of the ion-molecule reaction between the two reactants C_xH_y and CH, two possibilities would be allowed:



The different ionisation potentials of methyne and the hydrocarbon molecules could lead to charge transfers before the collision if the molecule with higher ionisation potential is charged, e. g.:



The released charge-transfer energy would be additionally distributed in the resulting product(s).

In this work, these effects are considered as undesirable. The removal has been achieved by choosing the ground state of reactions at initialisation point. It was given by the relation:

$$\min \left(E_{\text{CH}^{0/+}} + E_{\text{C}_x\text{H}_y^{+/0}} \right). \quad (3.11)$$

It is a rather hypothetical setup, since effects of the reaction potential energy surface between initial and collision point of the MD simulation are not taking into account.

4 Ion-molecule reactions between methyne and hydrocarbon ions, $C_xH_x^+$ (x=2–6): the formation of cyclic hydrocarbons

Good morning royal subjects. Enjoy your day in Janitoria. Labour until you tire and then labour some more.

JANITOR IN “SCRUBS”

In this chapter, the ion-molecule reactions between methylene and unsaturated, non-cyclic hydrocarbon ions $C_xH_x^+$ with $x = 2-6$ are presented. The objective is twofold: first, to evaluate the potential of CH based growth of unsaturated, non-cyclic hydrocarbon ions $C_xH_x^+$ resulting in cyclic and aromatic hydrocarbon ions $C_{x+y}H_{x+y}^+$, namely the benzene cation $C_6H_6^+$ and tropylium ion $C_7H_7^+$; and second, to evaluate the established computational methods (Chapter 2).

The chapter is divided into the following sections:

- 1.) Preview: introduces a scheme of potential benzene and tropylium formation routes, which are used for preselection of particular reactants and for comparison with resulting product distributions.
- 2.) Results: the results of the reaction between methyne and $C_xH_x^+$ obtained from MD simulations, property analysis, statistical rate theories and thermodynamics are presented. Each section corresponds to a different number of carbon atoms. In each section, the results of several reactants are presented. To achieve a connected formation route each reactant will be selected among the products of the previous reactions. The selection is done as described in Section 2.1.1.
- 3.) Summary and discussion: summarises and evaluates important results and provides generalised reaction mechanisms derived from the obtained results.

4.1 Preview on the formation of benzene cation and tropylium

A preview scheme of the formation routes of benzene cation and tropylium ion was generated (Figure 4.1). It is based on the reaction between CH and common structures of $C_xH_x^+$ in order to preselect important hydrocarbon reactants for the ion-molecule reaction $CH + C_xH_x^+$. Figure 4.1 shows three principle routes that are supposed to produce benzene cations and tropylium: first route, the formation of cyclic $C_3H_3^+$ and then stepwise insertion of CH under ring growth; and second and third route, the chain extension completed by its cyclisation. Since the objective – only to study the formation and growth of non-cyclic chain growth – was established, the first mechanism is not considered in the following chapter. The second and third route differ only in the first CH addition step. In both cases, two different molecules with a terminal methylene group ($-CH_2$) are proposed. This sidegroup is extended by CH insertion where at each step two configuration isomers, *cis* and *trans*, are formed. The ring closure is expected at each step, but requires the chain-like hydrocarbon to be in an all-*cis* configuration. The details of the ring closure and *cis-trans* isomerisations will be additionally described in this chapter.

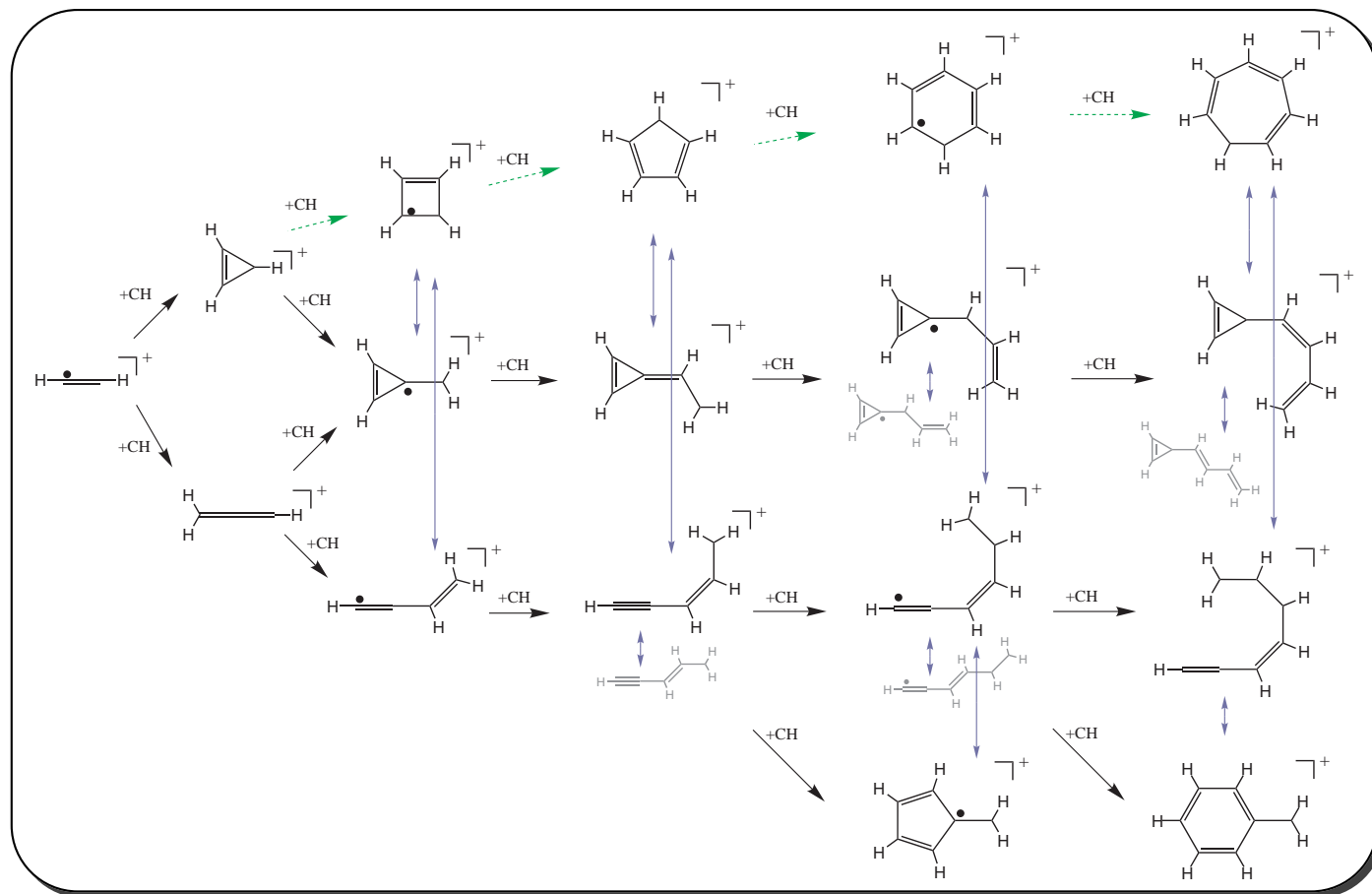


Figure 4.1: The constructed reaction network for the growth of non-cyclic hydrocarbons to benzene cation and tropylium based on the successive CH addition. This network considers that cyclic hydrocarbon are formed either by the ring extension or ring closure mechanism.

4.2 $C_2H_2 + CH^+$

In this section, computed results of the ion-molecule reaction between methyne and C_2H_2 are presented. Two constituents of C_2H_2 are known – the acetylene ($HC\equiv CH$) and vinylidene ($H_2C=C:$) [176]. In this work, the vinylidene was not considered.

The results of the reaction between acetylene and methyne are discussed according to the:

- 1.) MD simulation including production distribution, cross-sections of reactive channels and capture rate coefficients (Section 4.2.1);
- 2.) Product energy based population analysis (Section 4.2.2);
- 3.) Reaction path analysis including isomerisation and radiative rate coefficients of the energised products (Section 4.2.3).

Deviation in the ion-molecule setup

The obtained ionisation potential of acetylene as given in Table 4.1 exceeds the one of methyne (Table 3.1). In order to fulfil the own defined requirements for the MD simulations as given by Eq. (3.11) in Section 3.4, the reaction analysis was applied to the reactants: methyne cation and acetylene, hereafter abbreviated by **2**. The ground state configuration of the methyne cation and **2** is given by $X^1\Sigma^+$ and $\tilde{X}^1\Sigma_g^+$. The multiplicity of the total system corresponds to a singlet state.

Table 4.1: Ionisation energies (E_I) of acetylene in eV by different DFT and ab initio methods including zero-point energy correction.

	SD	Ptz4	Btz3	Mtz3	G3	<i>exp.</i>
E_I	12.0743	11.2402	11.2972	11.5225	11.4099	11.41 ^a

^aElectron impact technique [177]

Charge-transfer energy

Based on both ionisation potentials, the charge-transfer between the acetylene cation and CH would release 0.77 eV.

Abundance of interstellar methyne cation

Column densities of interstellar methyne cations in diffuse clouds based on different optical transitions has been reported by *Winnewisser et al.* [32]. These column densities are in considerable agreement with those of the CH neutral species. Considering similar abundances for CH and CH^+ and also for C_2H_2 and its corresponding cation $C_2H_2^+$, the interstellar encounter probabilities between the reactants remain the same.

4.2.1 DFTB based MD simulations

The applied setup corresponds to the description given in Section B.1. From the defined list of collision energies B.13, the value 0.50 eV was not used for the MD simulations. Note that the applied MD simulations based on the DFTB method do not result in a detailed electronic structure in terms of a many-particle system description. The application serves only for the conceptual introduction of the quasi-particle description (DFTB) as well as qualitative verification of the proposed reaction route.

4.2.1.1 Product channels obtained

Based on the bond analysis of the different snapshots at $t_{\text{postcoll}}^{\dagger 1} = 1$ and 6 ps, the following division into the different product configurations was made as follows:

- 1.) Linear $C_3H_3^+$. The class of products and identified structures are denoted by **ncy** and **3** respectively.
- 2.) Cyclic $C_3H_3^+$ (**cy-3**). Here, the number tag **4** is used for the identified structure.
- 3.) Fragmentations (**f-H₂**). It corresponds to the structures $C_3H^+ + H_2$ (**6**).
- 4.) Orbiting complexes (**cmplx**) represent the reactants orbiting each other.

The reaction energies and structures are given in Table 4.2.

4.2.1.2 Product distribution

Based on the defined product channels and the corresponding counting analysis (Section B.3), the product distribution was determined by calculating the product cross section. The results are given in Figure 4.2.

Product distribution at $t_{\text{postcoll}}=1$ ps

Based on the results given in Figure 4.2, the amount of all cross sections combined is lowering with the increase of the collision energy. An inverse collision energy trend relative to the cross sections indicates reaction characteristics as described by the *Langevin* model. The distribution of each product channel does not, however, correspond entirely to this trend. In detail, the cross sections of **cy-3** and **ncy** vary between 6 and 22 Å² without any trend. The ratio of **cy-3** to **ncy** increases from 1 at 0.001 eV to 2 at 0.25 eV. It indicates a higher production of cyclic C_3H_3 at the higher collision energy.

The ratio of **cmplx** to the total number of reactive collisions is estimated to be over 85% at 0.001 eV. It is reduced to less than 2% at 0.05 eV.

Product distribution at $t_{\text{postcoll}}=6$ ps

The total amount of **ncy** and its ratio to the total number of reactive collisions is increased relative to the distribution at 1 ps. The obtained fractions of the complex are 48% at 0.001 eV; lowering to 0 at 0.05 eV. The corresponding amount of this described loss is accounted to **ncy** and **cy-3**. Based on this increase, a clear inverse collision energy trend of both fraction can be suggested. The ratio of **cy-3** to **ncy** is, however, not well defined. It ranges from 0.88 at low collision energies to 1.12 at high collision energies.

^{†1}The definition is given in Section B.1.5.

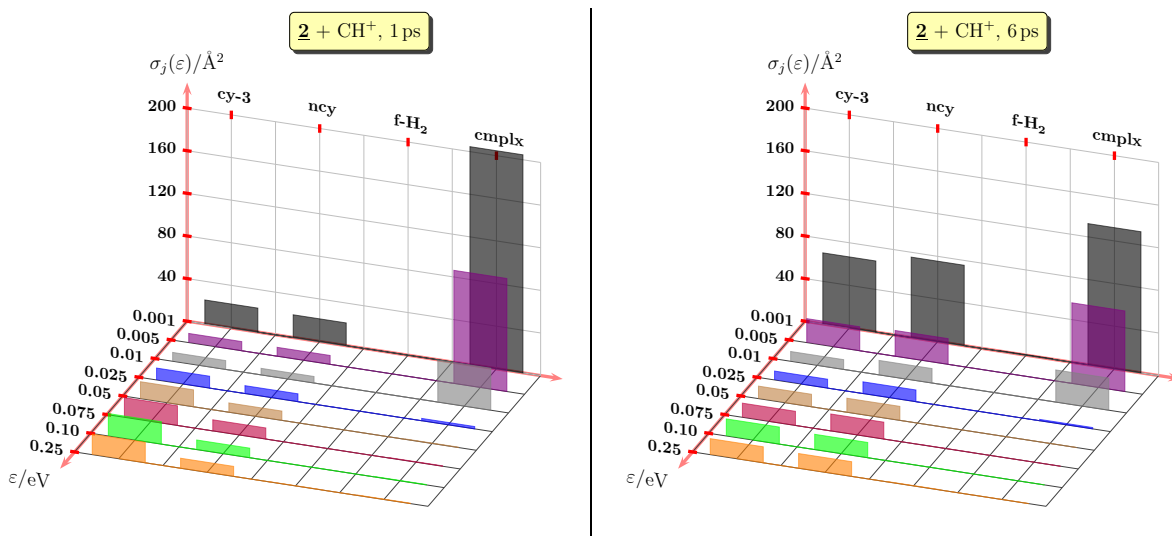


Figure 4.2: Calculated product cross sections $\sigma_{R,j}$ resulting from the reaction between **2** and methyne cation plotted vs. applied collision energy. Two different propagation times, 1 ps (left-hand panel) and 6 ps (right-hand panel) are shown. Abbreviations correspond to **cy-3** = cyclopropenyl cations, **ncy** = non-cyclic $C_3H_3^+$, **f-H₂** = H_2 fragmentation, and **cmplx** = orbiting complex.

*Comparison of **cy-3** and **ncy** distributions*

The increased amount of cyclic $C_3H_3^+$ over non-cyclic $C_3H_3^+$ at 1 ps indicates that the production of cyclic $C_3H_3^+$ is preferred in the collision of acetylene and methyne cation.

The time-dependent lowering of the ratio between **cy-3** and **ncy** indicates that the obtained energised cyclic $C_3H_3^+$ decay. Based on the observed ring opening, a cyclic $C_3H_3^+$ decay into non-cyclic products can be suggested which is also validated by the obtained cross sections.

Notice on fragmentations

Based on the obtained cross sections of the $C_3H^+ + H_2$ products at 6 ps, corresponding ratios range from 0.3% at 0.001 eV to about 1% at 0.25 eV which suggests a collision energy dependence. The fraction of $C_3H^+ + H_2$ also increases with time. Moreover, a synergic effect is observed.

4.2.1.3 Reaction probability versus collision parameter

The obtained fraction of **cmplx** over the collision parameter, i. e., $P(b)$, in the applied range of collision energies is given in Figure 4.3. This shows that the amount of **cmplx** enlarges with increasing collision parameter reaching its maximum close to b_{\max} . On the other side, the amount of **cmplx** decreases with increasing collision energy. The dependence on the collisional parameter b agrees with the *Langevin* model characteristics for the orbiting complexes where the available kinetic energy for overcoming the centrifugal barrier reduces with increasing b for a given collision energy.

Based on the results given in Figure 4.2, the average lifetime of the orbiting complex or association complex is higher at low collision energies. Such a complex occupies a energetic level close to the reactants; and the non-fixed energy required to overcome the (centrifugal) barriers is related with the collision energy. Higher collision energy provides a faster

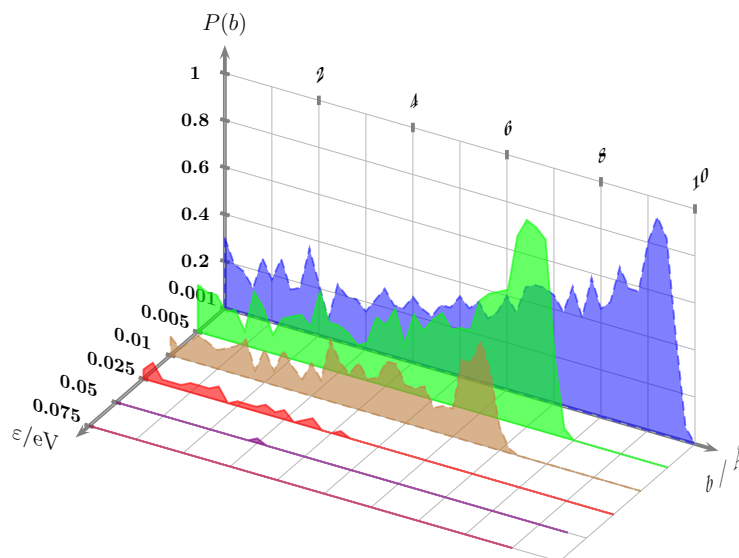


Figure 4.3: Reaction probability $P(b)$ of the orbiting complex over the collision parameter b vs. the collision energy ε taken from MD simulation snapshots ($t_{\text{postcoll}}=6$ ps).

transition to energetically lower-lying product configurations.

4.2.1.4 Capture rate coefficients

The capture rate coefficients were calculated based on total amount of product cross sections given in Figure 4.2 including the cross sections of the orbiting complex. The results are illustrated in Figure 4.4. For collision energies between 0.005 and 0.25 eV, $k_{\text{MD}}(\varepsilon)$ values are

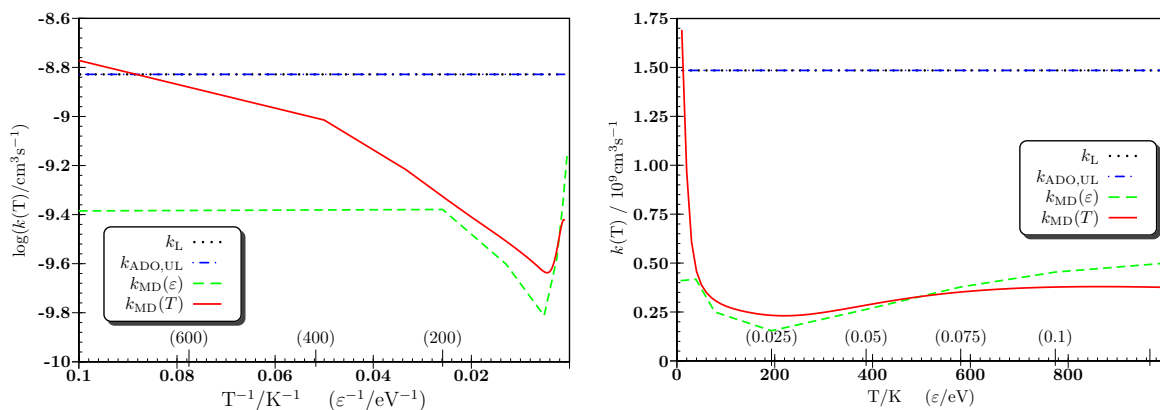


Figure 4.4: Calculated capture rate coefficients corresponding to the *Langevin* model (k_L) and ADO model (k_{ADO}), and MD simulations ($k_{\text{MD}}(\varepsilon)$, $k_{\text{MD}}(T)$). Two different representations are given: left) logarithmic k versus inverse T ($\varepsilon_{\text{coll}}$) and right) k versus T ($\varepsilon_{\text{coll}}$).

in qualitative and quantitative agreement with $k_{\text{MD}}(T)$ values (Figure 4.4). Note that the transferability of $\varepsilon_{\text{coll}}$ to the collision temperature was based on the equipartition theorem, viz. $\varepsilon_{\text{coll}} = 1.5 k_B T_{\text{coll}}$. All obtained thermal rate coefficients are 5 times lower than those values obtained with the phenomenological *Langevin* and ADO model. However, at temperatures below 20 K, obtained $k_{\text{MD}}(T)$ values exceed the values based on the phenomenological

models. Since acetylene has no dipole moment as stated in Table A.1, the calculated values of the *Langevin* and ADO model are identical in this work.

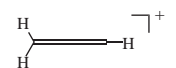
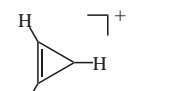
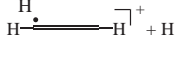
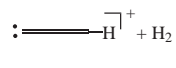
Explanation of the $k_{MD}(T)$ trend

Ion-permanent dipole interactions result in a inverse dependence of temperature on thermal rate coefficients^{†2}. Without this interaction, a inverse temperature trend of the reaction reactivity might be caused by the decrease of the scattering fraction with decreasing temperatures.

4.2.2 Product energetics

The reaction enthalpies of the products identified by the bond analysis are given in Table 4.2 in dependence of the applied quantum chemical method.

Table 4.2: Products of Ion-molecule between acetylene and CH cation: reaction energies $\Delta_R E$ and enthalpies at 0 Kelvin $\Delta_R H_{0K}$ obtained by different quantum theory methods

products	abbr.	geometry	$\Delta_R E/eV$	$\Delta_R H_{0K} (\Delta_R E)/eV$		
			SD	Btz1//Bdz1	Mtz3	G3
$\mathcal{A}\text{-C}_3\text{H}_3^+$	3		-6.8360	-7.2013 (-7.5173)	-7.0482 (-7.3627)	-6.6946 (-6.9675)
$\mathcal{B}\text{-C}_3\text{H}_3^+$	4		-7.0841	-8.2755 (-8.6541)	-8.3967 (-8.7698)	-7.8286 (-8.1665)
$\text{C}_3\text{H}_2^+ + \text{H}$	5		-0.7260	-2.8801 (-2.7897)	-2.4463 (-2.3473)	-2.3199 (-2.1648)
$\text{C}_3\text{H}^+ + \text{H}_2$	6		-1.8639	-2.8830 (-2.8323)	-2.7359 (-2.6753)	-2.5855 (-2.5141)

Based on the results of the reported reaction between neutral acetylene and methyne [178], the possibility of hydrogen abstraction from C_3H_3^+ has been considered. The corresponding reaction enthalpy and energy of the product $\text{C}_3\text{H}_2^+ + \text{H}$ (**5**) is given in Table 4.2. In the case of the B3LYP and MP2 method, a C_3H_3^+ structure in which all hydrogens are placed at one terminal carbon (methylacetylene carbene H_3CCC^+) is unstable.

Among the given products, the formation of cyclic C_3H_3^+ constitutes the highest reaction enthalpy. This structure also possesses the highest thermodynamic stability^{†3}. A lower stability of non-cyclic C_3H_3^+ ranges from 0.25 eV (DFTB) to 1.35 eV (MP2).

Based on the results obtained by B3LYP, MP2 and G3 methods, the reaction enthalpy of the H_2 and H cleavage products (**5** and **6**) ranges between -2.3 and -2.9 eV. Among both

^{†2}For the asymptotic potential (E.2), the capture rate coefficient k of a barrierless reactions corresponds to the collision energy $\varepsilon_{\text{coll}}$ as: $k \propto \varepsilon_{\text{coll}}^{(1/2-2/s)}$, where s relates to the order of multipole interaction. Based on this relation, the potential of the ion-permanent dipole interactions given in Eq. (2.9) constitutes an inverse $\varepsilon_{\text{coll}}$ dependence for $k \propto \varepsilon_{\text{coll}}$, and thus a inverse dependence on the temperature.

^{†3}Based on the given $\Delta_R H_{0K}$, the relative product enthalpies are calculated by $\Delta\Delta H_i = \Delta_R H_{0K,i} - \Delta_R H_{0K,\text{min}}$.

dissociation channels, the energetic level of 5 lies below 6 by maximum 0.29 eV.

4.2.2.1 Canonical population distribution

Based on the harmonic frequency analysis, the population distribution of all association products as given in Table 4.2 is depicted in Figure 4.5. Up to 4000 Kelvin, the thermodynamic

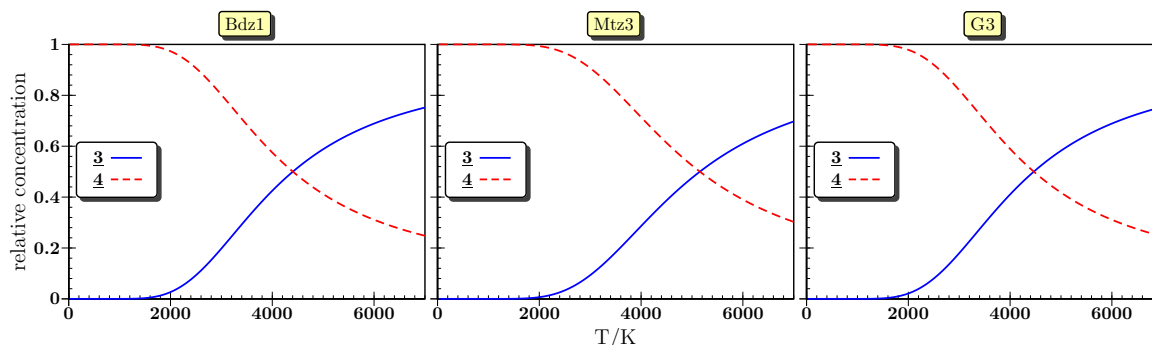


Figure 4.5: Canonical $C_3H_3^+$ product isomer distribution obtained by different methods.

equilibrium is shifted to the side of 4, above this temperature to the side of 3.

The comparison of the population distribution with the MD product distribution was based on the application of the equipartition theorem. Under this consideration, the non-fixed energy of the products corresponds to several thousand Kelvin. The population distribution would be, therefore, on the side of 3. It is in agreement with the obtained trend of the MD simulation that the amount of 3 is increasing with time at the cost of 4.

4.2.3 Reaction path analysis

The calculated stationary points of the chemical network between the given reactants and products of the reaction system are given in Figure 4.6. This scheme does not represent the

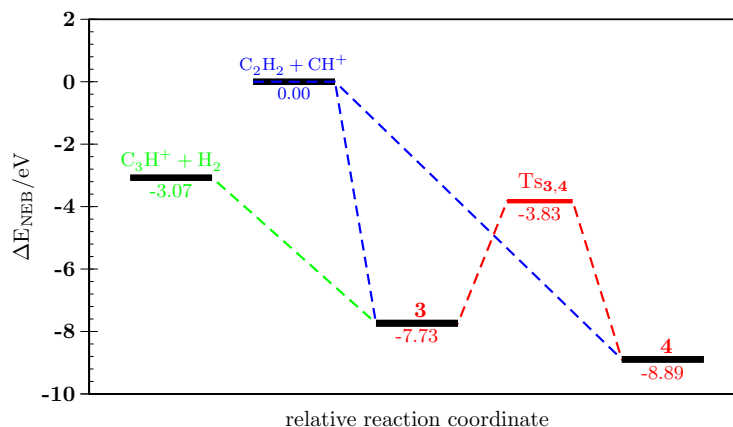


Figure 4.6: Stationary and transition points of the CH addition to C_2H_2 . C_3H_3 isomerisation and dissociation obtained by Bdz1.

complete reaction network, such as the elimination of hydrogen atoms.

Under the static consideration of the reaction path analysis, the reaction of acetylene with methyne cation to the products 3 and 4 is barrierless. The identified ring opening process of 4 constitutes a barrier of 3.9 eV at the Bdz1 level of theory. The corresponding reverse

process, a ring closure, possesses a barrier height of 5 eV. Based on the obtained results at the Bdz1 level, the removal of H_2 from the linear $C_3H_3^+$ (**3**) is barrierless. It is in agreement with the results reported by *Maluendes et al.* [179].

4.2.3.1 Isomerisation rates

The calculated unimolecular rate coefficients for the isomerisation between energised **3** and **4** and the radiative spontaneous rate coefficients are tabulated in Table 4.3. This includes the results of each applied method as described in Section 2.2.4.

Table 4.3: Unimolecular rate coefficients of radiative deactivation and isomerisation processes calculated by different approaches: Bdz1 energies are taken from the MEP and TS optimisation procedures. Two different internal, non-fixed energies are given: the first two rows correspond to $\Delta_R H_{0K}$ resulting from the reaction $CH^+ + \mathbf{2}$, while the last two rows represent the amount of energy to give the transition state 0.1 eV of non-fixed energy.

product	E_{vr}^a / eV	$k_r(E_{vr})$ / s^{-1}	Isomerisation					
			to	E_{vr}^\ddagger ^b / eV	$k_{DC}^v(E_{vib})^c$ / s^{-1}	$k_{WR}^v(E_{vib})^d$ / s^{-1}	$k_{WR}^{vr}(E_{vr})^e$ / s^{-1}	$k_m^{vr}(T_{vr})^f$ / s^{-1}
3	7.417	7.421×10^2	4	3.685	2.007×10^{11}	2.007×10^{11}	1.255×10^{11}	1.413×10^{11}
4	8.513	4.696×10^2	3	3.685	1.316×10^{12}	1.315×10^{12}	5.089×10^{11}	1.583×10^{12}
<i>low non-fixed energy impact</i>								
3	3.832	3.733×10^2	4	0.100	3.451×10^5	3.905×10^5	2.264×10^4	7.214×10^4
4	5.065	2.563×10^2	3	0.100	8.876×10^5	1.007×10^6	3.167×10^4	2.688×10^5

^a $= E_{vib}$, energy distributed either in rotvibrational or vibrational modes, corresponds to $\Delta_R H_{0K}$

^b $= \Delta_R H_{0K} - \Delta H^\ddagger$, energy distributed in the rotvibrational modes of the TS

^cDirect counting (DC) of vibrational states

^dWhitten-Rabinovitch (WR) approximation of vibrational states

^eWhitten-Rabinovitch (WR) approximation of rotvibrational states

^fModification of CTST method, compare Eq. (2.23)

Non-fixed energy corresponding to reaction energy

The non-fixed energy of **3**, **4**, and the transition state corresponds to 7.4 eV, 8.5 eV and 3.8 eV. The calculated isomerisation rates (k_{WR}^{vr}) of **3** and **4** exceed their corresponding radiative deactivation rates by factor of 150 million. Based on the obtained k_{WR}^{vr} values, the ratio between the ring opening and the ring closure $r_{WR, \mathbf{4} \leftrightarrow \mathbf{3}}^{vr}$ ^{†4} is evaluated with 4.055 to 1. This ratio is higher for the corresponding ratio $r_{DC, \mathbf{4} \leftrightarrow \mathbf{3}}^v$ yielding 6.557 to 1.

Non-fixed energy corresponding to level of $E_{TS} + 0.1$ eV

Despite the low radiative deactivation rate coefficients, the decrease of the amount of non-fixed energy can be expected. At the level of $E_{TS} + 0.1$ eV, **3** and **4** possess 3.8 eV and 5.1 eV. Based on this amount of energy, the k_{WR}^{vr} values of **3** and **4** are reduced by a factor of over 5 and 16 million relative to high energy impact as described above. Each k_r value is, however, reduced only by a factor of 2. In direct comparison, the ratio k_{WR}^{vr} to k_r values is now constituted by a factor of 60 to 120. The ratios $r_{WR, \mathbf{4} \leftrightarrow \mathbf{3}}^{vr}$ and $r_{DC, \mathbf{4} \leftrightarrow \mathbf{3}}^v$ are equal to

^{†4} $r_{WR, x \leftrightarrow y}^{vr}$ corresponds to the ratio of the rate coefficients k_{WR}^{vr} of isomerisation from x to y to isomerisation from y to x based on the WR approximation of the vibrational-rotational states, i. e., $k_{WR, x \rightarrow y}^{vr} / k_{WR, y \rightarrow x}^{vr}$.

1.399 and 2.572, respectively. The lowering of the ratios r for ring opening with decreasing non-fixed energy is in considerable agreement with the results obtained from the population analysis where at low temperatures $\underline{4}$ dominates the thermal equilibrium.

Quality and Quantity of rate coefficients

At the high energisation level, the results of the different methods are in good agreement. Values of k_{DC}^V and k_{WR}^V are nearly identical (deviation $\sigma = 0.05\%$ ^{†5}). As expected by the given equations in Section 2.2.4.1, the rate coefficients k_{WR}^{VR} are lowered relative to k_{WR}^V , since rotational-vibrational states and the non-fixed energy as the rotvibrational energy (E_{VR}) are considered. The ratio is given by $k_{WR}^{VR}/k_{WR}^V \approx 0.38-0.63$. The ratio of k_m^{VR} to k_{WR}^V ranges from 1.2-0.7.

At the low energisation level, each method results in considerably different values. The k_{DC}^V values are smaller by 11% relative to k_{WR}^V . The decrease of k_{WR}^{VR} over k_{WR}^V is much higher than be expected for cases of large non-fixed energy. These results indicate that at low non-fixed energies the contribution of rotational states to the total quantum states is larger.

Quality and quantity of ring opening to ring closure ratio

The methods which consider rotational modes constitute always smaller ratios r of ring opening to ring closure. It corresponds to the trend of these ratios to decrease with the lowering of the available non-fixed energy. This means that (in the case of equal amounts of non-fixed energy) methods considering rotational modes do have less energy available for the vibrational states, since its part is "lost" to the rotational modes. It also shows that the rotational modes do not contribute to the ring opening and ring closure process.

^{†5} $\sigma_{1,2} = \sqrt{(x_{1,i} - x_{2,i})^2/x_{1,i}^2/N}$

4.3 $C_3H_3^+ + CH$

In this section, the studies on growth of hydrocarbons by methyne are continued with **3** (propargyl cation, $\mathcal{A}\text{-}C_3H_3^+$) and **4** (cyclopropenyl cation, $\mathcal{B}\text{-}C_3H_3^+$) which are products of the previous described reaction $C_2H_2 + CH^+$.

Interstellar abundance of the hydrocarbon reactants

Although interstellar $C_3H_3^+$ molecules have been not directly identified by spectral observation, $C_3H_3^+$ is supposed to play an important role in the interstellar chemistry [180]. Based on experiments and theoretical investigations, C_3H^+ and $C_3H_2^+$ molecules are suggested as indicators for interstellar $C_3H_3^+$. Both molecule are linked to $C_3H_3^+$ by the dissociation channels $C_3H_2^+ + H$ and $C_3H^+ + H_2$ [179]. Both neutral radicals, C_3H (propynlidyne) [181, 182] and H_2C_3 (propadienylidene) [39, 183] have been identified as interstellar molecules. The relation between the neutral and cationic species are proposed by electron recombination and photoinduced electron-detachment reactions.

Charge distribution in the hydrocarbon reactants

For a qualitative assessment of the most probable reaction positions during the CH attack, the charge distribution were determined based on the *Mulliken* population analysis at the Btz1 level of theory (Figure 4.7). The results indicate that the attack of methyne on **3** might be focused at the position of the dihydrogenated carbon atom since it possesses the highest electronic density (Figure 4.7). For the structure **4**, the charge is equally distributed due to

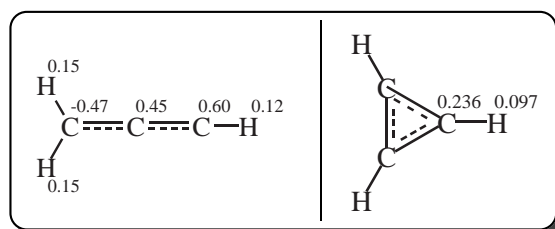


Figure 4.7: Mulliken atomic charges of **3** and **4** obtained by Btz1.

the D_{3h} symmetry. Both π -electrons are delocalised. The structure is aromatic according the $4n+2$ rule (*Hückel* rule).

Reactivity of the hydrocarbon reactants

The reactivity was estimated by the relative energetic stability given by the difference $\Delta\Delta H$ between the $\Delta_R H_{0K}$ values (Table 4.2). The results suggest that **3** has a higher reactivity than **4**.

4.3.1 DFTB based MD simulations

All obtained trajectories for each b_i from b_{\min} to b_{\max} and for each collision energies as given in List (B.14) are considered in the following results.

4.3.1.1 Identified product channels

Defined product channels and corresponding identified products are enlisted below:

- 1.) Non-cyclic products (labelled **ncy**): Linear $C_4H_4^+$ structures **7** and **8**.
- 2.) Cyclic products (**cy**): Identified structures are **9** (3-ring-membered structure) and **10** (4-ring-membered structure).
- 3.) Fragmentation products (**frag**) which consist of the product pairs $C_2H_2^+ + C_2H_2$ (**11**), $C_4H_2^+ + H_2$ (**12**) and $C_4H_3^+ + H$.
- 4.) Orbiting complexes (**cmplx**) which represent reactants orbiting each other.

The structural details are given in Table 4.4.

4.3.1.2 Product distribution corresponding to cross sections

The results based on the MD trajectory snapshots at $t_{\text{postcoll}} = 6$ ps are given in Figure 4.8.

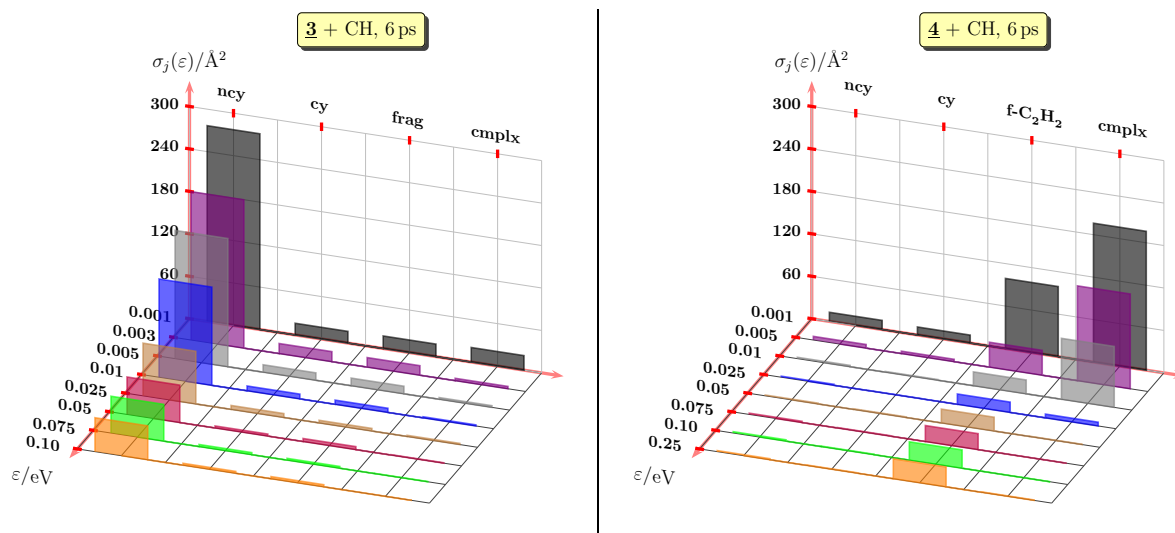


Figure 4.8: Calculated product cross sections $\sigma_{R,j}$ resulting from the reaction between $\mathcal{A}\text{-}C_3H_3^+$ (**3**), $\mathcal{B}\text{-}C_3H_3^+$ (**4**) and methyne. Both plots correspond to $t_{\text{postcoll}} = 6$ ps applied to different collision energies. Given abbreviations relate to **ncy** = non-cyclic, **cy** = cyclic, **frag** = fragmentation products including **f-C₂H₂** = $C_2H_2^+ + C_2H_2$, and **cmplx** = orbiting complex.

The product distributions of the non-cyclic (**3**) and the cyclic $C_3H_3^+$ reactants (**4**) differ by the ratio of formed products to the orbiting complex and by the amount of occurred fragmentations within the MD simulation time $t_{\text{postcoll}} = 6$ ps.

Reaction of 3 with methyne:

Between 90% and 95% of the reactive encounters (i. e., including the orbiting complex) are transformed in $C_4H_4^+$ products. The ratio of cyclic to total products amounts 5–6% in the range of the applied collision energies. The calculated ratio of fragmentations reach nearly the quantity of **cy**. The ratio between the three type of fragmentations, viz. **11**, **12**, and $C_4H_3^+ + H$, corresponds to 1:2:2.

*Reaction of **4** with methyne:*

Between 3% and 9% of all reactive encounters result in $C_3H_3^+$ products. Among the $C_3H_3^+$ products, the part of the cyclic products constitutes 30–50%. The residual reactive collisions, which are 91 to 97%, are divided between **cmplx** and **f-C₂H₂**. Their ratios to each other are strongly depending on the collision energy; they change from 70:30 at 0.001 eV to 0.1:99.9 at 0.10 eV.

Comparison between both reactants

The reaction system **3** + CH gives a higher amount of cyclic products than **4** + CH. The corresponding reaction cross section σ_R constitutes at 0.001 eV and $t_{\text{postcoll}} = 6 \text{ ps}$ 16.6 \AA^2 and 11.3 \AA^2 , respectively. However, the compositions of cyclic products differ, i. e., **3** + CH yields mostly **9**, while **4** + CH results in **10**. The formation of **10** was identified as the origin of the high amount of fragmentation products $C_2H_2^+ + C_2H_2$.

*Reaction of **4** with methyne after $t_{\text{postcoll}} = 100 \text{ fs}$:*

The amount of C_4H_4 is similar to the system $\mathcal{A}-C_3H_3^+$ (**3**) + CH at 6 ps. However, the C_4H_4 products entirely consists of **10**. The discrepancy between the product and fragmentation ratios at the different simulation times indicates that **10** is unstable and dissociates into $C_2H_2^+ + C_2H_2$.

*Instability of **10***

The ratio of fragmentation to the total amount of reactive collisions rises from 30% at 0.001 eV up to 90% at 0.5 eV which indicates a strong collision energy dependence on the instability of **10**. The instabilities arise from the unfavoured structural configuration which cause high bond angle strain. A ring opening would reduce the strain, but results in an unstable HCHC–CHCH⁺ configuration which decays.

Since reactions between **4** and CH mostly lead to **10**, which dissociates into acetylene, **4** is considered as an inhibitor in the hydrocarbon growth. It effectively recycles methyne to acetylene.

4.3.1.3 Calculated capture rate coefficients

The capture rate coefficients were calculated based on Eqs. (2.15) and (2.16). For comparison, k_L and $k_{\text{ADO}}(T)$ were evaluated. The corresponding dipole moments and polarisabilities (Table A.1) are taken from the DFT calculations. The results are given in Figure 4.9.

k_L , $k_{\text{ADO}}(T)$ and comparison with MD based values:

The capture rate coefficient (k_L) value is evaluated to be $1.12 \times 10^{-9} \text{ cm}^3 \text{ s}^{-1}$. Based on the methyne dipole moment (1.4413 Debye, Table A.1), $k_{\text{ADO}}(T)$ values show an inverse temperature dependence; values range from $10.54 \times 10^{-9} \text{ cm}^3 \text{ s}^{-1}$ at 20 K to $1.66 \times 10^{-9} \text{ cm}^3 \text{ s}^{-1}$ at 1000 K. However, obtained values of $k_{\text{MD}}(\varepsilon)$ and $k_{\text{MD}}(T)$ are below these capture rates.

Comparison between both reaction systems:

The $k_{\text{MD}}(\varepsilon)$ values of **3** + CH start above 0.025 eV to upshift by $4 \times 10^{-10} \text{ cm}^3 \text{ s}^{-1}$ in comparison to **4** + CH. Turning to lower collision energies, the value difference shrinks over $0.9 \times 10^{-10} \text{ cm}^3 \text{ s}^{-1}$ at 0.005 eV to $0.2 \times 10^{-10} \text{ cm}^3 \text{ s}^{-1}$ at 0.001 eV. With increasing collision

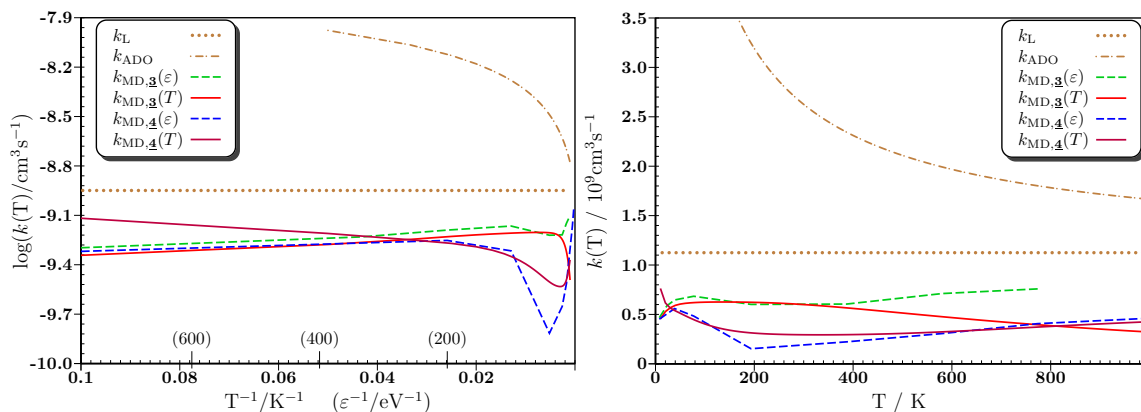


Figure 4.9: Calculated capture rate coefficients corresponding to the *Langevin* (k_L) and ADO theory (k_{ADO}), as well as based on the MD simulations ($k_{MD}(\varepsilon)$, $k_{MD}(T)$). Two different representations are given: left) logarithmic k versus inverse T (ε_{coll}) and right) k versus T (ε_{coll}).

energy, CH reaction with **4** become less reactive than with **3**. Therefore, the trend qualitatively agrees with the estimated reactivities. Since the reactivity was given by DFT, its agreement with the MD results is a good indication for the consistence of DFTB with DFT.

Comparison between $k_{MD}(T)$ and $k_{MD}(\varepsilon)$:

Two trends are given. In the case of **3** + CH system, the $k_{MD}(T)$ and $k_{MD}(\varepsilon)$ values are in agreement for collision energies below 0.05 eV but disagrees above. In contrast, $k_{MD}(T)$ and $k_{MD}(\varepsilon)$ values of **4** + CH system are consistent for collision energies above 0.005 eV, but disagrees below. In both cases the discrepancy is correlated with the chosen set of applied collision energy indicating a numerical problem which might be related with the determination and definition of Eq. (B.12)'s integrand. The quality of the integrand depends on the quality of the interpolated function $\sigma_R(\varepsilon_{coll})$ (cf. Section B.1.8). Based on these facts, the combined sets of collision energies (i.e., combined for comparison) are considered to provide only reliable values of $k_{MD}(T)$ between 50 and 400 K.

4.3.2 Product energetics

The reaction enthalpies of the identified products in dependence of the applied quantum chemical method are given in Table 4.4.

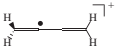
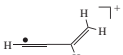
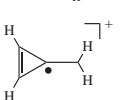
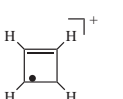
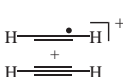
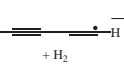
For the reaction of $\mathcal{A}\text{-}C_3H_3^+$ (**3**) + CH, the formation of the addition products, as given in Table 4.4, are strongly exothermic. The amount of non-fixed energies ranges from 5.3 to 7.8 eV at the G3 level of theory. The highest thermodynamic stability^{†6} corresponds to **9**. In comparison, the stability of **7** is lowered by about 0.03 eV at the G3 level of theory.

Comparison of the average CH addition enthalpy $\Delta_R \overline{H}_{0K}$

The CH addition to non-cyclic $C_xH_x^+$ forming non-cyclic $C_{x+1}H_{x+1}$ gives 5.6 eV for $x=3$ and 6.7 eV for $x=2$ at the G3 level of theory. Influences on the different values are related with the relative stability of the reactant $C_xH_x^+$.

^{†6}Based on the given $\Delta_R H_{0K}$, the relative product enthalpies $\Delta \Delta H_i$ are calculated by $\Delta_R H_{0K,i} - \Delta_R H_{0K,\min}$.

Table 4.4: Ion-molecule based reaction energies and enthalpies corresponding to the reference level $\mathcal{A}\text{-C}_3\text{H}_3^+(\mathbf{3}) + \text{CH}$ obtained by different quantum theory methods.

products	abbr.	geometry	$\Delta_R E/\text{eV}$	$\Delta_R H_{0\text{K}}/\text{eV}$		
			SD	Btz1//Bdz1	Btz2	G3
$\beta\text{-C}_4\text{H}_4^+$	7		-6.8019	-6.1773	-6.1692	-5.9075
$c\text{-C}_4\text{H}_4^+$	8		-6.5433	-5.9413	-5.9313	-5.7803
$\mathcal{D}\text{-C}_4\text{H}_4^+$	9		-5.9417	-6.2257	-6.2036	-6.1963
$\varepsilon\text{-C}_4\text{H}_4^+$	10		-6.0397	-5.7753	-5.7548	-5.7969
$\text{C}_2\text{H}_2^+ + \text{C}_2\text{H}_2$	11		-2.5463	-2.2992	-2.2967	-2.3621
$\text{C}_4\text{H}_2^+ + \text{H}_2$	12		-2.8025	-3.6923	-3.7292	-3.5181

Fragmentation channels:

The fragmentation channels $\text{C}_2\text{H}_2^+ + \text{C}_2\text{H}_2$ and $\text{C}_4\text{H}_2^+ + \text{H}_2$ are exergonic relative to the reactants $\mathcal{A}\text{-C}_3\text{H}_3^+(\mathbf{3}) + \text{CH}$; calculated enthalpies range between 2.5–3.5 eV. The chemical activation of **10** reaches roughly 6 eV.

Comparison of methods:

Based on the results of Table 4.4, the sequence of product stability is different for each quantum theory method. While G3 agrees with the DFT based sequence of product stability, except for **8** and **10**, DFTB constitutes a total different sequence. This discrepancy might effect the MD product distribution.

4.3.2.1 Temperature dependence of enthalpies

For each product of Table 4.4, the enthalpic and entropic effects over the temperature are plotted in Figure 4.10.

Calculated trends below 100 K:

The trends of $\Delta_R G$ are determined by the reaction entropy $\Delta_R S$. Calculated $\Delta_R S$ of the association products is evaluated to be -0.0015 eV/K, i. e., $\Delta_R G$ become more positive with increasing temperature. In contrast, $\Delta_R S$ of the fragmentation channel **12** ($\text{C}_4\text{H}_2^+ + \text{H}_2$) is 5 times lower. A lowering of the C_4H_2^+ symmetry decreases $\Delta_R S$ of channel **12** by 3%. In the case of **11**, $\text{C}_2\text{H}_2^+ + \text{C}_2\text{H}_2$, $\Delta_R S$ is about -0.0001 eV/K. These $\Delta_R S$ values increase by a factor of 8 if the high symmetry of C_2H_2 is broken.

Calculated trends above 1000 K:

The given $\Delta_R S$ values change slightly at high temperatures. However, the $\Delta_R S$ ratios between products and fragmentation products remain. This causes that the fragmentation

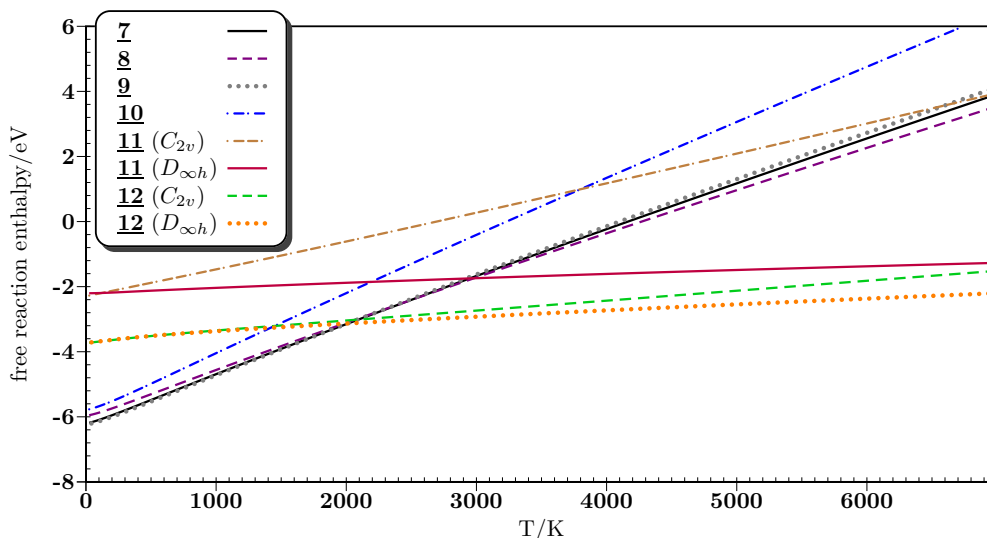


Figure 4.10: Free reaction enthalpies ($\Delta_R G(T)$) of product isomers of Table 4.4 obtained by Btz2 level of theory.

$C_4H_2^+ + H_2$ becomes thermodynamically favoured above all products at temperatures higher than 2000 K. In the case of $C_2H_2 + C_2H_2^+$, this transition is achieved at temperatures above 3000 K. Both cases indicate that in hot environments products of $C_4H_4^+$ are dominated by fragmentations.

4.3.2.2 Canonical population distribution

The population distribution of the products, 7, 8, 9 and 10, is given in Figure 4.11.

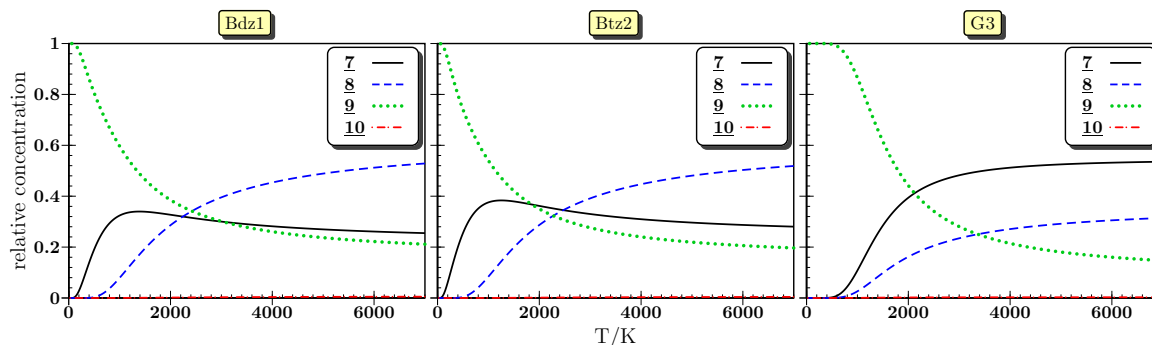


Figure 4.11: Canonical population analysis of $C_4H_4^+$ product isomers taken from Table 4.4 obtained by Bdz1 (left) Btz2 (middle) and G3 (right).

In a thermal bath with a temperature over 2500 K, the distribution of the given products is shifted to the non-cyclic products 7 and 8. This correlates with the production distribution of the MD simulations for 3 and CH at $t_{\text{postcoll}} = 6$ ps.

The difference between the distributions is the result of the different applied levels of theory. In the case of the HF based frequency analysis as part of the G3 method, the relative concentration of product 7 remains above 8. It disagrees with the results obtained at Bdz1 and Btz2 level of theory.

4.3.3 Reaction path analysis

The calculated MEP between the given reactants and products of this reaction system are given in Figure 4.12.

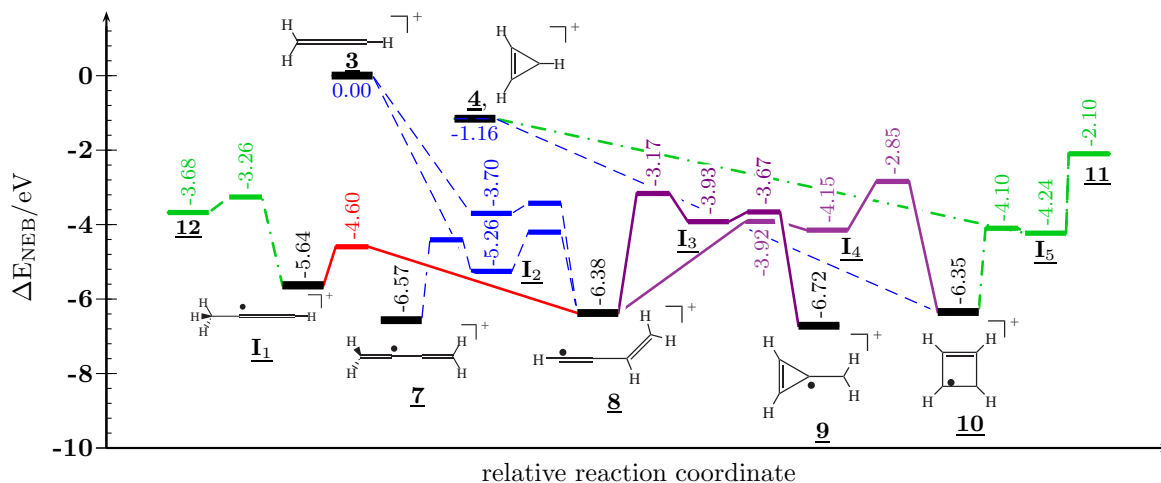


Figure 4.12: Stationary points of $C_3H_3^+-CH$ addition reaction paths, of isomerisation paths between non-cyclic products, of cyclisation paths and fragmentation paths obtained by Bdz1. Structures I_x represent stationary intermediates.

4.3.3.1 The chemical network and isomerisation rates

The addition of CH at **3** predominately attacks the terminal carbon with the highest electron density (blue dashed line of 0.00 to -5.26 eV at Figure 4.12). It is in agreement with the electron density of **3** obtained by the *Mulliken* population analysis. The resulting intermediate is labelled **I₂**.

The addition of methyne at the other terminal carbon atom of **3** is also barrierless. The resulting intermediate on this path to **8** lies at -3.70 eV relative to **3** and CH.

The barrierless addition of CH to **4** extends the ring structure to a 4-membered ring which corresponds to **10** (-6.4 eV at Figure 4.12)

*Isomerisations of the energised **I₂***

The intermediate **I₂** at -5.26 eV has two isomerisation channels; one leads to **7**, while the other to **8**. Both transition states lie between 0.85 and 1.05 eV above **I₂**. However, the isomerisation rate $k_{\text{WR}}^{\text{VT}}$ of **I₂** to **7** is twice the rate of **I₂** to **8** (Table 4.5). The corresponding back transformation rates into **I₂** are 4 times (**7** → **I₂**) and 7 times (**8** → **I₂**) slower.

*Isomerisations between energised **7** and **8***

Based on the approximation that the lowest rate determines the total rate in a combined process, the ratio of the isomerisation between **7** and **8**, $r_{\text{WR}}^{\text{VT}}, \underline{7} \leftrightarrow \underline{8}$, is about 4 to 14.

Isomerisations of energised **8**

Several isomerisation paths of **8** were studied. The structure **8** can be connected with the H₂ elimination from the C₄H₄⁺ system. The isomerisation of **8** to **I**₁ has a rate of $k_{\text{WR}}^{\text{vr}} = 3.378 \times 10^{11} \text{ s}^{-1}$. A dissociation rate for **I**₁ into diacetylene cation and H₂ (**12**) is evaluated to be $k_{\text{WR}}^{\text{vr}} = 1.752 \times 10^{10} \text{ s}^{-1}$. The effective rate coefficient from **8** to **12**, $k_{\text{eff, WR, 8} \rightarrow \text{12}}^{\text{vr}}$, based on Eq. (2.4) and the WR approximation of vibrational-rotational states is about 20 times slower than of the isomerisation of **8** to **7**.

Table 4.5: Unimolecular rate coefficients of radiative deactivation and of isomerisation processes based on different approaches. Energies (at Bdz1 level of theory) are taken from the MEP and TS optimisation (Figure 4.12). The internal energy is assumed to correspond in amount to the enthalpy at 0 K of the reaction **3** and methyne dissipated to the product **X**.

product	E_{vr}^a / eV	$k_r(E_{\text{vr}})$ / s ⁻¹	Isomerisation/Dissociation					
			to	$E_{\text{vr}}^\ddagger^a$ / eV	$k_{\text{DC}}^{\text{v}}(E_{\text{vib}})^a$ / s ⁻¹	$k_{\text{WR}}^{\text{v}}(E_{\text{vib}})^a$ / s ⁻¹	$k_{\text{WR}}^{\text{vr}}(E_{\text{vr}})^a$ / s ⁻¹	$k_{\text{m}}^{\text{vr}}(T_{\text{vr}})^a$ / s ⁻¹
7	6.309	2.243×10^2	I ₂	4.293	1.278×10^{12}	1.279×10^{12}	8.224×10^{11}	2.082×10^{12}
I ₂	5.027	4.409×10^2	7	4.293	5.607×10^{12}	5.613×10^{12}	3.178×10^{12}	2.731×10^{12}
			8	4.105	3.410×10^{12}	3.417×10^{12}	1.618×10^{12}	1.321×10^{12}
8	6.075	2.890×10^2	I ₁	4.441	6.954×10^{11}	6.941×10^{11}	3.378×10^{11}	2.350×10^{11}
			I ₂	4.105	6.265×10^{11}	6.262×10^{11}	2.343×10^{11}	1.525×10^{11}
			I ₄	3.765	9.160×10^{10}	9.156×10^{10}	5.261×10^{10}	2.906×10^{10}
I ₁	5.440	5.993×10^2	8	4.441	1.931×10^{11}	1.932×10^{11}	1.697×10^{11}	1.286×10^{11}
			12	3.240	2.982×10^{10}	2.993×10^{10}	1.752×10^{10}	9.538×10^9
I ₄	3.900	1.657×10^2	8	3.765	1.486×10^{13}	1.487×10^{13}	1.281×10^{13}	1.308×10^{13}
			10	2.707	9.077×10^{10}	9.102×10^{10}	4.498×10^{10}	2.890×10^{10}
10	6.002	1.467×10^2	I ₅	3.951	8.529×10^{12}	8.539×10^{12}	6.849×10^{12}	8.633×10^{12}
			I ₄	2.707	9.505×10^9	9.529×10^9	4.137×10^9	3.131×10^9
I ₅	4.062	3.432×10^2	10	3.951	7.014×10^{12}	7.024×10^{12}	6.282×10^{12}	6.141×10^{12}

^aCompare with footnotes of Table 4.3

Cyclisation of the energised **8**

The two cyclisations of energised **8** to **9** and **10** are defined by barriers of $\Delta E^\ddagger = 3.2$ and 3.5 eV. The rates coefficients of the two-step mechanism, i. e., 1) **8** → **I**₄ and 2) **I**₄ → **10** are evaluated to be $5.261 \times 10^{10} \text{ s}^{-1}$ and $4.498 \times 10^{10} \text{ s}^{-1}$. Each rate coefficient is at least by factor of 4 lower than the isomerisation rate of **8** to **7**.

Dissociation to C₂H₂ + C₂H₂⁺

The MD trajectories revealed that the dissociation channel C₂H₂ + C₂H₂⁺ (green dotted-dashed lines in Figure 4.12) originates either from the dissociation of **10** via **I**₅ (-4.2 eV, Figure 4.12) or from a direct transformation of CH + **4** into the intermediate **I**₅. The ring opening of **10** to **I**₅ is evaluated to have a rate of $k_{\text{WR}}^{\text{vr}} = 6.849 \times 10^{12} \text{ s}^{-1}$. It agrees with the high ratio of fragmentation obtained by the MD simulations. A non-dissociative ring opening

of **10** is only successful if a hydrogen shift is involved which corresponds the mechanism **10** to **8** via **I4**. However, the corresponding rate is 1000 times slower than the dissociative ring opening.

4.3.3.2 Comparison of isomerisation rates

Rates based on the direct count and the WR approximation of the vibrational states, i. e., k_{DC}^v and k_{WR}^v , deviate by 0.18%; this demonstrates the good agreement between the approximation and direct count method.

Without considering that a part of the non-fixed energy will distributed to rotational states, rate coefficients k_{WR}^v are overestimated by 15 to 55% relative to k_{WR}^{vr} . In the case of very small barriers, e. g. **I5** \rightarrow **10**, the deviation between the different WR approximations, k_{WR}^v and k_{WR}^{vr} , is only 11%. For large barriers, e. g. **10** \rightarrow **I4**, the deviation reaches over 55%.

The comparison between k_m^{vr} to k_{WR}^{vr} shows large deviations; the average is evaluated to be 50.6%. Nevertheless, these modified CTST values are closer related to k_{WR}^{vr} than the original CTST values which are normally one or two orders of magnitude too large.

4.4 $C_5H_5^+ + CH$

In this section, the hydrocarbon growth based on CH is studied by the reaction between CH and the reactants *cis*-pent-1-yn-4-en-3-yl cation (*cis*- \mathcal{A} - $C_5H_5^+$, **13**), and the 2-dehydro-2-vinylcycloprop-1-ene cation (\mathcal{D} - $C_5H_5^+$, **18**).

Note that all $C_5H_5^+$ co-reactants are products of the reaction $C_4H_4^+ + CH$ as depicted in the Appendix A.2, and, therefore, fit in a scheme of sequential growth.

Charge distribution in the hydrocarbon reactants

For a qualitative assessment of the CH attack positions, the charge distribution of the reactants **13** and **18** (Figure 4.13) was evaluated by the *Mulliken* population analysis. The obtained distribution is heterogeneous.

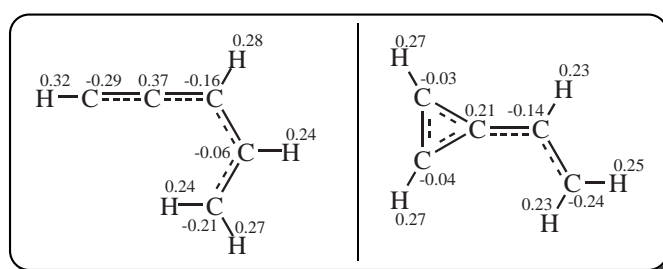


Figure 4.13: Mulliken atomic charges of **13** and **18** obtained by Bdz1.

In the case of **13**, positions of highest electron density are found at both terminal carbon atoms. The highest electron density of **18** is located at the dihydrogenated and terminal carbon atom. Under the terms of electrophicity of the methyne molecule, these obtained positions are supposed to be predominant in the CH addition reaction.

Reactivity of the hydrocarbon reactants

The computed thermodynamic stability of the reactants are given in Table A.2; since the stability of **13** is lower than of **18**, its reactivity can be, in turn, expected slightly increased.

4.4.1 DFTB based MD simulations

In order to sample the reaction potential energy surface, several thousand MD trajectories were computed; MD simulations thereby covered 9 different collision energies (List (B.14)), multiple randomised orientations and collision parameters between 0.2 and 10 Å. Details of the MD setup are described in Section B.1. The result are summarised in the following subsections.

4.4.1.1 Identified product channels

For systemic analysis of mechanisms, the product structures of each trajectory were sorted into product channels that are defined as follows:

- 1.) Non-cyclic products (labelled **ncy**): From the MD unbranched $C_6H_6^+$ structures **23** to **26** and branched $C_6H_6^+$ structures **27** and **28** were identified.

- 2.) Products containing one 3-membered ring: Structures were identified as **29** and **30**.
- 3.) Products containing one 4-membered ring: **31** was the only structure found. Due to its low quantity in the MD, they were summarised together with the 3-ring-membered products; this is abbreviated by **cy-3,4**.
- 4.) Products containing one 5-membered ring (**cy-5**): One structure (**I₁₀**) was identified. The thermodynamically most stable representative is the fulvene (**32**), which was not obtained by the MD simulations.
- 5.) Products containing one 6-membered ring (**cy-6**): The structures **I₁₁**, **I₁₂** and **I₁₃** were obtained by the MD simulations. However, the thermodynamically most stable structure corresponds to the benzene cation (**33**).
- 6.) Fragmentation products (**frag**): The pair $C-C_4H_4^+$ (**7**) and acetylene(**2**) was identified.
- 7.) Orbiting complexes (**cmplx**) which represent reactants circulating each other.

Structures and corresponding energies are given in Table 4.6.

4.4.1.2 Calculated product distribution

The product distribution was calculated based on the cross sections with respect to the defined product channels that are quantified by the counting analysis of MD trajectory snapshots at $t_{\text{postcoll}} = 6$ ps. The twofold dependence of the cross sections on the collision energy ε and the product channels is illustrated in Figure 4.14.

*Product cross section distribution of the reaction between **13** and methyne:*

The reaction between **13** and methyne yields 67–71% of non-cyclic $C_6H_6^+$ between 0.001 eV and 0.10 eV. Further reaction fractions vary between: 13–18% for **cy-3**, 2–4% for **cy-4**, 2–4% for **cy-5**, 4–6% for **cy-6** and less than 1% **frag**. The obtained fraction of **cmplx** decreases from 9% at 0.001 eV to less than 1% at 0.075 eV – decreasing further with growing ε . The ratio between the product fractions is almost constant between 0.001 eV and 0.10 eV. However, the sum of product fractions increases at the cost of the **cmplx** fraction with increasing collision energy.

*Product cross section distribution of the reaction between **18** and methyne:*

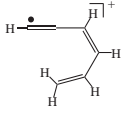
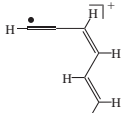
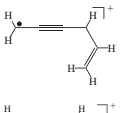
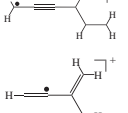
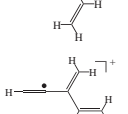
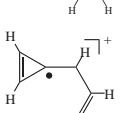
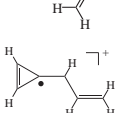
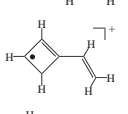
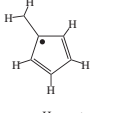
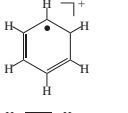
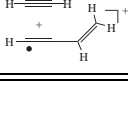
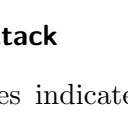
The reaction between **18** and methyne between 0.001 eV and 0.10 eV results in: 30–41% of **cy-3**, 16–23% of **ncy**, 5–15% of **cy-4**, and 16–32% of $C_4H_4^+ + C_2H_2$. The obtained fractions of **cy-5** and **cy-6** remain below 0.6%.

The fraction of **cmplx** decreases from 20% at 0.001 eV to 1% at 0.075 eV.

Comparison between both distributions:

The absolute amount of **cy-5** and **cy-6** products obtained by the reaction between **13** and methyne is a factor of 10 larger than the ones of reaction **18** + CH. On the other side, the reaction **18** + CH produces 15 to 30 times more acetylene which originates from an elimination process. Since reaction **18** + CH possesses a larger fraction of complexes at low collision energies, the lifetime of the orbiting complex is longer.

Table 4.6: Ion-molecule based reaction energies and enthalpies obtained by different quantum theory methods. For each reaction the educts *cis*- \mathcal{A} - $C_5H_5^+$ (**13**) and CH were considered.

products	abbr.	geometry	$\Delta_R E/eV$	$\Delta_R H_{0K}/eV$		
			SD	Btz1//Bdz1	Ptz4	G3
$\mathcal{A}a-C_6H_6^+$	23		-6.3379	-5.5869	-6.0165	-5.4791
$\mathcal{A}b-C_6H_6^+$	24		-6.4909	-5.8226	-6.2357	-5.6974
$\mathcal{B}a-C_6H_6^+$	25		-6.3498	-5.7926	-6.2530	-5.5634
$\mathcal{B}b-C_6H_6^+$	26		-6.4089	-5.9049	-6.3611	-5.6612
$\mathcal{C}a-C_6H_6^+$	27		-6.0778	-5.3508	-5.7627	-5.2859
$\mathcal{C}b-C_6H_6^+$	28		-6.1300	-5.4293	-5.8375	-5.3797
$\mathcal{D}a-C_6H_6^+$	29		-5.6878	-5.8317	-6.2602	-5.8405
$\mathcal{D}b-C_6H_6^+$	30		-5.7818	-5.9718	-6.3972	-5.9556
$\mathcal{E}-C_6H_6^+$	31		-5.7402	-5.1745	-5.7424	-5.3138
$\mathcal{F}-C_6H_6^+$	32		-7.8889	-7.1438	-7.6562	-7.1958
$\mathcal{G}-C_6H_6^+$	33		-8.6081	-7.6477	-8.1448	-7.7623
$c-C_4H_4^+ + C_2H_2$	34		-3.4669	-3.1980	-3.3907	-3.1042

4.4.1.3 Topology of CH attack

The obtained MD trajectories indicated that the reactant **13** is attacked by CH mostly at both of its terminal carbons, but rarely at the centred carbon. This correlates with the obtained charge distribution at Bdz1 level of theory. The observed attack at the monohydrogenated carbon mostly results in 3-membered ring structures, such as **29** and **30**. The attack at the dihydrogenated carbon is accompanied by a hydrogen rearrangement; the resulting product corresponds to a chain extended educt. The obtained *cis-trans* iso-

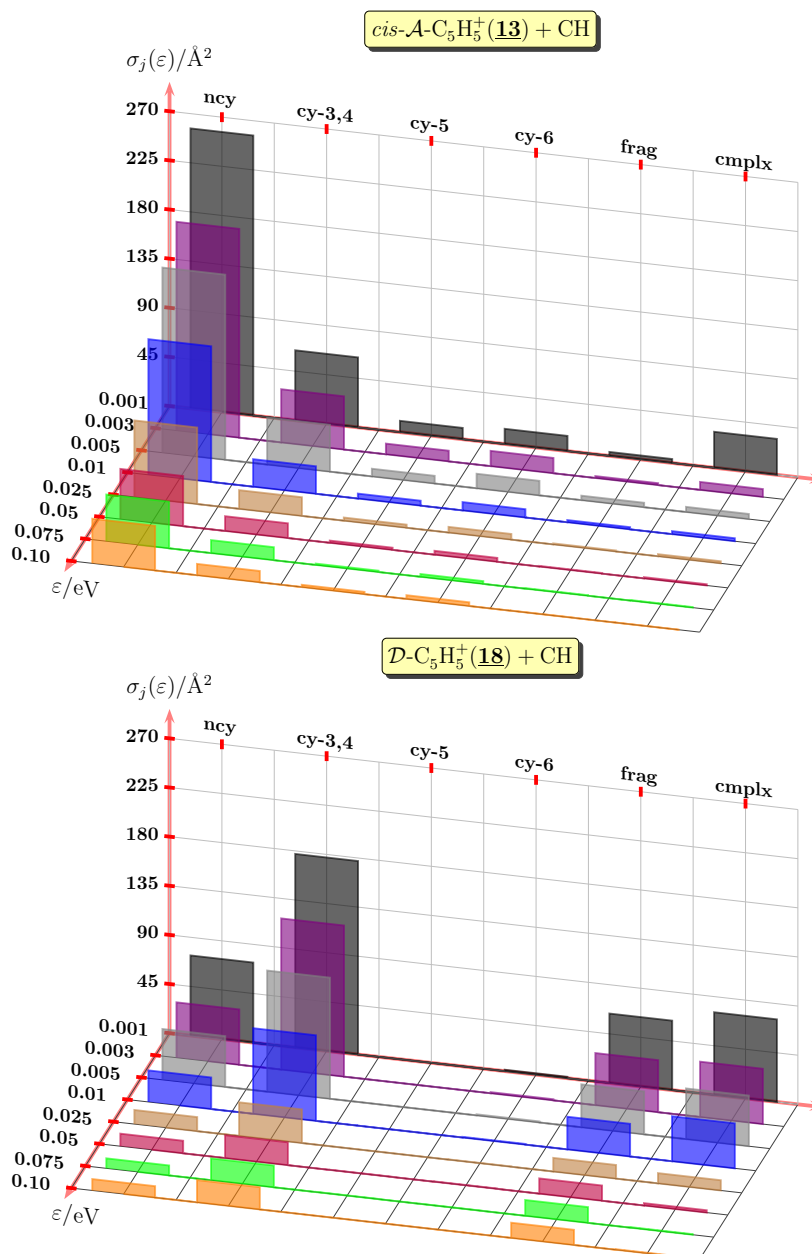


Figure 4.14: Calculated product cross sections $\sigma_{R,j}$ resulting from the reaction between **13** and methyne, **18** and methyne. Both plots correspond to $t_{\text{postcoll}} = 6$ ps applied to different collision energies. Abbreviations correspond to ncy = non-cyclic, cy-3,4 = one 3- or 4-membered ring, cy-5 = one 5-membered ring, cy-6 = one 6-membered ring, frag = fragmentation products, and cmplx = orbiting complex.

merism of the products is caused by the different orientations between the reactant and CH during the attack.

The reactant **18** is attacked by CH at the dihydrogenated terminal carbon and at the 3-membered ring. The attack at the ring structure either causes ring extension or the elimination of acetylene. The latter process can be described by three steps: (1st) CH attachment, (2nd) ring opening, and (3rd) dissociation of the product. The orientation of the CH attack decides whether the system will be extended or to dissociate.

4.4.1.4 Calculated capture rate coefficients

The determination of capture rate coefficients was based on the sum of all product cross sections (Figure 4.14) including the cross sections of the orbiting complex. These results are given in Figure 4.15.

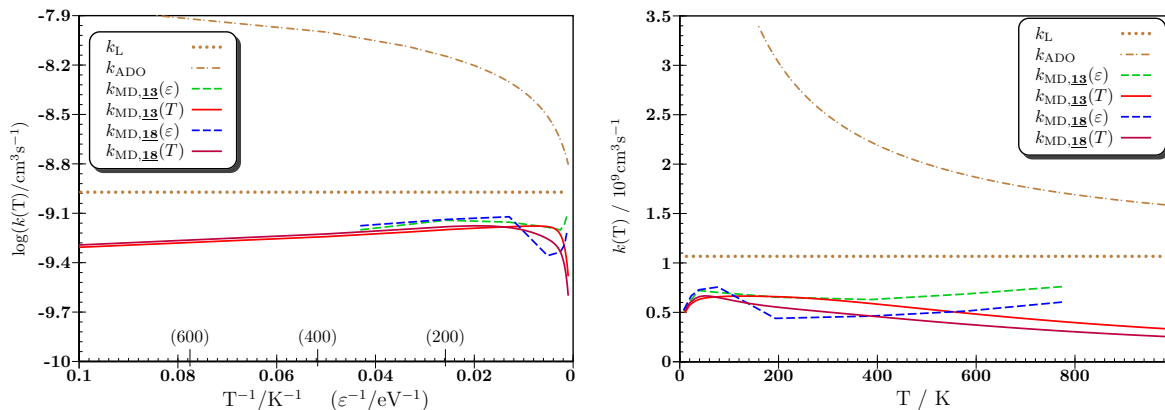


Figure 4.15: Capture rate coefficients of the **13** + CH and **18** + CH reaction systems calculated based on the *Langevin* model (k_L), ADO model (k_{ADO}), and the results of the MD simulations ($k_{\text{MD}}(\epsilon)$ and $k_{\text{MD}}(T)$). Two different representations are given: left) logarithmic k versus inverse T (ϵ_{coll}) and right) k versus T (ϵ_{coll}). Collisional energies and temperature are related by $\epsilon = 3/2k_B T$.

The *Langevin* and ADO values were calculated based on the molecular attributes of the reactants **13** and **18** as given in Table A.1. The temperature-independent *Langevin* value k_L is $1.06 \times 10^{-9} \text{cm}^3 \text{s}^{-1}$, while the ADO values $k_{\text{ADO}}(T)$ range from 1.58×10^{-9} at 1000 K to $10 \times 10^{-9} \text{cm}^3 \text{s}^{-1}$ at 20 K.

In comparison, the $k_{\text{MD}}(\epsilon)$ values of the **13**+CH reaction system range from 5.09×10^{-10} at 0.001 eV (7.7 K) to $7.60 \times 10^{-10} \text{cm}^3 \text{s}^{-1}$ at 0.10 eV (773.6 K). In the case of the **18**+CH reaction system, the $k_{\text{MD}}(\epsilon)$ values vary between 5.22×10^{-10} at 0.001 eV and $7.56 \times 10^{-10} \text{cm}^3 \text{s}^{-1}$ at 0.10 eV. While at collision energies below 0.025 eV the deviation of the $k_{\text{MD}}(\epsilon)$ values between the two systems is less than 5%, at higher energies the deviation reaches a constant value of $1.79 \times 10^{-10} \text{cm}^3 \text{s}^{-1}$. This correlates with the assumption that **13** is more reactive than **18**.

Comparison between $k_{\text{MD}}(T)$ and $k_{\text{MD}}(\epsilon)$:

A considerable agreement between the $k_{\text{MD}}(T)$ and the $k_{\text{MD}}(\epsilon)$ values is achieved in the range of 0.001 and 0.01 eV. However, the obtained $k_{\text{MD}}(T)$ values disagree with the corresponding $k_{\text{MD}}(\epsilon)$ ones at high collision energies and temperatures, since $k_{\text{MD}}(\epsilon)$ values show a positive temperature slope, while the $k_{\text{MD}}(T)$ values are characterised by a negative one. A similar effect is described earlier for the low collision energy/temperature range in Section 4.3.1.3. It is believed by the author that the origin is based on numerical problems in the calculation of the $k_{\text{MD}}(T)$ values.

4.4.2 Product energetics

The reaction enthalpies of the identified product channels are given in Table 4.6; they are obtained at SD, Btz1//Bdz1, Ptz4, and G3 level of theory.

Relative to the energetic level of the **13** reactant and methyne, the CH addition products as given in Table 4.6 are strongly exothermic, e. g. values at the G3 level are between -5.3 to -7.8 eV.

The more reaction energy is release the more stable product configurations are formed which in the case of $C_5H_5^+ + CH$ are the benzene cation (**33**) and the fulvene cation (**32**). Among the non-cyclic $C_6H_6^+$ ions (**23-28**), the highest thermodynamic stability at the G3 level of theory relates to **24**, which is in disagreement with the B3LYP and PW91 results. Here, **26** possesses the highest stability. Note that the relative energetic stability obtained by SD method are in qualitative agreement with the G3 results.

Deviations in the sequence of energy values sorted ascending can be found among the structures **29** and **30** if all methods are compared. In the case of SD method 3-ring-membered structures are less stable than all the **ncy** structures, which is vice versa for the G3 and DFT methods. In the case of B3LYP and PW91, the relative stability of **30** is exceptional; it remains below **24**.

Dissociation products:

The obtained $\Delta_R H_{0K}$ values ranges from 3.1 to 3.5 eV. The formation of fragmentation products **34** is, therefore, exothermic; but endothermic relative to **23** by 2.4 to 2.8 eV depending on the quantum chemical method used.

4.4.2.1 Temperature dependence of enthalpies

The enthalpic and entropic effects of each product ($\Delta_R G$) are plotted in Figure 4.16 as a function of the temperature.

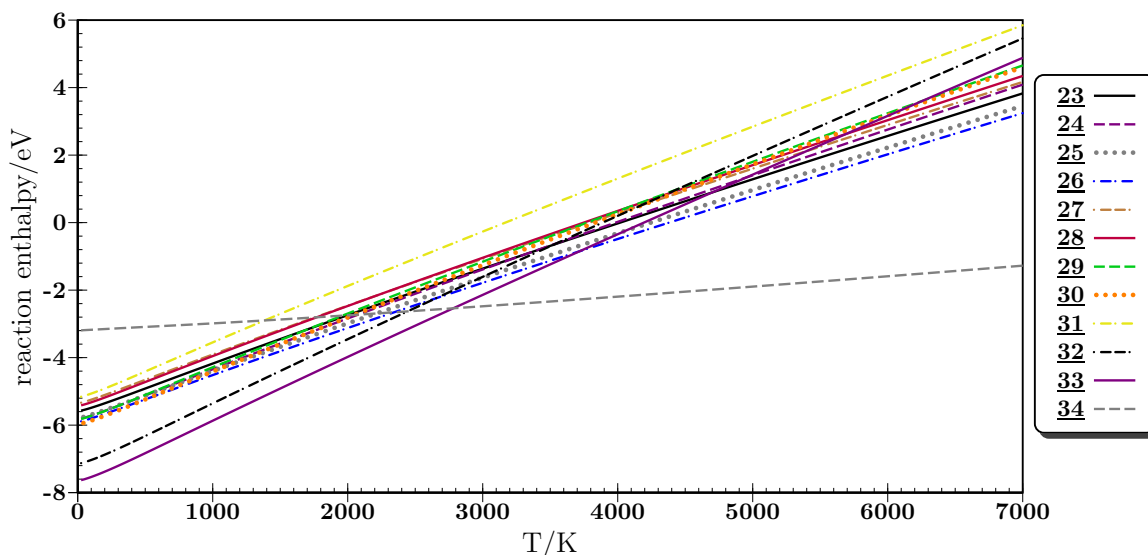


Figure 4.16: Free reaction enthalpies $\Delta_R G(T)$ of product isomers as given in Table 4.6 obtained at Bdz1 level of theory.

Calculated trends below 100 K:

The reaction entropy $\Delta_R S$ was identified as the main contributor on the positive temperature trend of $\Delta_R G$; for association products the slope of the 2nd term of $\Delta_R G$, i. e., $-T \Delta_R S$, is

equal to 0.0012–0.0014 eV/K, while for the fragmentation product it is only 0.0002 eV/K. The ratio between both the 2nd term slopes corresponds roughly to the total slopes of $\Delta_R G$ (Figure 4.16).

Calculated trends above 1000 K:

At reaction temperatures above 2800 K, $\Delta_R G$ of the channel $C_4H_4^+ + C_2H_2$ exceeds every other product channel. The temperature trends also indicates that the formation of non-cyclic $C_6H_6^+$ products is thermodynamically favoured over the formation of benzene cation at temperatures above 4000 K.

4.4.2.2 Canonical population distribution

The population distribution of all association products (Table 4.6) as depicted in Figure 4.17 was calculated based on their harmonic frequencies and the *Boltzmann* distribution.

The benzene cation represents the largest fraction in the thermodynamic equilibrium among the given $C_6H_6^+$ isomers for temperatures up to 4000 K at the G3 level of theory, but is replaced by **26** at temperatures above. This is in disagreement with the results obtained by PW91, where **25** replaces the benzene cation. At the thermodynamic equilibrium above 5000 K the amount of **23** increases to over 10% (B3LYP and G3).

4.4.3 MEP analysis by the NEB method and TS reoptimisation

The reaction paths between reactants and products, which were extracted from the DFTB-MD trajectories before, were optimised by the NEB method at Bdz1 level of theory. Resulting minimum energy paths (MEPs) of CH addition, *cis-trans* isomerisations, cyclisation and hydrogen rearrangements are depicted by their reoptimised local minima and transition states (Figure 4.18).

4.4.3.1 CH addition mechanism

The addition of the methyne at monohydrogenated and sp-hybridised carbon atom of **13** is barrierless and yields the 3-ring-membered structure **29**. The attachment of CH at the dihydrogenated and sp²-hybridised carbon atom results in an intermediate, which rearranges itself into **23** or **24**. The constitution depends on the orientation of the CH attack, i. e., the resulting methylene group is orientated either in *cis* or *trans* position.

4.4.3.2 Obtained isomerisation barriers and rate coefficients

Note that in this subsection isomerisation rate coefficients are discussed which were computed based on the *RRKM* theory and its WR approximation; the rates consider vibrational-rotational states. The results of other approaches and approximations are also given in Table 4.9. Any required molecular data was calculated at Bdz1 level of theory.

*Trans isomerisation of activated **23***

The isomerisation ratio between the conformers **23** and **24**, activated by more than 5.7 eV (Figure 4.19), $r_{WR, 23 \leftrightarrow 24}^{VF}$, is 1.02 to 1. Despite a higher stability of **24** by 0.23 eV, the forward and backward isomerisation rates are almost equal.

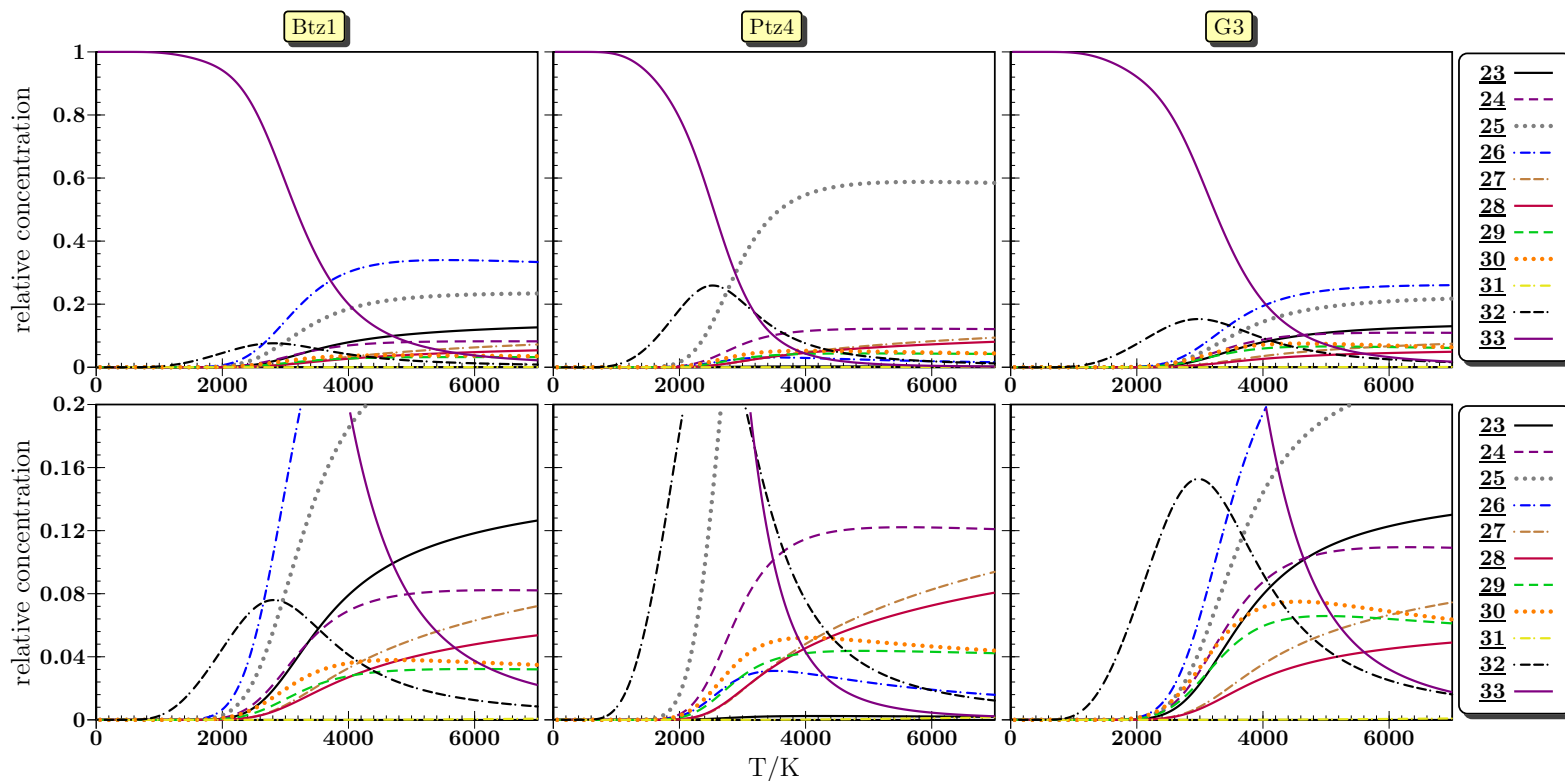


Figure 4.17: Canonical population analysis of $C_6H_6^+$ product isomers taken from Table 4.6 obtained at Btz1 (left) Ptz4 (middle) and G3 (right) level of theory. First row represents the molecule set in the concentration interval of 0 to 1, while the second row in the interval of 0 to 0.2.

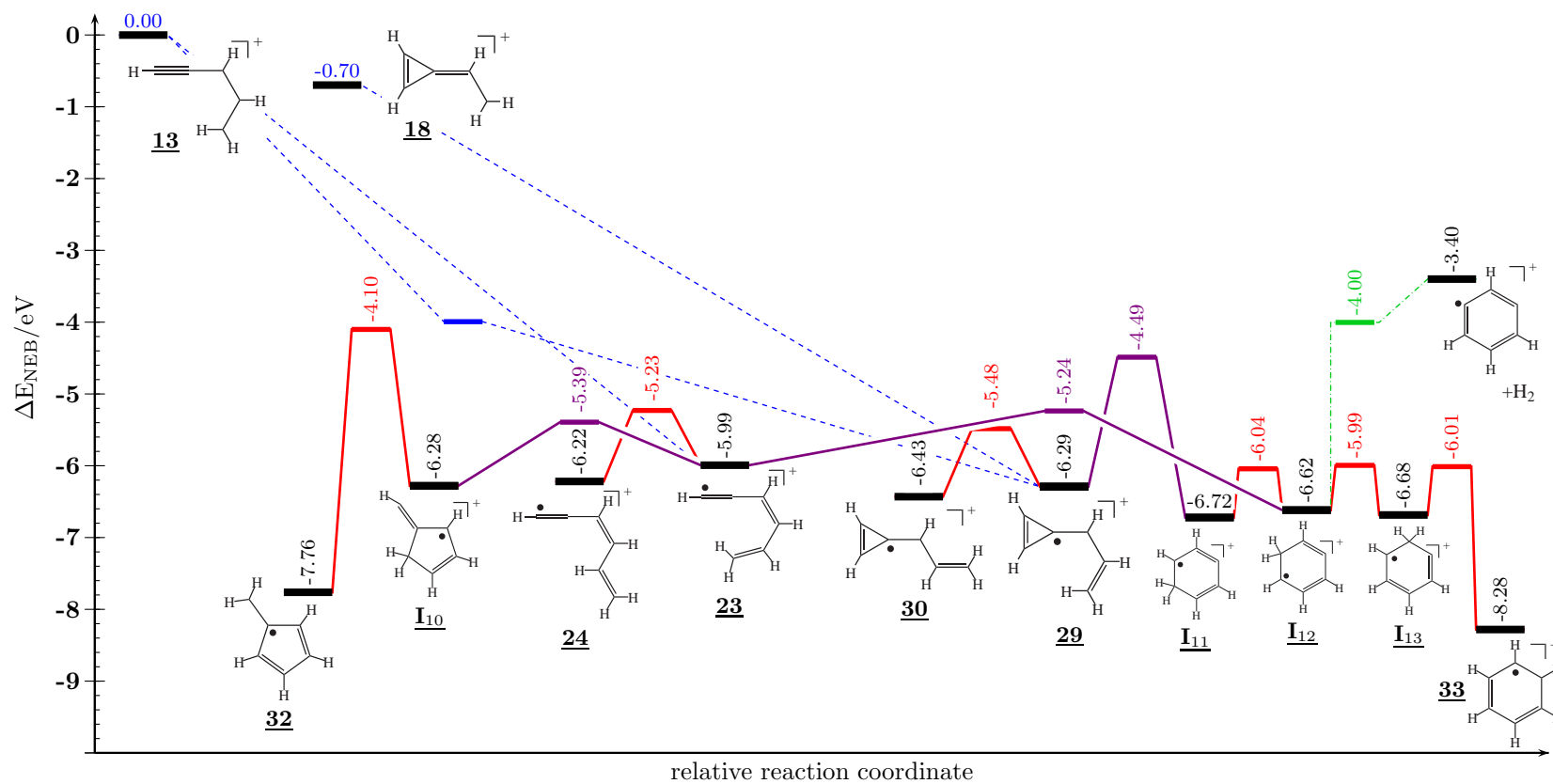


Figure 4.18: Stationary points of $C_5H_5^+ - CH$ addition reaction paths, of $C_6H_6^+$ isomerisation paths between conformers, of $C_6H_6^+$ cyclisation paths and $C_6H_6^+$ fragmentation paths obtained at Bdz1 level of theory.

Table 4.7: Unimolecular rate coefficients of radiative deactivation and isomerisation processes based on different approaches. Energies (at Bdz1 level of theory) are taken from the MEP and TS optimisation (Figure 4.18). The internal energy is assumed to correspond in amount to the enthalpy of the reaction **13** (*cis-A-C₅H₅⁺*) and methyne dissipated to the product **X** at 0 K.

product	E_{vr}^a / eV	$k_r(E_{\text{vr}})$ / s ⁻¹	Isomerisation / De-cyclisation					
			to	E_{vr}^\ddagger ^a / eV	k_{DC}^{v} ^a / s ⁻¹	k_{WR}^{v} ^a / s ⁻¹	$k_{\text{WR}}^{\text{vr}}$ ^a / s ⁻¹	k_{m}^{vr} ^a / s ⁻¹
32	7.401	1.734×10^2	I ₁₀	3.922	1.470×10^8	1.470×10^8	6.254×10^7	3.454×10^7
I ₁₀	5.960	1.896×10^2	23	5.157	3.368×10^{12}	3.369×10^{12}	3.143×10^{12}	2.432×10^{12}
			32	3.922	4.664×10^9	4.663×10^9	2.553×10^9	1.122×10^9
23	5.723	1.893×10^2	24	5.021	4.773×10^{11}	4.795×10^{11}	4.314×10^{11}	3.350×10^{11}
			I ₁₀	5.157	1.221×10^{11}	1.226×10^{11}	7.862×10^{10}	6.320×10^{10}
			I ₁₂	5.001	5.305×10^{10}	5.337×10^{10}	3.178×10^{10}	2.374×10^{10}
24	5.946	2.244×10^2	23	5.021	5.042×10^{11}	5.043×10^{11}	4.228×10^{11}	3.013×10^{11}
30	6.147	2.459×10^2	29	5.252	6.361×10^{11}	6.362×10^{11}	5.850×10^{11}	4.229×10^{11}
29	6.008	2.100×10^2	30	5.252	9.609×10^{11}	9.640×10^{11}	8.489×10^{11}	6.476×10^{11}
			I ₁₁	4.271	3.239×10^9	3.256×10^9	1.670×10^9	8.124×10^8
I ₁₁	6.376	1.821×10^2	I ₁₂	5.758	9.888×10^{11}	9.907×10^{11}	8.513×10^{11}	6.996×10^{11}
			29	4.271	2.822×10^{10}	2.828×10^{10}	1.821×10^{10}	8.247×10^9
I ₁₂	6.280	1.805×10^2	I ₁₁	5.758	1.075×10^{12}	1.077×10^{12}	9.402×10^{11}	7.965×10^{11}
			I ₁₃	5.710	8.849×10^{11}	8.847×10^{11}	7.663×10^{11}	6.362×10^{11}
			23	5.001	8.691×10^{11}	8.719×10^{11}	7.415×10^{11}	4.812×10^{11}
I ₁₃	6.335	1.954×10^2	I ₁₂	5.710	1.004×10^{12}	1.003×10^{12}	8.569×10^{11}	7.039×10^{11}
			33	5.740	1.322×10^{12}	1.322×10^{12}	1.133×10^{12}	9.515×10^{11}
33	7.922	1.134×10^2	I ₁₃	5.740	5.857×10^9	5.865×10^9	3.860×10^9	1.909×10^9

^aCompare with footnotes of Table 4.3

Cyclisation of activated **23**

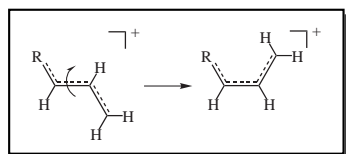


Figure 4.19: Rotation process around a partial CC double bond.

The cyclisation rate of **23** activated by 5.7 eV (**23**^{*}) towards the 5-ring-membered (I₁₀) and to the 6-ring-membered structures (I₁₂) is 5.5 and 13.5 times slower than the isomerisation rate to **24**, although the cyclisation barriers lie between 0.16 eV and 0.01 eV below the isomerisation barrier towards **24**. The ratios of cyclisation to decyclisation $r_{\text{WR}, \mathbf{23} \leftrightarrow \text{I}_{10}}^{\text{vr}}$ and $r_{\text{WR}, \mathbf{23} \leftrightarrow \text{I}_{12}}^{\text{vr}}$ are equal to 0.025 and 0.043. Since the decyclisation rates are higher than of the corresponding

cyclisation, the cyclisation process is considered to be a slow and rare event.

Considering the process **23**^{*} → **32**^{*}

In the case of isomerisation of activated **23** to the fulvene cation (**32**), i. e., **23** → I₁₀ → **32**, the slowest mechanism step is given by I₁₀ → **32** with $k_{\text{WR}}^{\text{vr}} = 2.553 \times 10^9 \text{ s}^{-1}$. Another lim-

iting factor is the isomerisation ratio of intermediate \underline{I}_{10} that contributes to the formation $\underline{32}$. This isomerisation rate ratio $f_{WR, \underline{I}_{10} \rightarrow \underline{32}}^{vr}$ is only 0.00081 at the given activation energy. Thus, the estimated effective formation rate at the given activation energy results in $k_{WR}^{vr} = 2.072 \times 10^6 \text{ s}^{-1}$.

Considering the process $\underline{23}^ \rightarrow \underline{33}^*$*

In the case of the thermal isomerisation to $\underline{33}$, i. e., $\underline{23} \rightarrow \underline{I}_{12} \rightarrow \underline{I}_{13} \rightarrow \underline{33}$, the slowest step is assigned to $\underline{23} \rightarrow \underline{I}_{12}$ with $k_{WR}^{vr} = 3.178 \times 10^{10} \text{ s}^{-1}$. The obtained isomerisation rate ratios are given with $f_{WR, \underline{I}_{12} \rightarrow \underline{I}_{13}}^{vr} = 0.3130$ and $f_{WR, \underline{I}_{13} \rightarrow \underline{33}}^{vr} = 0.5694$. The effective formation rate can be, therefore, estimated with $k_{WR}^{vr} = 5.664 \times 10^9 \text{ s}^{-1}$. This suggests that $\underline{23}$ is a highly potential structure for the formation of benzene cation.

Based on the obtained effective rates, the formation of benzene cation from activated $\underline{23}$ is about 2500 times more likely than the fulvene formation from $\underline{23}^*$.

Formation and isomerisations of the energised $\underline{29}$

The structure $\underline{29}$ is produced by a barrierless addition of methyne to the dihydrogenated carbon of $\underline{18}$. The freedom in the orientation of methyne and the accompanied hydrogen rearrangement during the attack on the dihydrogenated carbon of $\underline{18}$ allows also the formation of the conformer $\underline{30}$. The isomerisation rate ratio between these two conformers, $r_{WR, \underline{29} \leftrightarrow \underline{30}}^{vr}$, is equal to 1.45.

A cyclisation of $\underline{29}$ to the benzene cation was considered to be similar to the cyclisation of $\underline{23}$; the slowest step during the cyclisation is related with the ring closure process, i. e., $\underline{29} \rightarrow \underline{I}_{11}$. Multiplying this process with isomerisation rate ratios of \underline{I}_{11} to \underline{I}_{12} (0.9791), \underline{I}_{12} to \underline{I}_{13} , and \underline{I}_{13} to $\underline{33}$, the effective formation rate k_{WR}^{vr} is equal to $2.914 \times 10^8 \text{ s}^{-1}$. This means that the formation of benzene by activated $\underline{29}$ is 20 times less slower than by $\underline{23}$.

4.4.3.3 Comparison of isomerisation rates

Rates based on the direct count and the WR approximation of the vibrational states, i. e., k_{DC}^v and k_{WR}^v , deviate by 0.3%; this demonstrates the good agreement between the approximation and direct count method. Without considering that a part of the non-fixed energy will distributed to rotational states, rate coefficients k_{WR}^v are overestimated in average by 28.7% relative to k_{WR}^{vr} . The comparison between k_{m}^{vr} to k_{WR}^{vr} shows large deviations; the average is evaluated to be 33.5% which is smaller than the computed deviation in Section 4.3.3.

4.5 $C_6H_6^+ + CH$

In this section, the hydrocarbon growth based on CH is studied by the reaction between CH and the reactants *cis,cis*-hex-1-yn-3,5-dien-3-yl cation ($\mathcal{A}a-C_6H_6^+$, **23**), and the *cis,trans*-hex-1-yn-3,5-dien-3-yl cation ($\mathcal{A}b-C_6H_6^+$, **24**).

Additionally, MD trajectories of the reaction between 2-dehydro-2-allylcycloprop-1-ene cation ($\mathcal{D}a-C_6H_6^+$, **29**) and methyne were computed. Those results were of particular interest for finding alternative cyclisation pathways.

Note that all $C_6H_6^+$ co-reactants are products of the reaction $C_5H_5^+ + CH$ described in the previous section.

4.5.1 DFTB based MD simulations

In order to sample the reaction potential energy surface, several thousand MD trajectories were computed; MD simulations thereby covered 9 different collision energies (List (B.14)), multiple randomised orientations and collision parameters between 0.2 and 10 Å. Details of the MD setup are described in Section B.1.

4.5.1.1 Identified product channels

Product channels were derived from the analysis of all MD trajectories; characteristic structures that represent a channel are:

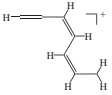
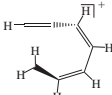
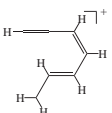
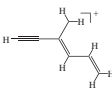
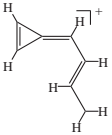
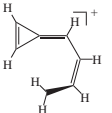
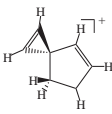
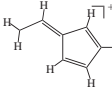
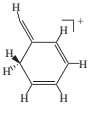
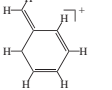
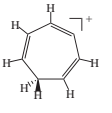
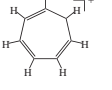
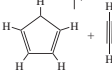
- 1.) Non-cyclic $C_7H_7^+$ products: This channel is referred to as **ncy** hereafter. Assigned unbranched structures are **35** to **37**. Additionally, a branched structure (**38**) was identified.
- 2.) A combined class of $C_7H_7^+$ containing either one 3- or one 4-membered ring (**cy-3,4**): **39** and **40** were identified representatives.
- 3.) Products containing one 5-membered ring (**cy-5**): From the MD **41** and **41a** were obtained, while the thermodynamically most stable structure **42** was not found.
- 4.) A class $C_7H_7^+$ with one 6-membered ring (**cy-6**): The only identified structure was **43**, which is hydrogen-displaced constituent of the thermodynamic more stable structure **44**.
- 5.) A class $C_7H_7^+$ with one 7-membered ring (**cy-7**): Structures **45** and **45a** were obtained. The thermodynamic related tropylium structure **46** was not found by the MD.
- 6.) Orbiting complexes (**cmplx**) representing the reactants circulating each other.

Structures and corresponding energies are given in Table 4.8.

4.5.1.2 Calculated product distribution

The product distribution was calculated based on the cross sections with respect to the defined product channels that are quantified by the counting analysis of MD trajectory snapshots at $t_{\text{postcoll}} = 200$ fs and 6 ps. The twofold dependence of the cross sections on the collision energy ε and the product channels is depicted in Figure 4.20.

Table 4.8: Ion-molecule based reaction energies and enthalpies obtained by different quantum theory methods. For each reaction the educts $Aa-C_6H_6^+$ (**23**) and CH were considered.

products	abbr.	geometry	$\Delta_R E/eV$	$\Delta_R H_{0K}/eV$		
			SD	Btz1//Bdz1	Ptz4	G3
$Aa-C_7H_7^+$	35		-7.6552	-6.4195	-6.8649	-6.5931
$Ab-C_7H_7^+$	36		-7.3588	-6.0711	-6.5345	-6.3136
$Ac-C_7H_7^+$	37		-7.6074	-6.4096	-6.8518	-6.5943
$Ca-C_7H_7^+$	38		-7.1640	-5.9908	-6.3720	-6.2969
$Da-C_7H_7^+$	39		-7.0594	-6.0456	-7.1674	-6.9881
$Db-C_7H_7^+$	40		-6.8649	-6.4732	-6.9159	-6.8072
$Fa-C_7H_7^+$	41		-7.4349	-6.4923	-7.2064	-6.9776
$Fb-C_7H_7^+$	42		-8.5092	-7.1101	-7.6309	-7.5493
$Ga-C_7H_7^+$	43		-7.4699	-5.8037	-6.4767	-6.2990
$Gb-C_7H_7^+$	44		-10.0510	-8.6752	-9.1757	-9.0661
$Ha-C_7H_7^+$	45		-7.9883	-6.2823	-6.9661	-6.7609
$Hb-C_7H_7^+$	46		-10.4352	-9.0437	-9.5410	-9.3658
$\mathcal{F}-C_5H_5^+ + C_2H_2$	47		-5.4337	-4.3621	-4.6520	-4.8328

Product distribution at 200 fs:

At the collision point t_0 , all reactive collisions were considered to be in a configuration corresponding to the association complex (**cmplx**). According the results in Figure 4.20,

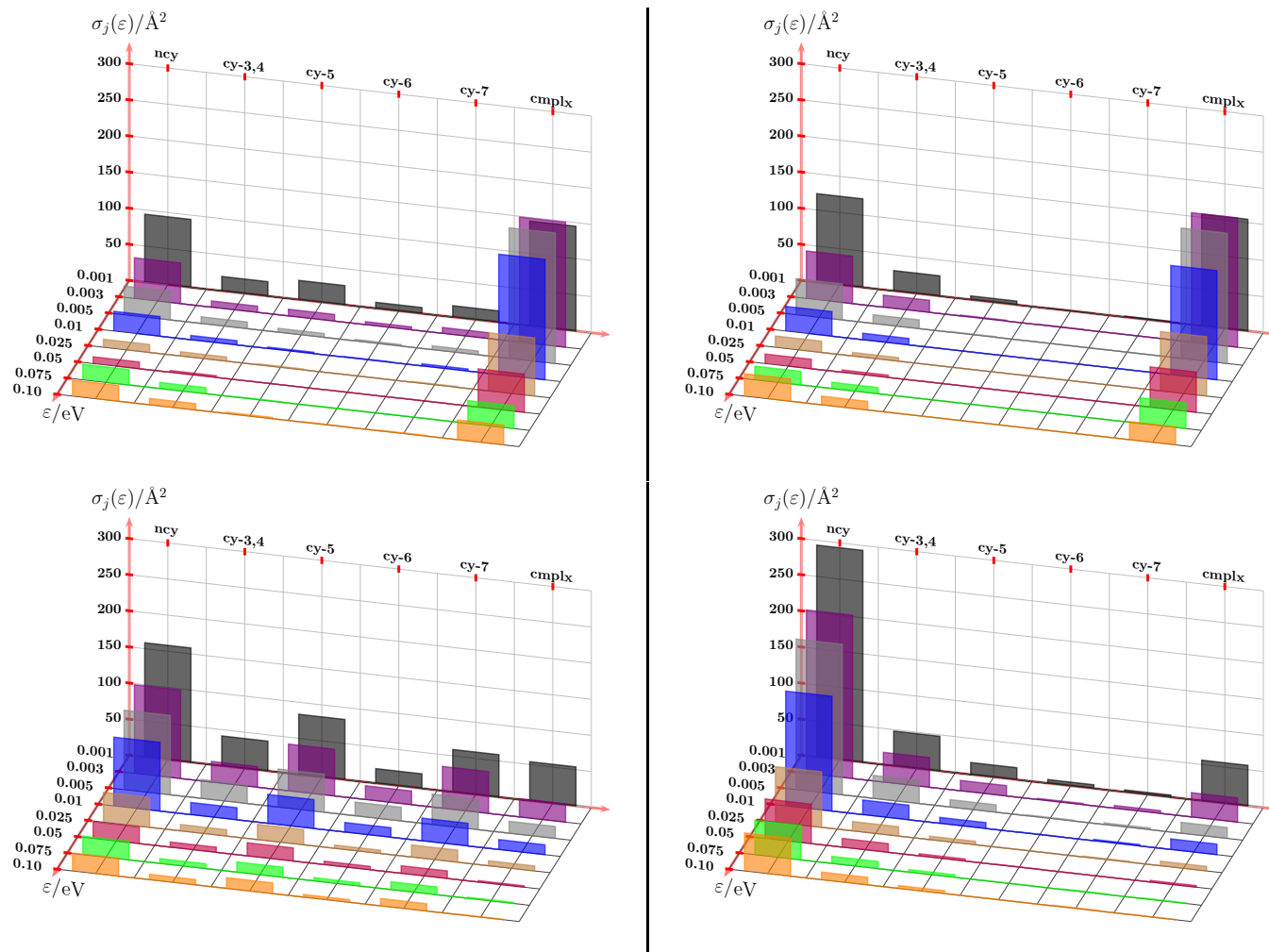


Figure 4.20: Calculated product cross sections $\sigma_{R,j}$ resulting from the reaction between **23** (left), **24** (right) and methyne. The plots correspond to $t_{\text{postcoll}} = 200$ fs (top) and 6 ps (bottom) applied to different collision energies. Abbreviations correspond to ncy = non-cyclic, cy-3,4 = one 3- or 4-membered ring, cy-5 = one 5-membered ring, cy-6 = one 6-membered ring, cy-7 = one 7-membered ring, and cmplx = orbiting complex.

25–50% of this association complex decays within 200 fs propagation time. Moreover, the obtained distribution of the products depends on the *cis-trans* constitution of the reactants **23** and **24**.

In the case of the reaction **23** + CH, the ratio between the fraction of product channels is composed as follows: 57–75% **ncy**, 10–29% **cy-3,4**, 1–16% **cy-5**, 1–5% **cy-6**, and 1–10% **cy-7**. The yielded variation of each fraction is systematic, i. e., fraction **cy-3,4** enlarges at the costs of the other fractions with increasing collision energy.

In the case of the reaction **24** + CH, the ratio between the fraction of product channels consists of 68–79% **ncy**, 18–31% **cy-3,4**, 0–3% **cy-5**, 0–1% **cy-6**, and 0–1% **cy-7**. Similar to **23** + CH, fraction **cy-3,4** increases at the costs of the other fractions with increasing collision energy.

The comparison between the distributions shows that the formation of cyclic products is a direct process of the initial CH attack and depends on the *cis-trans* configuration of the $C_6H_6^+$ reactants. In the case of an all *cis* configuration of the $C_6H_6^+$ reactant, the CH molecule links both terminal carbon atoms forming a ring structure. Based on the results of the MD simulations, an isomerisation of non-cyclic $C_7H_7^+$ to $C_7H_7^+$ containing one 6- or 7-membered is also possible. The obtain of a **cy-7** fraction from **24** + CH, which does not permit the ring formation by “linking”, indicates that the isomerisation is a fast process due to the impact of high and non-fixed reaction energy on the molecules (Table 4.8).

Product distribution at 6 ps:

The obtained fraction of association complex was decreased to 1–13% with respect to all reactive collisions; this decrease is inverse proportional to the MD time but also the collision energy $\varepsilon_{\text{coll}}$. The residual fractions of products are distributed as follows:

- 1.) 36–48% of **ncy**, 9–12% of **cy-3,4**, 20–29% of **cy-5**, 6–8% of **cy-6**, and 16–20% of **cy-7** in the case of the reaction between **23** + CH. The comparison with the fraction values at 200 fs shows a shifted distribution. The amount of **ncy** and **cy-3,4** are decreased relative to the 5-, 6- and 7-membered ring structures. Under the assumption that the product distribution at 200 fs excludes transformation between the products, this decrease of fractions can be only explained by isomerisation of non-cyclic and 3- and 4-membered ring structures into larger ring structure. Corresponding to the obtained ratios, the isomerisation leads primarily to pentagons, but less to heptagons and least to hexagons.
- 2.) In the case of the reaction between **24** + CH, the distributions is splitted into 77–83% of **ncy**, 10–17% of **cy-3,4**, 4–6% of **cy-5**, 0–1% of **cy-6**, and 1–2% of **cy-7**. In comparison with the obtained distribution at 200 fs, the relative amounts of **ncy**, **cy-5** and **cy-7** are increased, while the fraction of **cy-3,4** is lowered.

Based on these fraction shifts, it can be concluded that longer simulation time provides and favours the isomerisation to 5- and 7-membered ring structures.

4.5.1.3 Topology of CH attack

Based on the MD simulation, each reactant was attacked by CH at both its terminal carbons. In each case, the observed attack at the monohydrogenated carbon mostly results in 3-membered ring structures, such as **39** and **40**. The attack at the dihydrogenated carbon is accompanied by a hydrogen rearrangement resulting in chain extension. A resulting *cis-trans* isomerism of the products is caused by the different orientations and alignments between the reactant and CH.

Topology of direct cyclisation:

The methyne molecule "bridges" in a two-step sequence both terminal carbons of the reactant **23**.

4.5.1.4 Calculated capture rate coefficients

According to the results in Figure 4.21, the $k_{MD}(\varepsilon)$ values of both reaction systems range from 5.5×10^{-10} to 9.0×10^{-10} $\text{cm}^3 \text{s}^{-1}$. Since the deviation between both sets remains below 5%, the reactivity of **23** and **24** can be assumed as nearly equal.

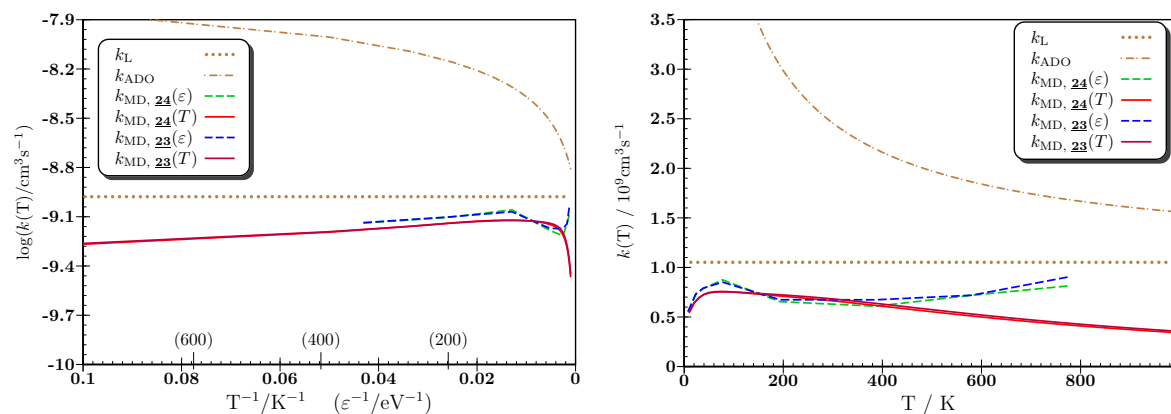


Figure 4.21: Capture rate coefficients of the **23** + CH and **24** + CH reaction systems based on the *Langevin* model (k_L), ADO model (k_{ADO}), and the results of the MD simulations ($k_{MD}(\varepsilon)$ and $k_{MD}(T)$). Two different representations are given: left) logarithmic k versus inverse T ($\varepsilon_{\text{coll}}$) and right) k versus T ($\varepsilon_{\text{coll}}$). Collisional energies and temperature are related by $\varepsilon = 3/2k_B T$.

The *Langevin* and ADO values were calculated based on the molecular attributes of the reactants **23** and **24** as given in Table A.1. In comparison with the k_L value, 1.05×10^{-9} $\text{cm}^3 \text{s}^{-1}$, and with $k_{ADO}(T)$ values, which range from 9.87×10^{-9} at 20 K to 1.56×10^{-9} $\text{cm}^3 \text{s}^{-1}$ at 1000 K, the MD based rate values, $k_{MD}(\varepsilon)$, are roughly twice to 10 times lower.

Moreover, the computed $k_{MD}(T)$ values disagree with slope of the corresponding $k_{MD}(\varepsilon)$ values at high collision energies or temperatures. The $k_{MD}(\varepsilon)$ values result in a positive temperature slope while $k_{MD}(T)$ values correspond to a negative one. However, a considerable agreement between the $k_{MD}(T)$ and the $k_{MD}(\varepsilon)$ values is given in the range of $\varepsilon_{\text{coll}} = 0.001$ eV and $\varepsilon_{\text{coll}} = 0.01$ eV.

4.5.2 Product energetics

CH addition products of **23** (Table 4.8) are formed in a strongly exothermic process; the corresponding values at the G3 level of theory range from -6.3 to -9.3 eV.

The thermodynamic stability of the products was estimated by the formation enthalpy at 0 Kelvin $\Delta_R H_{0K}$, after what the highest stability is given by the tropylium cation (**46**) and the benzyl cation (**44**). The thermodynamic stability of intermediates containing one 6- and 7-membered ring, **43** and **45**, is by comparison about 2.5 eV lower. Among the given non-cyclic $C_7H_7^+$ ions (**35–38**), the highest thermodynamic stability at the G3 level of theory was assigned to **37**. In the case of B3LYP, PW91 and SD methods the highest stability is, however, to be assigned to the structure **35**. Moreover, this class of non-cyclic products has the lowest thermodynamic stability among the product classes given in Section 4.5.1.

The enthalpic difference (ΔH) between the isomers **35**, **36** and **37** as well as **39** and **40** remains between 0.2 and 0.3 eV; all-*cis* configurations (**24** and **40**) provide the lowest energetic stability. This is related due to steric hindrance which even causes all-*cis* configurations to be a non-planar molecular system.

Dissociation products:

The formation energy of **47** was computed to be -4.83 eV at G3 level of theory. However, the dissociation has to be considered endothermic relative to the energetic levels of any association product.

4.5.2.1 Temperature dependence of enthalpies

The calculated $\Delta_R G(T)$ value of each product (Table 4.8), which combine the enthalpic and entropic effects over the temperature, are plotted in Figure 4.22.

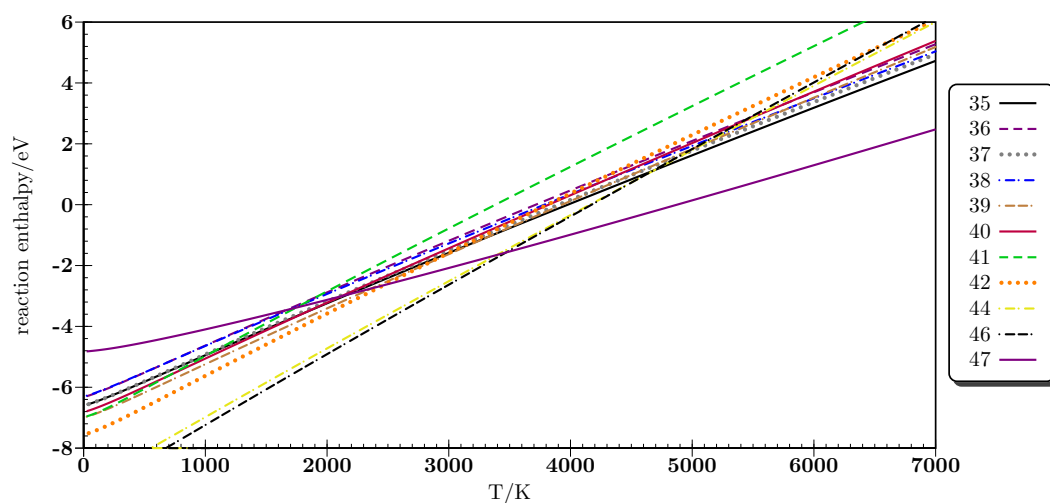


Figure 4.22: Free reaction enthalpies $\Delta_R G(T)$ of product isomers of Table 4.8 obtained at G3 level of theory.

Based on the results in Figure 4.22, the free enthalpy of each product increases with temperature steadily.

Calculated trends below 100 K:

As a consequence of molarity reduction, the obtained average reaction entropy $\Delta_R S$ decreased by -0.0014 eV/K. The term $\Delta_R H/T$ gave a slope of -0.00027 eV/K. Based on these results^{†7}, $\Delta_R S$ is the main contributor to the increase of the free reaction enthalpy. The entropic and enthalpic contributions of the dissociation channel **47** were computed with -0.00045 eV/K ($\Delta_R S$) and -0.0004 eV/K ($\Delta_R H/T$). The ratio between these entropic and enthalpic contributions is lowered relative to the association products, thus the slope of $\Delta_R G$ was less steep.

Calculated trends above 1000 K:

The results of Figure 4.22 show that the ratios between entropic and enthalpic contributions keep nearly constant up to temperatures of 7000 K. At reaction temperatures above 3475 K, the free entropy of **47** remains below the association products hence being the most exergonic reaction channel. This result matches with obtained trends of the previous reaction systems (Section 4.4.2)

4.5.2.2 Canonical population distribution

The population distributions of different sets of products were calculated (Figure 4.23) from the obtained harmonic frequencies and electronic energies. The set №1 contains all association products as given in Table 4.8 excluding the cyclic intermediates **43** and **45**. The set №2 contains all association products found by MD simulations – this excludes **42**, **44**, and **46**.

Set №1:

The obtained thermal equilibrium is placed on the side of tropylium (**46**) and benzylium (**44**) for temperatures up to 4000 K. At higher temperatures the equilibrium constitutes in a mixture of **35**, **37** and **38** including smaller fractions of **39** and **40**.

Set №2:

The removal of the most stable constituents containing one 5-, 6- or 7-membered ring results in a different population distribution at temperatures below 4000 K compared to set №1. At the B3LYP and G3 level of theory, the thermal equilibrium is placed on the side of **39**.

4.5.3 MEP analysis by the NEB method and TS reoptimisation

The reaction paths based on the DFTB-MD trajectories between reactants and products were optimised by the NEB method at the Bdz1 level of theory. Resulting minimum energy paths (MEPs) of CH addition, *cis-trans* isomerisations, cyclisation, and hydrogen shifts are represented by their reoptimised local minima and transition states (Figure 4.24).

4.5.3.1 Obtained CH addition mechanism

Reaction paths of the CH addition at **23** and **29** were computed to be barrierless.

^{†7}Note that the effects of both contributions to the free enthalpy are opposite.

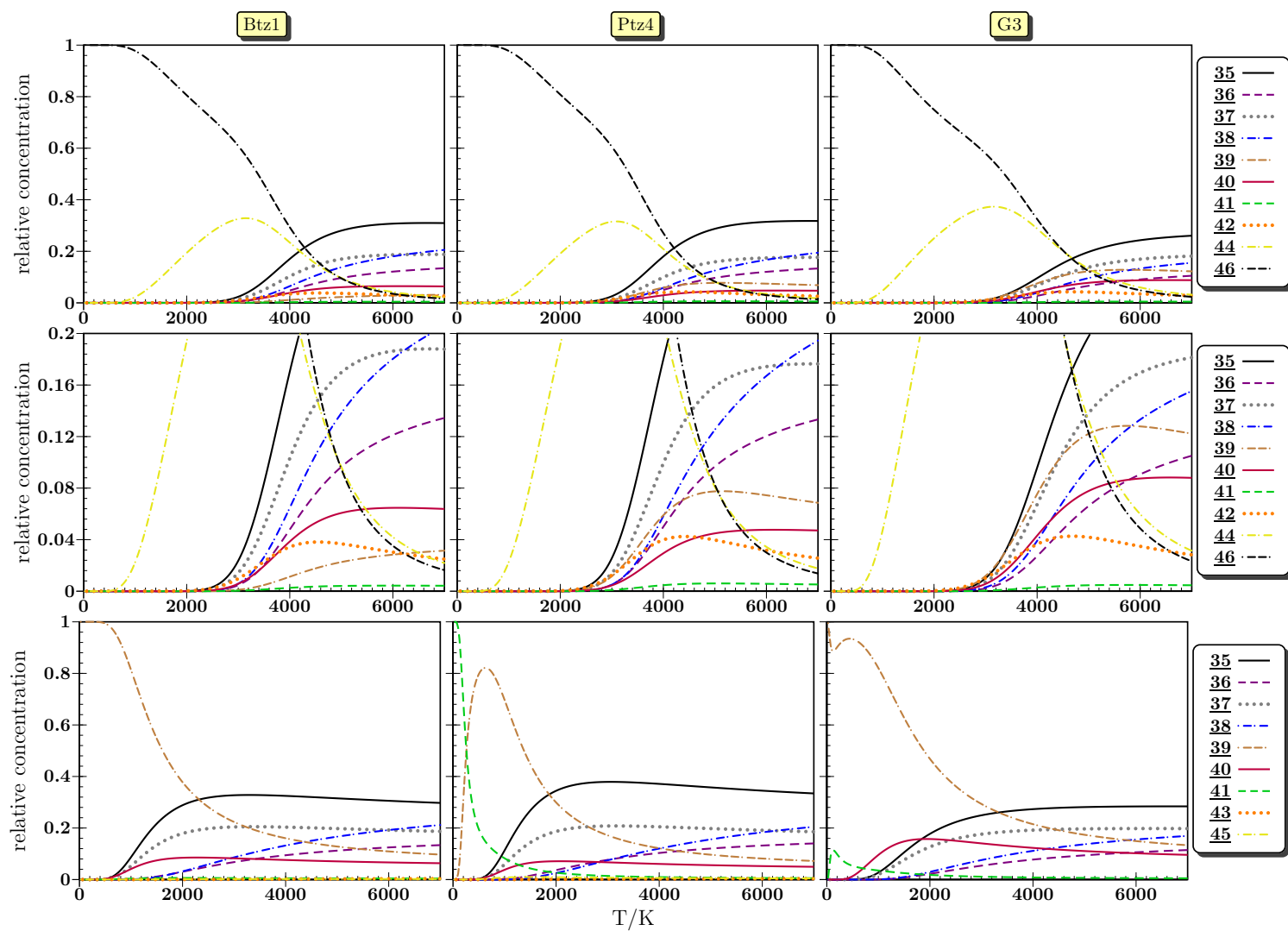


Figure 4.23: Canonical population analysis of $C_7H_7^+$ product isomers taken from Table 4.8 obtained at Btz1 (left column) Ptz4 (middle column) and G3 (right column) level of theory. First row represents the molecule set №1 in the concentration interval of 0 to 1, and the second row the №1 in the interval of 0 to 0.2, while the last row represents the set №2.

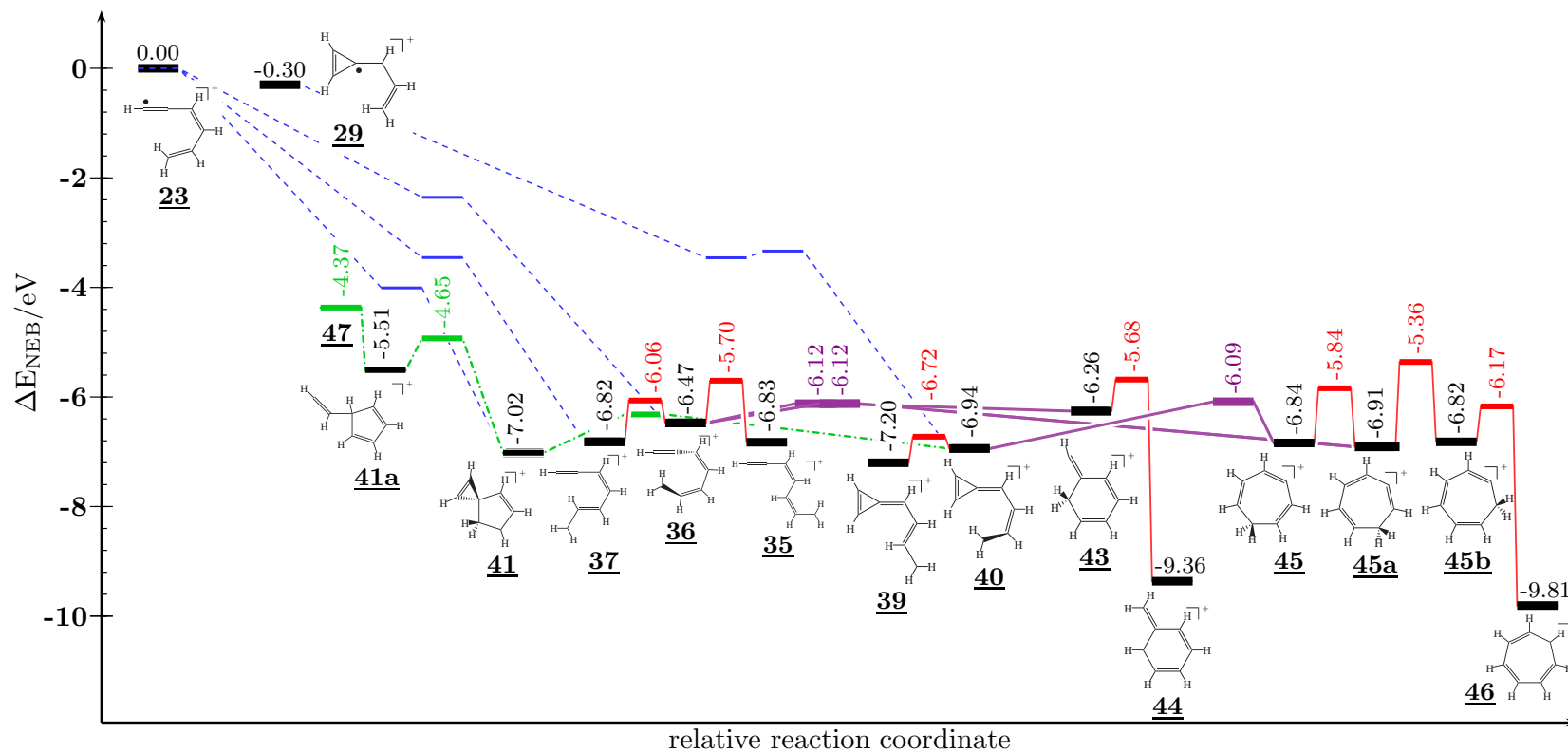


Figure 4.24: Stationary points of $C_6H_6^+$ -CH addition reaction paths, of $C_7H_7^+$ isomerisation paths between conformers, of $C_7H_7^+$ cyclisation paths and of $C_7H_7^+$ fragmentation paths obtained at Bdz1 level of theory.

CH attack on terminal dihydrogenated carbon

For each $C_6H_6^+$ reactant the CH attack leads to an unstable intermediate at the terminal dihydrogenated, sp^2 -hybridised carbon position. In that case, the sp^2 -hybridised terminal carbon of the intermediate becomes sp^3 -hybridised. A hydrogen shift from this former terminal carbon to the carbon of the attached CH molecule, re-establishes a stable structure, hence the attached CH becomes a methylene group. The conformation of the new structure depends on the orientation of the CH attack, i. e., the obtained methylene group is either in *cis* or *trans* position to the residual molecule.

CH attack on terminal monohydrated carbon

The CH attack on the terminal monohydrated, sp -hybridised carbon (compare with structure **23**) leads to 3-ring-membered structures such as **40** based on the MEP analysis. The computed MD trajectories also showed that during the formation of the 3-membered ring (cyclopropen structure) another link can occur with the other end of the molecule if all-*cis* configured. The resulting structure **41** (spiro[2.4]heptadienylium) transforms under the ring opening to **40**. The obtained ring opening and ring closure rate coefficient ratio $r_{WR, 41 \leftrightarrow 40}^{VT}$ is 11.18 to 1. In the case **41** contains 6.69 eV of non-fixed energy, the absolute ring opening rate coefficient to overcome a barrier of 0.66 eV (leading to **40**) is $9.19 \times 10^{-12} \text{ s}^{-1}$.

4.5.3.2 Obtained isomerisation barriers and rate coefficients

The calculation setup is described in Section 4.4.3.

*Cis-trans isomerisation of energised **36***

According to the results of the MD simulations, **36** is formed in large quantity. This structure is, however, of lower thermodynamic stability than related *cis-trans* conformers. A transformation to other conformers corresponds to the described rotation around partial C=C double bonds shown in Figure 4.19. The rate coefficient ratio of **36** to **35**, $r_{WR, 36 \leftrightarrow 35}^{VT}$, is 5.3 to 1 at the level of released formation energy, while the ratio of **36** to **37**, $r_{WR, 36 \leftrightarrow 37}^{VT}$, is lowered to 3.2 to 1. These kinetic results indicate that **36**, produced by CH addition reaction, is transformed fast into the thermodynamically more stable conformers **35** and **37**.

*Cyclisation of the energised **36***

Structure **36** was also identified as an intermediate in the formation of 6- and 7-membered ring structures. However, the obtained k_{WR}^{VT} values of the cyclisation characterise the cyclisation processes to be at least 6 times slower than the *cis-trans* isomerisation of energised **36**. A cyclisation of **36** results in the intermediates **43** and **45a**, which have a lower stability than **36**. This low stability is also indicated by the obtained rate ratios $r_{WR, 36 \leftrightarrow 43}^{VT} = 0.016$ and $r_{WR, 36 \leftrightarrow 45a}^{VT} = 0.040$, respectively.

Table 4.9: Unimolecular rate coefficients of radiative deactivation and of isomerisation processes based on different approaches. Energies (at Bdz1 level of theory) are taken from the MEP and TS optimisation (Figure 4.24). The internal energy is assumed to correspond in amount to the enthalpy of the reaction **23** ($Aa-C_6H_6^+$) and methyne dissipated to the product **X** at 0 K.

product	E_{vr}^a / eV	$k_r(E_{vr})$ / s^{-1}	Isomerisation / De-cyclisation					
			to	$E_{vr}^\ddagger{}^a$ / eV	$k_{DC}^v{}^a$ / s^{-1}	$k_{WR}^v{}^a$ / s^{-1}	$k_{WR}^{vr}{}^a$ / s^{-1}	$k_m^{vr}{}^a$ / s^{-1}
41a	5.232	1.262×10^2	41	4.718	3.310×10^{11}	3.305×10^{11}	2.777×10^{11}	2.234×10^{11}
41	6.690	2.236×10^2	40	6.026	7.278×10^{12}	7.282×10^{12}	9.192×10^{12}	7.165×10^{12}
			41a	4.718	6.760×10^9	6.779×10^9	4.587×10^9	2.015×10^9
35	6.509	5.253×10^2	36	5.455	2.331×10^{11}	2.342×10^{11}	1.897×10^{11}	1.252×10^{11}
36	6.160	3.109×10^2	37	5.801	2.160×10^{12}	2.166×10^{12}	2.077×10^{12}	1.844×10^{12}
			35	5.455	1.099×10^{12}	1.100×10^{12}	1.000×10^{12}	7.660×10^{11}
			45a	5.816	2.233×10^{11}	2.237×10^{11}	1.566×10^{11}	1.344×10^{11}
			43	5.816	2.233×10^{11}	2.237×10^{11}	1.566×10^{11}	1.344×10^{11}
37	6.494	4.328×10^2	36	5.801	8.293×10^{11}	8.286×10^{11}	6.458×10^{11}	4.995×10^{11}
39	6.862	4.488×10^2	40	6.420	1.456×10^{12}	1.460×10^{12}	1.326×10^{12}	1.135×10^{12}
40	6.609	3.028×10^2	39	6.420	3.565×10^{12}	3.584×10^{12}	3.611×10^{12}	3.421×10^{12}
			41	6.026	8.976×10^{11}	9.019×10^{11}	8.221×10^{11}	6.609×10^{11}
			45	5.772	1.549×10^{10}	1.565×10^{10}	9.348×10^9	6.459×10^9
43	5.929	1.182×10^2	36	5.816	9.317×10^{12}	9.311×10^{12}	9.818×10^{12}	9.582×10^{12}
			44	5.398	2.194×10^{11}	2.197×10^{11}	1.828×10^{11}	1.455×10^{11}
44	8.916	2.081×10^2	43	5.398	2.010×10^8	2.018×10^8	1.020×10^8	5.852×10^7
45	6.475	1.171×10^2	40	5.772	3.867×10^{11}	3.877×10^{11}	3.280×10^{11}	2.493×10^{11}
			45a	5.560	1.352×10^{11}	1.356×10^{11}	1.128×10^{11}	7.920×10^{10}
45a	6.526	1.588×10^2	36	5.816	4.060×10^{12}	4.057×10^{12}	3.887×10^{12}	3.081×10^{12}
			45	5.560	1.601×10^{11}	1.603×10^{11}	1.282×10^{11}	8.957×10^{10}
			45b	5.097	3.437×10^{10}	3.438×10^{10}	2.485×10^{10}	1.409×10^{10}
45b	6.464	1.107×10^2	46	5.877	5.612×10^{11}	5.615×10^{11}	5.001×10^{11}	4.018×10^{11}
			45a	5.097	3.513×10^{10}	3.511×10^{10}	2.627×10^{10}	1.491×10^{10}
46	9.308	5.190×10^1	45b	5.877	6.004×10^9	6.011×10^9	3.212×10^9	1.472×10^{10}

^aCompare with footnotes of Table 4.3

Considering the process **36**^{*} \rightarrow **44**^{*}

The slowest elementary process in the transformation of the energised **36** forming the benzylium (**44**) is the ring closure. The rate of the hydrogen shift from **43** to **44** is slightly higher. Another limiting factor in this process is related with the competitive isomerisation to **43** which leads to the formation of benzylium. According to the obtained k_{WR}^{vr} values, the isomerisation rate coefficient for the ring opening is about 50 times higher than the competitive rate to **44** at the released reaction energy. The effective total rate ($0.029 \times 10^{11} s^{-1}$) for

the process was derived from the combination of the rate fraction $f_{\text{WR}, \underline{43} \rightarrow \underline{44}}^{\text{VT}} = 0.018$ and the slowest elementary process (ring closure, $2.233 \times 10^{11} \text{ s}^{-1}$).

Considering the process $\underline{36}^ \rightarrow \underline{46}^*$*

The total process of the isomerisation of the energised **36** to tropylium (**46**) includes, according to the obtained path in Figure 4.24, the intermediates **45a** and **45b**. The slowest elementary process was given by step **45a** to **45b**. The evaluated rate fractions $f_{\text{WR}, \underline{45a} \rightarrow \underline{45b}}^{\text{VT}}$ and $f_{\text{WR}, \underline{45b} \rightarrow \underline{46}}^{\text{VT}}$ are 0.0062 and 0.9501, which in combination with the slowest elementary rate coefficient results in an effective rate coefficient of $0.0015 \times 10^{11} \text{ s}^{-1}$. Therefore, the formation rate of tropylium from the given energised **36** is about 20 times slower than the formation of benzylium. This low rate fraction $f_{\text{WR}, \underline{45a} \rightarrow \underline{45b}}^{\text{VT}}$ might explain the corresponding transition could not be found in the MD simulations.

Considering the process $\underline{40}^ \rightarrow \underline{46}^*$*

A combined minimum energy path from energised **40** to **46** via the intermediates **45**, **45a** and **45b** was evaluated in this work by the reaction path analysis. The slowest step corresponding to the $k_{\text{WR}}^{\text{VT}}$ values is represented by the ring closure process **40** to **45**. The rate fraction $f_{\text{WR}, \underline{45} \rightarrow \underline{45a}}^{\text{VT}}$ with 0.2559 together with the other rate fractions on the reaction path reduce the rate coefficient of the slowest step effectively to $0.00014 \times 10^{11} \text{ s}^{-1}$. This rate demonstrates that the product rate coefficient of tropylium from **40** is 10 times slower than the production rate coefficient of tropylium from **36**. This qualitatively confirms the results obtained by the analysis of the MD simulations.

4.6 Summary and discussion

In the present chapter, the properties of hydrocarbon growth through the reaction of CH with $C_xH_x^+$ ($x=2-6$) were studied. The results show that for $x=2-6$ the addition of CH to the unsaturated ion $C_xH_x^+$ is barrierless. Moreover, all the studied isomerisation barriers between the products as well as the fragmentation barriers are below the non-fixed reaction energy, which corresponds to the chemical activation. These facts indicate that $CH + C_xH_x^+$ reactions ($x=2-6$) take place in the ISM; this includes the formation of cyclic and aromatic structures such as the benzene cation ([44](#)) and tropylium ([46](#)) by successive CH addition.

4.6.1 DFTB based MD simulations

The DFTB based MD product distribution, the static DFT, and *ab initio* thermodynamic product distribution are partially in agreement. The comparison of MD and thermodynamics indicates that the reactions are mainly thermodynamically driven. However, discrepancies between the different distributions arise due to 1) dynamic effects and effective barriers, that hinder a thermodynamic based distribution, and 2) the different representing time regimes. In particular, while a thermodynamic product distribution corresponds to the equilibrium state equal to $t_{\text{postcoll}} = \infty$, in the case of the MD approach, the distribution corresponds to $t_{\text{postcoll}} = 6$ ps.

Comparison of k_{MD} with k_{L} and $k_{\text{ADO}}(T)$

The evaluated k_{L} values corresponding to $C_xH_x^+ + CH$ ($x=3-6$) systems range only between $1.05 \times 10^{-9} \text{ cm}^3 \text{ s}^{-1}$ and $1.12 \times 10^{-9} \text{ cm}^3 \text{ s}^{-1}$, since the ratio of the obtained polarisabilities of the reactants and the reduced mass of the reaction system is kept nearly constant. On the other hand, the calculated $k_{\text{ADO}}(T)$ values at 20 K reach roughly $10 \times k_{\text{L}}$. Note that the first reaction system is exceptional since the carrier of the charge is defined to be at CH. In this case, k_{L} and $k_{\text{ADO}}(T)$ are equal since acetylene is a non-polar molecule.

For each reaction system, the obtained $k_{\text{MD}}(\varepsilon)$ values remain a factor of 2–3 below the corresponding k_{L} values. This factor shrinks with the increase of the molecular dimensionality of the hydrocarbon reactant. The $k_{\text{MD}}(\varepsilon)$ graph pattern of each system is found to be the same in each case indicating a nearly equal capture process of each studied reaction. The graphs show a characteristic descend below $\varepsilon_{\text{coll}} = 0.005-0.01$ eV, an increase above $\varepsilon_{\text{coll}} = 0.01$ eV, and an additional increase above $\varepsilon_{\text{coll}} = 0.025$ eV. To explain this behaviour, several effects are considered: 1) the increase of reactivity with lowering collision energies due to the reduction of scattering, 2) the attractive forces that cause a temperature dependence of $k_{\text{MD}}(\varepsilon)$, and 3) the uncertainty due to finite reactant distance in the MD setup.

Influence of dispersion forces as implemented in DFTB

The influence of the dispersion forces ($V \propto R^{-6}$) on the calculated capture cross sections and the capture rate coefficients can be described to $\sigma_{\text{R}} \propto \varepsilon_{\text{coll}}^{-1/3}$ and $k \propto \varepsilon_{\text{coll}}^{1/6}$ (compare [[184](#)]). These values agree with the obtained positive collision energy slope for $k_{\text{MD}}(\varepsilon)$ values above 0.025 eV. The exponents are computed to be roughly 0.2.

Uncertainty due to finite reactant distance in the MD setup

Due to the technical setup consideration of a finite distance between the reactants at the initialisation point of the MD simulation, an uncertainty of about 0.001 eV was taken into account (i. e., details in Section B.1.1). Therefore, at the applied collision energies between 0.001 and 0.005 eV the uncertainty ranges between 20 and 100%.

$k_{\text{MD}}(\varepsilon)$ and $k_{\text{MD}}(T)$ comparison

Values of $k_{\text{MD}}(\varepsilon)$ and $k_{\text{MD}}(T)$ are mostly divergent at both ends of the applied collision energy / temperature ranges. The divergence of the $k_{\text{MD}}(T)$ values relative to $k_{\text{MD}}(\varepsilon)$ is considered to be of numerical origin caused by the applied integration of the spline-interpolated data sets $k_{\text{MD}}(\varepsilon_{\text{coll},i})/\varepsilon_{\text{coll},i}$. Within the integration regime, each given temperature defines a different subset of $k_{\text{MD}}(\varepsilon_{\text{coll},i})$ and $\varepsilon_{\text{coll},i}$ values required to cover the integrand area sufficiently (compare Figure B.4). Any insufficient subset consideration leads to high uncertainties. This is the case for $k_{\text{MD}}(T)$ values below 50 K, since the lowest applied collision energy is 0.005 eV.

Correction of $k_{\text{MD}}(T)$ values

By the definition of the DFTB setup, calculated $k_{\text{MD}}(T)$ and $k_{\text{MD}}(\varepsilon)$ do not consider permanent dipole-ion interactions. However, since CH is a polar molecule, permanent dipole-ion interactions exist. The addition of this type of interaction to the $k_{\text{MD}}(T)$ and $k_{\text{MD}}(\varepsilon)$ values can be estimated by the ratio between $k_{\text{ADO}}(T)$ and k_{L} , since both quantities differ by the permanent dipole-ion interaction (Section 2.2.2). The correction to $k_{\text{MD}}(T)$, named $k_{\text{MD}}^{\text{PDI}}(T)$, is extrapolated by the relation:

$$k_{\text{MD}}^{\text{PDI}}(T) \approx \frac{k_{\text{ADO}}(T)}{k_{\text{L}}} \times k_{\text{MD}}(T) \quad (4.1)$$

The ratio $k_{\text{ADO}}(T)/k_{\text{L}}$ between 20 K and 1000 K is in the range 10–1.5 and defines the scaling factor for $k_{\text{MD}}(T)$.

4.6.2 Reaction energies

The calculated energies for CH addition reactions resulting in thermodynamic stable products range between 6 and 8 eV. Each applied quantum chemical method leads to similar sequence of molecule in terms of relative thermodynamic stability and reaction energies. The quantitative deviations between the methods are systematic, for example the SD results are approximately 15% larger than the Btz1//Bdz1 results, while the G3 results are 7% larger than the Btz1//Bdz1 results. The deviation between SD and Btz1//Bdz1 is even larger since for SD the zero-point energies are omitted. In the case of zero-point energies correction, the deviation between SD and Btz1//Bdz1 is reduced to 7%. This qualitative convergence between DFTB, DFT and *ab initio* methods supports the established analysis scheme for the study of chemical reactions.

Electronic excitation

The high energy impact seems to be sufficient for the electronic excitation of the products. However, the internal conversion of electronic excited products into their highly vibrational-

rotational excited ground states is considered to be short enough and to not effect the product distribution. Thus, a instant conversion into highly vibrational-rotational excited ground states can be considered as conducted in the MD simulations.

Thermodynamical stability

Among the resulting products, $C_{x+1}H_{x+1}$ structures containing 3-, 5-, 6- and 7-membered rings are found to be thermodynamically more stable than the non-cyclic structures. Therefore, the cyclisation of non-cyclic $C_{x+1}H_{x+1}$ to their corresponding ring structures is exothermic.

In contrast, the fragmentation of products to $C_{x-1}H_{x-1} + C_2H_2$ is found to be endothermic, but also entropy-controlled. At high reaction temperatures or high reaction energy impacts as simulated by the CH addition, the fragmentation process becomes exergonic.

IR chemiluminescence

The spontaneous emission of radiation by the products energised by the non-fixed energy (reaction energy) are evaluated at a rate of $1 \times 10^1 \text{ s}^{-1} - 1 \times 10^3 \text{ s}^{-1}$. Since isomerisation rates of the same energised products are at rates above $1 \times 10^8 \text{ s}^{-1}$, any isomerisation equilibrium can be achieved before the radiative deactivation.

The impact of non-fixed energy by the chemical reaction is comparable to the energy amount provided by UV photons in the ISM. Both energies lead to highly vibrational-rotational excited ground states which emit IR photons [9]. Based on these facts, IR chemiluminescence of CH based reactions is found to contribute to the proposed interstellar IR emission features of hydrocarbons and PAHs.

4.6.3 Generalisation of chain growth for unsaturated hydrocarbons

Based on the minimum energy path optimisation by NEB at Bdz1 level of theory, each CH addition is followed by multiple bond rearrangement processes with barrier between 0.5 and 4 eV. Rearrangement processes result in chain extension, and fragmentations as well as cyclisation in the case of hydrocarbons containing more than 5 carbon atoms. The corresponding chemical activation provides rate coefficients of $1 \times 10^7 \text{ s}^{-1}$ to $1 \times 10^{12} \text{ s}^{-1}$.

For hydrocarbon ions of more than 5 carbon atoms, *cis-trans* isomerisations barriers are at 1 eV and isomerisation rates at $1 \times 10^{11} \text{ s}^{-1}$ to $1 \times 10^{12} \text{ s}^{-1}$ under the chemical activation. The cyclisation barriers for $C_5H_5^+$ are found to be between 2.8 and 3.1 eV, for $C_6H_6^+$ between 0.75 and 2.0 eV, and for $C_7H_7^+$ between 0.3 and 0.8 eV. At barrier heights below 1 eV, the cyclisation reaches higher rate coefficients than the corresponding *cis-trans* isomerisations. Cyclisations to ring sizes smaller than the number of carbons are also obtained but with higher barriers: for example, $C_6H_6^+$ to cyclopenta moiety requires 2.8 eV. The isomerisation of cyclised hydrocarbons to aromatic cyclic hydrocarbons requires to overcome another barriers between 0.7 eV, for $C_6H_6^+$ system, and 1.6 eV, for $C_7H_7^+$. Effective rate coefficients from non-cyclic hydrocarbons to aromatic cyclic hydrocarbons are evaluated to be rates over 1000 times slower than the corresponding *cis-trans* isomerisation rate coefficients.

From the present results, a generalised chain growth by the attack of CH on unsaturated hydrocarbons is derived below.

Chain growth and cyclisation

The chain growth will take place at the terminal methylene group of a $C_xH_x^+$ hydrocarbon (Figure 4.25).

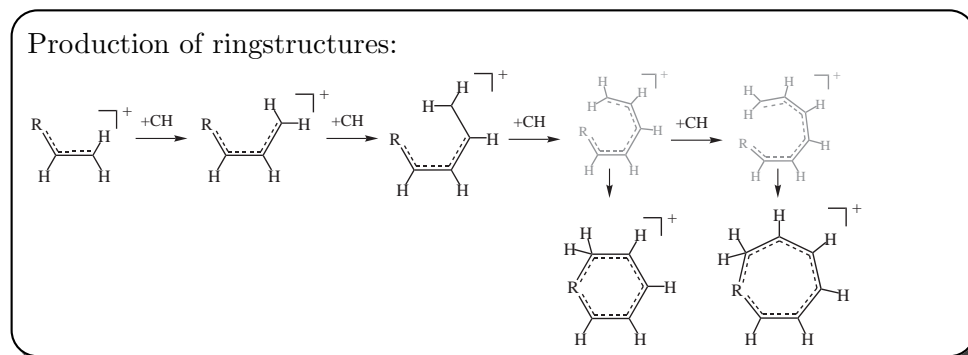


Figure 4.25: Schematic chain growth by multiple CH addition at a terminal methylene group of a $C_xH_x^+$ hydrocarbon. In the case of an all-*cis* configuration of C_4H_4 , C_5H_5 and C_6H_6 moieties, the cyclisation leads to the thermodynamic favoured pentagonal, hexagonal and heptagonal structures.

CH is added at the methylene group and under an α, β -hydrogen shift resulting in a new terminal methylene group at the $C_{x+1}H_{x+1}^+$ hydrocarbon. The different orientation of the CH attack and of the transition of the described hydrogen shift allows the formation of *cis* and *trans* configurations of $C_{x+1}H_{x+1}^+$. This addition of the methylene groups continues until the chain reaches 5, 6 or 7 carbon atoms. At this length, the proper isomerisation between all *cis* and *trans* configurations leads to an all *cis* configuration that, under electrocyclic ring closure, leads to a thermodynamic stabilised cyclic ring (Figure 4.25).

Acetylene formation - a hydrocarbon catalysed path

The MD simulations and the reaction path analysis indicate that the attach of CH at a terminal acetylenyl group leads to the formation of a terminal cyclopropenyl group, which, under an attack of CH, opens at least 2 reaction channels: 1) ring extension forming a cyclobutadienyl group and 2) ring opening and forming a C_2H_2 sidegroup. Both configurations are considered to be not stable and to lead to the dissociation of the hydrocarbon under acetylene elimination (Figure 4.26).

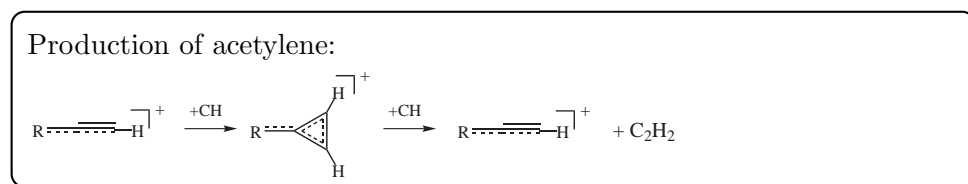


Figure 4.26: Schematic of the acetylene formation by the twofold CH addition at a terminal acetylenyl group of a $C_xH_x^+$ hydrocarbon.

5 Ion-molecule reactions between methyne and monocyclic hydrocarbon ions, $C_xH_x^+$ ($x=5-9$): the formation of bicyclic hydrocarbons

A summary of the reactions between methyne and monocyclic hydrocarbons $C_xH_x^+$ ($x=5-10$) is presented.

The CH insertion at cyclic carbon structures is also described in Chapter 6. In both chapters the CH insertion leads to growth of the ring size whereas the strain from the ring tension increases. It leads potentially to ring constriction, i. e., a so-called electrocyclic ring closure, of the monocyclic carbon structure resulting in a bicyclic hydrocarbon. In case of a H_2 elimination, $C_xH_x^+ \rightarrow C_xH_{x-2}^+ + H_2$, this bicyclic hydrocarbon would become a PAH or would at least fulfil the requirement for the stepwise ring addition mechanisms in the growth of PAHs as described in Section 1.3.4.1.

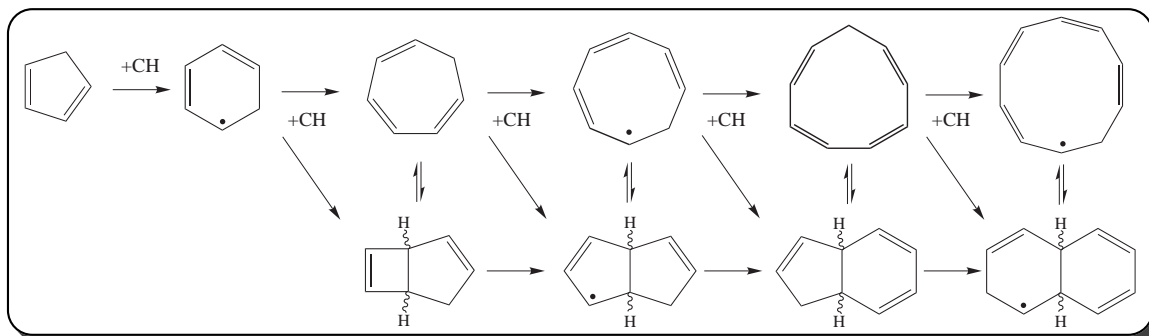


Figure 5.1: Schematic growth of monocyclic hydrocarbon ions ($C_xH_x^+$) by stepwise insertion of methyne



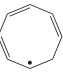
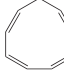

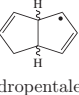
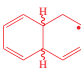
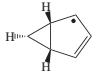
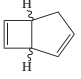
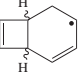
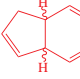
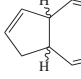
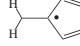
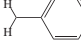

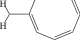
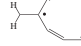
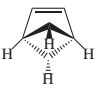

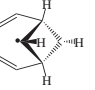
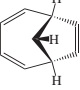
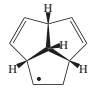
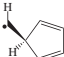
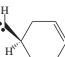
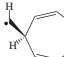
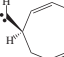
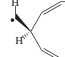
5.1 DFTB-MD simulations

MD simulations were applied for the structural analysis of the collisions between CH and unsaturated monocyclic hydrocarbons of the type C_xH_x with $x = 5 - 9$ including the analysis of the product distribution, cross sections and capture rate coefficients.

5.1.1 Production distribution

The manifold collisional products obtained from the final MD simulation structures were divided into monocyclic products labelled α - $C_{x+1}H_{x+1}^+$, symmetric (β) and unsymmetric^{†1} (γ) bicyclic $C_{x+1}H_{x+1}^+$, products with a methylene sidegroup (δ) and methyno-bridged products (ε). Additionally identified structures during an initial state of the collision are referred to as methylenide-sidegroup products (ξ). The corresponding thermodynamic stable structures of the product classes for each reaction system x in $C_xH_x^+ + CH \rightarrow C_{x+1}H_{x+1}^+$ are given in Table 5.1.

Table 5.1: Selected product structures and their relative formation energies (ΔE) of the reaction $C_xH_x^+ + CH \rightarrow C_{x+1}H_{x+1}^+$ ($x=5-9$) obtained from the final MD simulation structures at SD, Btz1//Bdz1 and G3 level of theory. Monocyclic (α), symmetric and asymmetric bicyclic (β and γ) structures are shown in the first three rows. Methylene sidegroup (δ) and methyno-bridged (ε_i) isomers are given in the fourth and fifth rows. CH addition complexes at the initial phase of the collision (ξ) are also included (last row). The hydrogen atoms of sp^2 -hybridised carbon atoms are not sketched.

$C_5H_5^+ + CH \rightarrow$ $C_6H_6^+$	$C_6H_6^+ + CH \rightarrow$ $C_7H_7^+$	$C_7H_7^+ + CH \rightarrow$ $C_8H_8^+$	$C_8H_8^+ + CH \rightarrow$ $C_9H_9^+$	$C_9H_9^+ + CH \rightarrow$ $C_{10}H_{10}^+$
abbr., name DFTB/B3LYP/G3	abbr., name DFTB/B3LYP/G3	abbr., name DFTB/B3LYP/G3	abbr., name DFTB/B3LYP/G3	abbr., name DFTB/B3LYP
 α , benzeniumyl 0.0 / 0.0 / 0.0	 α , tropylum 0.0 / 0.0 / 0.0	 α , cyclooctatetraeniumyl 0.7391 / 0.9035 / 1.1501	 α , cyclononatetraeniumyl 1.1290 / 0.7150 / 0.9858	 α , cyclodecapentaeniumyl 1.3626 / 0.8743
		 β , dihydropentaleniumyl 0.8072 / 1.3595 / 1.1285		 β , dihydronaphthaleniumyl 0.0 / 0.0
 γ , bicyclo[3.1.0]- hexendiyl cation 3.0249 / 2.5627 / 2.3681	 γ , bicyclo[3.2.0]- heptadienyl cation 2.1562 / 2.2640 / 1.9801	 γ , bicyclo[4.2.0]- octatrieniumyl 1.3423 / 1.6442 / 1.4093	 γ , dihydro- indeniumyl 0.0 / 0.0 / 0.0	 γ , dihydro- azuleniumyl 0.6558 / 0.3756
 δ , fulveniumyl 0.7192 / 0.5039 / 0.5665	 δ , benzylum 0.3842 / 0.3685 / 0.2997	 δ , heptafulveniumyl 0.0 / 0.0 / 0.0	 δ , nonafulveniumyl 0.7058 / 0.3441 / 0.6667	 δ , nonafulveniumyl 1.2753 / 0.7121
 ε_1 , bicyclo[2.1.1]- hexendiyl cation 2.9336 / 2.3683 / 2.1731	 ε_1 , bicyclo[2.2.1]- heptadienyl cation 2.7666 / 2.2764 / 1.6912	 ε_1 , bicyclo[4.1.1]- octatrieniumyl 2.7704 / 2.3081 / -	 ε_1 , bridged complex 0.3832 / 1.5405 / 1.4048	 ε_1 , triquinaceniumyl ε_2 , bridged complex ε_3 , bridged complex 0.0200 / 0.4008 0.4442 / 0.5092 1.5821 / 1.3279
 ξ , 3.8530 / 4.5353 / 4.4657	 ξ , 3.8530 / 4.5353 / 4.4657	 ξ , 3.8530 / 4.5353 / 4.4657	 ξ , 3.8530 / 4.5353 / 4.4657	 ξ , - / 4.2031

^{†1}It refers to the size of both fused rings. The term “symmetric” corresponds to equal ring sizes, “unsymmetric” to unequal ring sizes.

Trends until $t_{\text{postcoll}} = 6$ ps

A distribution of each reaction system at $\varepsilon_{\text{coll}} = 0.050$ eV and $t_{\text{postcoll}} = 6$ ps based on the counting of trajectories is given in Table 5.2.

Table 5.2: Evaluated product fractions $C_{x+1}H_{x+1}^+$ of the reaction $C_xH_x^+ + CH \longrightarrow C_{x+1}H_{x+1}^+$ in percentage of all reactive trajectories corresponding to a collision energy $\varepsilon_{\text{coll}} = 0.050$ eV and $t_{\text{postcoll}} = 6$ ps.

channel	$C_6H_6^+$	$C_7H_7^+$	$C_8H_8^+$	$C_9H_9^+$	$C_{10}H_{10}^+$
α	>95%	<10%	>60%	<10%	<15%
β	-	-	<20%	-	>34%
γ	i. ^a	<5%	<1%	>60%	>34%
δ	<5%	<1%	<5%	<15%	<5%
ε	i.	<5%	i.	<5%	<5%
ξ	i.	>80%	<10%	<5%	<2%
frag. ^b	-	-	-	>5%	<5%

^aidentified by at least one trajectory

^bfragmentation channels mainly $C_{x-1}H_{x-1}^+ + C_2H_2$

System $C_5H_5^+ + CH$:

Based on the analysis of the MD trajectories, the products are dominated by monocyclic isomers. Methylene sidegroup products constitute in a small fraction. Methyldene-sidegroup structures of the initial state represent the smallest fraction.

System $C_6H_6^+ + CH$:

The methyldene-sidegroup structures constitute the largest fraction. It indicates a substantial stability of the benzene cation against the CH insertion. It agrees with the aromatic character of benzene. Among the residual products, monocyclic products form the largest fraction. The appearance of bicyclic and methyno-bridged structures exceeds the methylene sidegroup structures.

System $C_7H_7^+ + CH$:

Compared to the previous distributions, the fraction of bicyclic (β) isomers is enlarged. High amounts of ξ indicate again a high stability of the reactant. It agrees with the aromatic characteristics of the tropylium ion.

System $C_8H_8^+ + CH$:

The fraction of bicyclic (β) isomers exceeds for the first time the fraction of monocyclic structures. It corresponds to the changed thermodynamic stabilities (Table 5.1); the bicyclic exceed the stability of the monocyclic one.. The attack of CH on monocyclic $C_8H_8^+$ produced also acetylene in moderate quantities.

System $C_9H_9^+ + CH$:

The largest fractions refers to the two thermodynamic most stable products. The attack of CH on monocyclic $C_9H_9^+$ also forms triple-bridged methyne $C_{10}H_{10}^+$ structures (triquinace-

niumyl ions). The formation of acetylene indicates a low energetical and structural stability of the monocyclic $C_9H_9^+$ reactant as demonstrated in Table 5.1.

5.1.2 Production distribution based on the cross sections

The time and collision energy dependence of the product distribution are studied by analysis of the cross sections.

Evolution of $C_9H_9^+$ –CH product distribution

Figure 5.2 shows the time-dependent cross sections corresponding to the different isomers of the system $C_9H_9^+ + CH$.

This figure reveals correlations between the different isomers in terms of formation and depletion mechanisms. Whereas the amount of α , β , γ and δ increases with simulation time,

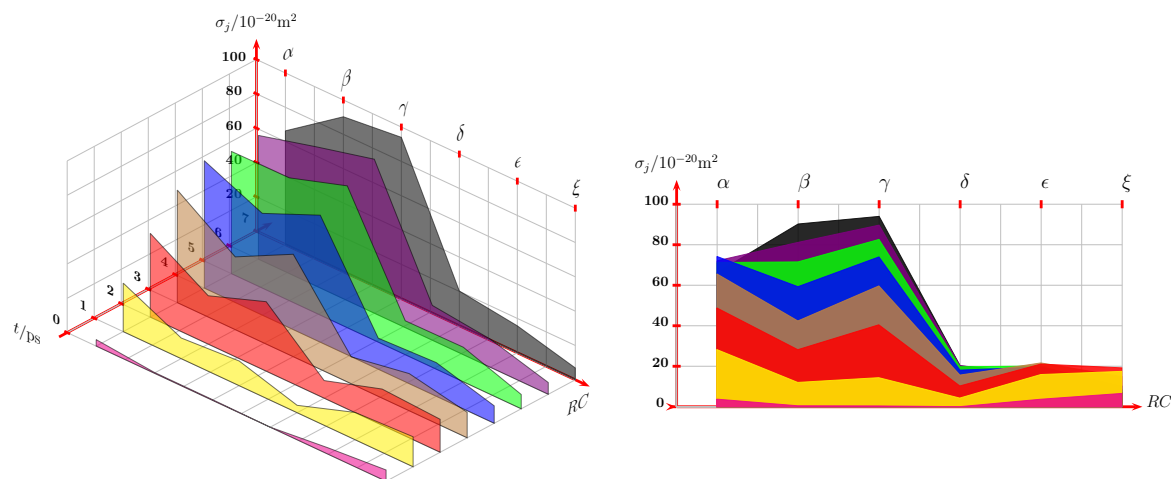


Figure 5.2: Cross-sections (σ_j) versus reaction channels (RC) and simulation time (t) of the reaction system $C_9H_9^+ + CH$ at a collision energy of 0.005 eV. $t = 0$ is defined as the point of collision, i. e., $t_{\text{postcoll}} = 0$.

the amount of ϵ and ξ peaks only at around 2 ps. This result suggests that either the latter isomers are not formed in a large amount or, once formed, they are easily depleted into the monocyclic, bicyclic, and methylene based isomers. Additionally, a correlation between the monocyclic and the bicyclic isomers is observed, with the ratio between the amount of α and β isomers decreasing as the simulation time increases. This indicates the formation of the bicyclic structure due to the depletion of the monocyclic (α) isomer. Both, α and β , are again linked with the ϵ isomer since they increase while ϵ is depleting.

Energy dependence of $C_9H_9^+$ –CH product distribution

The dependence of the product distribution on the collision energy (Figure 5.3) shows that the total amount of isomers decreases with the collision energy due to inelastic scattering, while the ratio between the different isomers remains nearly constant. This suggests that the depletion and formation mechanisms depend only weakly on the collisional energy in the energetic range considered in the simulations.

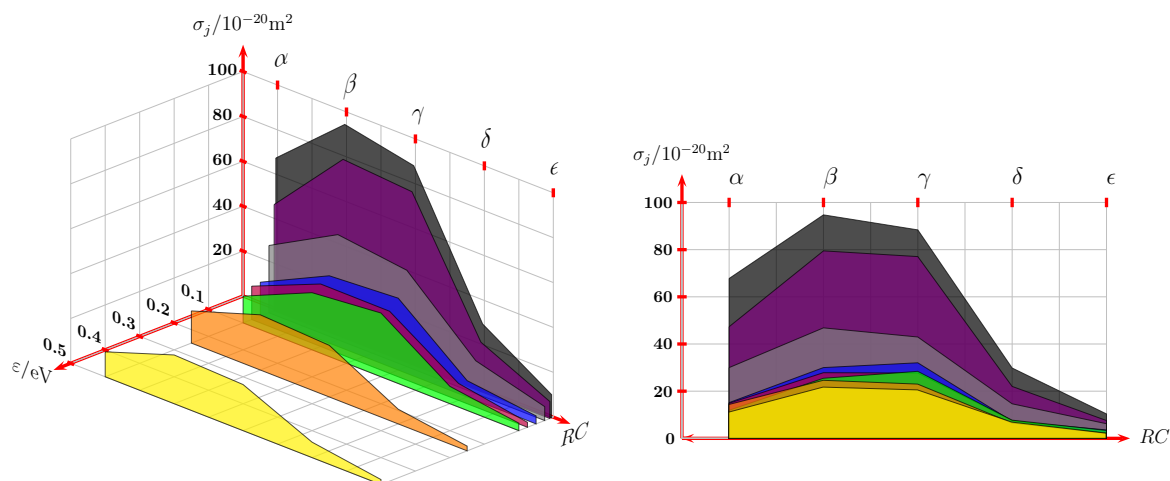


Figure 5.3: Cross-sections (σ_j) versus reaction channels (RC) and collision energy (ϵ) of the reaction system $C_9H_9^+ + CH$ after simulation time of 6.5 ps relative to the closest encounter between reactants. The collision energies are 0.005 eV (back), 0.010 eV, 0.025 eV, 0.050 eV, 0.075 eV, 0.100 eV, 0.250 eV and 0.500 eV (front), respectively.

Energy dependence of the total cross section

The total cross sections are given in Figure 5.4. For each reaction system, the reaction cross sections σ_R increase with ϵ_{coll} closely to $\sigma \propto \epsilon^{-0.5}$ which is the dependence given by the *Langevin* model. The σ_R increases with the growth of the system size, since σ_R depends also on the diameter of the participating molecules. However, values of the reaction system $C_6H_6^+ + CH$ only partly follow this trend. It indicates a lowered reactivity function $P(b)$ due to lowered reactivity of the benzene cation.

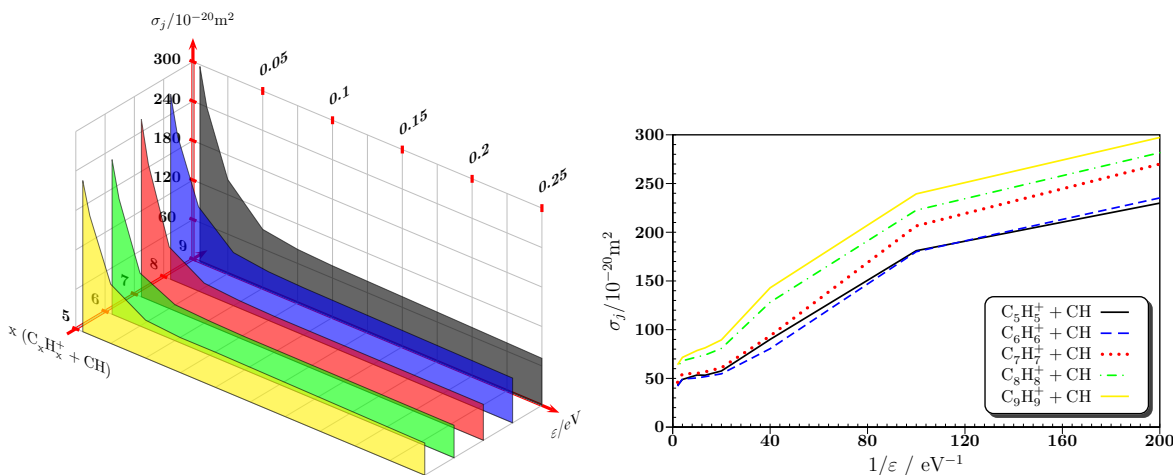


Figure 5.4: Reaction cross-sections (σ_j) versus collision energy (ϵ) for different reactions $C_xH_x^+ + CH$ in the range $x = 5$ to 9.

5.1.3 Capture rate coefficients

The calculated capture rates $k_{\text{MD}}(\epsilon)$ are given in Figure 5.5. The $k_{\text{MD}}(\epsilon)$ slope of each system are of the same pattern, only shifted corresponding the system size to higher values.

The values of the reaction system $C_6H_6^+ + CH$ and $C_7H_7^+ + CH$ are exceptional low due to the lowered reactivity of benzene cation and tropylium ion relative to the monocyclic $C_5H_5^+$, $C_8H_8^+$ and $C_9H_9^+$. The $k_{MD}(\varepsilon)$ trend of each reaction system is similar to the description of previous reactions of CH with hydrocarbons. For temperatures between 400 and 800 K, $k_{MD}(\varepsilon)$ values evidently increase due to the effects of the dispersion force; it is opposite to the scattering which is of smaller effect. Downwards 400 K, the scattering decreases, thus the the reactivity increases, which gives an overall inverse temperature dependence of $k_{MD}(\varepsilon)$. Calculated k_L values (Section 2.2) are approximately equal to $1 \times 10^{-9} \text{ s}^{-1}$, which is up to twice the $k_{MD}(\varepsilon)$ values.

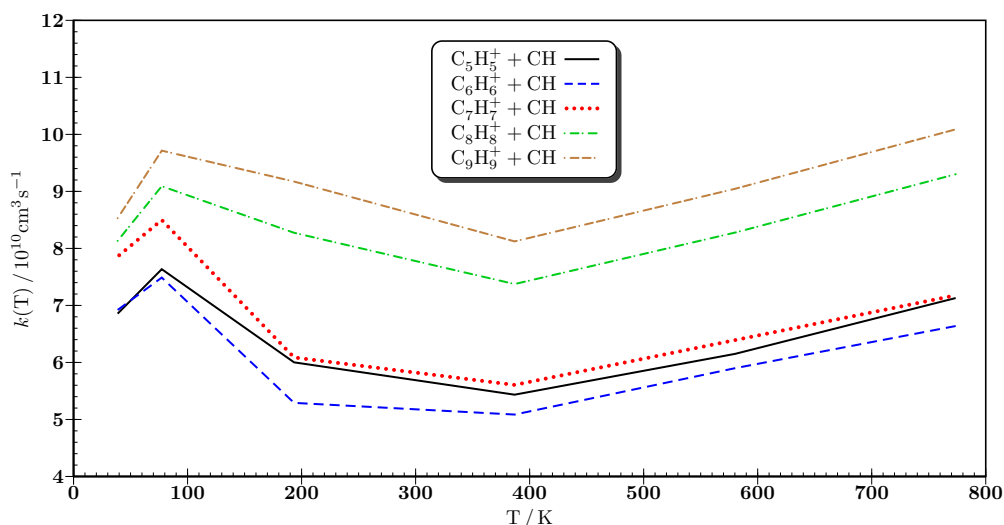


Figure 5.5: Capture rate coefficients $k_{MD}(T)$ of the reaction $C_xH_x^+ + CH \longrightarrow C_{x+1}H_{x+1}^+$ ($x=5-9$).

5.2 Energetic considerations

5.2.1 Thermodynamic product stabilities

Structural and energetic analysis of the products are performed based on geometry optimisation of the MD structures with different. According to the results given in Table 5.1, the DFTB (approximate DFT), the B3LYP (hybrid DFT), and the G3 (post-Hartree-Fock) method are in qualitative agreement. All methods suggest that the most stable structure changes from monocyclic (α), $C_6H_6^+$ and $C_7H_7^+$, via isomers with a methylene based side-group (δ), $C_8H_8^+$, towards bicyclic (γ), $C_9H_9^+$, and (β), $C_{10}H_{10}^+$.

This thermodynamic stability sequence correlates with the product distribution obtained from the MD simulations, except for the reaction system $C_7H_7^+ + CH$. This also indicates low or negligible barriers for the product formation which are, therefore, thermodynamically driven.

5.2.2 Reaction energies

The reaction energies of monocyclic $C_xH_x^+ + CH \longrightarrow$ monocyclic $C_{x+1}H_{x+1}^+$ are enlisted in Table 5.3. The obtained values demonstrate that the CH insertion into unsaturated

monocyclic hydrocarbons is highly exothermic, with values ranging from 4.2 to 8.1 eV for all given systems and computational approaches.

Table 5.3: Reaction energies of monocyclic $C_xH_x^+ + CH \rightarrow$ monocyclic $C_{x+1}H_{x+1}^+$ using different methods.

x =	$\Delta_R E / \text{eV}$			
	SD	Btz1//Bdz1	Ptz4	G3
5	-7.3710	-7.7536	-8.1297	-7.2775
6	-6.1458	-7.3951	-7.8230	-7.0827
7	-4.6859	-4.3160	-4.8071	-4.2443
8	-5.8525	-5.8260	-6.4307	-6.1804
9	-6.1156	-5.4932	-5.8207	-

The maximum deviation between DFTB and each enlisted method is below 13%. Independently of the method, the insertion of CH into the monocyclic $C_7H_7^+$ to form the monocyclic $C_8H_8^+$ releases the lowest amount of energy among the systems investigated. This result agrees with the high stability of the $C_7H_7^+$ structure arising from its aromaticity.

Temperature dependence of $\Delta_R G$

The temperature dependence of the molar and free reaction enthalpy, $\Delta_R H$ and $\Delta_R G$, of the reaction between monocyclic $C_xH_x^+$ and CH to monocyclic $C_{x+1}H_{x+1}^+$ is depicted in Figure 5.6.

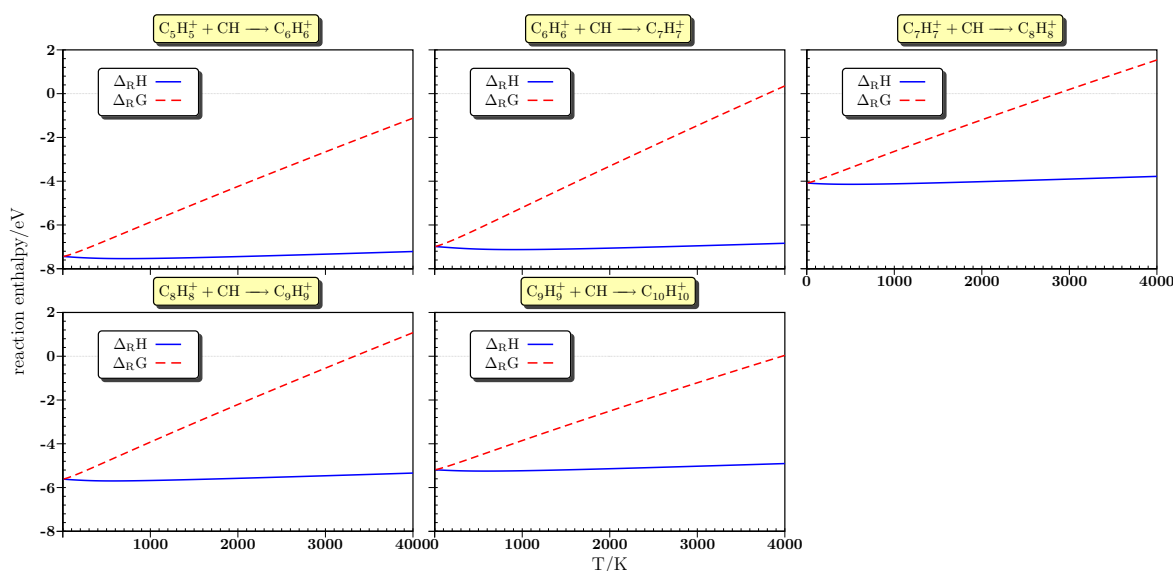


Figure 5.6: Reaction enthalpies of reaction scheme Figure 5.1 obtained by Btz1//Bdz1.

For each reaction system x the amount of $\Delta_R H$ is lowered by less than 0.5 eV in the given temperature range. Since the reduction of molarity leads to negative $\Delta_R S$ values, $\Delta_R G$ increases with growing temperatures. Therefore $\Delta_R G$ is entropic controlled.

5.2.3 Population distribution

The thermal equilibrium between the products of each system is depicted in Figure 5.7. For all reactions up to 1000–1500 K, the equilibrium is shifted to the side of the energetically most stable product. However, the thermal equilibrium of each system alters with increasing temperature to a different distribution. In the case of $C_9H_9^+$ products, it changes to the methylene sidegroup product. In the case of $C_{10}H_{10}^+$, the change occurs from bicyclic to methylene sidegroup and monocyclic products.

The described concentrations of the products is only partial in agreement with the results obtained from the MD simulations. For instance, the formation of methylene sidegroup products relate in the MD simulations to a much lower fraction than predicted by the population analysis. It indicates that the formation methylene sidegroup products is less thermodynamically driven and constitutes higher reaction barriers than the other products.

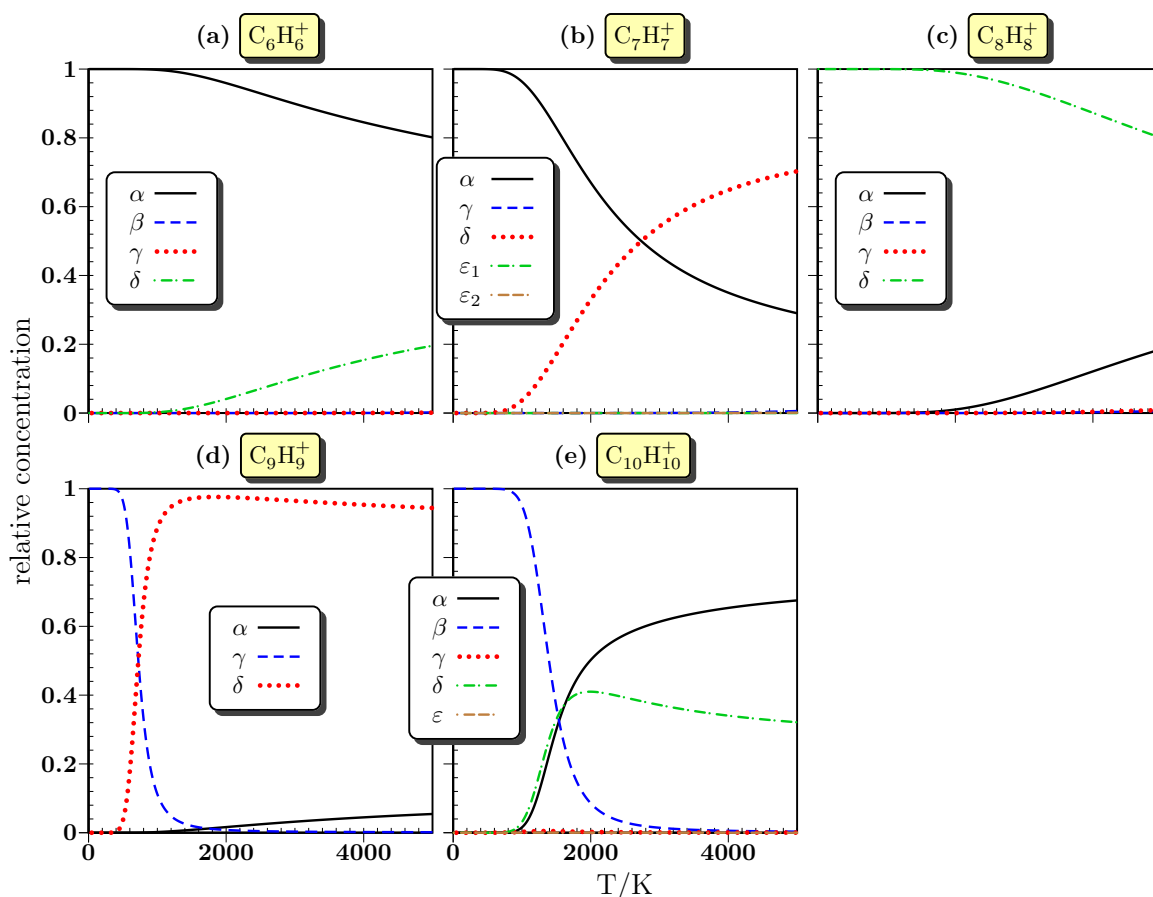


Figure 5.7: Product distribution versus temperature considering the thermal and entropic influence for reactions $C_xH_y^+ + CH \rightarrow C_{x+1}H_{y+1}^+$ at Bdz1 level of theory: a) $x=5$, b) $x=6$, c) $x=7$, d) $x=8$ and e) $x=9$.

5.3 MEP analysis by the NEB method and TS reoptimisation

The results of the MD trajectories point out the possibility of monocyclic rings to transform into bicyclic rings. The corresponding barriers were obtained by the reaction path analysis as described in Section 2.5. Additionally, two mechanisms for the hydrogen elimination are presented.

5.3.1 Constriction

The constriction refers to the transformation of the monocyclic isomers (α) into a bicyclic isomer (β or γ). The mechanism can be described as an electrocyclic reaction, i. e., a reaction with the transformation of one π bond into a σ bond. In the case of monocyclic $C_xH_x^+$, two carbon atoms in opposite positions of a monocyclic structure move in close position and form a bond dividing the monocyclic ring into a bicyclic one. Depending on the electronic and structural properties, the ring closure is described by either a con- or disrotatory movement of the sidegroups attached to the two carbon atoms. The barrier heights of each reaction system are illustrated in Figure 5.8.

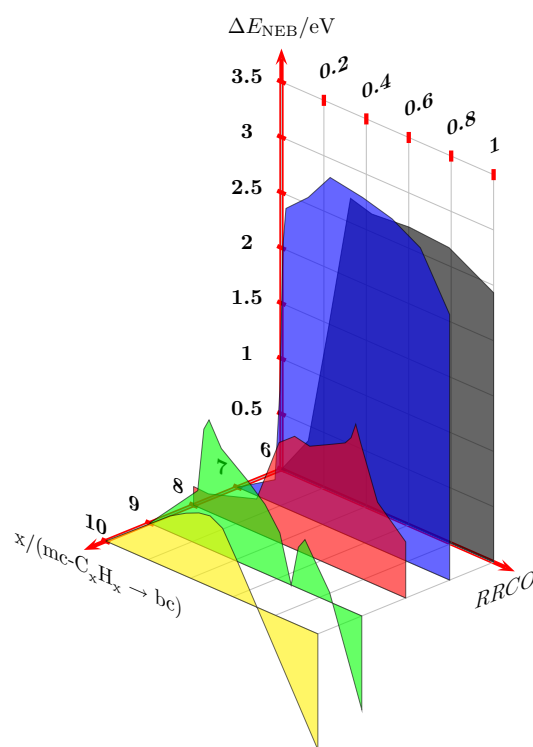


Figure 5.8: Constriction barriers of monocyclic (α - $C_xH_x^+$) to bicyclic isomers (β, γ - $C_xH_x^+$) for ring sizes x between 6 and 10. The last position of the relative reaction coordinate (RRCO= 1) shows the relative stability of the bicyclic isomers relative to the monocyclic.

According to the calculated results, the barrier height drops with increasing size of the monocyclic ring. In the case of the reaction systems $C_5H_5^+ + CH$ and $C_6H_6^+ + CH$, the energetic levels of bicyclic $C_6H_6^+$ and $C_7H_7^+$ lie at least 2.5 eV above the monocyclic structures. The

corresponding barriers are, therefore, at least 2.5 eV high. Since the stability of the bicyclic structures increase relative to the monocyclic one, the barrier heights also decrease.

According to the mnemonic rules for pericyclic reactions, the predicted structural configuration of involved sidegroups in a thermal driven ring closure reaction is suprafacial^{†2} if $4n + 2$ π -electrons are involved. In the case of $4n$ π -electrons, the ring closure process leads to disrotatory movement of the sidegroups. However, only conrotatory ring closures take place for each monocyclic ring $C_xH_x^+$ between $x = 7-10$ according to the results of the MD simulations. In the case of small monocyclic $C_xH_x^+$, the formation of a bicyclic product based on the disrotatory movement (resulting in an antarafacial configuration) is hindered. Such a resulting structure would be under higher structural strain than the opposite suprafacial configuration. Moreover, the application of the mnemonic rules lead to ambiguous results: Considering the complete ring, the conclusions on the mnemonic rules are opposite to the conclusions based on the partial structure, which is at least required for the electrocyclic ring closure.

5.3.2 Thermal elimination of H_2

The barrier heights of the thermal H_2 elimination from bicyclic structures with suprafacial hydrogens depend on the actual positions of these two hydrogens but also depends on the ring size of the bicyclic structure.

Elimination from adjacent ternary^{†3} sp^3 -hybridised carbons

In the case that the electrocyclic ring closure was situated inside the monocyclic ring, the resulting structure contains two hydrogens placed at the adjacent ternary sp^3 -hybridised carbons, which are shared by both rings. The barrier heights of H_2 elimination from these positions are depicted in Figure 5.9.

Based on the results given in Figure 5.9, H_2 elimination from bicyclic (*bc*) $C_7H_7^+$ requires about 3.1 eV, from *bc*- $C_8H_8^+$ 2.3 eV, from *bc*- $C_9H_9^+$ 3.2 eV, and from *bc*- $C_{10}H_{10}^+$ 1.7 eV. This means that the lowest barrier relates to the dihydrogenated naphthalene cation (*bc*- $C_{10}H_{10}^+$). Moreover, the elimination is only exothermic in the case of the dihydrogenated naphthalene cation. However, under the impact of the reaction energy from CH addition, products of all reaction systems are provided with sufficient non-fixed energy to pass this H_2 elimination barrier. These results demonstrate that H_2 elimination from the formed bicyclic $C_xH_x^+$ remains below the limit of the hydrogen atom elimination from a sp^2 -hybridised or aromatic carbon atoms which is equal to 4.5 eV [185].

Thermal isomerisation and H_2 elimination of $C_7H_7^+$

The H_2 elimination pathways from adjacent secondary and ternary sp^3 -hybridised carbon atoms of bicyclic $C_7H_7^+$ is depicted in Figure 5.10. If the formation of bicyclic $C_7H_7^+$ is based on the constriction of the monocyclic $C_7H_7^+$, the isomerisation to bicyclic $C_7H_7^+$ with secondary sp^3 -hybridised carbon atoms is achieved by hydrogen shifts.

^{†2}Topological description for rearrangement processes in or around a reaction center where suprafacial denotes for changes occurring at the same face.

^{†3}Ternary carbon atoms are bonded to three other carbon atoms.

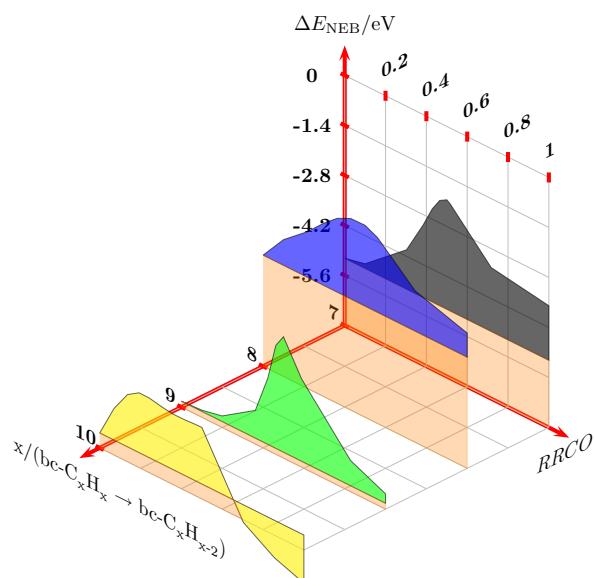


Figure 5.9: H_2 elimination barriers of bicyclic C_xH_x^+ for ringsizes x between 7 and 10. Both adjacent hydrogen are placed at ternary sp^3 -hybridised carbons, which are shared by both fused rings. Energies obtained by the NEB method at the Bdz1 level of theory (ΔE_{NEB}) are shifted relative to monocyclic (mc) $\text{C}_{x-1}\text{H}_{x-1}^+$ and CH.

The comparison between the isomeric bicyclic C_7H_7^+ shows that the H_2 elimination from the original ternary sp^3 -hybridised carbon atoms (red filled curve in Figure 5.10) constitutes the lowest barrier.

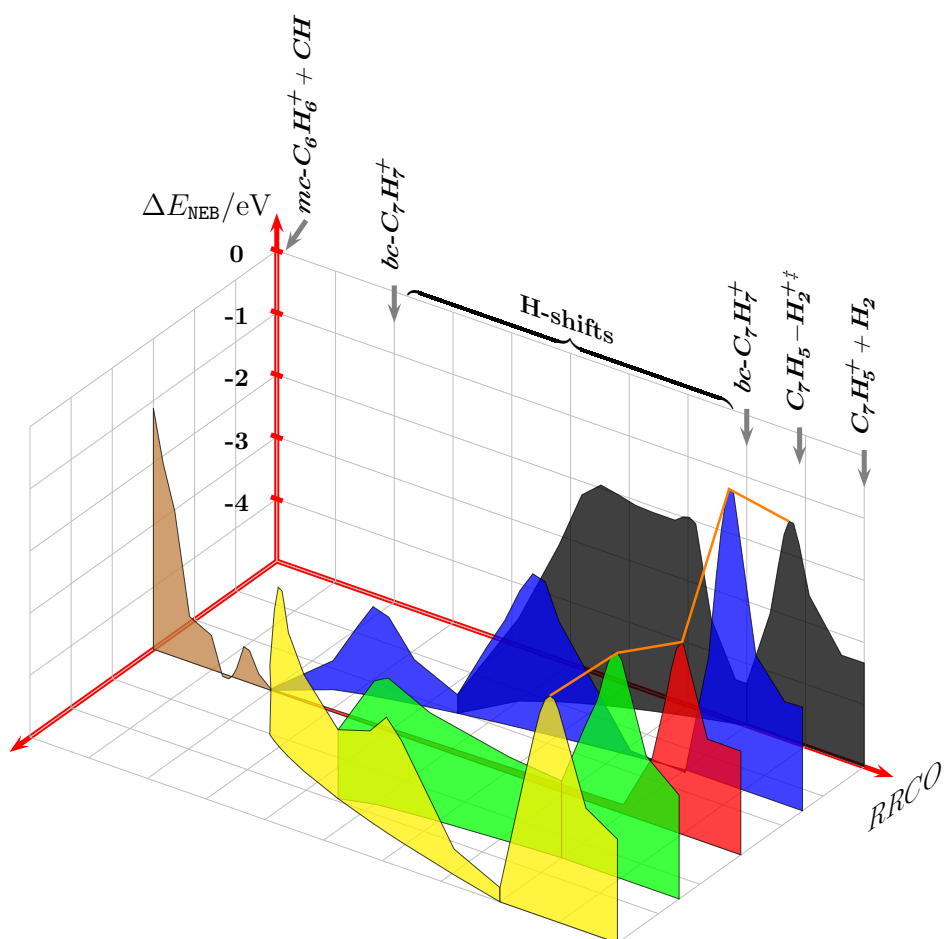


Figure 5.10: Relative reaction coordinate (RRCO) of the formation path of bicyclic (*bc*) $C_7H_7^+$ and different dissociation channels resulting in bicyclic $C_7H_5^+$ and H_2 . Energies obtained by the NEB method at the Bdz1 level of theory (ΔE_{NEB}) are shifted relative to monocyclic (*mc*) $C_6H_6^+$ and CH. The relative positions of the transition states of the H_2 elimination are depicted by the orange line perpendicular to the pathways.

5.4 Summary

In the present chapter, the properties of hydrocarbon ring growth by the addition of CH to monocyclic $C_xH_x^+$ ($x=5-9$) were studied and described. The CH insertion at monocyclic hydrocarbon ions is a barrierless process. The capture rate coefficients range between $0.5 \times 10^{-9} \text{ cm}^3 \text{ s}^{-1}$, for $x = 5$, and $1 \times 10^{-9} \text{ cm}^3 \text{ s}^{-1}$, for $x = 9$. The increase of the capture rate coefficients with the molarity agrees with the results of Chapter 4. The obtained $k_{\text{MD}}(T)$ values also agree with those of Chapter 4. The values of reaction systems $x = 5$ and 6 correspond to the non-cyclic reaction $C_xH_x^+ + \text{CH}$ with $x = 5, 6$ of Chapter 4. The average reaction energy of the ring extension, i. e., from ring size 5 to 6 until 10, range between 4.2 and 8.1 eV. The maximum deviation of method SD relative to Btz1//Bdz1, Ptz4 and G3 is below 13%. Besides monocyclic hydrocarbons, the MD product distribution consists of bicyclic and methylene sidegroup containing products. With increasing molarity, thermodynamic stability changes from monocyclic to bicyclic products. This is in agreement with the MD based product distribution. The energetic stability sequence, i. e., relative isomer energies, of DFTB and the B3LYP method are in qualitative agreement.

Based on the results of the MD simulations, two formation mechanisms for bicyclic hydrocarbons are existing: the 1st path starts with the formation of a methyno-bridged intermediate which is turned under bond rearrangement into a bicyclic hydrocarbon, and the 2nd path describes the electrocyclic ring closure of a monocyclic hydrocarbon. The barriers of the latter mechanism decrease with increasing number of carbons. For monocyclic hydrocarbons with ring size of 9 and 10, the ring closure is exothermic having barriers of 1.1 and 0.6 eV, respectively.

Since the thermal elimination of H_2 from adjacent ternary sp^3 -hybridised carbon positions in bicyclic $C_{10}H_{10}^+$ (dihydronaphthalene) is exothermic and requires to overcome a barrier of 1.7 eV, which is about 1/3 of the formation energy by $C_9H_9^+ + \text{CH}$. Therefore, the formation of naphthalene by the successive CH addition to monocyclic hydrocarbons is highly likely in the ISM.

6 Ion-molecule reactions between methyne and hydrocarbon ions, $C_xH_{x-2}^+$ ($x=10-13$): the formation of bi- and tricyclic hydrocarbons

This chapter describes the ion-molecule reactions between methyne and selected bicyclic hydrocarbon ions which have the chemical formula C_xH_{x-2} with $x=10-13$. The content is divided as follows:

- 1.) A preview on the growth of PCH or PAH: Ring growth, the constitution of an additional ring and the H_2 elimination are set up by the example of CH based naphthalene growth.
- 2.) Results of the reactions study. The partition of the sections corresponds to the number of carbon atoms. In each section, reaction between methyne and 1–3 reactants are described. The selected reactants are the products of previous reactions; the selection is determined by the workflow scheme given in Section 2.1.1.
- 3.) A summary where generalised mechanisms are derived from the obtained results.

6.1 Preview on the growth of PCHs and PAHs by CH

For the growth of PCH and PAH the formation of additional rings of hexagonal and pentagonal structure is essential. In the previous chapter, results of the growth of non-cyclic hydrocarbon by CH as well as the formation of benzene cation $C_6H_6^+$ and tropylium ion $C_7H_7^+$, i. e., the formation of monocyclic ring structure, is described. In terms of PCH and PAH growth, it corresponds to the formation of an additional ring based on chain growth finalised by cyclisation. In the following sections the ring growth based on the CH addition will be addressed. Such a ring growth mechanism requires a step or a certain transformation in order to provide the new additional ring. This will be another investigation objective of this chapter. In the case of PAHs with n rings such a step or transformation (compare Section 1.3.4.1) would lead to a dihydrogenated PAH with $n + 1$ rings. Possibilities of the H_2 elimination in order to regain a PAH structure will be also addressed.

A number of proposed steps important for the growth of PCHs and PAHs will be investigated by the naphthalene growth to phenanthrene. The proposed CH based growth path is depicted in Figure 6.1.

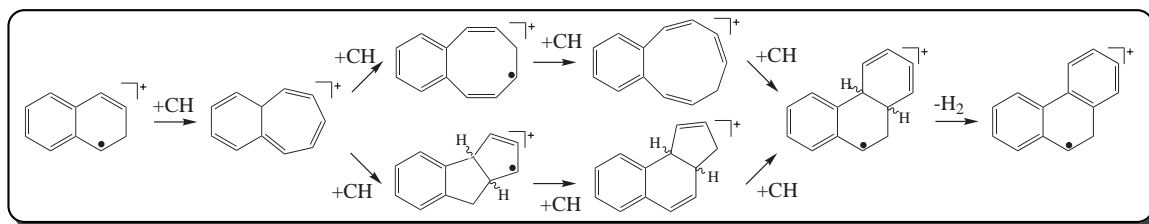


Figure 6.1: CH based growth reaction scheme from naphthalene cation to phenanthrene cation involving the ring growth, transformation into three rings and elimination of H_2 .

According to Figure 6.1, the transformation to the tricyclic carbon structure and the H_2 elimination takes place after 3 or 4 CH addition steps; the circumstances will be described in the following sections.

6.2 Reaction of $C_{10}H_8^+$ with CH

In this section, the study of this work on the ion molecule reactions between methyne and naphthalene cation ($C_{10}H_8^+$, [48](#)) is presented.

6.2.1 DFTB based MD simulations

The following analysis includes each trajectory between the collision energies 0.005 and 0.50 eV, of all the collision parameters sampled between 0.2Å and b_{\max} , and of all sampled orientations.

6.2.1.1 Identified product channels

Product channels were derived from the analysis of all MD trajectories; channels are:

- 1.) Bicyclic products of fused 6- and 7-membered rings, i. e., a carbon hexagon structure fused with a heptagon. These are labelled **bcy-6.7**^{†1}. The corresponding energetically stable structure is [53](#).
- 2.) Tricyclic products (**tcy-4.5.6**) containing 1 tetragon, 1 pentagon and 1 hexagon which are pericondensed in arbitrary sequence. Corresponding structures are [51](#) and [52](#).
- 3.) CH-ring-bridging^{†2} products (**brdg**): The identified structures relate to [54](#).
- 4.) CH-attached complexes^{†3} (**R-CH**): Based on the symmetry of naphthalene two different structures are observed, [49](#) and [50](#).
- 5.) Products with methyldene sidegroups (**R-CH₂**): Observed representatives are [55](#) and [56](#).
- 6.) Orbiting complexes (**cmplx**) representing the reactants circulating each other.

Structures and corresponding energies are given in Table [6.1](#).

6.2.1.2 CH attack

The formation of bicyclic and tricyclic structures is the result of rearrangements inside methyno-bridged and **R-CH** structures. Note that methyno-bridged structures are formed themselves by rearrangements of **R-CH** structures.

A minor fraction of tricyclic structures is generated by rearrangements inside the heptagon unit of the bicyclic structures **bcy-6.7**. This is triggered by the impact of a large amount of non-fixed energy (i. e., reaction energy), which allows two opposite carbons inside one heptagon to move to each other by vibration and forming a bond. This process corresponds to a constriction which formally increases the number of rings by one in a structure. As

^{†1}Polycyclic product classes are labelled $\langle X \rangle \text{cy} \langle \text{ringsize}_1 \rangle \dots \langle \text{ringsize}_n \rangle$ where X is the one-character abbreviation for the ring amount, i. e., $X = b$ for bicyclic, t for tricyclic and 4 for tetracyclic. Ringsize_i represents the ring size of each ring, e. g. 5.5.6 relates to 2 pentagonal and 1 hexagonal ring.

^{†2}also referred to as methyno bridge

^{†3}also referred to as methyldene sidegroup

a result, it is expected to take place for each ring system under bond angle strain. The corresponding inverse process, i. e., the ring opening (de-constriction) was also identified in the obtained MD trajectories.

6.2.1.3 Product distribution as given by cross sections

The results based on the MD trajectory snapshots at $t_{\text{postcoll}} = 6$ ps are given in Figure 6.2.

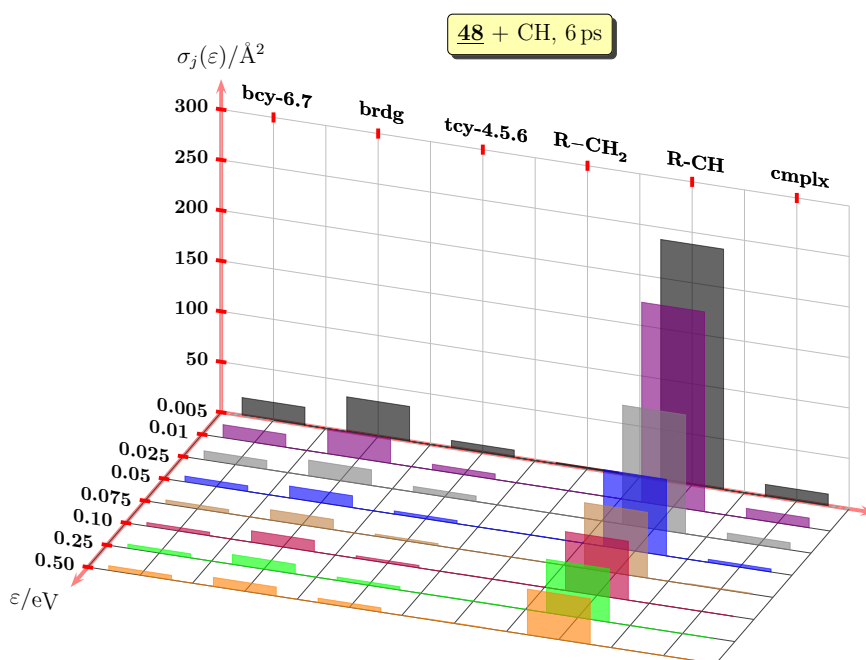


Figure 6.2: Calculated cross section distribution of $C_{11}H_9^+$ products at different collision energies ε for product channels: **bcy-6.7** (one 6- and one 7-membered ring), **brdg** (methyno-bridged), **tcy-4.5.6** (tricyclic), **R-CH₂** (methylene sidegroup), **R-CH** (methylidene sidegroup), and **cmplx** (orbiting complex). The distribution corresponds to $t_{\text{postcoll}} = 6$ ps.

Over 70% of the trajectories remain in the state of **R-CH** which, in detail, shrinks from 79% to 71% with increasing collision energy. The amount of the orbiting complex drops to zero for collision energies $\varepsilon_{\text{coll}}$ of 0.075 eV and higher. The fraction amounts of the bicyclic (**bcy-6.7**), tricyclic (**tcy-4.5.6**), and methyno-bridged (**brdg**) structures increase at the cost of **R-CH**. For comparison, the ratio $\Sigma\sigma_{\text{R}}/\sigma_{\text{R,R-CH}}$ is equal to 0.16 at 0.005 eV but is increased to 0.31 at 0.50 eV.

Trends of bcy-6.7, brdg and tcy-4.5.6

The fraction of **brdg** decreases relative to **tcy-4.5.6** by 60% and relative to **bcy-6.7** by 20% in the $\varepsilon_{\text{coll}}$ range between 0.005 and 0.50 eV. This is an indication for the transformation of **brdg** to **bcy-6.7** and **tcy-4.5.6**. This agrees with the structural similarities between the given product channels. Additionally, the fractions of bicyclic structures decrease by 50% relative to tricyclic structures in the range of collision energies used in this study. This indicates rearrangement processes such as the constriction described in Section 5.3.1.

The $\mathbf{R-CH}_2$ fraction

The fraction of $\mathbf{R-CH}_2$ ranges between 0 and 0.8% relative to the total amount of trajectories. The slope of $\mathbf{R-CH}_2$ is proportional to the collision energy for energies above 0.025 eV.

6.2.1.4 Calculated capture rate coefficients

The capture rate coefficients were calculated based on Eqs. (2.15) and (2.16). For comparison, k_L and $k_{ADO}(T)$ were evaluated. The corresponding dipole moments and polarisabilities (Table A.1) are taken from the DFT calculations. All results are composed in Figure 6.3.

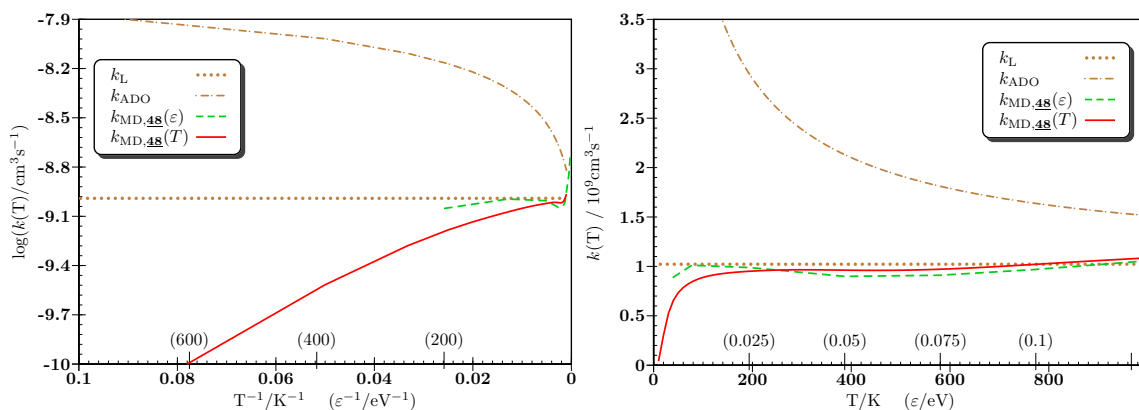


Figure 6.3: Calculated capture rate coefficients k_L , $k_{ADO}(T)$, $k_{MD}(\epsilon)$ and $k_{MD}(T)$ of the reactions between **48** (naphthalene cation) and CH. Left side shows more details of the low ϵ_{coll} range and the right side of the high ϵ_{coll} range. Collisional energies and temperature are related by $\epsilon_{\text{coll}} = 3/2k_B T$.

k_L , $k_{ADO}(T)$ and comparison with MD based values:

The calculation of the capture rate coefficient (k_L) value gave $1.02 \times 10^{-9} \text{ cm}^3 \text{ s}^{-1}$. The dipole corrected values, $k_{ADO}(T)$, range from $9.59 \times 10^{-9} \text{ cm}^3 \text{ s}^{-1}$ at 20 K to $1.51 \times 10^{-9} \text{ cm}^3 \text{ s}^{-1}$ at 1000 K. Within the collision energy interval of 0.01 and 0.50 eV, the obtained $k_{MD}(\epsilon)$ values vary between 0.99×10^{-9} and $1.01 \times 10^{-9} \text{ cm}^3 \text{ s}^{-1}$, which is similar to the evaluated k_L values. Below this interval, the $k_{MD}(\epsilon)$ values drop to $0.88 \times 10^{-9} \text{ cm}^3 \text{ s}^{-1}$, and increase to $1.8 \times 10^{-9} \text{ cm}^3 \text{ s}^{-1}$ above it. The increase at higher temperatures might be caused by the dispersion forces as discussed in Section 4.6. This can be also considered as characteristic feature in the reactivity function which is defined by the short-range potential.

Comparison between $k_{MD}(T)$ and $k_{MD}(\epsilon)$:

Deviations between $k_{MD}(T)$ and $k_{MD}(\epsilon)$ arise at collision energies below 0.025 eV (193 K). The origin is suggested to be a numerical problem as discussed in Section 4.3.1.

6.2.2 Product energetics

The reaction enthalpies of the identified products are given in Table 6.1; they are obtained at SD, Btz1//Bdz1, and Mdz1 level of theory.

Table 6.1: Ion-molecule based reaction energies and enthalpies relative to the reference level $C_{10}H_8^+$ (**48**) + CH obtained by different quantum theory methods.

products	abbr.	geometry	class	$\Delta_R E/eV$	$\Delta_R H_{0K}/eV$	
				SD	Btz1//Bdz1	Mdz1
$\mathcal{A}a-C_{11}H_9^+$	49		R-CH	-3.6764	-1.9480	-2.6864
$\mathcal{A}b-C_{11}H_9^+$	50		R-CH	-3.4658	-1.7536	-2.4971
$\mathcal{B}a-C_{11}H_9^+$	51		tcy-4.5.6	-5.3679	-4.1963	-5.5001
$\mathcal{B}b-C_{11}H_9^+$	52		tcy-4.5.6	-5.1623	-3.9331	-5.2681
$\mathcal{C}a-C_{11}H_9^+$	53		bcy-6.7	-7.2742	-6.1559	-7.3548
$\mathcal{D}a-C_{11}H_9^+$	54		brdg	-4.5444	-4.0665	-5.9233
$\mathcal{E}a-C_{11}H_9^+$	55		R-CH2	-6.9624	-5.8629	-6.9674
$\mathcal{E}b-C_{11}H_9^+$	56		R-CH2	-7.0568	-5.8705	-6.9788
$\mathcal{B}a-C_{11}H_7^+ + H_2$	57		f-H2 ^a	-1.8186	-2.8293	-4.1770
$\mathcal{B}b-C_{11}H_7^+ + H_2$	58		f-H2 ^a	-1.7585	-2.7953	-4.1742
$\mathcal{B}a-C_9H_7^+ + C_2H_2$	59		f-C2H2 ^a	-3.6061	-2.8662	-2.5107

^anot observed during the MD simulation of 6 ps

Comparison between **bcy-6.7** and **tcy-4.5.6** structures:

The highest reaction enthalpy and energy of the CH addition at naphthalene is released by forming **53**, i. e., **53** possesses the highest thermodynamic stability among the given products. Based on the obtained results at SD, B3LYP and MP2 level of theory, the relative stability of the **bcy-6.7** structures (**53**) is higher than the stability of the **tcy-4.5.6** structures as well as of the methyno-bridged structure. These energy differences are less than 2 eV at each level of theory.

Introduction of fragmentation products:

Based on the results of the reaction $CH + C_xH_x^+$ with $x = 2-6$ given in Chapter 4, fragmentation products can be expected, although the obtained MD simulations did not indicate anything after $t_{\text{postcoll}} = 6$ ps. Fragmentations were proposed in this work for **51** and **52**. The latter dissociates into $C_{11}H_7^+$ and molecular hydrogen, while **51** dissociates into $C_9H_7^+$ (indene structure) and acetylene. The corresponding product pairs are given by **57**, **58** and **59**.

Each fragmentation process is endothermic relative to the **bcy-6.7** and **tcy-4.5.6** structures. However, the fragmentation process becomes exothermic if the formation energy of **bcy-6.7** and **tcy-4.5.6** generated by the reaction $C_{10}H_8^+ + CH$ is taken into account.

The relative stabilities of the fragmentation products are not consistent among the applied quantum chemistry methods. This relative stability increase from **58** over **57** to **59** using SD or B3LYP. The C_2H_2 elimination (**59**) is preferred over the H_2 elimination (**57**, **58**) by 2 eV (SD) and 0.1 eV (B3LYP) However, in the case of the MP2 level of theory the fragmentation product **59** is considered to be of lowest stability. The H_2 elimination is here preferred over the C_2H_2 elimination by 1.7 eV.

6.2.2.1 Temperature dependence of enthalpies

The temperature dependent change of the free reaction enthalpies is given in Figure 6.4. The values are based on the energies and harmonic frequencies calculated at Mdz1 level of theory.

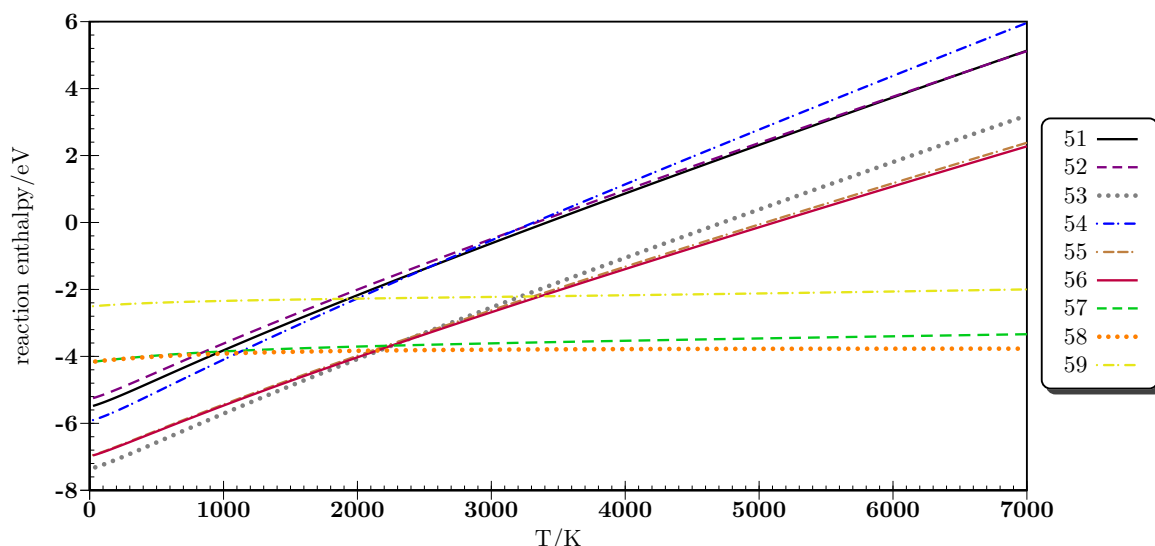


Figure 6.4: Free reaction enthalpies $\Delta_R G$ of product isomers as shown in Table 6.1 obtained at Mdz1 level of theory.

Calculated trends below 100 K:

The free enthalpies $\Delta_R G$ of each product increases with temperature. The effect of the temperature is, however, steadily; the product sequence concerning their relative stabilities remains as given in Table 6.1.

Calculated trends above 1000 K:

The temperature slope of each product $\Delta_R G$ changes in favour of fragmentation products $C_{11}H_7^+ + H_2$. Its origin can be traced to the lower $\Delta_R S$ values, since reaction molarity of the reaction $C_{10}H_8^+ + CH \rightarrow C_{11}H_7^+ + H_2$ is unchanged. According to Figure 6.4, the highest amount of released $\Delta_R G$ corresponds to the fragmentation products at temperatures above 2200 K. The free formation enthalpy of $C_9H_7^+ + C_2H_2$ becomes larger than of any $C_{11}H_9^+$ association product at temperatures above 3300 K.

6.2.2.2 Canonical population distribution

The temperature dependent population distribution of the products **51** to **58** is plotted in Figure 6.4.

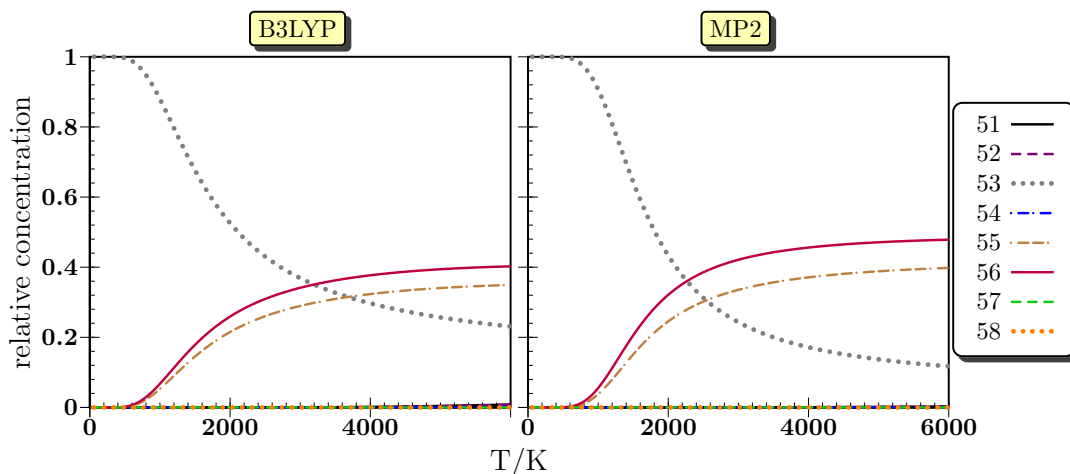


Figure 6.5: Canonical population analysis of $C_{11}H_9^+$ product isomers taken from Table 6.1, Btz1//Bdz1 (left) and Mdz1 (right).

The structure **53** forms the largest fraction in such a thermal equilibrium for temperatures up to 3000 K (B3LYP) or 2200 K (MP2).

Above these temperatures the equilibrium undergoes a major transition to the species **55** and **56** with nearly equal fraction amounts – around 30–40% each. All other structures of Table 6.1 populate only tiny fractions of the equilibrium at any temperature.

6.2.3 Reaction path analysis

Results of the reaction path analysis of the CH attack at $C_{10}H_8^+$, isomerisation between bicyclic and tricyclic $C_{11}H_9^+$ products, and elimination of H_2 and C_2H_2 from $C_{11}H_9^+$ are plotted in Figure 6.6. The reaction paths are only represented by the stationary points and transition states obtained at the Bdz1 level of theory. The corresponding isomerisation rate coefficients based on the RRKM theory and CTST are given in Table 6.2.

6.2.3.1 Calculated isomerisation barriers and rate coefficients

CH addition mechanism

The CH attack at naphthalene is barrierfree and leads to **49**, **50**, and **54**, which is in agreement with the results of the MD simulations. The stability of **49** and **50** was quantified by the reaction path search. The relative isomerisation barriers of **49** and **50** to any other products are below 0.4 eV. In contrast, the amount of the non-fixed energy from the CH addition at $C_{10}H_8^+$ to **49** and **50** is about 2 eV. The isomerisation rate coefficients k_{WR}^{VT} of **49** and **50** are, therefore, over $6 \times 10^{11} \text{ s}^{-1}$, which is very high for such amounts of non-fixed energies. However the relative barrier and the isomerisation rate coefficients do not correlate with results of the DFTB based MD simulations. According to the calculated cross sections at $t_{\text{postcoll}} = 6 \text{ ps}$ (Figure 6.2), the lifetime of **49** and **50** is considerably higher.

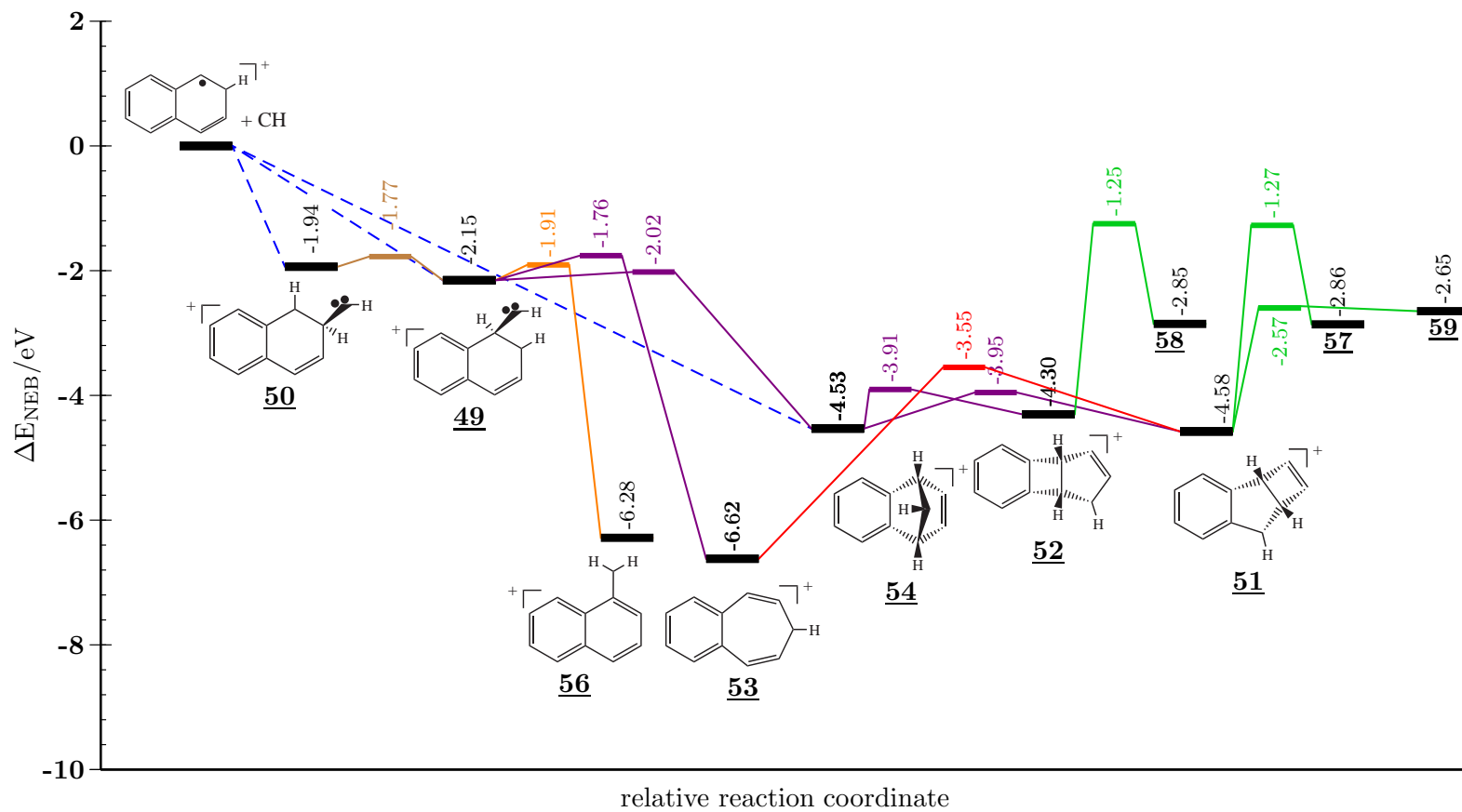


Figure 6.6: Stationary points of $C_{10}H_8^+ - CH$ addition reaction paths, of $C_{11}H_9^+$ isomerisation paths between conformers, of $C_{11}H_9^+$ cyclisation paths, and of $C_{11}H_9^+$ fragmentation paths obtained at Bdz1 level of theory.

Table 6.2: Unimolecular rate coefficients of radiative deactivation and of isomerisation processes based on different approaches. Energies (at Bdz1 level of theory) are taken from the MEP and TS optimisation (Figure 6.6). The internal energy is assumed to correspond in amount to the enthalpy of the reaction **48** and methyne dissipated to the product **X** at 0 K.

product	E_{vr}^a / eV	$k_r(E_{\text{vr}})$ / s^{-1}	Isomerisation/Dissociation					
			to	$E_{\text{vr}}^\ddagger^a$ / eV	$k_{\text{DC}}^{\text{v}}(E_{\text{vib}})^a$ / s^{-1}	$k_{\text{WR}}^{\text{v}}(E_{\text{vib}})^a$ / s^{-1}	$k_{\text{WR}}^{\text{vr}}(E_{\text{vr}})^a$ / s^{-1}	$k_{\text{m}}^{\text{vr}}(T_{\text{vr}})^a$ / s^{-1}
49	1.987	4.592×10^1	54	1.861	9.631×10^{11}	9.622×10^{11}	8.614×10^{11}	1.009×10^{12}
			56	1.757	6.617×10^{11}	6.661×10^{11}	5.866×10^{11}	7.939×10^{11}
56	5.983	1.408×10^2	49	1.757	8.765×10^{-2}	8.593×10^{-2}	2.639×10^{-2}	2.282×10^{-2}
53	6.274	5.829×10^1	51	3.337	1.030×10^5	1.011×10^5	4.821×10^4	1.415×10^4
54	4.222	1.986×10^1	51	3.708	4.874×10^{11}	4.872×10^{11}	4.353×10^{11}	3.672×10^{11}
			52	3.652	3.216×10^{11}	3.208×10^{11}	2.794×10^{11}	2.316×10^{11}
			49	1.861	6.060×10^4	6.034×10^4	3.273×10^4	5.408×10^4
52	4.046	4.000×10^1	54	3.652	1.719×10^{11}	1.715×10^{11}	1.431×10^{11}	1.254×10^{11}
			58	1.256	1.347×10^1	1.218×10^1	4.505×10^0	5.024×10^1
51	4.313	8.153×10^1	54	3.708	5.876×10^{10}	5.871×10^{10}	4.716×10^{10}	3.769×10^{10}
			53	3.337	1.101×10^{10}	1.106×10^{10}	8.791×10^9	6.402×10^9
			59	2.459	1.757×10^8	1.782×10^8	1.163×10^8	8.482×10^7
			57	1.280	4.007×10^0	3.649×10^0	1.262×10^0	1.132×10^1

^aCompare with footnotes of Table 4.3

Isomerisation of energised **49**

The isomerisation rate coefficients $k_{\text{WR}}^{\text{vr}}$ of the energised **49** range from 5.8 to $8.6 \times 10^{11} \text{ s}^{-1}$ leading to the **54**, **53** and **56** structures. In each case the reverse process is effectively suppressed, since the isomerisation ratios $r_{\text{WR}, \text{49} \leftrightarrow \text{54}}^{\text{vr}}$ and $r_{\text{WR}, \text{49} \leftrightarrow \text{53}}^{\text{vr}}$ are below 1×10^{-7} . The barrier heights from **49** to **54**, **53** and **56** disagree with the amount of products obtained by the MD simulations. Particularly, the fraction of **56** in the MD simulations is much lower. This can be explained by dynamic effects that are not considered in the reaction path analysis.

Isomerisation of the energised **54**

The structure **54** possesses isomerisation barriers of less than 0.6 eV for the formation of tricyclic structures **51** and **52**.

The energetic level of **54**, **51** and **52** are nearly equal at the B3LYP level of theory. In contrast, the corresponding forth and back isomerisation rate coefficients between **54** and **51** relate as 9.2:1, while the forth and back ratio between **54** and **52** is 2:1.

Isomerisation of the energised **51**

The stability of the both tricyclic structures is limited by the ring opening barrier of 1 eV leading to **53**. The opposite process, i. e., the heptagon constriction of **53**, constitutes a barrier of 3 eV. The forth and back isomerisation rate ratio between **51** and **53**, $r_{\text{WR}, \text{51} \leftrightarrow \text{53}}^{\text{vr}}$,

is computed with 182348:1. The MD simulations performed in this work indicate a much lower ratio for which the constriction and de-constriction rates are found to be much more equalised.

According to the proposed H_2 elimination (Section 6.1), the dissociation of H_2 from energised **51** is expected to take place by concerted removal of two hydrogens placed at the two sp^3 -hybridised carbons leading to **57**. The process constitutes a relative barrier height of 3.3 eV. The calculated isomerisation rate coefficient $k_{WR, \mathbf{51} \rightarrow \mathbf{57}}^{vr}$ is about 7×10^9 times slower than the competing ring opening (i. e., the de-constriction) $k_{WR, \mathbf{51} \rightarrow \mathbf{53}}^{vr}$. This low rate may explain the failed observation of H_2 elimination during the MD simulations.

On the other side, the rate of the C_2H_2 elimination from **51** leading to **59** is evaluated with $k_{WR}^{vr} = 1.2 \times 10^8 \text{ s}^{-1}$. It is only 76 times slower than the competing ring opening $k_{WR, \mathbf{51} \rightarrow \mathbf{53}}^{vr}$. The mechanism consists of a stepwise C-C bond rapture in the 4-membered ring via the intermediate structure C_9H_7-CHCH .

*Isomerisation of the energised **52***

The H_2 elimination from the energised **52** is as slow as from the energised **51**, since the elimination barrier has an equal height.

6.3 Reaction of $C_{11}H_9^+$ with CH

In this section, the study of the ion molecule reactions between methyne and the $C_{11}H_9^+$ isomers [51](#), [53](#) and [55](#) is presented. All $C_{11}H_9^+$ reactants are products of the reaction $C_{10}H_9^+ + CH$ as described in the previous section.

6.3.1 DFTB based MD simulations

The following analysis includes each trajectory between the collision energies 0.005 and 0.50 eV, of all the collision parameters sampled between 0.2Å and b_{\max} , and of all sampled orientations. are considered in the following results.

6.3.1.1 Identified product channels

All three reactions provide a large variety of product configurations due to the low selectivity of the CH addition. After $t_{\text{postcoll}} = 6$ ps the variety is even enlarged since isomerisation processes lead to new products. The sorting and classification of the products is based on structural attributes such as number of rings, size of rings, type of fusion between the rings, and type of sidegroups. The division and abbreviations are made as follows:

1.) Four channels of different tricyclic structures:

- **tcy-5.5.6:** Linear and non-linear catacondensed tricyclic structures that consist of 2 pentagons and 1 hexagon fused together. A corresponding energetically stable structure is [60](#).
- **tcy-4.6.6:** Linear and non-linear catacondensed tricyclic structures that consist of 2 hexagons and 1 tetragon fused together. Structure [61](#) belongs to this class.
- **tcy-4.5.7:** Linear and non-linear catacondensed tricyclic structures that consist of 1 heptagon, 1 pentagon and 1 tetragon fused together. One of the identified structure is labelled [62](#).
- **tcy-5.6.6:** Pericondensed tricyclic structures that consist of 2 hexagons and 1 pentagon fused together. One carbon is shared by all rings. A representative structures for this group is [63](#).

2.) Two channels of different bicyclic structures:

- **bcy-7.7:** Structures consist of 2 fused heptagons. It is commonly referred to as heptalene. Its label is [64](#).
- **bcy-6.8:** Structures formed by fused a hexagon and an octagon. A corresponding energetically stable structure is [65](#).

3.) Three channels of different CH bridged (methyno-bridged) and C_2H_2 bridged (ethyno-bridged) structures (**brdg**):

- **brdg-1:** Pericondensed tricyclic structures that consist of 2 pentagons and 1 heptagon fused together. The carbon atoms shared by all rings are hydrogenated and sp^3 -hybridised. Structures [66](#) is a representative configuration.
- **brdg-2:** Bicyclic structures with 1 heptagon and 1 octagon, which is represented by [67](#).
- **brdg-3:** Ethyno-bridged naphthalene, which corresponds to [68](#).

- 4.) Two channels with different sidegroups which are summarised to:
 - **R-CH₂**: Methylene sidegroup. Identified structures of the MD simulations are **69–71**.
 - **R-C₂H₃**: Vinyl sidegroup. Identified structures **72** was found to originate from **55**.
- 5.) Fragmentation channels (**frag**) that consist of acetylene eliminated from $C_{10}H_8^+$ ions (**f-C₂H₂**) and $C_3H_3^+$ eliminated from $C_9H_7^+$ ions.
- 6.) CH-attached (methylidene) sidegroup (**R-CH**).
- 7.) Orbiting complexes (**cmplx**) representing the reactants circulating each other.

Structures and corresponding energies are given in Table 6.3.

6.3.1.2 Product distribution as given by cross sections

The results based on the MD trajectory snapshots at $t_{\text{postcoll}} = 6$ ps are given in Figure 6.7.

*Distribution of **51** and methyne:*

The reaction of the tricyclic **51** with methyne exhibits the following distribution: 21–26% of all reactive collisions lead to **tcy-5.5.6**, 13–18% to **tcy-4.6.6**, 20–28% to **tcy-4.5.7**, and 5–7% to **bcy-6.8**. Furthermore, the fraction of methylidene sidegroup structures constitutes 17–25%. Up to 7% of all trajectories at $\varepsilon_{\text{coll}} = 0.005$ eV remain in the assigned status of an orbiting complex. Further, but minor fractions of reaction collisions are **tcy-5.6.6** with 1–4%, **R-CH₂** with 1–5%, and **brdg** with about 1%. Moreover, about 1–3% of formed polycyclic structures undergo a ring opening and another 1% fragmentates into $C_{10}H_8^+ + C_2H_2$ and $C_9H_7^+ + C_3H_3$.

The fairly equal distribution among the tricyclic products indicates that each ring unit in **51** is equally likely extended by CH insertion. It also demonstrates that every carbon position of **51** is equally attacked by CH. The fraction of **tcy-4.6.6** decreases with increasing $\varepsilon_{\text{coll}}$ while the fraction **bcy-6.8** enlarges. These results indicate that with increasing non-fixed energy the stability of **tcy-4.6.6** is lowered; it converts to **bcy-6.8**.

*Distribution of **53** and methyne:*

The total cross section is divided into 8%–14% of **tcy-5.5.6**, 35–46% of **bcy-7.7**, 32–40% of **bcy-6.8** as well as minor fractions of **tcy-4.6.6** (1%), **tcy-5.6.6** (1%), **R-CH₂** (1–5%), and **brdg** (1–3%). Moreover, about 1–3% of formed polycyclic structures undergo a ring opening. The fraction of methylidene sidegroup structures constitutes 3–8%. Up to 7% of all trajectories at $\varepsilon_{\text{coll}} = 0.005$ eV remain in a status assigned to the orbiting complex. Due to structural relations, the depletion of **bcy-6.8** and **R-CH** with increasing collision energy is supposed to be related with the increase of **tcy-5.5.6**.

*Distribution of **55** and methyne:*

The product distribution in the applied range of collision energy consists of 29–32% **tcy-4.6.6**, 39–47% **R-CH₂** and 7–9% **R-CH**. Furthermore, the fraction of methylidene sidegroup structures ranges from 15 to 19%, while a minor fraction (below 1%) is assigned to **tcy-5.6.6**.

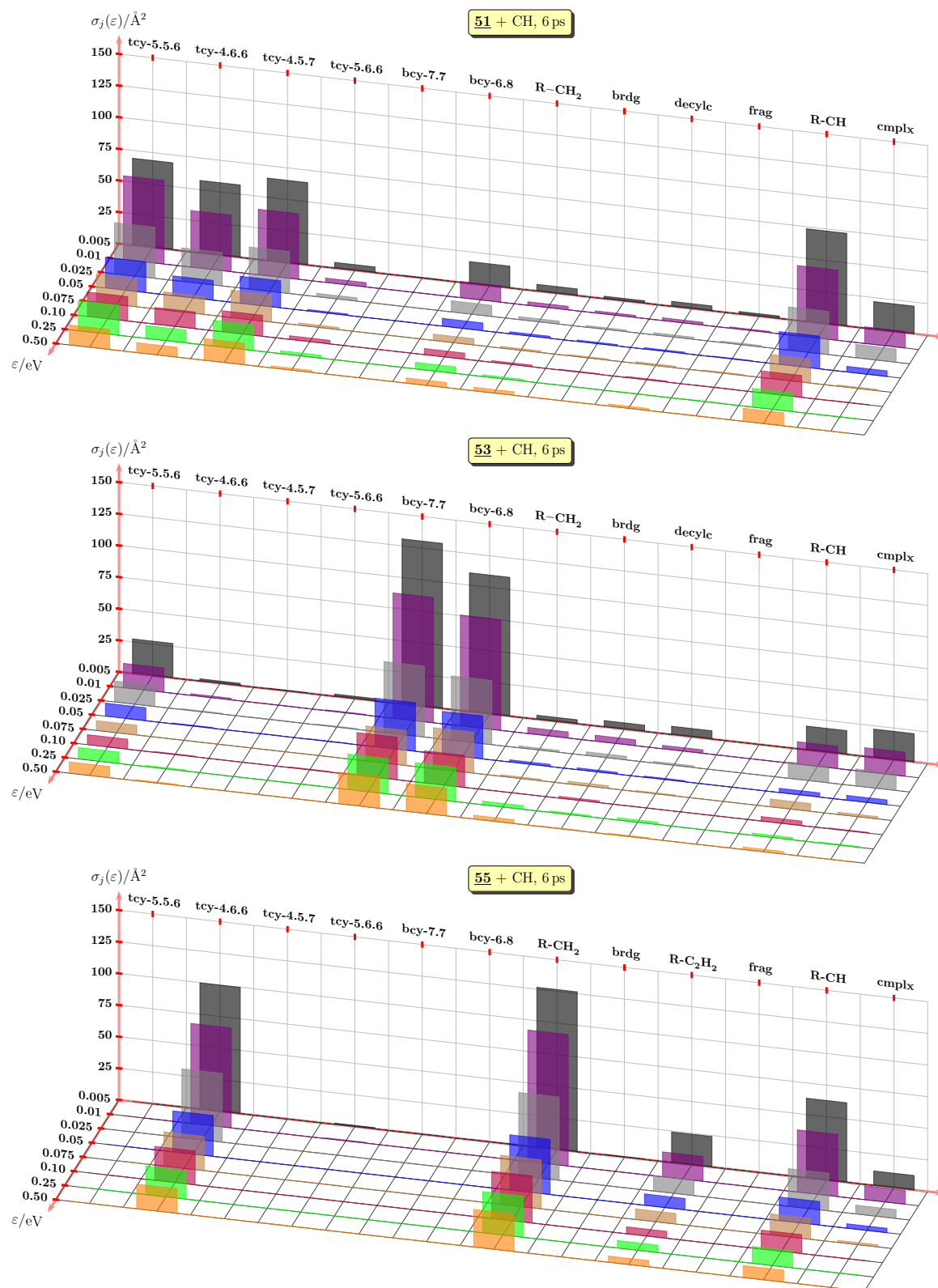


Figure 6.7: Calculated product cross sections $\sigma_{R,j}$ resulting from the reaction between **51**, **53** or **55** and methyne after $t_{\text{postcoll}} = 6 \text{ ps}$ and at different collision energies ϵ . Abbreviations of given channels are defined in Section 6.3.1.

structures. The fraction amount of the orbiting complex drops from 4% at 0.005 eV to zero at 0.10 eV.

Comparison of the different product distributions:

The **R-CH** fractions resulting from reaction of **53** with methyne is low relative to the other systems. This indicates that the insertion of CH into to carbon structures containing a heptagonal moiety is fast although **53** has the highest thermodynamic stability among the given $C_{11}H_9^+$ reactants.

Ring opening processes result in structures of monocyclic and bicyclic moieties, which are of increased stability. The probability of non-cyclic moieties to be eliminated is reduced.

6.3.1.3 Calculated capture rate coefficients

The capture rate coefficients were calculated based on Eqs. (2.15) and (2.16). Rate coefficients k_L and $k_{ADO}(T)$ were evaluated for comparison. The corresponding dipole moments and polarisabilities (Table A.1) are taken from DFT calculations. The results are given in Figure 6.8.

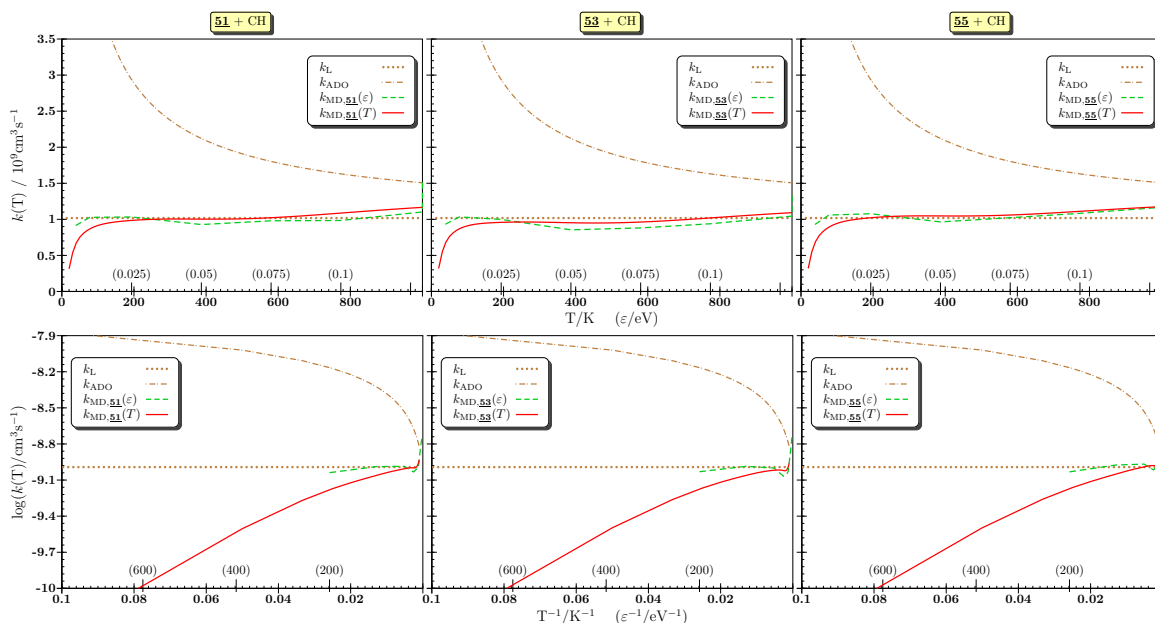


Figure 6.8: Capture rate coefficients of the **51** + CH, **53** + CH and **55** + CH reaction systems based on the *Langevin* model (k_L), ADO model (k_{ADO}), and the results of the MD simulations ($k_{MD}(\epsilon)$ and $k_{MD}(T)$). Two different representations are given: bottom) logarithmic k versus inverse T (ϵ_{coll}) and top) k versus T (ϵ_{coll}). Collisional energies and temperature were related by $\epsilon = 3/2k_B T$.

k_L , $k_{ADO}(T)$ and comparison with MD based values:

The computation of the capture rate coefficient (k_L) gives a value of $1.02 \times 10^{-9} \text{ cm}^3 \text{ s}^{-1}$. The dipole corrected values, $k_{ADO}(T)$, range from $9.54 \times 10^{-9} \text{ cm}^3 \text{ s}^{-1}$ at 20 K to $1.51 \times 10^{-9} \text{ cm}^3 \text{ s}^{-1}$ at 1000 K. For the interval between 0.005 and 0.50 eV, the obtained $k_{MD}(\epsilon)$ values of each reaction system are nearly equal to the evaluated k_L values. The increase at higher temperatures might be caused by the dispersion forces as discussed in Section 4.6.

Since all reactants capture CH at nearly equal rates (Figure 6.1), their different energetic stabilities do not effect the overall reactivity.

Comparison between $k_{MD}(T)$ and $k_{MD}(\varepsilon)$:

Deviations arise at collision energies below 0.025 eV (193 K), which correspond to the $k_{MD}(T)$ slope as described in the Chapter 4. The possible origin is suggested to be a numerical problem as discussed in Section 4.3.1.

6.3.2 Product energetics

The reaction enthalpies of the identified products are given in Table 6.3. The reaction

Table 6.3: Ion-molecule based reaction energies and enthalpies obtained by different quantum theory methods. For each reaction the educts **55** and CH were considered.

products	abbr.	geometry	class	$\Delta_R E/\text{eV}$	$\Delta_R H_{0\text{K}}/\text{eV}$	
				SD	Btz1//Bdz1	Ptz4
$\mathcal{B}a\text{-}C_{12}H_{10}^+$	60		tcy-5.5.6	-5.3966	-4.2784	-4.9675
$\mathcal{B}b\text{-}C_{12}H_{10}^+$	61		tcy-4.6.6	-4.6655	-3.6311	-4.2622
$\mathcal{B}c\text{-}C_{12}H_{10}^+$	62		tcy-4.5.7	-4.0856	-3.2490	-3.8821
$\mathcal{B}d\text{-}C_{12}H_{10}^+$	63		tcy-5.6.6	-4.5059	-3.2223	-3.9488
$\mathcal{C}a\text{-}C_{12}H_{10}^+$	64		bcy-7.7	-5.3235	-4.5050	-4.9883
$\mathcal{C}b\text{-}C_{12}H_{10}^+$	65		bcy-6.8	-5.1567	-4.2388	-4.7470
$\mathcal{D}a\text{-}C_{12}H_{10}^+$	66		brdg	-5.5293	-4.2916	-4.9830
$\mathcal{D}b\text{-}C_{12}H_{10}^+$	67		brdg	-3.7625	-3.0017	-3.6062
$\mathcal{D}c\text{-}C_{12}H_{10}^+$	68		brdg	-5.2497	-3.8388	—
$\mathcal{E}a\text{-}C_{12}H_{10}^+$	69		R-CH₂	-5.7147	-4.9895	-5.4281
$\mathcal{E}b\text{-}C_{12}H_{10}^+$	70		R-CH₂	-5.8059	-5.0508	-5.4808
$\mathcal{E}c\text{-}C_{12}H_{10}^+$	71		R-CH₂	-5.7681	-4.8619	-5.3200
$\mathcal{F}a\text{-}C_{12}H_{10}^+$	72		R-C₂H₃	-6.3153	-5.4008	-5.8336
$\mathcal{B}a\text{-}C_{12}H_8^+ + H_2$	73		f-H₂^a	-3.3816	-4.0155	-4.5508
$\mathcal{B}d\text{-}C_{12}H_8^+ + H_2$	74		f-H₂^a	-4.1134	-4.7050	-5.1841
$\mathcal{A}\text{-}C_{10}H_8^+ + C_2H_2$	75		f-C₂H₂	-4.0810	-3.5824	-3.7958

^anot observed during the MD simulation of 6 ps

enthalpy $\Delta_R H_{0K}$ ranges among the given $C_{12}H_{10}^+$ products from 3.6 eV to 5.8 eV at Ptz4 level of theory. The amount increases by about 2 eV if the total energies of **55** + CH is used as reference. The comparison of the enthalpy values between: 1) the reaction from naphthalene to the most stable bicyclic $C_{11}H_9^+$ (**53**) and 2) the reaction from **53** to the most stable bicyclic $C_{12}H_{10}^+$ (**64**) shows a reduction from -6.2 eV to -4.5 eV (at Btz1//Bdz1 level of theory). This indicates high energetic stability of **53**.

Comparison between tricyclic and bicyclic products

The vinylnaphthalene cation (**72**) has the energetically highest stability at each level of theory. This structure is about 0.8–1.2 eV more stable than the tricyclic structures **60** and **66**.

Consideration of fragmentation products

The H_2 elimination marks an essential step for the growth of PAHs by CH molecules. Therefore, it is suggested that the tricyclic products **60** and **63** dissociate into H_2 and their corresponding $C_{12}H_8^+$ structures. The resulting product pair **73** is only 0.3–0.4 eV less stable (Btz1//Bdz1, Ptz4) than **60**. This elimination is, therefore, almost thermoneutral. On the other side, the H_2 elimination from **63** resulting in **74** is exothermic by 1.5 eV at Btz1//Bdz1 level of theory. The H_2 elimination is, therefore, thermodynamically favoured.

6.3.2.1 Canonical population distribution

In order to compare the relative product stabilities with increasing temperature the set of products, as given in Table 6.3, were splitted into subsets. The most stable isomers of each subset are again composed to one subset (last column of Figure 6.9).

The thermal equilibrium of tricyclic products is dominated by **60**, the one of the bicyclic products by **64**, the one of the bridged products by **66**, and the one of the methylene sidegroup products by **70** (below 2000 K) and **71** (above 2000 K) in the applied temperature range. The thermal equilibrium between these most stable products and **72** is, however, dominated by **72**. At high temperatures the ratio between **71** (methylene sidegroup containing $C_{12}H_{10}^+$) and **64** (bicyclic $C_{12}H_{10}^+$) is evaluated with 3–4 to 1. However, the MD based fraction of methylene sidegroup products is much lower.

6.3.3 Reaction path analysis

Results of the reaction path analysis of the CH attack at $C_{11}H_9^+$, of the isomerisation between bicyclic and tricyclic $C_{12}H_{10}^+$ products, and of the elimination of H_2 and C_2H_2 from $C_{12}H_{10}^+$ are plotted in Figure 6.6. The reaction paths are only represented by the stationary points including transition states obtained at Bdz1 level of theory. The isomerisation rate coefficients based on the RRKM theory and CTST are given in Table 6.4.

6.3.3.1 The chemical network and isomerisation rates

CH addition mechanism:

According to the results depicted in Figure 6.10, each CH association pathway is barrierless (blue dashed lines). The resulting structures belong to the product class **R-CH**.

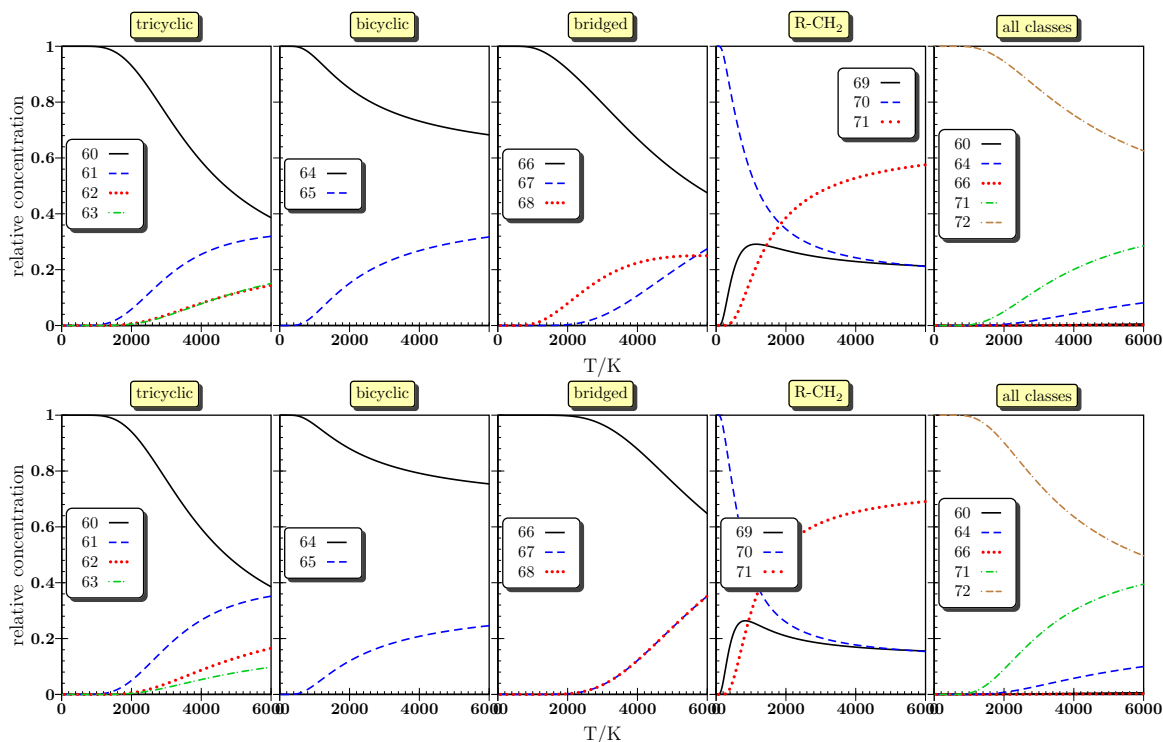


Figure 6.9: Canonical population analysis of $C_{12}H_{10}^+$ product isomers taken from Table 6.3 obtained by Btz1//Bdz1 (top) and Ptz4 (bottom) level of theory. The equilibrium between the most stable products of each class is depicted in the last column.

*Cyclisation and decyclisation between **62**↔**64**:*

The structure **64** is formed by the reactions **53** + CH and **51** + CH. In the first case the formation results from the ring extension of **53**, and in the other case from the ring opening of **62**. This corresponding ring opening barrier is 1.2 eV. The isomerisation rate coefficient ratio of **62** to **64**. $r_{WR,62\leftrightarrow 64}^{vr}$ is 44760:1.

*Cyclisation and decyclisation between **61**↔**65**↔**60**:*

The decyclisation barriers for **61**→**65** is 0.98 eV, and for **60**→**65** is 1.38 eV. The cyclisation barrier to **61** is 1.6 eV, while the cyclisation to **60** has a barrier of 1.32 eV. The resulting isomerisation rate coefficient ratios are based on the resulting non-fixed energy from the CH addition reaction, thus result in $r_{WR,61\leftrightarrow 65}^{vr} = 313:1$ and $r_{WR,60\leftrightarrow 65}^{vr} = 4:1$. Based on these ratios the concentrations between **61**, **65** and **60** is about 0% to 81% to 19%.

*H₂ elimination from **66**:*

The H₂ elimination from **66** has a barrier of 2.36 eV. The corresponding isomerisation rate coefficient is $8.24 \times 10^5 \text{ s}^{-1}$ which is over 800 times slower than the decyclisation of **60** to **65**.

*H₂ elimination from **60**:*

The barrier of **60** to **73** is evaluated with a height of 2.81 eV. The isomerisation rate coefficient is, however, about 1500 times slower than the H₂ elimination from **66**. In the case of an indirect pathway of **60** to **73** via **I₁₇** and **I₁₈** (**60**→**I₁₇**→**I₁₈**→**73**), the lowest step is **60**→**I₁₇**. From **I₁₇** only the fraction $f_{WR,I_{17}\rightarrow I_{18}}^{vr} = 0.15$ and from **I₁₈** only

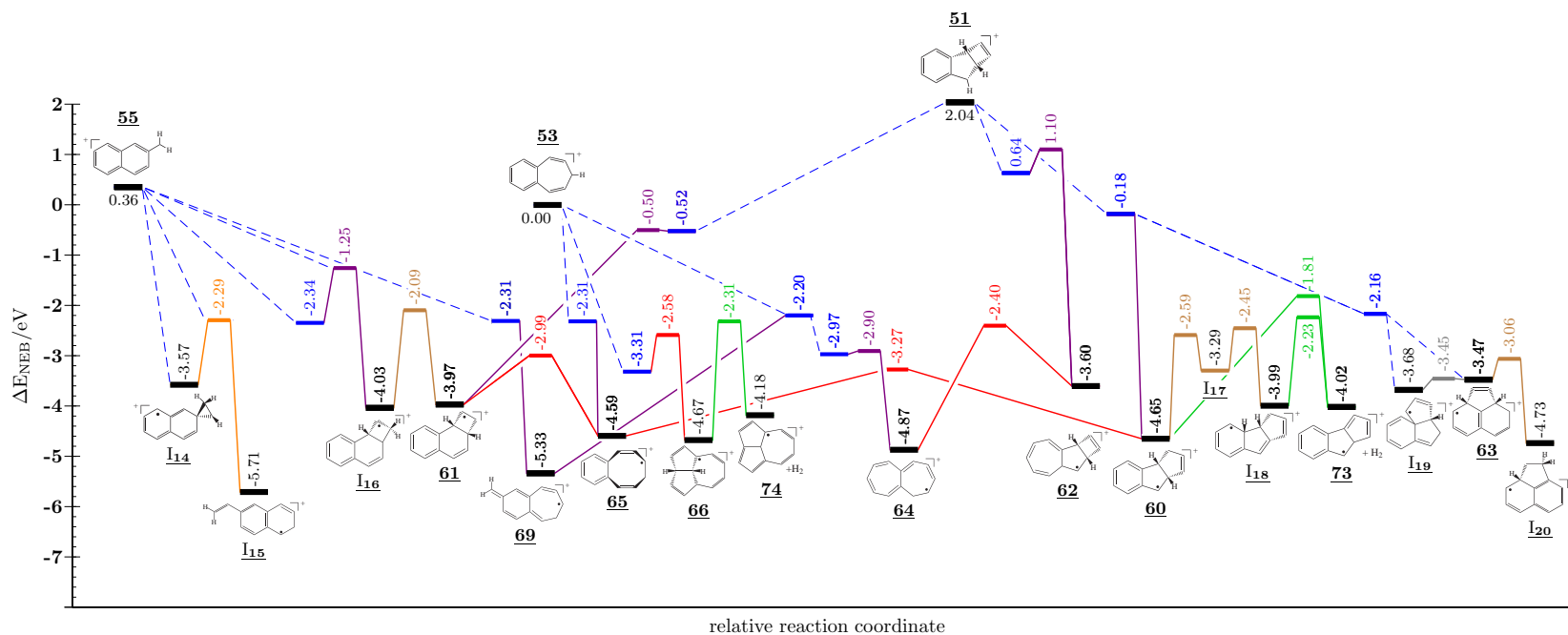


Figure 6.10: Stationary points of $C_{11}H_9^+ - CH$ addition reaction paths, of $C_{12}H_{10}^+$ isomerisation paths between conformers, of $C_{12}H_{10}^+$ cyclisation paths and fragmentation paths obtained at Bdz1 level of theory. Underlined labels represent molecules and intermediates I_{xx} as defined in the text.

Table 6.4: Unimolecular rate coefficients of radiative deactivation and of isomerisation processes based on different approaches. Energies (at Bdz1 level of theory) are taken from the MEP and TS optimisation (Figure 6.10). The internal energy is assumed to correspond in amount to the enthalpy of the reaction **53** and methyne dissipated to the product **X** at 0 K.

product	E_{vr}^a / eV	$k_r(E_{\text{vr}})$ / s^{-1}	Isomerisation/Dissociation					
			to	$E_{\text{vr}}^\ddagger^a$ / eV	$k_{\text{DC}}^{\text{v}}(E_{\text{vib}})^a$ / s^{-1}	$k_{\text{WR}}^{\text{v}}(E_{\text{vib}})^a$ / s^{-1}	$k_{\text{WR}}^{\text{vr}}(E_{\text{vr}})^a$ / s^{-1}	$k_{\text{m}}^{\text{vr}}(T_{\text{vr}})^a$ / s^{-1}
61	3.764	5.400×10^1	65	2.856	5.815×10^9	5.807×10^9	4.515×10^9	4.587×10^9
65	4.334	3.828×10^1	60	3.133	2.626×10^8	2.615×10^8	1.584×10^8	1.309×10^8
			61	2.856	2.504×10^7	2.503×10^7	1.441×10^7	1.272×10^7
60	4.423	5.315×10^1	65	3.133	9.048×10^8	9.043×10^8	6.716×10^8	5.305×10^8
			I17	2.529	1.209×10^6	1.185×10^6	7.587×10^5	7.962×10^5
			73	1.892	1.180×10^3	1.101×10^3	5.362×10^2	1.355×10^3
I17	3.119	1.748×10^2	60	2.529	2.155×10^{10}	2.115×10^{10}	1.773×10^{10}	2.235×10^{10}
			I18	2.371	4.043×10^9	3.972×10^9	3.164×10^9	4.697×10^9
I18	3.782	5.066×10^1	73	2.334	9.692×10^7	9.407×10^7	5.900×10^7	8.019×10^7
			I17	2.371	2.610×10^7	2.570×10^7	1.692×10^7	2.498×10^7
66	4.430	5.959×10^1	74	2.392	1.501×10^6	1.463×10^6	8.240×10^5	9.184×10^5
64	4.632	7.816×10^1	62	2.265	1.468×10^4	1.494×10^4	7.033×10^3	1.711×10^4
62	3.391	2.835×10^1	64	2.265	4.426×10^8	4.444×10^8	3.148×10^8	5.070×10^8
I19	3.485	4.660×10^1	63	3.276	4.992×10^{11}	4.990×10^{11}	4.851×10^{11}	4.844×10^{11}
63	3.319	4.365×10^1	I19	3.276	1.585×10^{12}	1.588×10^{12}	1.458×10^{12}	1.467×10^{12}
			I20	2.971	1.643×10^{11}	1.639×10^{11}	1.499×10^{11}	1.567×10^{11}
I20	4.514	5.732×10^1	63	2.971	3.231×10^7	3.194×10^7	2.120×10^7	1.721×10^7

^aCompare with footnotes of Table 4.3

$f_{\text{WR}, \text{I18} \rightarrow \text{73}}^{\text{vr}} = 0.78$ contributes to the formation speed. This gives an effective rate coefficient $k_{\text{eff}, \text{WR}, \text{60} \rightarrow \text{73}}^{\text{vr}} = 0.88 \times 10^5 \text{ s}^{-1}$ which is about 9.3 times slower than the H_2 elimination from **66**.

6.4 Reaction of $C_{12}H_{10}^+/C_{13}H_{11}^+$ with CH

In this section, the results of the DFTB-MD collision simulations and reaction path analysis between methyne and $C_{12}H_{10}^+$ as well as between methyne and $C_{13}H_{11}^+$ are presented.

6.4.1 DFTB based MD simulations of $C_{12}H_{10}^+ + CH$

The $C_{12}H_{10}^+$ structures **64** and **65** have been selected as reactants based on the proposed pathway as given in Figure 6.1. Tricyclic structures such as **60** were not considered. Furthermore, neither $C_{12}H_{10}^+$ containing methylene nor vinyl sidegroups were considered since the scope of this section is related with the ring extension.

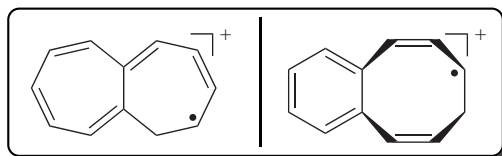


Figure 6.11: Structures of $C_{12}H_{10}^+$ reactants: (left) **64** and (right) **65**.

6.4.1.1 Identified products of the reaction between **64** / **65** and methyne

A summary of identified product classes and corresponding structures are given in Table 6.5.

Table 6.5: Energetically stable structures of bicyclic and tricyclic product channels identified and obtained from the MD collisions between **64** / **65** and methyne. The numbers within the defined abbreviation of each reaction channel refer to the combined ring size of the polygons, e. g. **tcy-5.6.6** states a tricyclic structure consisting of 1 pentagon and 2 hexagons.

class	tcy-5.6.6	tcy-4.5.8	bcy-7.8	bcy-6.9	R-CH₂	tcy-5.6.7	tcy-5.5.8	tcy-6.6.7
product								
abbr.	81	82	83	84	85	86	87	88

Tricyclic and bridged structures among bicyclic structures were identified in this work. This indicates the presence of postcollisional processes which are different from the CH insertion mechanism. For instances, **81** and **82** are the result of an electrocyclic ring closure inside an existing ring (also referred to as constriction in this work). The existence of **86** suggests a CH insertion between two ternary sp^2 -hybridised carbon atoms, i. e., the carbon atoms shared by both ring units. The resulting intermediate increases its stability by forming another bond between the methyno bridge and a carbon at the opposite position of the fused ring which leads to **86**. Structures **87** and **88** represent products in which CH bridges opposite carbon atoms belonging to the same ring unit. The MD simulations suggest here a two-step, viz. a non-concerted mechanism.

Other products, but not given in Table 6.5, refer to the following product channels: fragmentations containing acetylene (**f-C₂H₂**), complexes of methylenide sidegroups (**R-CH**),

and orbiting complexes (**cmplx**). The latter two configurations are considered to be initial intermediates of the collision.

6.4.1.2 Product distribution corresponding to cross sections

The results based on the MD trajectory snapshots at $t_{\text{postcoll}} = 6$ ps are illustrated in Figure 6.12.

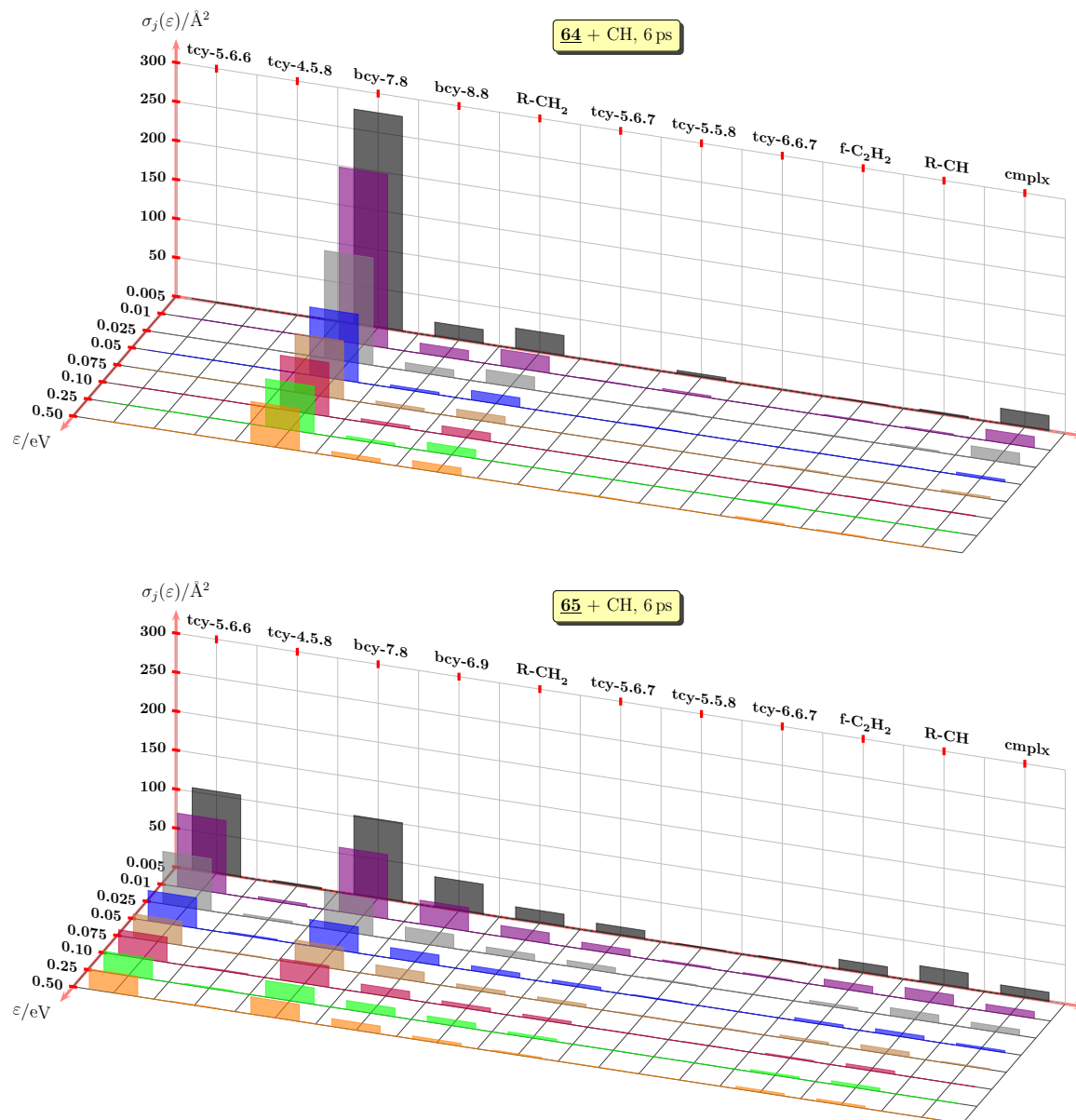


Figure 6.12: Calculated product cross sections $\sigma_{R,j}$ resulting from the reaction between **64**/**65** and methyne after $t_{\text{postcoll}} = 6$ ps and at different collision energies ε . Abbreviations of the channels are defined in Section 6.4.1.1.

*Distribution resulting from the reaction between **64** and methyne:*

Cross sections are divided into 72–81% of **bcy-7.8**, 3–8% of **bcy-8.8**, 8–15% of **R-CH₂**, and 0–8% of **cmplx** for all given collision energies $\varepsilon_{\text{coll}}$. The fraction of **cmplx** shrinks with increasing collision energy while **bcy-8.8** increases. Minor fractions are related with

tcy-5.6.7 (1%) and **f-C₂H₂** (1%). Since the fraction of **R-CH** disappears within 6 ps, a fast CH insertion is indicated. This requires an increased structural flexibility.

*Distribution resulting from the reaction between **65** and methyne:*

The distribution is structured as follows: 32–39% of **tcy-5.6.6**, 27–32% of **bcy-7.8**, 10–14% of **bcy-6.9**, 5–10% of **R-CH₂**, and 4–7% of **R-CH** for all given collision energies ϵ_{coll} . Minor fractions belong to **tcy-5.6.7** (3–4%), **f-C₂H₂** (2–4%) and **cmplx** (0–4%). No explicit collision energy dependence was identified except for **cmplx**

Comparison between both distributions

Due to the symmetry of **64** the arbitrary ring extension leads to the same bicyclic product, i. e., **bcy-7.8**. In the case of **65**, the ring insertion leads to either **bcy-7.8** or **bcy-6.9**. Due to structural relation between **tcy-5.6.6** and **bcy-6.9** by ring opening / closure, their amounts can be summed up, which then exceeds **bcy-7.8**. The ratio between the combined and **bcy-7.8** fraction agrees with a proposed, statistically distributed attack of CH at **65**. The ratio of **tcy-5.6.6** to **bcy-6.9** is roughly 3:1. This means that the formed 9-membered rings of **bcy-6.9** structures isomerise very fast to a fused pentagon-hexagon unit. In the case of **bcy-7.8**, the missing of a corresponding tricyclic structure indicates that the 8-membered ring isomerise very slow to a fused pentagon-pentagon unit. Products of the reactant **64** are, therefore, unfavoured for ring closure mechanisms.

6.4.2 DFTB based MD simulations of $C_{13}H_{11}^+ + CH$

The structure of both selected $C_{13}H_{11}^+$ reactants are given in Figure 6.13.

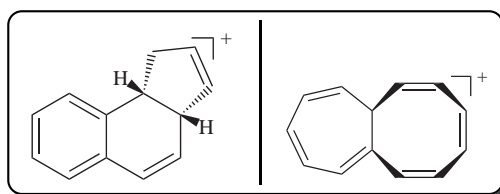


Figure 6.13: Structures of $C_{13}H_{11}^+$ reactants: (left) **81** and (right) **83**.

Both reactants are products of the previous reaction system which constituted the largest quantities. The selection of **81** is also based on its potential growth to dihydronaphthalene by a CH based ring extension.

6.4.2.1 Identified products of the reaction between **81** / **83** and methyne

A summary of identified product classes and corresponding structures are given in Table 6.5.

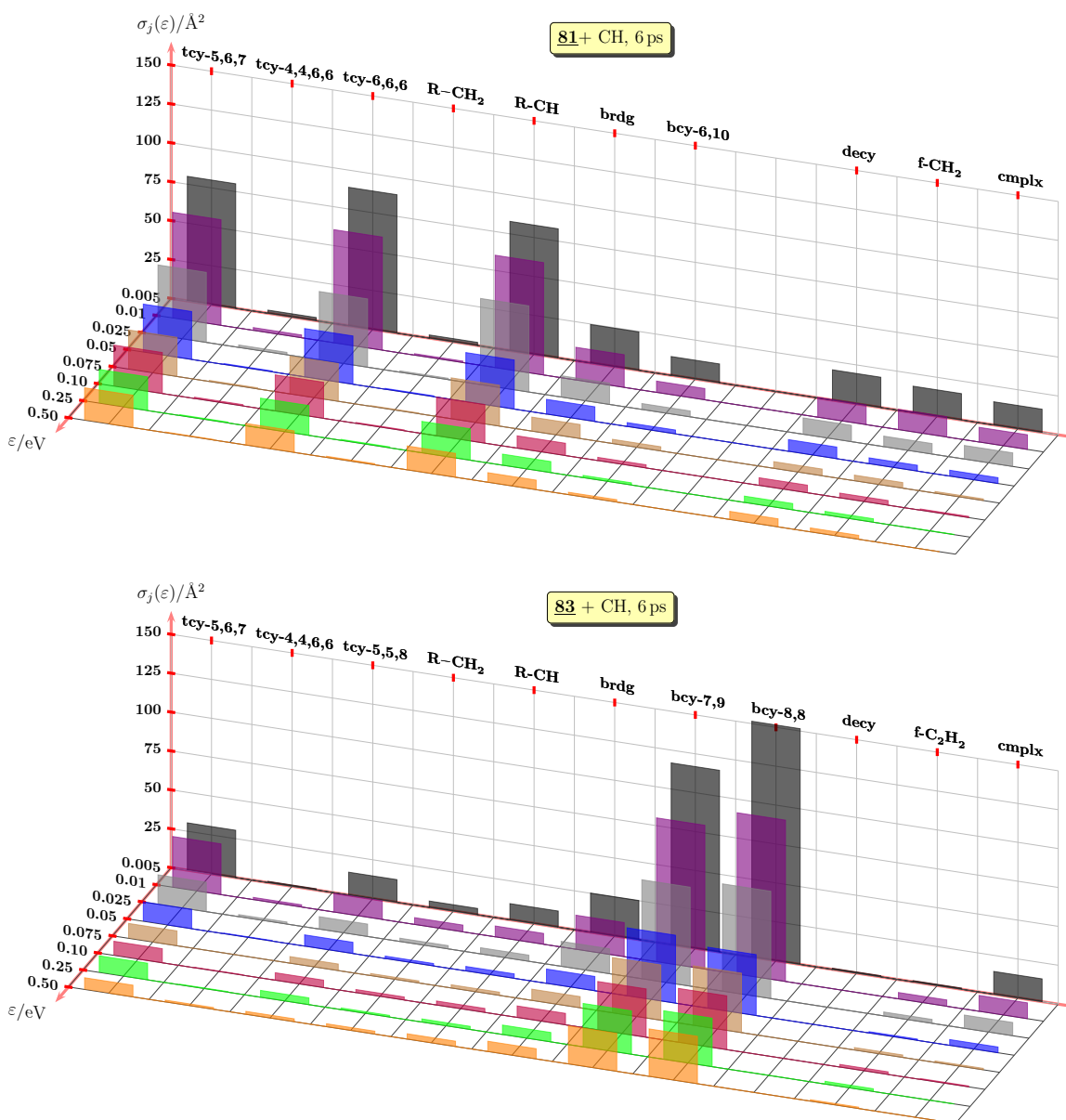
The identified product channels **tcy-6.6.6** and **f-CH₂** are most favourable to the hypothesis of PAH formation based on the CH precursor. The product channel **tcy-6.6.6** corresponds to dihydrogenated phenanthrene. The **f-CH₂** channel accounts for the hydrogen stripping by CH. This means that the precursor provides itself a possibility to remove excessive hydrogen in order to reach aromatic structures such as phenanthrene.

Table 6.6: Energetically stable structures of bicyclic and tricyclic product channels identified and obtained from the MD collisions between **81**/**83** and methyne.

class	tcy-5.6.7	4cy-4.4.6.6	tcy-6.6.6	R-CH ₂	brdg	bcy-7.9	bcy-8.8	f-CH ₂
product								
abbr.	89	90	91	92	93	94	95	96

6.4.2.2 Product distribution as given by cross sections

The results based on the MD trajectory snapshots at $t_{\text{postcoll}} = 6$ ps are illustrated in Figure 6.14.

**Figure 6.14:** Calculated product cross sections $\sigma_{R,j}$ resulting from the reaction between **81**/**83** and methyne after $t_{\text{postcoll}} = 6$ ps and at different collision energies ε . Abbreviations of given channels are defined in Section 6.4.1.1.

*Distribution resulting from the reaction between **81** and methyne:*

The total reaction cross section is composed of **tcy-5.6.7** with 23–31%, **tcy-6.6.6** with 21–26%, and **R-CH** with 23–29%. The large fraction of **R-CH** indicates that **81** possesses a higher stability against CH insertion than other investigated reactants such as **83**. The fraction of **tcy-6.6.6** shrinks with increasing collision energy while the fractions of **tcy-5.6.7** follows the opposite trend. The fraction of bridged structures **brdg** such as **93** structures constitute 7% at low collision energies and increases to 9% as the collision energy increases. A fraction of 4–8% is assigned to decyclized products (**decy**) which correspond to the bicyclic products with different kind of sidegroups.

Between 3–5% of all reactive collisions with CH lead to hydrogen stripping, i. e., formation of $C_{13}H_{10}^+ + CH_2$.

*Distribution resulting from the reaction between **83** and methyne:*

The obtained distribution shows that tricyclic structures such as **tcy-5.6.7** can be formed out of **83**. The total amount of tricyclic structures ranges between 12 and 18% after 6 ps MD simulation. This demonstrates that the formation of tricyclic products is a very fast process. The largest fractions, however, belong to the ring extension products **bcy-7.9** and **bcy-8.8** (31–36% and 32–42%)

Comparison between both distributions:

The insertion of CH into the carbon framework of **81** is slower than of **83**, since the former shows much larger amounts of **R-CH** complexes. The nearly equal amounts of formed tricyclic products for **81** and of formed bicyclic products in the case of **83** suggest a nearly equal distributed CH attack at each reactant ion.

Secondary mechanism for the formation of tricyclic structures

The analysis of the MD simulations suggests that, besides the ring closure mechanism, the formation of tricyclic molecules also takes place by the isomerisation of methyno-bridged molecules as depicted in Figure 6.6 and described in Section 6.2.3.

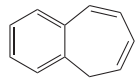
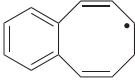
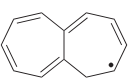
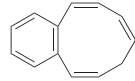
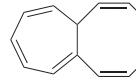
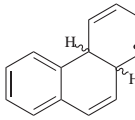
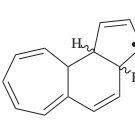
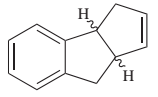
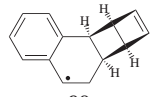
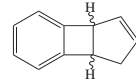
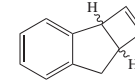
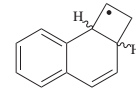
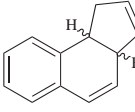
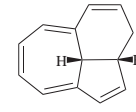
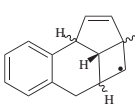
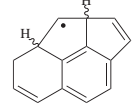
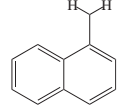
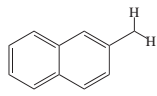
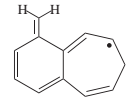
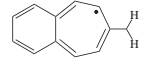
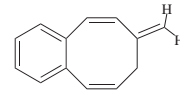
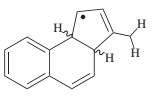
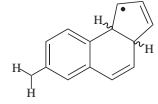
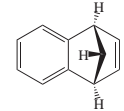
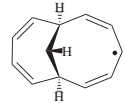
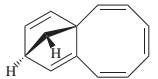
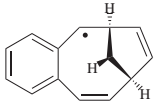
6.4.3 Product energetics

The relative energies of selected products of both reaction systems are summarised in Table 6.7. It also includes the products of the previous two reaction systems $C_{10}H_8^+/C_{11}H_9^+ + CH$ as reported above. According to the results of Table 6.7, the energetically most stable product structure changes from bicyclic $C_{11}H_9^+$ to bicyclic methylenyl structure ($C_{12}H_{10}^+$) and then finally to tricyclic $C_{13}H_{11}^+/C_{14}H_{12}^+$ structures. The energetically most stable tricyclic structures **81** and **91** are precursors of tricyclic aromatic structures. This change of energetic stability is in agreement with the results of the monocyclic hydrocarbons growing by CH (Section 5.2).

6.4.4 Reaction path analysis of selected mechanisms

Reoptimised minimum energy paths and TS structures of selected mechanisms obtained at Bdz1 level of theory are presented. In summary, barriers heights of cyclisations and thermal

Table 6.7: Selected product structures and their relative energies (ΔE) of the reactions $C_xH_{x-2}^+ + CH \longrightarrow C_{x+1}H_{x-1}^+$ ($x=10-13$) obtained at SD, Bdz1 and Mdz1 level of theory. The hydrogen atoms corresponding to the residual carbon atoms are not represented.

$C_{10}H_8^+ + CH \rightarrow$ $C_{11}H_9^+$ products	$C_{11}H_9^+ + CH \rightarrow$ $C_{12}H_{10}^+$ products	$C_{12}H_{10}^+ + CH \rightarrow$ $C_{13}H_{11}^+$ products	$C_{13}H_{11}^+ + CH \rightarrow$ $C_{14}H_{12}^+$ products
abbr. (name)	abbr. (name)	abbr. (name)	abbr. (name)
ΔE / eV at SD / Bdz1 / Mdz1	ΔE / eV at SD / Bdz1 / Mdz1	ΔE / eV at SD / Bdz1 / Mdz1	ΔE / eV at SD / Bdz1 / Mdz1
 53 (benzo[7]annulenylium) 0.0 / 0.0 / 0.0	 65 (benzo[8]annulenylium) 0.6492/0.8121/-	 64 (heptaleniumyl) 0.4825/0.5458/-	 84 (benzo[9]annulenylium) 1.0549/0.6775/1.1191
		 83 1.0580/0.6651/1.1310	 91 (dihydrophenanthreniumyl) -0.0751/0.1409/-
			 89 0.7582/0.5127/-
	 60 (benzodihydropentalenyliumyl) 0.4093/0.7724/-		 90 1.6406/1.4610/-
 52 2.1120/2.2208/2.0955	 51 1.9063/1.9596/1.8912	 61 1.1404/1.4198/-	 81 (benz[f]-indeniumyl) 0.0 / 0.0 / 0.0
			 86 0.1338/0.1130/0.3224
			 brdg 1.6184/1.5780/-
			 93 1.5535/1.7596/-
 56 (1-methylenyl-naphthylum) 0.2175/0.2854/0.3106	 55 (2-methylenyl-naphthylum) 0.3118/0.2930/0.3494	 R-CH₂ (methylenyl-benzo[7]annulenyliumyl) 0.0 / 0.0 / 0.0	 70 (3-methylenyl-benzo[7]annulenyliumyl) 0.1771/0.3027/-
			 85 (methylenyl-benzo[8]annulenyliumyl) 0.9162/0.5481/0.9981
			 92 (methylenyl- γ -C ₁₃ H ₁₁) 0.0 / 0.0 / 0.0
			 R-CH₂ (methylenyl- γ -C ₁₃ H ₁₁) 0.6977/0.6033/-
 54 (methyno-bridged naphthylum) 2.7299/2.0894/1.4483	 66 (methyno-bridged [9]annulenyliumyl) 2.0435/2.0492/-	 87 (methyno-bridged benzo[8]annulenyliumyl) 3.5496/2.9067/2.7808	 brdg (methyno-bridged benzo[9]annulenyliumyl) 1.9084/1.7747/-

H_2 elimination are in qualitative agreement with the results of monocyclic hydrocarbon growth (Section 5.3).

6.4.4.1 Cyclisation path of energised $C_{13}H_{11}^+$

Based on results as plotted in Figure 6.15, the electrocyclic conrotatory ring closure of I₂₃ to 81 constitutes a barrier of 0.3 eV. This barrier is 0.8 eV below the one of the electrocyclic ring closure of monocyclic $C_9H_9^+$ which is considered to be related with I₂₃; both have a 9-membered ring.

6.4.4.2 H_2 elimination path of energised $C_{13}H_{11}^+$

Reaction paths of H_2 elimination from energised $C_{13}H_{11}^+$ are plotted in Figure 6.15. Two pathways of the elimination of H_2 were considered: 1) *syn*-elimination of hydrogens from the adjacent ternary carbon positions, and 2) *syn*-elimination from one adjacent ternary and one secondary carbon positions. The first pathway constitutes a relative barrier height of 3.16 eV which is close to the 3.2 eV high barrier of the related bicyclic $C_9H_9^+$ structure. The second pathway involves two hydrogen shifts forming the structure I₂₂ which has a relative barrier height of 2.97 eV for the corresponding thermal H_2 elimination. Since the energetic stability of I₂₂ is higher than of 81 ($\Delta E = 1.06$), more non-fixed energy is available to the molecular system which increases the rate of the elimination.

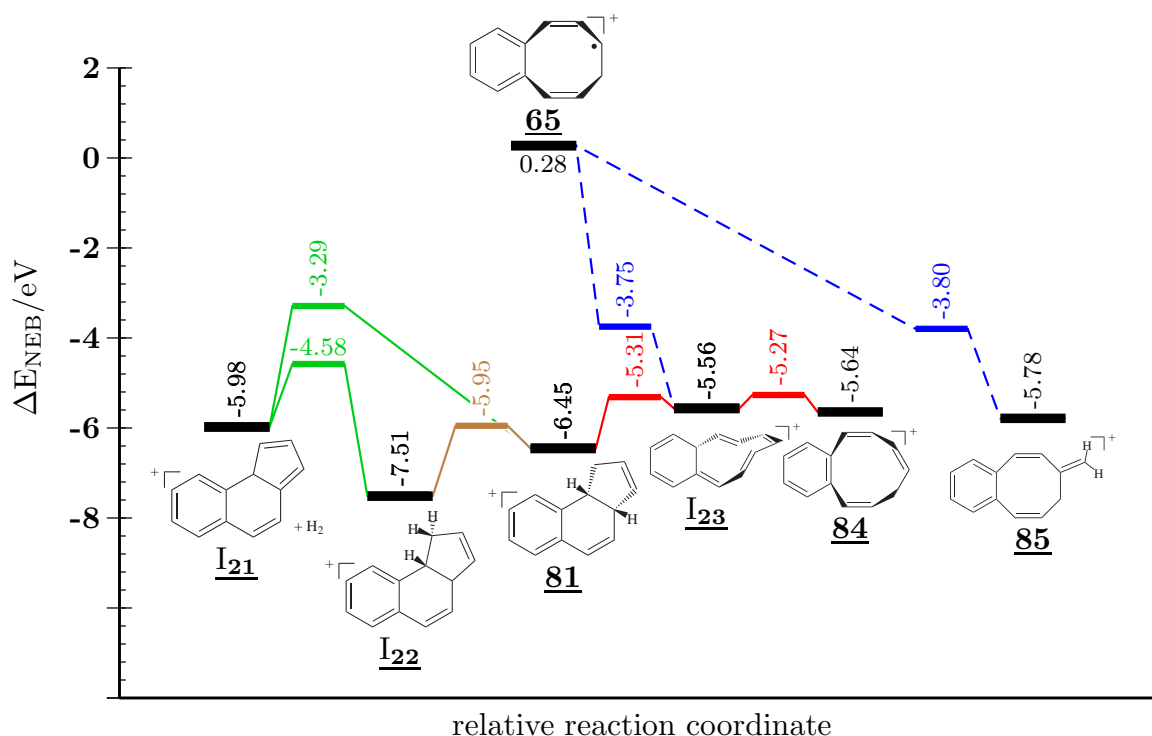


Figure 6.15: Stationary points of $C_{12}H_{10}^+-CH$ addition reaction paths, of $C_{13}H_{11}^+$ isomerisation paths between conformers, and H_2 elimination path obtained at Bdz1 level of theory. Underlined labels represent molecules and intermediates I_{xx} as defined in the text.

6.4.4.3 Hydrogen transfer by CH

The MD based phenomenon of the hydrogen transfer by CH was investigated by the reaction path analysis.

Based on these results, the hydrogen transfer depends on the structural configuration of the hydrocarbon reactant and the attack orientation of CH. In the case of **83**, both hydrogens are placed at adjacent sp^3 -hybridised tertiary carbon atoms. Both hydrogens are considerably weakly bonded (compare barrier heights of thermal dissociation). Under these circumstances the attack of CH from a nearly frontal position (collision angle above 45° relative to the molecular plane) leads to barrierless and exothermic hydrogen transfer. Further investigations suggest that the described attack position of CH and the structural configuration of **83** allows also the barrierfree and exothermic transfer of H_2 which leads to $CH_3 + C_{13}H_9^+$.

6.5 Summary and discussion

In the present chapter, the properties of ion-molecule reactions between CH and bicyclic / tricyclic $C_xH_{x-2}^+$ with $x=10-13$ are presented. The results show that the CH insertion at ring units leads to their growth and expansion. Moreover, the extreme high reactivity of CH allows the extension of aromatic ring units. By expansion to ring sizes $n > 7$, a monocyclic moiety becomes energetically less stable than its corresponding bicyclic structure. The isomerisation can be described as a constriction of a monocyclic moiety into a bicyclic moiety based on an electrocyclic ring closure mechanism. In terms of the four-fold CH addition at naphthalene, it shows that this mechanism leads to dihydrogenated phenanthracene which is another PAH structure. The possible dehydrogenation path takes place by thermal H_2 elimination or by hydrogen transfer to a suitable collision partner. Both are achieved by the CH based reactions. In particular, CH based reactions provide high impact of non-fixed energy which is above the energetic barrier of the H_2 elimination and therefore results in a high H_2 elimination probability. Moreover, CH can act as a hydrogen acceptor, i. e., “stripping” hydrogen atoms from weak C-H bonds such as those at adjacent ternary sp^3 -hybridised carbon positions.

6.5.1 DFTB based MD simulations

Based on the obtained product distributions, CH addition to bicyclic and tricyclic hydrocarbons is characterised by a large diversity of products ranging from ring-size extension, over methyno-bridging and methyldene sidegroups to increased numbers of rings.

Comparison of k_{MD} with k_L and $k_{ADO}(T)$

The k_L values of the reaction systems $C_xH_{x-2}^+ + CH$ ($x=10-13$) are equal to $1 \times 10^{-9} \text{ cm}^3 \text{ s}^{-1}$, which are similar to those obtained in the case of $C_xH_x^+ + CH$ with $x=2-6$. This is due to the fact that the reduced mass of the system μ is almost unchanged. Considering the approximation of the hydrocarbons formula by $(CH)_n$, the reduced mass μ in the reaction with methyne becomes:

$$\tilde{\mu} = \frac{n}{n+1} \times M_{CH} \quad (6.1)$$

where M_{CH} is the molarity of CH. As a result, the k_L values, which are based on $\tilde{\mu}$, are reduced by less than 4.8% for $(CH)_n$ systems from $n = 5$ to $n = 13$. A similar correlation was found for $k_{ADO}(T)$ since these values also depend on the reduced mass (compare Eq. (2.12)). In agreement with the results in Chapter 4, the ratio of $k_{ADO}(T)$ to k_L reaches a factor of 10 at 20 K, but is reduced down to 1.5 at 1000 K. In contrast, $k_{MD}(\varepsilon)$ values increase with the molarity of the hydrocarbon reactant beyond Eq. (6.1). In the interval between 0.025 eV and 0.10 eV, $k_{MD}(\varepsilon)$ values of the system $C_{10}H_8^+, C_{11}H_9^+ + CH$ reach about $1 \times 10^{-9} \text{ cm}^3 \text{ s}^{-1}$, which is a factor of 1.5 larger than the values obtained from $C_6H_6^+ + CH$ (Section 4.5.1). Based on MD results, the reactivity of CH remains almost unchanged for each hydrocarbon reactant. This result indicates that the k_L and $k_{ADO}(T)$ values are erroneous. An explanation for this wrong behaviour can be related with the point-shaped approximation of particles. The

results show that for larger reaction systems as the ones described in this chapter, molecular dimensions can not be ignored.

$k_{MD}(\varepsilon)$ and $k_{MD}(T)$ comparison and correction of $k_{MD}(T)$ values

Based on the results of the systems $C_{10}H_8^+ + CH$ and $C_{11}H_9^+ + CH$, $k_{MD}(\varepsilon)$ and $k_{MD}(T)$ values are found to be in qualitative agreement in the temperature range between 200 K (0.025 eV) and 800 K (0.1 eV). The shape of the $k_{MD}(\varepsilon)$ and $k_{MD}(T)$ graphs reproduces the description in Section 4.6.

The extrapolation of the permanent dipole-ion interactions for $k_{MD}(T)$, which is based on the relation Eq. (4.1), leads to values between $6 \times 10^{-9} \text{ cm}^3 \text{ s}^{-1}$ at 50 K (which is 10 times the original $k_{MD}(T)$) and $1.8 \times 10^{-9} \text{ cm}^3 \text{ s}^{-1}$ at 600 K (1.8 times $k_{MD}(T)$).

6.5.2 Reaction energies

The obtained reaction energies which correspond to CH addition at C_xH_{x-2} leading to energetically stable $C_{x+1}H_{x-1}$ products ranges between 3 to 7 eV; it depends on the level of theory and reaction system. These values are slightly lower than the reaction energies of the related reaction between monocyclic hydrocarbons and methyne. Based on the thermodynamic quantities $\Delta_R H_{0K,i}$, a qualitative agreement between the SD, DFT and *ab initio* methods was obtained. The most considerable agreement was found for reaction energies of the CH addition products. DFTB based reaction energies of fragmentations are underestimated compared to DFT and *ab initio* methods, while energies of stable CH complexes (**R-CH** class) are overestimated.

Thermodynamical stability

The thermodynamic stability of products resulting from ring expansion decreases relative to corresponding tricyclic structures in agreement with the results of Chapter 5. The transition takes place at ring sizes of 8 carbon atoms. The increase of ring numbers during the CH based ring growth is, therefore, thermodynamically driven.

IR chemiluminescence

The energetic impact due to CH addition suggests IR chemiluminescence, which may coincide with proposed photoluminescence of interstellar PAHs (Section 4.6). The spontaneous emission of radiation of the products energised by the non-fixed energy (reaction energy) are equal to values of $2 \times 10^1 - 2 \times 10^2 \text{ s}^{-1}$. In comparison to previous, smaller reaction systems, these rates are reduced since the level of energetic impact remains almost constant. This is the consequence of increasing degrees of freedom. Since the most of the rearrangement rate coefficients constitute values above the radiative process, the isomerisation equilibrium can be achieved before deactivation.

6.5.3 Generalisation of ring growth for unsaturated hydrocarbons

Minimum energy paths were obtained by the application of the NEB method and structural reoptimisation of transition states at Bdz1 level. Isomerisation barriers of ring closure and opening, hydrogen shifts, and H_2 elimination are comparable to the results obtained from reactions of methyne with monocyclic hydrocarbons. Although ratios of non-fixed energy

to barrier heights remain nearly the same compared to monocyclic reaction systems, the resulting rate coefficients are smaller due to the increased molarity. Based on the obtained results of Chapter 5 and the present chapter, a generalised mechanism for the growth and formation of ring structures and fragmentation was derived (Figure 6.16).

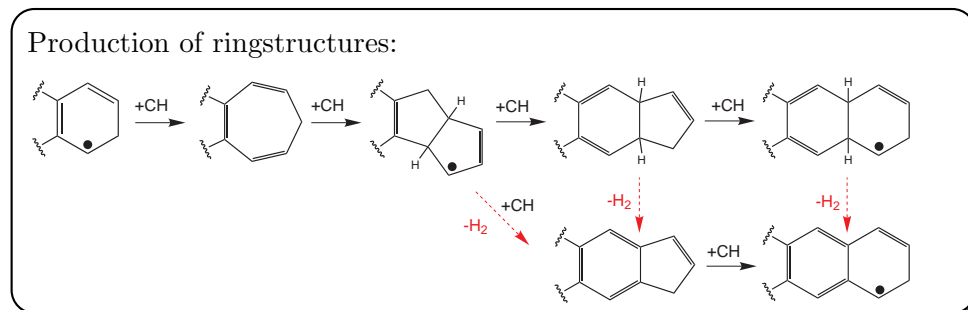


Figure 6.16: Schematic CH based ring growth of hydrocarbons.

This mechanism proposes that multiple insertion reactions of CH at a 6-membered ring of a hydrocarbon or PAH molecule results in fused penta- and hexagonal rings. Their formation is the result of an electrocyclic process inside of enlarged ring moieties but also the result from a dynamic process where CH bridges the ring. The resulting intermediate isomerises under carbon bond rearrangement. The removal of hydrogen by thermal elimination or hydrogen transfer would reestablish an aromatic structure.

7 Ion-molecule reactions between methyne and PAH ions, $C_xH_{x/2}^+$ ($x=20, 24$)

The results of ion-molecule reactions between CH and polycyclic aromatic hydrocarbon ions $C_xH_{x/2}^+$ ($x=20, 24$) are presented in this chapter. The objective is to analyse the aspects of the CH addition as well as CH insertion between ternary sp^2 -hybridised carbon positions within the polycyclic framework. It will include the study of differences between pentagonal and hexagonal moieties assembled by ternary and secondary sp^2 -hybridised carbons. Therefore, two $C_{20}H_{10}^+$ isomers and one $C_{24}H_{12}^+$ isomer with different constitutions of hexagonal and pentagonal moieties were selected (Figure 7.1).

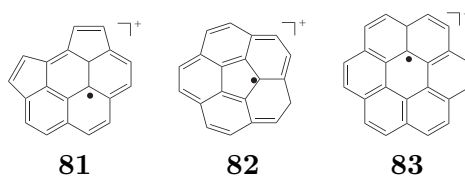


Figure 7.1: Schematic structures of two $C_{20}H_{10}^+$ and one $C_{24}H_{12}^+$ reactants.

The $C_{20}H_{10}^+$ structure **81** (dicyclopentapyreniumyl ion) is planar consisting of two peripheral pentagons and 4 hexagonal rings, while **82** (corannulene cation) possesses a non-planar, convex-like structure due to the constitution of 5 pericondensed hexagonal rings centred by a pentagonal ring. In contrast, the selected $C_{24}H_{12}^+$ hydrocarbon, **83** (coronene cation), consists only of pericondensed hexagonal rings which constitute a planar structure.

The selection of these three reactants is also motivated by reports that coronene and corannulene are considered to be interstellar abundant molecules [4, 186, 187]. They are also considered to be precursors and constituents of (hydrogenated) amorphous carbon [188]. Moreover, it is assumed that the non-planar corannulene is an intermediate structure in the formation of fullerenes [189].

7.1 $C_{20}H_{10}^+ + CH$

This section describes the results of the studied reactions between methyne and **81** as well as **82**. In particular, the different behaviour of the CH attack at the pentagonal and hexagonal ternary sp^2 -hybridised carbon positions was analysed.

7.1.1 DFTB based MD simulations

7.1.1.1 Identified product channels

Since the objective is to analyse the routes of ring extension by CH insertion, the variety of products resulting from the MD simulations is divided according ring size and their amounts. In the case of the reactant **81** the channels are defined as follows:

- 1.) **cy-7**: Products that contain one heptagonal ring. Corresponding structures are **93**, **94**, and **95**;
- 2.) **cy-6**: Products that consist of one pentagonal ring and 5 hexagonal rings, e. g., structure **92**.

In contrast, for the reactant **82** the channels are defined as follows:

- 1.) **cy-7**: Products that contain one heptagonal ring and one pentagonal ring. Corresponding structures are **101** and **102**.
- 2.) **cy-6**: Products that contain no pentagonal ring, e.g structure **103**.

The residual channels are addressed to structures that are categorised as defined for previous reactions: **R-CH**, **R-CH₂** and **cmplx**. The structural details are given in Tables 7.1 and 7.2.

Connection between channels

The MD simulation showed that structures of the **R-CH** channel are subjected to isomerisation resulting in products of channel **cy-7**, **cy-6** and **R-CH₂**, whereas **R-CH** results from the initial encounter complex.

7.1.1.2 Calculated product distribution

The cross sections of each reaction system, each product channel and each collision energy were calculated based on all collected trajectory snapshots that passed the collision point by 6 ps.

*Product cross sections resulting from **81** + methyne:*

The total cross section at 0.005 eV is divided into **cy-7** with 10%, **cy-6** with 36%, **R-CH** with 49%, and **cmplx** with 4%. The cross section ratio of residual product channels such as **R-CH₂** is below 1%. The increase of the collision energy changes the distribution of products slightly in favour of **cy-7** and **cy-6** whereas the ratio between **cy-7** and **cy-6** remains nearly constant. The MD simulations show that at collision energies above 0.075 eV the depletion rate of **R-CH** is slightly increased. This indicates that ϵ_{coll} contributes slightly to the available non-fixed energy. The increase of ϵ_{coll} causes, therefore, an increase of the isomerisation rates.

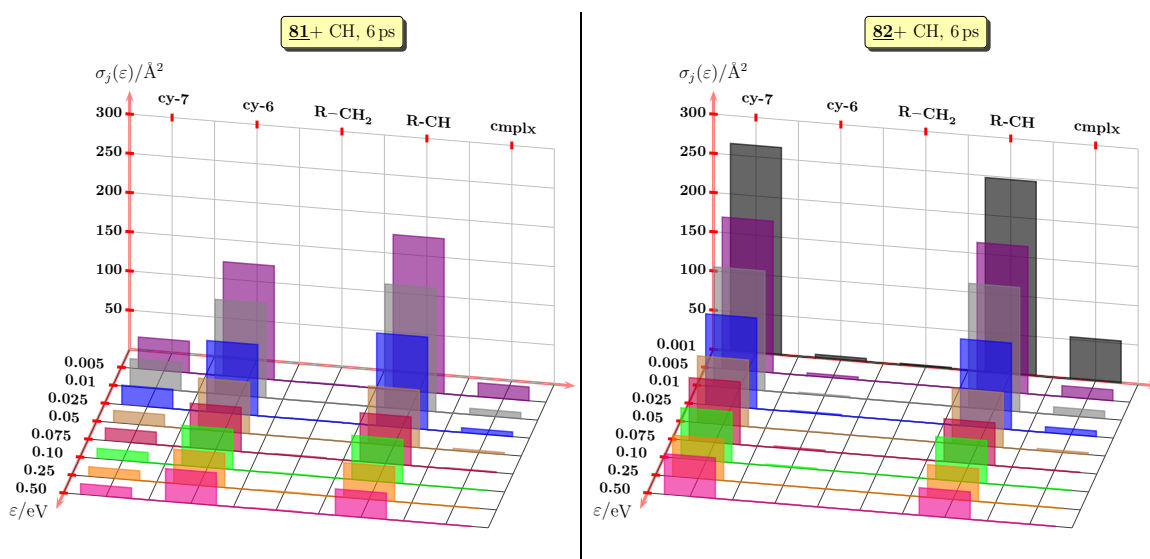


Figure 7.2: Calculated product cross sections $\sigma_{R,j}$ resulting from the reaction between **81** and methyne (left) and **82** and methyne. Both plots correspond to $t_{\text{postcoll}} = 6$ ps applied to different collision energies. Abbreviations of given channels are defined in Section 7.1.1.

*Product cross sections resulting from of **82** + methyne:*

Cross sections at 0.005 eV are divided into **cy-7** (48%), **R-CH** (47%), and **cmplx** (4%). The cross section ratio of **cy-6** yields about 1%, whereas the fraction of **R-CH₂** remains below 1%.

Comparison

The cross sections of the **R-CH** and **cmplx** channel of each reaction systems are nearly identical in the applied collision energy range. The disappearance of orbiting complexes at high collision energies is in agreement with previously described methyne addition reactions (Chapter 6). It confirms that higher collision energies reduce the lifetime of the orbiting complex. The nearly equal amounts of **R-CH** indicate that formation and depletion of **R-CH** in both reaction system is nearly equal.

Migration of attached CH

The structural analysis of individual trajectories showed that the CH sidegroup attached to ternary carbons tend to migrate to the periphery rather than be invoked into the local structure e. g., formation of methyno bridges. At the peripheral positions, CH sidegroups (**R-CH**) are then depleted by being invoked in the carbon frame. Based on the MD simulations, the attachment of CH directly at peripheral carbon positions lead to fast insertion in the carbon frame of the PAH structure.

7.1.1.3 Calculated capture rate coefficients

The rate coefficients corresponding to the reactive addition process are plotted in Figure 7.3. All $k_{\text{MD}}(\epsilon)$ values of each reaction system are larger than the k_{L} value which is $0.99 \times 10^{-9} \text{ cm}^3 \text{ s}^{-1}$. Above 800 K (0.10 eV), $k_{\text{MD}}(\epsilon)$ values also exceed the $k_{\text{ADO}}(T)$ values. However, $k_{\text{MD}}(\epsilon)$ values of both reaction systems decrease from $1.9 \times 10^{-9} \text{ cm}^3 \text{ s}^{-1}$ at 0.25 eV

(≈ 1900 K) to $1.1 \times 10^{-9} \text{ cm}^3 \text{ s}^{-1}$ at 0.005 eV (≈ 75 K) which represents a slope opposite to the ADO values.

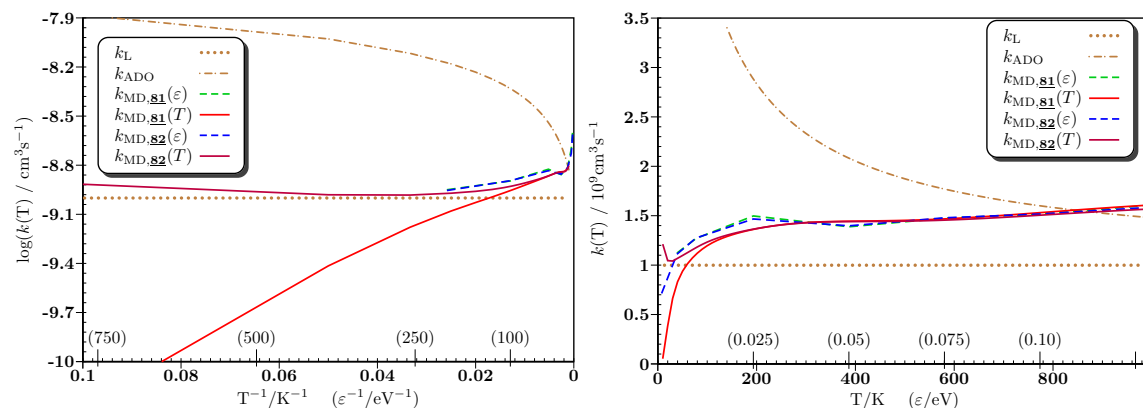


Figure 7.3: Calculated capture rate coefficients of the reactions between **81** + CH and **82** + CH based on the *Langevin* model (k_L), ADO model (k_{ADO}), and MD simulations ($k_{MD}(\varepsilon)$ and $k_{MD}(T)$). Two different representations are given: left) logarithmic k versus inverse T (ε_{coll}) and right) k versus T (ε_{coll}).

$k_{MD}(T)$ slopes

Deficiencies between $k_{MD}(T)$ and $k_{MD}(\varepsilon)$ at low temperatures and energies are suggested to be caused by the numerical integration required for $k_{MD}(T)$ (Section 4.3.1.3). Therefore, the reliability of the $k_{MD}(T)$ is questionable at low temperatures.

7.1.2 Product energetics

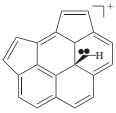
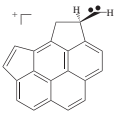
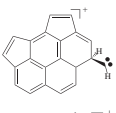
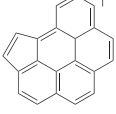
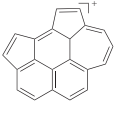
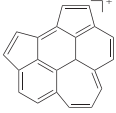
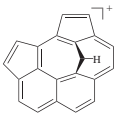
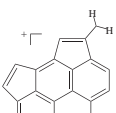
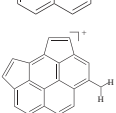
7.1.2.1 **81** + methyne

Based on the results given in Table 7.1, the highest amount of reaction energy is released by the formation of **92**. Therefore, **92** possesses also the highest energetic stability among the given set of structures. Its formation is the result of CH insertion at one of the pentagons in **81**, which results in the ring expansion of the pentagon. CH insertion at one hexagon adjacent to one pentagon results in structure **93** which is the second most stable, among the given isomers. CH insertion at the hexagon, which is not adjacent to any pentagon, results in **94**. Its stability relative to **92** is $+1.1 \text{ eV}$ (at B3LYP level of theory). The structure **96** (i.e., it has a sidegroup CH_2 at one of the pentagons) possesses a similar stability. The formation of the residual structures **89**, **90**, and **91** is also exothermic. However, the amount of reaction enthalpy yields only $1\text{--}2 \text{ eV}$, which is $5\text{--}6 \text{ eV}$ less than **92** yields. The formation of the methyno-bridged structure **95** releases about 2.5 eV . The corresponding electronic level lies 4.6 eV above **92**.

Comparison between SD and Btz1//Bdz1

A constant shift in the values is the results of the missing zero-point energy (ZPE) correction in the DFTB calculations. Reaction energies at the B3LYP level without ZPE correction are given in Figure 7.5. In this case, the comparison between DFTB and B3LYP reveals a small deviation of $0.1\text{--}0.2 \text{ eV}$. Considering Btz1//Bdz1 level of theory as the reference point,

Table 7.1: Ion-molecule based reaction energies and enthalpies corresponding to the reference level **81** + CH obtained by different quantum theory methods.

products	abbr.	geometry	class	$\Delta_R E/eV$ SD	$\Delta_R H_{0K}/eV$ Btz1//Bdz1
$\mathcal{A}a-C_{21}H_{11}^+$	89		R-CH	-2.7304	-1.1862
$\mathcal{A}b-C_{21}H_{11}^+$	90		R-CH	-3.7869	-2.2782
$\mathcal{A}c-C_{21}H_{11}^+$	91		R-CH	-3.2989	-1.7293
$\mathcal{B}a-C_{21}H_{11}^+$	92		cy-6	-8.2921	-7.1143
$\mathcal{C}a-C_{21}H_{11}^+$	93		cy-7	-7.3081	-6.2229
$\mathcal{C}b-C_{21}H_{11}^+$	94		cy-7	-7.0887	-6.0757
$\mathcal{D}a-C_{21}H_{11}^+$	95		cy-7	-3.8820	-2.4560
$\mathcal{E}a-C_{21}H_{11}^+$	96		R-CH₂	-6.9984	-5.9920
$\mathcal{E}b-C_{21}H_{11}^+$	97		R-CH₂	-6.6632	-5.5981

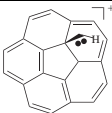
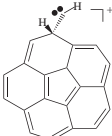
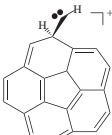
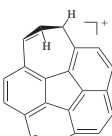
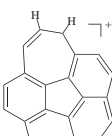
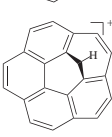
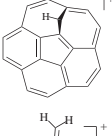
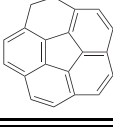
SD overestimates the stability of **R-CH** products by 0.4–0.5 eV. The small deviations point out the good accuracy of DFTB applied to large systems.

7.1.2.2 **82** + methyne

The reaction energies related with the stationary points of each product channel (Figure 7.2) are summarised in Table 7.2.

The highest amount of reaction energy is released by the formation of **102** (7.2 eV at Btz1//Bdz1 level of theory). The structural analysis of the MD simulation reveals that besides of **102** another isomer exists, namely **101**, which has two adjacent hydrogens in the heptagonal ring being in *trans* position. The results show that **101** is energetically less stable than **102**; the energetic difference is equal to 2.37 eV. The formation of the methyno-bridged

Table 7.2: Ion-molecule based reaction energies and enthalpies corresponding to the reference level **82** + CH obtained by different quantum theory methods.

products	abbr.	geometry	class	$\Delta_R E/eV$ SD	$\Delta_R H_{0K}/eV$ Btz1//Bdz1
$\mathcal{A}d-C_{21}H_{11}^+$	98		R-CH	-3.8763	-2.2612
$\mathcal{A}e-C_{21}H_{11}^+$	99		R-CH	-3.8343	-2.2315
$\mathcal{A}f-C_{21}H_{11}^+$	100		R-CH	-3.6896	-2.0509
$\mathcal{C}c-C_{21}H_{11}^+$	101		cy-7	-6.1003	-4.8672
$\mathcal{C}d-C_{21}H_{11}^+$	102		cy-7	-8.2867	-7.2392
$\mathcal{D}b-C_{21}H_{11}^+$	103		cy-6	-5.5686	-4.0488
$\mathcal{D}c-C_{21}H_{11}^+$	104		cy-7	-4.7901	-3.4190
$\mathcal{E}c-C_{21}H_{11}^+$	105		R-CH₂	-7.0570	-5.9621

molecules, **103** and **104** yields 3.4–4.0 eV. Both electronic levels lie 3.2–3.8 eV above the one of **102**. The energetic stability of **103** is increased in comparison with the methyno-bridged molecule **95** of the other reaction system. This also increases its lifetime. The products of the **R-CH**, **98**, **99**, and **100**, yield a reaction enthalpy of 2 eV which is, however, 5 eV less than the formation of **102** produces. It suggest a very low lifetime in terms of thermodynamics. The relatively low stability of **R-CH** is in agreement with the **R-CH** structures of the reaction system **81** + CH.

7.1.2.3 Canonical population distribution

81 + methyne

According to Figure 7.4, the thermodynamic distribution is dominated by 92 for the entire given temperature range. However, the ratio of 92 reduces with increasing temperature. This indicates that structures containing heptagonal ring have at high temperatures a lower stability than **R-CH₂** structures.

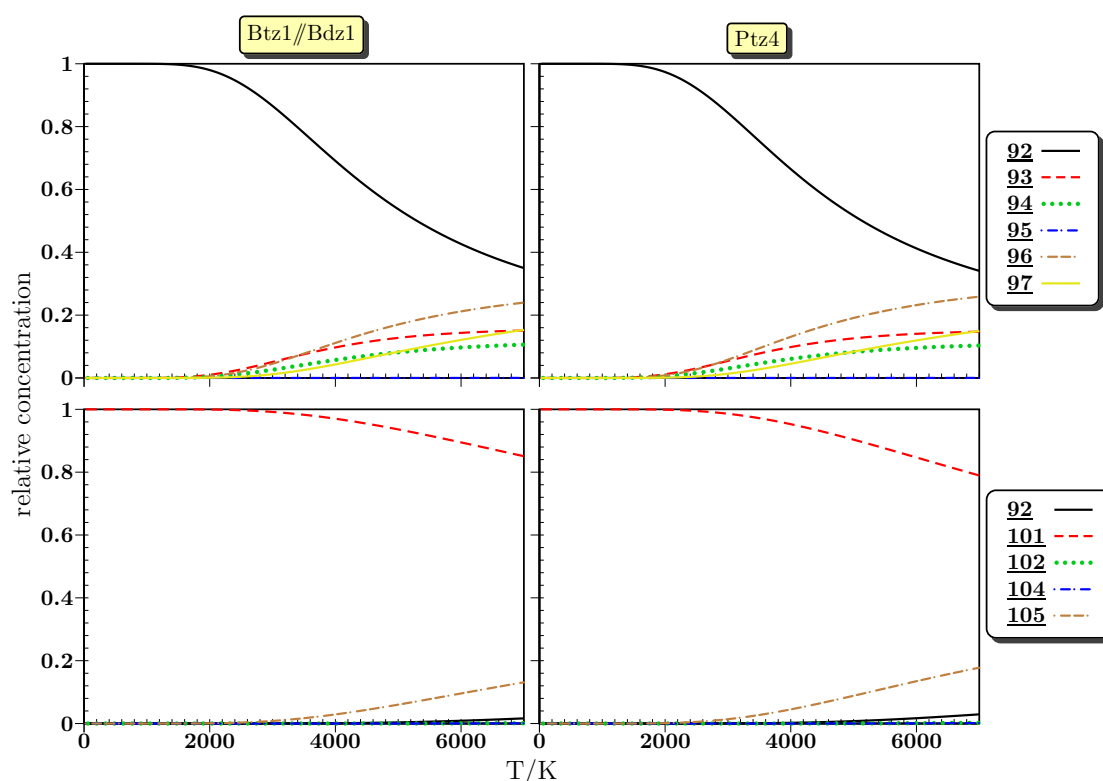


Figure 7.4: Canonical population analysis of $C_{20}H_{10}^+$ product isomers taken from Table 7.1 (top) and Table 7.2 (bottom) obtained at Btz1//Bdz1 (left) and Ptz4 (middle) level of theory.

82 + methyne

The thermodynamic distribution is dominated by 102 at all temperatures. The structures 103 and 104, which result from CH insertion at the centred pentagonal ring, do not contribute to the distribution at high temperatures. It indicates that this type of CH insertion is thermodynamically unfavoured at higher temperatures.

7.1.3 Reaction path analysis

Based on the reaction path analysis of the MD trajectories, the scheme of the stationary points including transition states for CH addition at 81 is plotted in Figure 7.5. The corresponding scheme of CH addition at 82 is shown in Figure 7.6.

7.1.3.1 81 + methyne

The formation and attachment of CH at any carbon atom of 81 is barrierfree. However, the structures 89, 90, and 91, which represent the initial step in the reactive collision, are

hardly stable due to low isomerisation barriers (Figure 7.5).

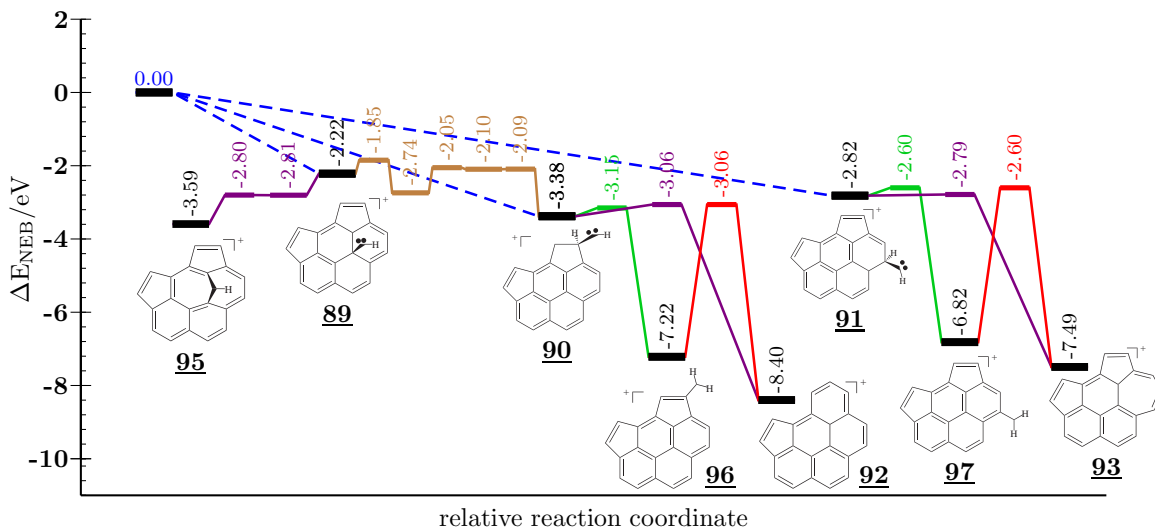


Figure 7.5: Stationary points of the reaction between **81** and CH obtained by Bdz1: addition, isomerisations between $R-CH_2$ and ring-extended groups, ring extension, $R-CH_2$ formation and CH migration. Structures are defined in Table 7.1.

For instance, structure **89** has at least two isomerisation pathways: 1st) the insertion of CH forming **95**, and 2nd) the shift of CH to a different carbon atom. Although the reaction path analysis prefers the insertion due to the lower barrier, the MD simulations indicate a preference for the shift process.

CH migration

The migration of the CH by several carbon shifts does not exceed barrier heights of 0.7 eV. Depending on the migration path either structure **90** or **91** is formed (the path to **91** is not shown in Figure 7.5). Both structures are of higher energetic stability than **89**.

Depletion of peripheral attached CH groups

The isomerisation barriers to other, more stable structures are less than 0.3 eV high which indicates a low lifetime of **90** and **91**. In the case of **90**, the isomerisation barrier to **96** is below the isomerisation barrier to **92**. In the case of **91**, the barrier to **93** is below the one to **97**. However, the MD simulations show neither the formation of **96** nor of **97**.

Thermal isomerisation between $R-CH_2$ and ring-extended products

The energetic level and structure of the transition states between $R-CH_2$ and ring-extended products are identically with those transition states between $R-CH_2$ and $R-CH$. The barrier of 4–5 eV effectively impedes the isomerisation processes. The barrier is so high, that it is in competition with the hydrogen loss mechanism which constitutes a barrier of about 4.5 eV.

7.1.3.2 **82** + methyne

In agreement to reaction system **81** + CH, the formation and attachment of CH at any carbon atom of **82** is barrierfree (Figure 7.6). Moreover, the structures, **98**, **99** and **100**, have ring

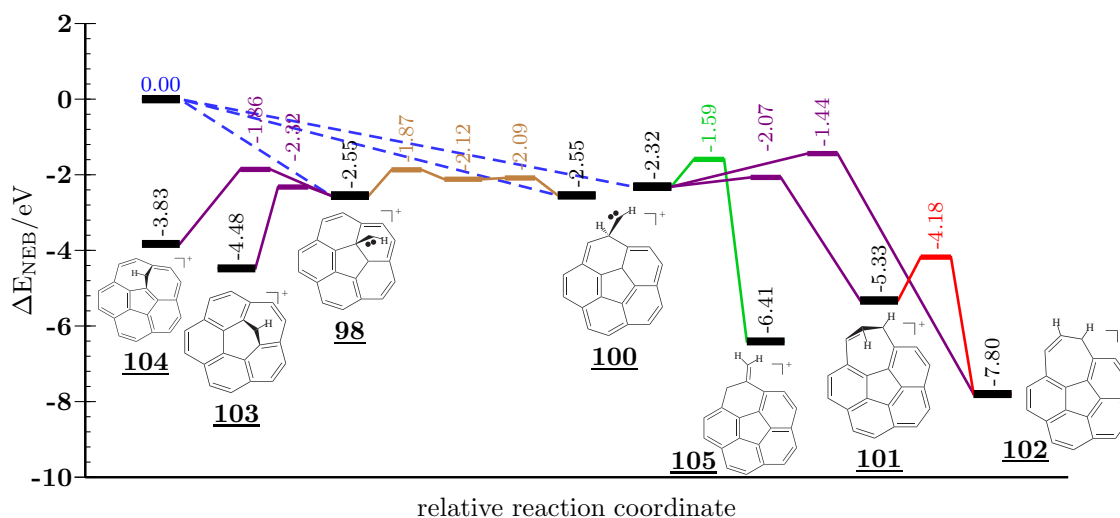


Figure 7.6: Stationary points of the reaction between **82** and CH obtained by Bdz1: addition, isomerisations between $R-CH_2$ and ring-extended groups, ring extension, $R-CH_2$ formation and CH migration. Structures are defined in Table 7.2.

insertion barrier heights similar to **90** and **91**. However, the barriers for the formation of methylene sidegroups (structure **105**) and the migration of CH (from one ternary carbon to another one) are increased.

CH migration

The curvature of **82** provides a more stable attachment of CH at the pentagon since the formation of sp^3 -hybridised carbons is sterically less impeded. As a result, the migration of the CH group to the periphery is hindered; the barrier height is 0.7 eV. The CH insertion at the pentagon exhibits a barrier of only 0.3 eV which competes with the migration process; it makes the migration less effective relative to the planar PAHs structures. Note that the attachment of CH group at the pentagon from the concave was found to be impossible. Such structural optimisation resulted finally in a CH attachment at a peripheral carbon atom.

Depletion of peripheral attached CH groups

The isomerisation barriers of peripheral attached CH groups are plotted in Figure 7.6. Due to the curvature of **92**, two different types of attachment are possible: the CH group at the concave (**100**) or at the convex side (**99**). The insertion of CH into the hexagon from the concave side requires only 0.25 eV resulting into structure **101** in which two adjacent hydrogens are in *trans* position. The *cis-trans* isomerisation to **102** constitutes a barrier of about 1.2 eV. The direct formation of **102** out of **100** shows a barrier of 0.9 eV. The formation barrier of **102** from the convex side (**99**) is lowered to 0.3 eV.

7.2 $C_{24}H_{12}^+ + CH$

The results of the reaction between methyne and **83** (coronene) are presented in this section. In summary, the CH insertion is slightly sterically hindered at non-peripheral, ternary carbon

positions. An insertion at such positions was also found to be energetically unfavoured relative to peripheral positions. A migration of attached CH to peripheral positions is likely which resembles the CH addition at [81](#) and [82](#) of Section 7.1.

7.2.1 DFTB based MD simulations

7.2.1.1 Product channels

Four channels were predefined: products containing one 7-membered rings (**cy-7**), products containing one methyldene group (**R-CH₂**), and CH-hydrocarbon complexes (**R-CH** and **cmplx**). Based on the MD simulations, channel **cy-7** was refined as follows:

- 1.) **cy-7a**: product channels containing one 7-membered ring at the periphery, and
- 2.) **cy-7b**: product channels containing one 7-membered ring at the structural centre (non-peripheral),

in order to understand better where ring insertion take place.

7.2.1.2 Calculated product distribution

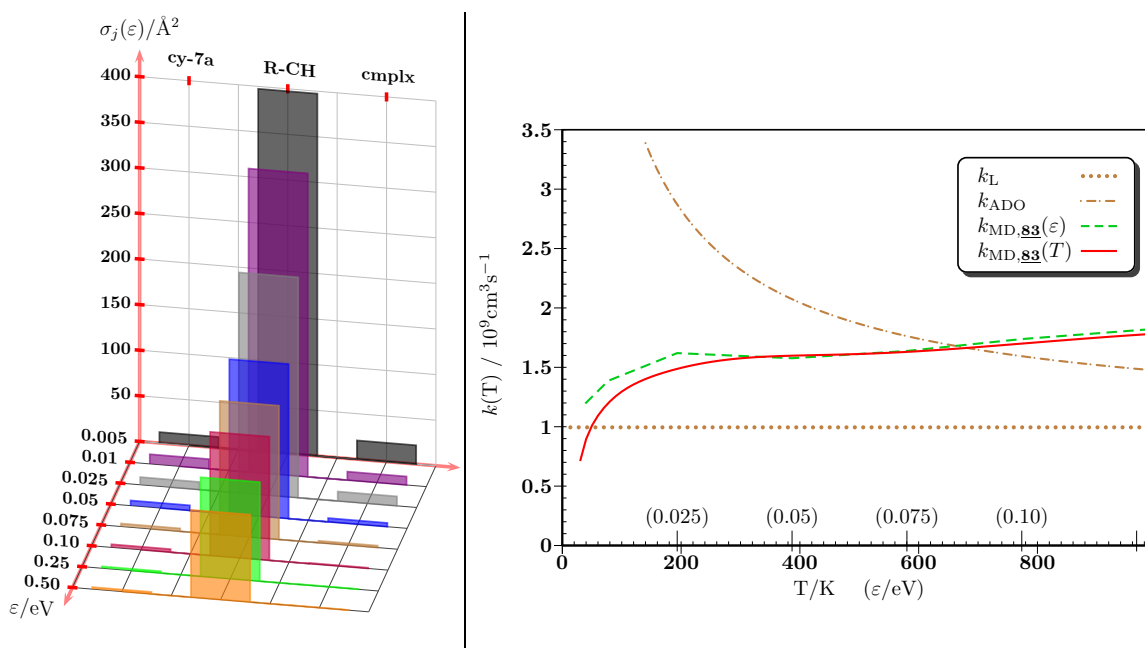


Figure 7.7: Calculated product cross sections $\sigma_{R,j}$ (left) and capture rate coefficients (right) resulting from the reaction between [83](#) and methyne. The product cross section plot corresponds to $t_{\text{postcoll}} = 6$ ps applied to different collision energies. Abbreviations of given channels are defined in Section 7.2.1.

The distribution after 6 ps as given in Figure 7.2 is dominated by **R-CH**, which represents 92 – 98% of all reactive trajectories. While the amount of products containing one non-peripheral 7-membered ring (**cy-7b**) is zero, the amount of products of one peripheral 7-membered ring is at 2–3%. The residual amount of reactive trajectories with a maximum of 4% was assigned to the **cmplx** channel.

The amount of **R-CH** exceeds all calculated **R-CH** amounts of previous CH based reaction systems. Since CH is a highly reactive molecule, it demonstrates that coronene exhibits the highest steric hindrance concerning the ring extensions at ternary carbon position within the polyhexagonal carbon frame.

A migration of CH was obtained by the MD simulations, but the migration rates are below the ones of the reaction **81** + CH. Since the **R-CH** formation energies of these both systems are similar, the lowered migration rates are related with the reduced available of energy per degrees of freedom.

7.2.1.3 Calculated capture rate coefficients

The capture rate coefficients are calculated based on Eqs. (2.15) and (2.16). For comparison, k_L and $k_{ADO}(T)$ were calculated. Required dipole moments and polarisabilities (Table A.1) are taken from the DFT calculations.

The capture rate coefficient (k_L) value is $0.995 \times 10^{-9} \text{ cm}^3 \text{ s}^{-1}$. The dipole corrected values, $k_{ADO}(T)$, range from $9.329 \times 10^{-9} \text{ cm}^3 \text{ s}^{-1}$ at 20 K to $1.472 \times 10^{-9} \text{ cm}^3 \text{ s}^{-1}$ at 1000 K. The obtained $k_{MD}(\varepsilon)$ values range between 1.195×10^{-9} and $2.733 \times 10^{-9} \text{ cm}^3 \text{ s}^{-1}$ for the collision energies between 0.005 and 0.50 eV. The $k_{MD}(\varepsilon)$ values are also exceeding the $k_{ADO}(T)$ values for $\varepsilon_{\text{coll}} \geq 0.09$ eV. Except for $\varepsilon_{\text{coll}}$ below 0.025 eV, $k_{MD}(\varepsilon)$ are nearly constant, but reveal a slightly positive temperature slope which might be caused by the dispersion forces as discussed in Section 4.6.

7.2.2 Product energetics

The reaction enthalpies of the identified products are given in Table 7.3.

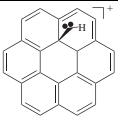
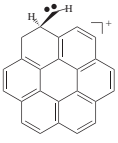
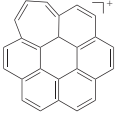
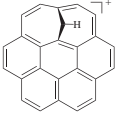
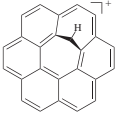
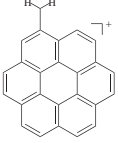
The highest amount of reaction energy is released by the formation of **111**; followed by **108**. This constellation is analogue to the results of the reaction system $C_6H_6^+ + CH$ (Table 5.1). Since reaction energies are related with the energetic stability of the molecules, the low amount of reaction energy for **109** and **110**, which are formed by ring extension at ternary carbon positions, is related with a low energetic stability. Relative to DFT level of theory, SD overestimates the energetic stabilities of the CH-attached complexes **106** and **107** as well as the energetic stabilities of **109** and **110**. In the case of MD simulations at DFT level of theory, this would cause an even lower probability for the formation of 7-membered rings at non-peripheral positions. The stability of CH-attached groups would be reduced which suggests a faster migration to the peripheral carbon positions at DFT level of theory.

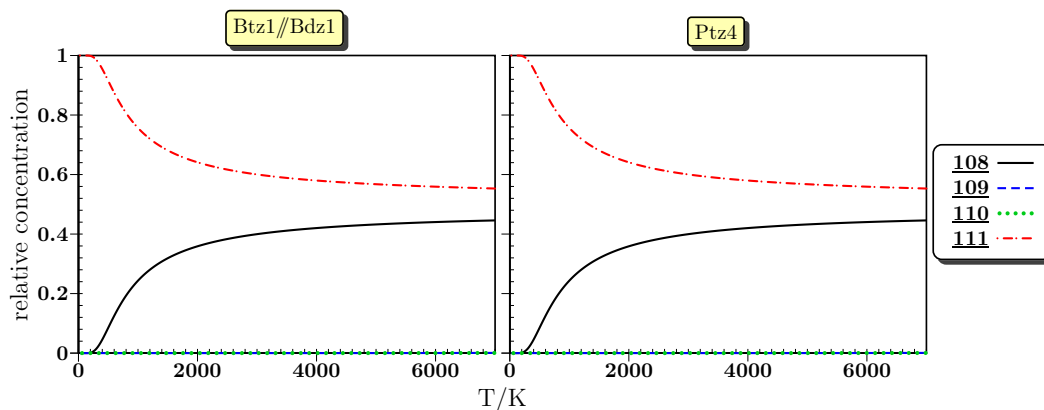
Canonical population distribution

A thermal equilibrium between products as given in Table 7.3 would be dominated by **111** (Figure 7.8). At higher temperatures (above 4000 K) the distribution of $C_{25}H_{13}^+$ products would consist of a ratio of **111** to **108** which is equal to 60 to 40%.

The formation energy causes each product at least 1000 K of internal temperature if the non-fixed energy is extrapolated by the equipartition theorem. At this estimated temperature, a comparison between the thermodynamic distribution and the MD distribution leads to no agreement, since the formation of **R-CH₂** products during the MD simulations was not observed. This indicates a non-thermodynamically driven formation mechanism of **111**.

Table 7.3: Ion-molecule based reaction energies and enthalpies corresponding to the reference level **83** + CH obtained by different quantum theory methods.

products	abbr.	geometry	class	$\Delta_R E/eV$ SD	$\Delta_R H_{0K}/eV$ Btz1//Bdz1
$Aa-C_{25}H_{13}^+$	106		R-CH	-2.6575	-1.1558
$Ab-C_{25}H_{13}^+$	107		R-CH	-3.4200	-2.0043
$c-C_{25}H_{13}^+$	108		cy-7a	-6.5213	-5.4189
$Da-C_{25}H_{13}^+$	109		cy-7b	-3.7456	-2.4041
$Db-C_{25}H_{13}^+$	110		cy-7b	-3.3870	-1.9716
$\varepsilon-C_{25}H_{13}^+$	111		R-CH₂	-6.6979	-5.5455

**Figure 7.8:** Population analysis of selected $C_{25}H_{13}^+$ ions taken from Figure 7.3.

7.2.3 Reaction path analysis

Based on the reaction path analysis of the MD trajectories, the scheme consisting of stationary points (including transition states) for CH addition at **83** is plotted in Figure 7.9. This CH addition resembles the results of Figures 7.5 and 7.6. The attachment of CH at any carbon position of **83** is barrierfree and results in the release of about 1 eV to the molecular

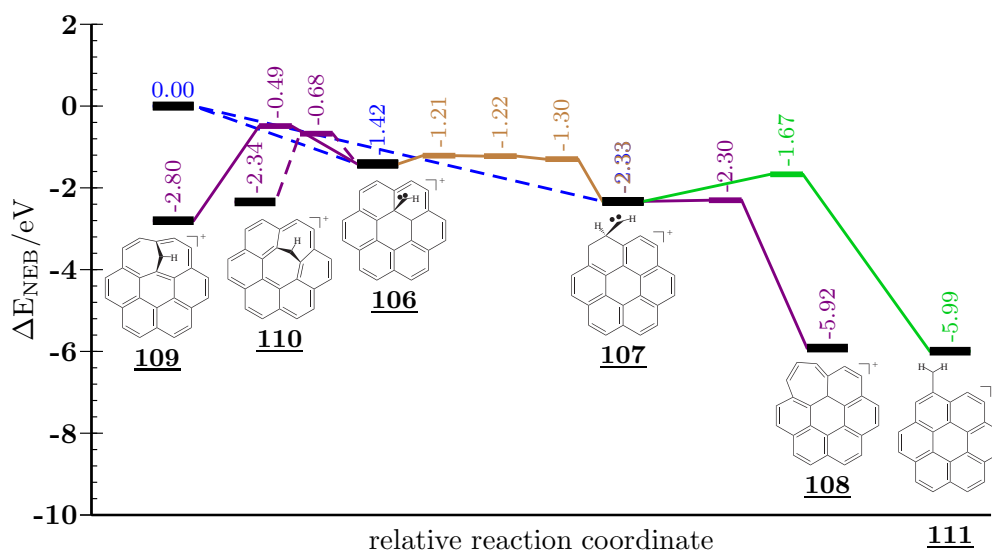


Figure 7.9: Stationary points of the reaction between **83** and CH obtained by Bdz1: addition (blue encoded), ring extension (violet), **R-CH₂** formation (green) and CH migration (brown). Structures are defined in Table 7.3.

system due to bond formation.

In the case of **106**, the insertion CH at non-peripheral position constitutes barriers between 0.7 and 1.0 eV, which is much higher than the barriers for the position change of the CH group; they are 0.1–0.2 eV high. The barrier of each migration step remains at the same energetic level, which suggests that the migration of CH to the peripheral positions is dominant. At ternary positions, any insertion in the carbon framework is dynamically impeded. At a peripheral carbon position the insertion in the carbon framework results in: 1) ring extension, or 2) the formation of a methylene sidegroup. While the barrier height of the ring extension is negligible small, the second mechanism constitutes a barrier height of 0.66 eV. The difference in the barrier height provides an explanation for the dominance of **108** over **111** as obtained by the DFTB-MD simulations. In summary, the DFTB based MD simulations can be considered as qualitative correct relative to DFT calculations. Moreover, it shows that the formation of the **R-CH₂** products is not thermodynamically driven.

7.3 Summary

In the present chapter, the properties of the ion-molecule reaction between methyne and PAH ions $C_xH_{x/2}^+$ with $x = 20$ and 24 were presented. The initial CH attachment at any positions of the PAH ion is exothermic. However, the insertion of CH at ternary carbon position of PAHs is dynamically and thermodynamically regioselective which is related with the level of the degradation of the aromaticity and the increase of the structural strain. Planar PAH structures will be bended due to the formation of sp^3 -hybridised carbon atoms. Moreover, the results show that the attached CH rather migrates than to be incorporate in the carbon framework until a peripheral carbon position is reached where the structural strain of ring extension is the lowest. These facts demonstrate that the CH incorporation is effectively restricted to peripheral positions. Therefore, the CH addition reactions at large PAHs is suitable to provide a convergent path to even larger PAH molecules. The capture rate coefficients $k_{MD}(T)$ of the reaction presented in this chapter exceed the corresponding values of the *Langevin* model and at temperatures above 800 K also the values of the ADO model. This indicates that the evaluation of the capture rate coefficients for large system sizes is limited and the point-shaped approximation of molecules by phenomenological models is insufficient.

7.3.1 Generalisation of the CH insertion at ternary positions in PAHs

Minimum energy paths were obtained by the application of the NEB method and structural reoptimisation of transition states at Bdz1 level of theory. Based on the obtained results of

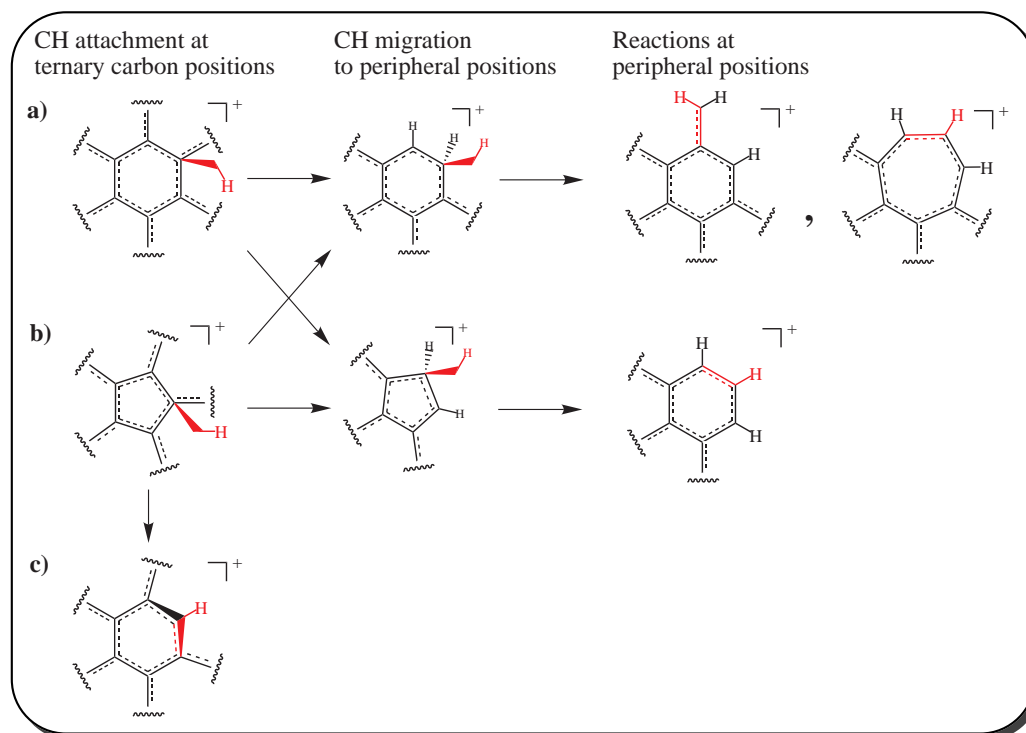


Figure 7.10: Schematic pathway of CH addition on large polycyclic hydrocarbons.

the present chapter, a generalised mechanism for CH insertion at ternary carbon positions in PAHs was derived as depicted in Figure 7.10. It suggests:

1. The CH attack at an arbitrary non-peripheral positions of a PAH ion leads to two different types of intermediates: a) CH attached at a hexagonal unit of a PAH ion, and b) at a pentagonal unit.
2. a) The migration of CH to peripheral positions since they are thermodynamically more stable and the insertion is thermodynamically unfavoured due to the bending of the system. In the case of b), the barriers for the migration and insertion, which leads to c), are similar and, therefore, both processes are competing. However, the stability of structures such as c) is below corresponding peripheral configurations.
3. Reactions at peripheral positions leading to sidegroups and ring extension which have the highest stability among the product isomers..

8 Summary and conclusions

The objective of this work was to study the formation and growth mechanisms of hydrocarbons and PAHs under the conditions of the dense interstellar medium.

Based on the chemical and physical conditions of the ISM, ion-molecule reactions were selected as the archetype for the growth mechanisms of interstellar hydrocarbons and PAHs, i. e., $C_xH_y^+ + C_mH_n$ -type reactions with $x \geq y$ were studied. A novel growth mechanism was found; it is based on the methyne molecule, which is highly abundant in the ISM and a known reactive hydrocarbon. According to the found growth scheme, 3 to 4 CH addition steps are required in order to form a new hexagonal or pentagonal moiety inside of a PAH or hydrocarbon. Starting from an aromatic structures, such moieties will contain two excess hydrogen atoms in order to remain aromatic.

The analysis of the chemical reactions was established by the combination of several models of theoretical chemistry. Molecular dynamics was used to study the dynamics of the collisional process, which includes the variation of reactant orientations, collision energies and the collision impact parameter. The calculation of atomic forces during the MD simulations was provided by the DFTB method. Based on the resulting product distributions, trajectories (i. e., reaction paths) of highest probability were selected and optimised as a 1-dimensional path by the NEB method at DFT level of theory in order to estimate and to find the minimum energy path. The selection of trajectories based on statistical weighting is an important feature of this work. Local minima and transition states of each obtained minimum energy path (or close approximation of it) were reoptimised. Based on the molecular properties, the isomerisation and radiative deactivation rates were calculated in the framework of statistical rate theories such as the RRKM theory. A qualitative comparison between the DFTB, DFT and *ab initio* methods was done; it is based on the thermodynamic quantities. Thermodynamical product distributions were compared with MD based product distributions in order to estimate the impact of the reaction dynamics.

The impact of CH as precursor for the formation of hydrocarbons and PAHs was studied through different reaction systems.

The first objective of this work was to study the growth of non-cyclic hydrocarbon ions $C_xH_x^+$ into aromatic structures $C_6H_6^+$ and $C_7H_7^+$. In the case of ion-molecule reactions between methyne and non-cyclic hydrocarbons ions $C_xH_x^+$, it was shown successfully that successive CH addition beginning with C_2H_2 leads to chain growth as well as to aromatic structures

by cyclisation. For chain lengths of 6 and 7 carbon atoms, isomerisation routes lead to thermodynamically favoured cyclic and aromatic hydrocarbons; these energy barriers are below 1 eV, which represent only a fraction of the non-fixed energy provided by the chemical activation.

All involved rate coefficients such as those of *cis-trans* isomerisation, ring closure and hydrogen shifts resulted in values that are several magnitudes above the radiative deactivation. The formation of aromatic $C_6H_6^+$ and $C_7H_7^+$ occurs, therefore, before radiative deactivation. Capture rate coefficients based on MD simulation using DFTB are between 1.5 to 3 times smaller than the calculated *Langevin* capture rate coefficients in the collision energy range 0.01–0.10 eV. In order to include ion-permanent dipole interactions, DFTB-MD based capture rate coefficients were scaled based on the comparison between calculated values of the ADO and the *Langevin* model; the scaling factor is inversely proportional to temperature and ranges between 1.5 and 10 at 50 to 1000 K.

The second objective of this work was to study the CH addition at cyclic hydrocarbon ions. Two classes of hydrocarbons were considered for the reaction with methyne: (1st) monocyclic hydrocarbon ions $C_xH_x^+$ with $x = 5-9$, and (2nd) bicyclic and tricyclic hydrocarbon ions $C_xH_{x-2}^+$ with $x = 10-13$. The results show that CH insertion at ring unit leads to ring growth. The extreme high reactivity of CH allows the extension of aromatic ring units. However, for the growth to ring sizes $n > 7$, an additional C-C bond is formed likely which divides effectively the ring into two ring units. This was observed by two processes: (1st) an electrocyclic ring closure mechanism inside the ring, and (2nd) a carbon bond rearrangement inside the ring which is bridged by CH formed during the CH attack. Energetic barriers of the ring closure decrease for ring sizes $n = 9$ and $n = 10$ to 1.1 eV and 0.6 eV; for $n = 9, 10$ these processes are also exothermic. Aromatic structures can be re-established by the removal of hydrogen – two hydrogens in the case of a CH based growth per one new ring. Such a thermal H_2 elimination was computed to have barriers down to 1.7 eV in case of a *syn*-elimination from adjacent ternary sp^3 -hybridised carbon positions in a fused hexagonal ring unit. A barrierless transfer of hydrogen is possible by the reaction with CH.

The third objective was to study the CH addition at PAH ions ($C_xH_{x/2}^+$ with $x = 20$ and 24), which included aspects of steric hindrance concerning this CH addition / insertion. The capture process is determined by rate coefficients that exceed the values of the *Langevin* model. Moreover, an insertion of CH was sterically hindered at non-peripheral and ternary carbon positions. The insertion at such positions is thermodynamically unfavoured relative to the peripheral carbon positions. On the other hand, attached CH was found to migrate to peripheral positions, where the insertion led to ring extension and methylenide sidegroups by the mechanisms similar to those found for smaller reaction systems.

The results show that methyne (CH) based growth of hydrocarbons and PAH is indeed possible in the dense ISM; it likely represents a part of the interstellar PAH chemistry. The CH based mechanism is superior to the proposed C or C^+ based mechanisms [22] since it converges to polycyclic structures rather than to chain-like molecule. Moreover, the CH based mechanism is also superior to C_2H_2 based ones, since reactivity and high chemical activation

leads to formation of hydrocarbons and PAHs even at temperatures close to 0 K. The level of chemical activation of the products was computed to be in the energetic range of UV photon impact. Such a high energy impact excites, therefore, products into a high vibrational mode, which can be only deactivated by radiation since collisional deactivation is not permitted. Based on this fact, chemiluminescence originated by CH addition reactions likely contributes to the interstellar IR emission features. Moreover, the obtained reaction parameters can be used to improve the modelling of interstellar chemistry of large hydrocarbons and PAHs. In particular, the capture rate coefficients of this work show that the commonly assumed values of 1×10^{-9} – 2×10^{-9} $\text{cm}^3 \text{s}^{-1}$ [25, 93] are underestimating ion-molecule collisions at very low temperatures if large and/or polar molecules are involved.

The approximate temperature independence of the mechanisms and product distributions up to 1000 K indicates that CH based growth mechanisms of hydrocarbons and PAHs can be also applied for high temperature hydrocarbon pyrolysis processes.

Finally, this work had established a tool for the dynamic and static analysis of chemical reactions which can be used for further studies on formation mechanisms and chemical routes involving large PAHs, especially by considering large precursors. In particular, the DFTB method applied to MD simulations of collisions proved to be efficient for finding and qualitatively predefining mechanisms for large systems. Recent developments of the DFTB method for treating nonadiabatic transitions will provide the possibility of studying electronic transitions during collision dynamics.

Appendix A Calculated molecular and reaction data

A.1 Dipole moment and polarisability of various hydrocarbons

Table A.1: Dipole moment μ_D , elements of the symmetric polarisability tensor a_{ij} , and isotropic polarisability $\langle a \rangle$ of various hydrocarbon ions obtained at Bdz1 level of theory. Non-charged species are labelled by a dagger. The spin contaminant was obtained at Btz1//Bdz1 level of theory.

species $\langle S^2 \rangle$	μ_D / Debye	polarisability / bohr ³						
		a_{11}	a_{21}	a_{22}	a_{31}	a_{32}	a_{33}	$\langle a \rangle$
<u>1</u> [†] 0.7532	1.3828	6.894	0	8.332	0	0	12.792	9.339
<u>1</u> [†] (Btz2) 0.7532	1.4571	15.489	0	13.143	0	0	16.897	15.176
CH ⁺	1.4582	6.313	0	6.313	0	0	8.506	7.044
<u>2</u> [†]	0.0000	7.864	0	7.864	0	0	27.853	14.527
C ₂ H ₂ ⁺ 0.7520	0.0000	7.181	0	7.431	0	0	23.418	12.677
<i>products of C₂H₂ + CH⁺ reaction: C₃H₃⁺</i>								
<u>3</u>	0.4292	10.344	0	14.798	0	0	50.020	25.054
<u>4</u>	0.0000	25.624	0	25.624	0	0	10.917	20.722
<i>products of C₃H₃⁺ + CH reaction: C₄H₄⁺</i>								
<u>7</u> 0.7658	0.0000	14.590	0	21.877	0	0	93.306	43.258
<u>8</u> 0.7676	0.4580	29.809	-10.513	75.236	0	0	13.903	39.649
<u>9</u> 0.7541	0.5908	14.350	0	33.677	0	0	49.605	32.544
<u>10</u> 0.7519	0.0000	41.115	0	39.021	0	0	14.470	31.535
C ₄ H ₂ ⁺ 0.7670	0.0000	12.636	0	12.607	0	0	83.809	36.351
<i>products of C₄H₄⁺ + CH reaction: C₅H₅⁺</i>								
<u>13</u>	0.5690	89.586	-1.125	47.083	0	0	17.092	51.254
<u>14</u>	0.7419	118.238	-0.548	33.768	0	0	17.191	56.399
<u>15</u>	0.7840	124.436	-0.677	35.926	0	0	16.944	59.102
<u>16</u>	0.4644	27.571	7.217	122.941	0	0	22.345	57.619
<u>17</u>	1.4789	95.742	27.819	40.464	0	0	22.694	52.967

Continued on next page

species $\langle S^2 \rangle$	μ_D / Debye	polarisability / bohr ³							
		a_{11}	a_{21}	a_{22}	a_{31}	a_{32}	a_{33}	$\langle a \rangle$	
18	1.6822	46.611	8.674	70.650	0	0	17.636	44.966	
19	0.2411	50.647	-0.004	56.226	0	0	17.427	41.433	
$\mathcal{A}\text{-C}_5\text{H}_3^+$	0.2197	16.185	0	104.399	0	0	30.999	50.528	
<i>products of $C_5H_5^+ + CH$ reaction: $C_6H_6^+$</i>									
23	0.7738	0.5268	106.525	1.528	71.427	0.006	0.001	20.432	66.128
24	0.7741	0.8271	107.402	40.591	92.163	0	0	20.570	73.378
25	0.7864	0.8320	105.524	48.107	104.787	0	0	20.270	76.860
26	0.7870	0.1414	66.560	54.465	169.210	0	0	20.383	85.384
27	0.7651	0.9636	133.772	19.537	66.824	0	0	20.539	73.712
28	0.7674	0.6164	108.829	-0.029	83.303	0	0	20.490	70.874
29	0.7669	2.1765	59.978	6.073	97.975	0	0	20.978	59.644
30	0.7662	2.0052	98.118	32.476	75.122	0	0	21.109	64.783
31	0.7866	2.2544	106.883	-2.977	53.876	2.997	0.296	24.525	61.761
32	0.7627	0.1647	20.482	0	62.409	0	0	90.769	57.887
33	0.7635	0.0005	64.595	-0.008	72.699	-0.004	0.001	20.214	52.503
<i>products of $C_6H_6^+ + CH$ reaction: $C_7H_7^+$</i>									
35		0.9949	109.448	-57.010	136.963	0	0	23.794	90.068
36		0.5966	107.173	5.082	88.879	2.459	0.052	33.148	76.400
37		1.0877	132.727	-17.950	94.604	0	0	23.733	83.688
38		3.1896	88.136	-20.665	132.922	0	0	23.858	81.639
39		2.5730	133.463	23.192	73.451	0	0	24.311	77.075
40		2.7448	101.538	-2.578	73.184	-5.101	-0.783	33.245	69.322
41		0.1605	90.777	1.531	61.119	-0.001	-0.002	44.138	65.345
42		1.7030	100.702	31.745	92.720	0	0	23.913	72.445
43		2.7506	99.057	0.538	69.842	-3.159	1.100	32.832	67.244
44		1.6256	23.346	0	73.635	0	0	109.178	68.720
45		0.8211	81.233	-4.760	75.477	2.873	-2.158	36.463	64.391
46		0.0000	85.935	0	85.935	0	0	23.016	64.962
<i>$C_{10}H_8^+$ reactant</i>									
48	0.7628	0.0000	31.765	0	169.578	0	0	111.434	104.259
<i>products of $C_{10}H_8^+ + CH$ reaction: $C_{11}H_9^+$</i>									
49		2.7096	171.971	-5.091	139.295	0.494	0.783	46.281	119.182
50		1.3633	203.742	-4.025	115.502	-1.116	1.079	45.259	121.501
51		1.0199	153.158	-9.224	111.048	-3.518	-1.614	54.349	106.185
52		4.6428	144.505	-0.001	110.492	1.231	0	59.459	104.819
53		1.1684	34.733	0	123.220	0	0	186.980	114.978
54		6.3102	127.833	-0.003	102.955	0.910	0.001	54.171	94.986
55		2.4958	212.192	-33.833	127.218	0	0	34.982	124.797

Continued on next page

species (S^2)	μ_D / Debye	polarisability / bohr ³							
		a_{11}	a_{21}	a_{22}	a_{31}	a_{32}	a_{33}	$\langle a \rangle$	
56	2.0754	174.912	-6.752	141.355	0	0	34.829	117.032	
$B_{a-}C_{11}H_7^+$ (57)	2.0779	192.545	-18.188	114.090	0	0	34.643	113.759	
$B_{b-}C_{11}H_7^+$ (58)	0.0821	34.668	0.001	203.148	0	0	104.251	114.022	
$B_{a-}C_9H_7^+$ (59)	1.0977	133.369	12.761	101.847	0	0	28.900	88.039	
<i>products of $C_{11}H_9^+$ + CH reaction: $C_{12}H_{10}^+$</i>									
60	0.7701	1.3767	208.437	4.366	125.262	5.215	0.646	68.960	134.220
61	0.7628	27.0177	89.776	-33.251	179.003	-23.011	-27.549	107.291	125.357
62	0.7651	1.8946	185.255	10.777	128.300	-4.977	1.690	58.421	123.992
63	0.7769	1.8544	173.190	5.338	141.962	-0.751	-2.182	57.467	124.206
64	0.7869	0.0000	249.820	-0.002	137.017	0	0	37.899	141.579
65	0.7553	0.9586	225.717	0	144.944	-5.451	0	43.737	138.133
66	0.7749	0.5882	56.259	1.639	185.127	0	0	141.442	127.609
67	0.7959	0.8333	193.026	-0.003	146.207	-1.866	-0.002	50.818	130.017
68	0.7560	0.7560	202.474	0	115.658	-0.035	0	87.192	135.108
70	0.7709	1.8331	197.853	-62.060	188.719	0	0	38.068	141.547
71	0.7843	1.7036	38.121	0	163.814	0	0	251.055	150.997
72	0.7699	0.7885	236.687	-81.710	199.543	0	0	38.205	158.145
<i>products of $C_{24}H_{12}^+$ + CH reaction: $C_{25}H_{13}^+$</i>									
108	29.5054	313.144	146.623	235.136	-78.293	87.146	340.077	296.119	
109	31.0333	283.521	-53.027	363.245	117.711	61.850	199.505	282.090	
110	30.3072	281.441	-38.793	351.557	119.457	59.897	207.033	280.010	
111	28.6642	353.306	154.444	230.859	73.817	343.891	0.000	194.722	

A.2 $C_4H_4^+ + CH$

This section summarises the results of methyne addition to but-1-yn-2-ene cation (\mathcal{C} - $C_4H_4^+$, **8**), methyne and cyclopropenylmethylene cation (\mathcal{D} - $C_4H_4^+$, **9**), and methyne and cyclobutadiene cation (\mathcal{E} - $C_4H_4^+$, **10**). The structure of presentation follows sections such as $C_3H_3^+ + CH$ (Section 4.3).

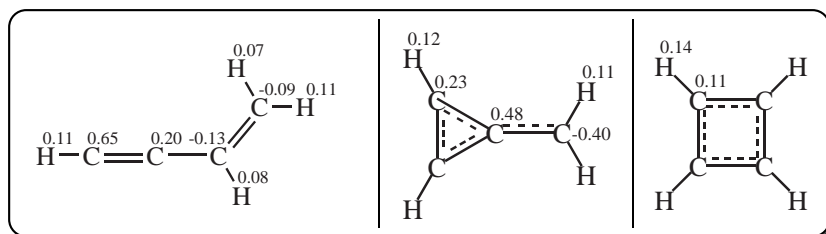


Figure A.1: Mulliken atomic charges of **8**, **9** and **10** obtained at Btz1 level of theory.

Table A.2: Ion-molecule based reaction energies and enthalpies obtained by different quantum theory methods. For each reaction the educts \mathcal{E} - $C_4H_4^+$ (**10**) and CH were considered.

products	abbr.	geometry	$\Delta_R E/eV$	$\Delta_R H_{0K}/eV$		
			SD	Btz1//Bdz1	Ptz4	G3
$cis\text{-}A\text{-}C_5H_5^+$	13		-7.8883	-6.5403	-7.1012	-6.7230
$trans\text{-}A\text{-}C_5H_5^+$	14		-7.9314	-6.6481	-6.9935	-6.8131
$B\text{-}C_5H_5^+$	15		-7.8302	-6.6857	-7.1667	-6.7700
$ca\text{-}C_5H_5^+$	16		-8.0359	-6.5908	-7.1821	-6.6359
$cb\text{-}C_5H_5^+$	17		-7.4670	-5.9680	-6.4995	-6.1184
$\mathcal{D}\text{-}C_5H_5^+$	18		-7.6112	-7.1607	-7.5975	-7.4410
$\mathcal{F}\text{-}C_5H_5^+$	19		-8.3046	-6.7510	-7.2760	-7.2077
$A\text{-}C_3H_3^+ + C_2H_2$	20		-4.8120	-3.7970	-4.0347	-4.0468
$A\text{-}C_4H_2^+ + CH_3$	21		-2.9312	-2.3469	-2.6197	-2.6043
$A\text{-}C_3H_3^+ + H_2$	22		-4.2449	-4.3560	-4.7139	-4.5136

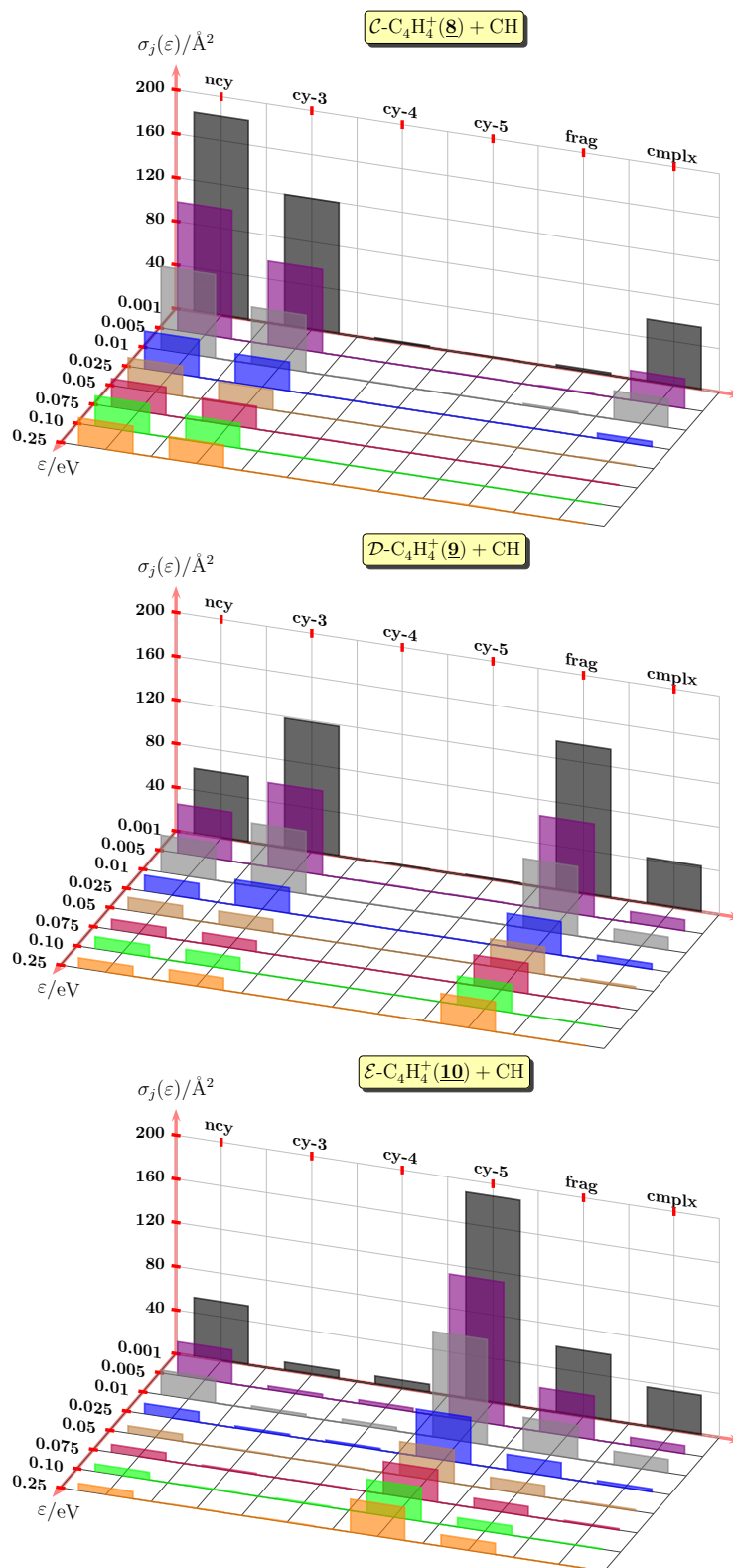


Figure A.2: Calculated product cross sections $\sigma_{R,j}$ resulting from the reaction between \mathcal{C} -, \mathcal{D} - and \mathcal{E} - $C_4H_4^+$ (**8**, **9**, and **10**) and methyne. Both plots correspond to $t_{\text{postcoll}} = 6$ ps applied to different collision energies. Abbreviations correspond to ncy = non-cyclic, cy-3 = one 3-membered ring, cy-4 = one 4-membered ring, cy-5 = one 5-membered ring, frag = fragmentation products, and cmplx = orbiting complex.

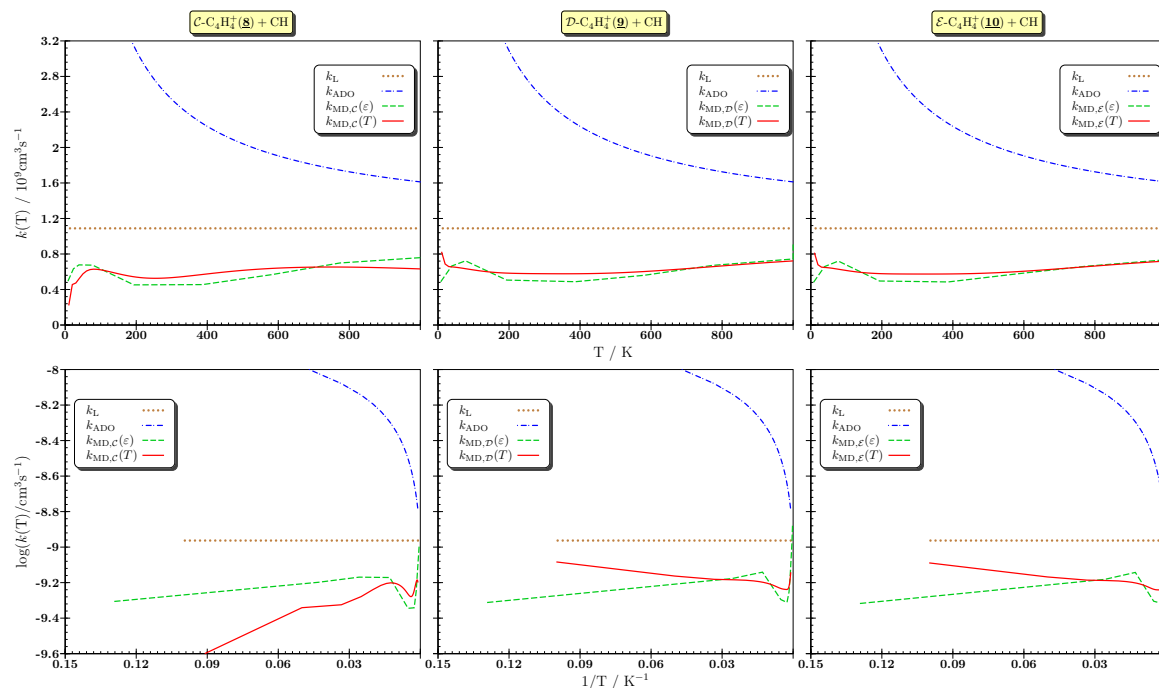


Figure A.3: Capture rate coefficients of the $C_4H_4^+ + CH$ reaction system calculated based on the *Langevin* model (k_L), ADO model (k_{ADO}), and the results of the MD simulations ($k_{MD}(\varepsilon)$ and $k_{MD}(T)$). Two different representations are given: left) logarithmic k versus inverse T (ε_{coll}) and right) k versus T (ε_{coll}).

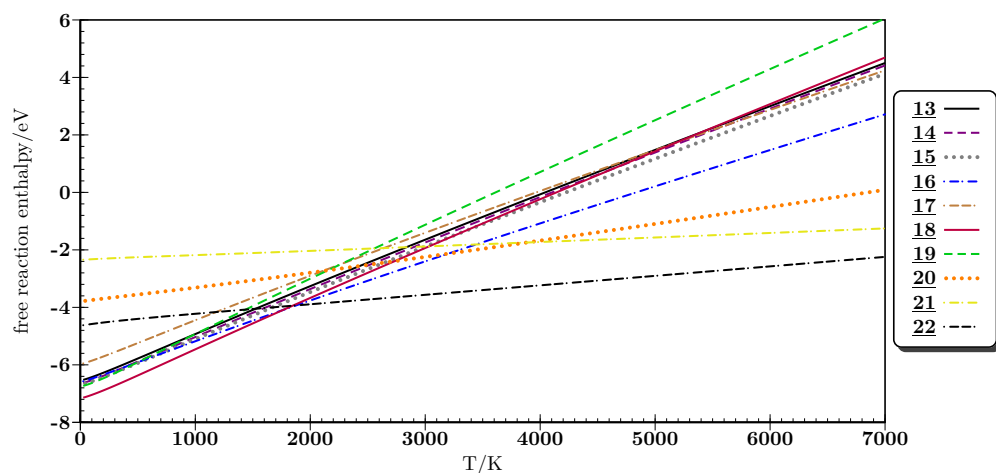


Figure A.4: Free reaction enthalpies of product isomers of Table A.2 obtained at Bdz1 level of theory.

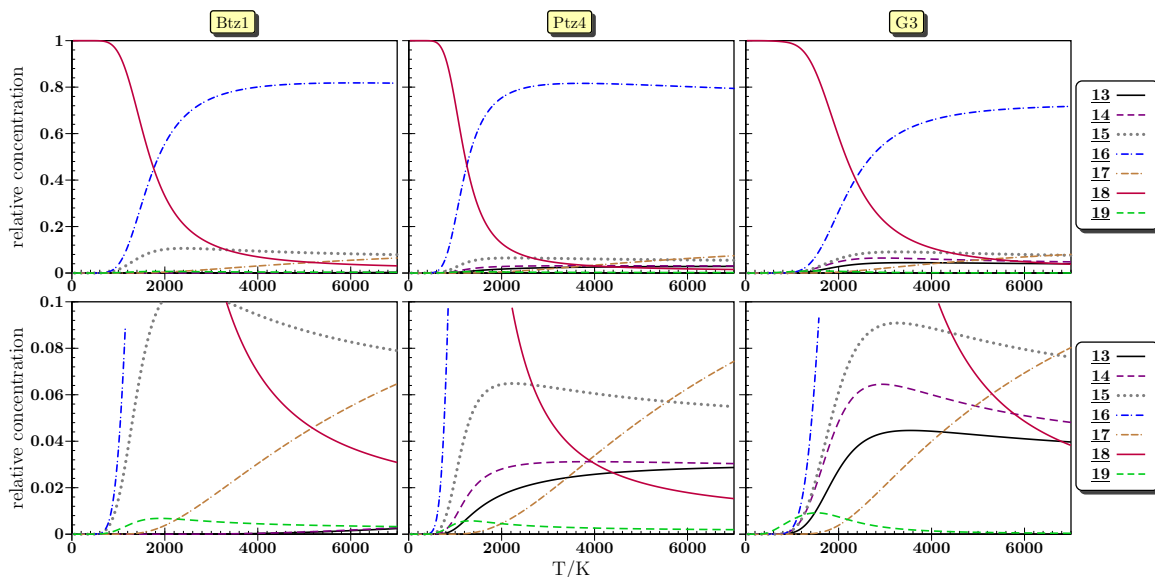


Figure A.5: Canonical population analysis of $C_5H_5^+$ product isomers taken from Table A.2 obtained at Bdz1 (left), Ptz4 (middle), and G3 (right) level of theory. The second row of plots repeats, in detail, the area of relative concentrations between 0 and 0.1.

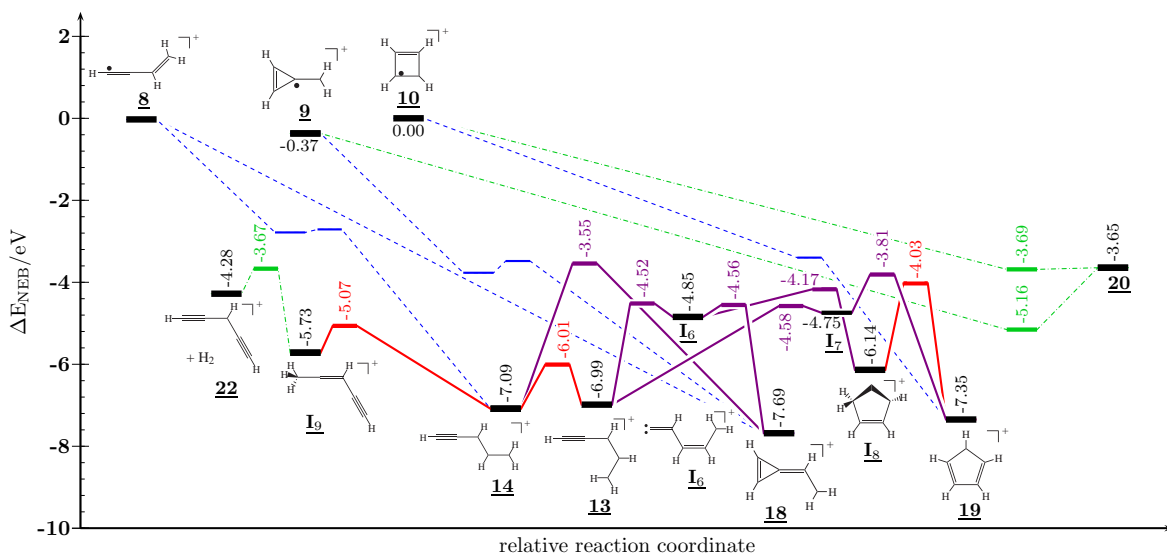


Figure A.6: Stationary points of $C_4H_4^+ + CH$ addition reaction paths, of $C_5H_5^+$ isomerisation paths between conformers, of $C_5H_5^+$ cyclisation paths and $C_5H_5^+$ fragmentation paths obtained at Bdz1 level of theory.

Table A.3: Unimolecular rate coefficients of radiative deactivation and isomerisation processes based on different approaches. Energies (at Bdz1 level of theory) are taken from the MEP and TS optimisation (Figure A.6). Each internal energy is assumed to correspond in amount to the reaction enthalpy of **8** ($c\text{-C}_4\text{H}_4^+$) and methyne dissipated to the product **X** at 0 K.

product	E_{vr}^a / eV	$k_r(E_{\text{vr}})$ / s^{-1}	Isomerisation/Dissociation					
			to	$E_{\text{vr}}^\ddagger{}^a$ / eV	$k_{\text{DC}}^{\text{v}}(E_{\text{vib}})^a$ / s^{-1}	$k_{\text{WR}}^{\text{v}}(E_{\text{vib}})^a$ / s^{-1}	$k_{\text{WR}}^{\text{vr}}(E_{\text{vr}})^a$ / s^{-1}	$k_{\text{m}}^{\text{vr}}(T_{\text{vr}})^a$ / s^{-1}
13	6.639	4.732×10^2	14	5.737	1.621×10^{12}	1.625×10^{12}	1.335×10^{12}	1.068×10^{12}
			I ₇	4.380	3.165×10^{10}	3.176×10^{10}	1.893×10^{10}	9.560×10^9
			I ₆	4.322	2.887×10^{10}	2.897×10^{10}	1.699×10^{10}	8.410×10^9
14	6.741	5.988×10^2	13	5.737	9.664×10^{11}	9.660×10^{11}	1.040×10^{12}	8.067×10^{11}
			I ₉	4.862	1.145×10^{11}	1.143×10^{11}	9.048×10^{10}	5.391×10^{10}
			18	3.364	3.939×10^9	3.945×10^9	2.042×10^9	8.196×10^8
I ₇	4.462	2.664×10^2	13	4.380	2.451×10^{14}	2.450×10^{14}	2.345×10^{14}	3.146×10^{14}
			19	3.608	2.179×10^{12}	2.184×10^{12}	1.284×10^{12}	1.195×10^{12}
19	6.965	2.451×10^2	I ₇	3.608	1.337×10^9	1.338×10^9	7.300×10^8	2.471×10^8
			I ₈	3.766	4.110×10^8	4.112×10^8	1.907×10^8	6.602×10^7
I ₈	5.756	1.436×10^2	I ₆	3.917	5.504×10^{11}	5.516×10^{11}	5.678×10^{11}	3.056×10^{11}
			19	3.766	1.990×10^{10}	1.996×10^{10}	1.226×10^{10}	6.034×10^9
I ₆	4.540	2.927×10^2	13	4.322	6.514×10^{12}	6.516×10^{12}	6.779×10^{12}	6.707×10^{12}
			18	4.305	1.316×10^{12}	1.317×10^{12}	1.121×10^{12}	1.053×10^{12}
			I ₈	3.917	5.401×10^{11}	5.407×10^{11}	5.004×10^{11}	3.953×10^{11}
18	7.308	3.305×10^2	14	3.364	3.466×10^9	3.472×10^9	1.540×10^9	5.493×10^8
			I ₆	4.305	3.060×10^9	3.064×10^9	1.649×10^9	6.665×10^8
I ₉	5.475	3.013×10^2	14	4.862	2.062×10^{11}	2.075×10^{11}	1.550×10^{11}	1.271×10^{11}
			22	3.603	1.166×10^{10}	1.176×10^{10}	6.683×10^9	3.578×10^9

^aCompare with footnotes of Table 4.3

Appendix B Realisation of applied methods

B.1 MD simulation setup

The MD simulation of the chemical reactions have been performed with a particular setup that fulfils the statistical approach of Sections 2.2.3 and 2.4.3.1. The setup defines the initialisation of the MD simulation.

In detail, the setup generates:

1. A coordinate matrix $\vec{R}(\vec{r}_1, \vec{r}_2, b, d, \theta_i)$:
which contains the reactant coordinates (\vec{r}_1, \vec{r}_2) modified by the collision parameter (b) , the centre-of-mass distance $(d_{1,2})$ and the pseudo-randomised orientation (ϑ_i, φ_i) ;
2. A velocity matrix $\vec{V}(\varepsilon_{\text{coll}})$:
which considers for each atom the applied collisional energy and the conservation of the collision centre of mass, $R_{\text{CoM}} = \text{const.}$

The conservation of the collision centre of mass implies that both reactant momenta ($\vec{p}_i = m_i \vec{v}_i$, $i = 1, 2$) are equal by value, but opposite in direction. The total momentum (\vec{P}) remains zero before and after the collision:

$$\vec{p}_1 = -\vec{p}_2 \quad (\text{B.1})$$

$$\vec{P} = \sum_i p_i = 0 \quad (\text{B.2})$$

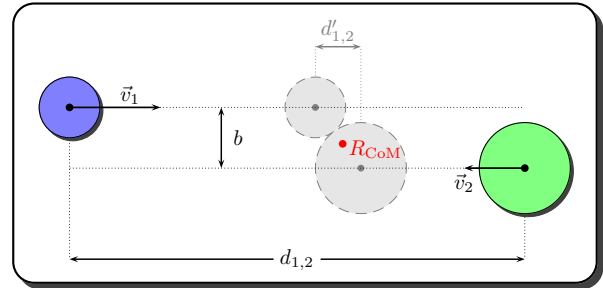


Figure B.1: Schematics and parameter relation of the centre-of-mass system applied for the MD simulation setup.

B.1.1 Definition of the distance $d_{1,2}$

The attractive interaction between ions and molecules (Section 2.2.2) ranges to infinite distances. The initialisation of the MD at infinite distance is, however, technically not realisable. The centre-of-mass distance $d_{1,2}$ between the two reactants is, instead, defined as follows:

$$d_{1,2} = 8\text{\AA} + r_{1,\text{max}} + r_{2,\text{max}} \quad (\text{B.3})$$

where each $r_{i,\text{max}}$ represents the maximum molecular radius.

Due to the cut at $d_{1,2}$, a small fraction of collision energy will be omitted which is gained by the approach of both reactants in the attractive potential. Based on the ion-induced

molecule interaction (Eq. (2.6)) and the polarisability of CH, the average gain in terms of collision energy between the distances 10 Å – 11 Å and infinity Å is estimated to be around 0.001 eV.

B.1.2 Pseudo-random orientations

To fulfil the statistic approach, the orientations between the reactants were altered each time by a random rotation of each molecule. In order to reproduce the rotations, a set of pseudo-random angles ϑ_j were introduced. These angles were calculated from pseudo-random numbers n_{rdm} as follows:

$$\vartheta_{j,\text{rdm}} = 2\pi n_{k,\text{rdm}} \quad (\text{B.4})$$

where $n_{k,\text{rdm}}$ is the k -th element of a pseudo-random number list generated by a seed of several non-random numbers, such as computer date and time.

The coordinates \vec{r}_i^0 ($i = 1, 2$) were rotated relative to their molecular centre $\vec{r}_{i,\text{CoM}}^0$ around each unit vector \vec{e}_j of the 3D dimensional coordinate system. The new coordinates \vec{r}_i^* were determined by:

$$\vec{r}_i^* = \sum_{j=1}^3 \Omega(\vec{e}_j, \vartheta_{j,\text{rdm}}) \cdot (\vec{r}_i^{j-1} - \vec{r}_{i,\text{CoM}}^0) \quad (\text{B.5})$$

where $\Omega(\vec{e}_j, \vartheta_{j,\text{rdm}})$ represents the rotational matrix and $\vartheta_{j,\text{rdm}}$ the pseudo-random angles.

B.1.3 Definition of \vec{R}

The entire coordinate matrix \vec{R} was generated by:

$$\vec{R}(\vec{r}_1^*, \vec{r}_2^*, b, d_{1,2}) = \begin{bmatrix} \vec{r}_1^* + d_{1,2}/2 + b \\ \vec{r}_2^* - d_{1,2}/2 \end{bmatrix}. \quad (\text{B.6})$$

In this representation the collision centre of mass does not necessarily correspond to the coordinate origin (0,0,0).

B.1.4 Definition of \vec{V}

The velocities of the reactants, \vec{v}_i ($i = 1, 2$), were defined by the collisional energy $\varepsilon_{\text{coll}}$; they are independent of the collision parameter b and the distance $d_{1,2}$. Based on the centre-of-mass system (Figure B.1), the translational velocity of each reactant $\vec{v}_{i,\text{coll}}$ was then determined by:

$$\vec{v}_{i,\text{coll}} = \sqrt{\frac{2\varepsilon_{\text{coll}}}{\frac{m_i^2}{m_{j \neq i}} + m_i}}. \quad (\text{B.7})$$

The entire velocity matrix \vec{V} was generated by:

$$\vec{V}(\varepsilon_{\text{coll}}, \varepsilon_{\text{kin}}) = \begin{bmatrix} \vec{v}_{1,\text{coll}} + \vec{v}_{1,\text{kin}} \\ \vec{v}_{2,\text{coll}} + \vec{v}_{2,\text{kin}} \end{bmatrix}. \quad (\text{B.8})$$

However, only the translation of frozen coordinates were considered, i. e., initial vibration and rotational were suppressed ($\vec{v}_{i,\text{kin}} = 0$). This is reasonable for highly energetic and

reactive collisions with energetic impact far above internal energy, i. e., $\vec{v}_{i,\text{rct+coll}} \gg \vec{v}_{i,\text{kin}}$. This represents approximately the reaction type investigated in this work.

B.1.5 Definition of t_0

The timeline was divided into pre-collisional and post-collisional regions, t_{precoll} and t_{postcoll} (Figure B.2). The time t_0 was defined as the moment of collision or in the case of non-collision

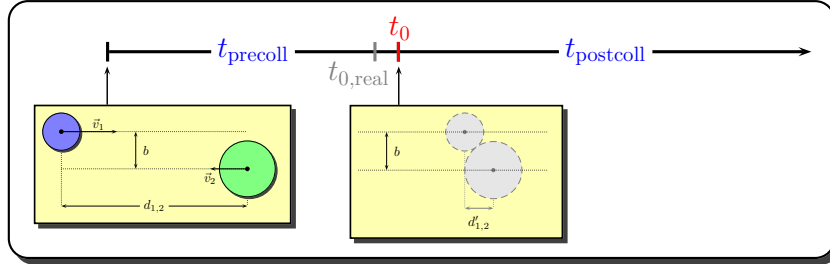


Figure B.2: Schematic timeline of MD based collision simulations. The pre-collisional and the post-collisional time are separated by the time of collision t_0 . The definition of t_0 is estimated by the initial velocities and the distance $d_{1,2}$. Due to possible acceleration in an attractive potential in the real MD simulation, the real moment of collision $t_{0,\text{real}}$ might occur before the estimated t_0 .

($b > r_{1,\text{max}} + r_{2,\text{max}}$) as the moment of closest encounter. The value t_0 was determined by the estimation of t_{precoll} . A constant t_{postcoll} was chosen in order to compare the evolution of the product distribution between the different collisional energies. The total MD simulation time t_{tot} is, therefore, defined as follows:

$$t_{\text{tot}} = \underbrace{d_{1,2}/(\vec{v}_{1,\text{coll}} + \vec{v}_{2,\text{coll}})}_{t_{\text{precoll}}} + \underbrace{t_{\text{postcoll}}}_{\text{const}}. \quad (\text{B.9})$$

The post-collisional time, t_{postcoll} , was set to 5 and 6 ps, respectively. Note that the real t_0 ($t_{0,\text{real}}$) might slightly differ from the defined t_0 , since the pre-collisional time was estimated based on the distance $d_{1,2}$ (Eq. (B.3)) and initial velocities. Smaller $d_{1,2}$ (caused by orientations differed to the alignment of the maximum radii) and the acceleration of reactants (caused by attractive interactions) might lead to $t_{0,\text{real}} < t_0$ on the MD timescale.

B.1.6 Definition of b and P

In order to determine the cross sections as given in Section 2.2.3, the probability function $P(b)^{\dagger 1}$ had to be evaluated. This function was determined by the discretisation of b denoted by b_i and the resulting P denoted by P_i . The continuous function $P(b)$ was determined by cubic spline interpolation of the discrete values P_i (Section B.2).

The interval between the discrete b_i values was set to 0.2 Å. At a particular b_i , the probability P_i was determined by the ratio of the counted number of successful over the total number of collisions:

$$P_i(b_i) = \frac{N_{\text{success}}}{N}, \quad (\text{B.10})$$

^{†1}It is also referred as the reactivity function

where N was set to a maximum of 50 for each b_i . The technical definition of successful collisions, i. e., the successful occurrence of the j -th type of reaction, is described in Section B.3. The variation of parameters for each collision at a particular b_i was restricted to the relative orientation between the reactants. The cross sections and the capture rate coefficients are derived within in this setup as depicted in Figure B.3.

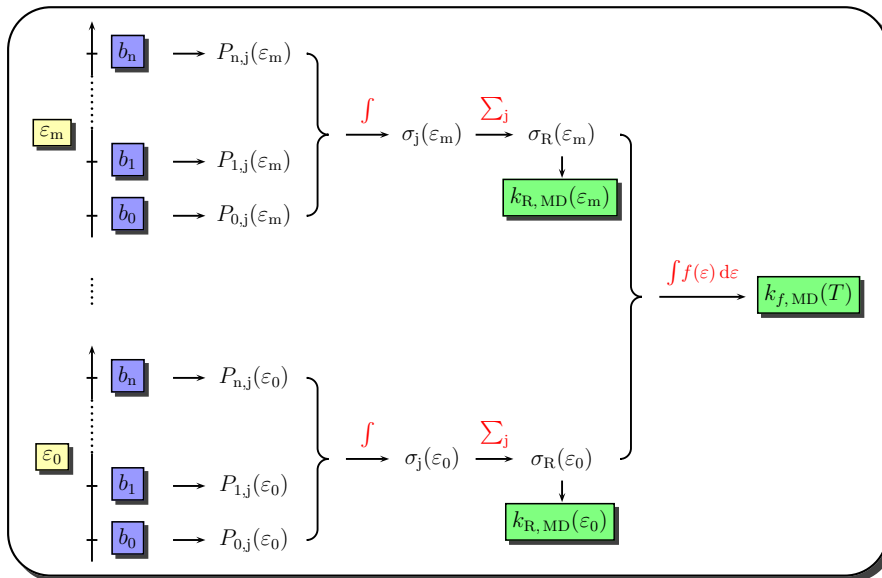


Figure B.3: Scheme of the MD simulation setup under the consideration of b_i , P_i and $\varepsilon_{\text{coll},i}(= \varepsilon_i)$ and their resulting quantities, i. e., cross sections and rate coefficients. Note that \int represents the numerical integration, \sum_j the summation over all channels j , and $\int f(x)dx$ the numerical integration weighted by the *Maxwell-Boltzmann* distribution $f(x)$.

B.1.7 Definition of N

According to the numerical integration of the cross sections σ_R , P_i is weighted b_i^2 . This means that the determination of P_i at $b_i = 0$ can be neglected. Moreover, the accuracy of P_i at large b_i values is of bigger impact than at small b_i values. This fact was used to reduce the computational demand for the statistical framework. N was defined as a function of b_i :

$$N_i(b_i) = \frac{N_{\text{max}} - N_{\text{min}}}{(b_{\text{max}} - b_{\text{min}})^2} \cdot b_i^2 + N_{\text{min}}, \quad (\text{B.11})$$

where N_{max} corresponds to the former N , and N_{min} is the desired and smaller value of N . Based on Eq. (B.11), the reduction relative to N_{max} is given by $\sum_i N_i(b_i) / \sum_i N_{\text{max}}(b_i)$. For very large values of $b_{\text{max}} - b_{\text{min}}$, the ratio leads approximately to $N_{\text{min}}/N_{\text{max}}$. Since the ratio of N_{min} to N_{max} was defined in this work by 1 : 3, the overall reduction of the computational demand shrinks to 1/3 at maximum.

B.1.8 Definition of $\varepsilon_{\text{coll}}$

The ε values were chosen based on the conditions in the ISM for which the temperature is supposed to range from 50 K to 200 K.

Based on the equipartition theorem applied to the ideal gas, the given temperature interval corresponds to collision energies between 7 to 26 meV (Table B.1). In order to determine, however, $k_{\text{MD}}(T)$ in the interval of $T = 50\text{-}200$ K, a $\varepsilon_{\text{coll}}$ interval for each temperature has to be taken into account in order to reach a sufficient numerical integration. In the case of a *Langevin*-type ion-molecule reaction, $k_{\text{MD}}(T)$ is defined as follows:

$$k_{f,\text{MD}}(T) = \mathcal{A}(T) \int_0^{\infty} \sigma_{\text{R}}(\varepsilon_{\text{coll}}) \cdot \varepsilon_{\text{coll}} \cdot e^{(-\varepsilon_{\text{coll}}/k_{\text{B}}T)} d\varepsilon \approx \mathcal{A}(T) \int_0^{\varepsilon_{\text{coll},\tau}} \mathcal{I}(\varepsilon_{\text{coll}}) d\varepsilon_{\text{coll}}. \quad (\text{B.12})$$

Three $\varepsilon_{\text{coll}}$ intervals for the integrand $\mathcal{I}(\varepsilon_{\text{coll}})$ at 50, 100, and 200 K are depicted in Figure B.4. It was found that 99% of the integrand's area between 0 and ∞ can be approximated by

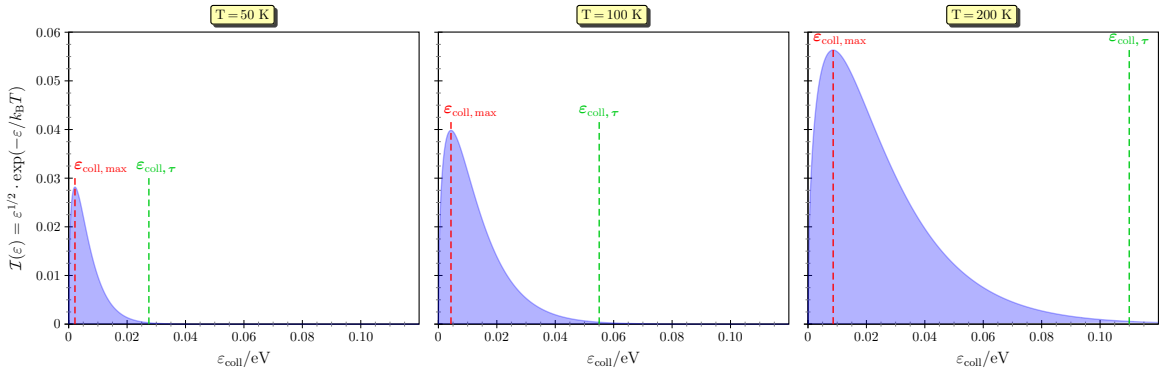


Figure B.4: Characteristics of the integrand $\mathcal{I}(\varepsilon_{\text{coll}}) = \varepsilon_{\text{coll}}^{1/2} \cdot \exp(-\varepsilon_{\text{coll}}/k_{\text{B}}T)$. Both collisional energy values, $\varepsilon_{\text{coll,max}}$ and $\varepsilon_{\text{coll},\tau}$, are related by $\mathcal{I}(\varepsilon_{\text{coll,max}}) = 100 \cdot \mathcal{I}(\varepsilon_{\text{coll},\tau})$.

the interval $[0, \varepsilon_{\tau}]$ where ε_{τ} represents the upper limit for which 99% of this entire area is covered. The upper limit, $\varepsilon_{\text{coll},\tau}$, was found to relate to $\mathcal{I}(\varepsilon_{\text{coll,max}}) = 100 \cdot \mathcal{I}(\varepsilon_{\text{coll},\tau})$. Based

Table B.1: Different approximations for the relation between collisional energy and temperature.

T / K	$\varepsilon_{\text{coll}} / \text{eV}$ $= 3/2 k_{\text{B}}T$	$\mathcal{I}(\varepsilon_{\text{coll}}) = \varepsilon_{\text{coll}}^{1/2} \cdot \exp(-\varepsilon_{\text{coll}}/k_{\text{B}}T)^a$	
		$\varepsilon_{\text{coll,max}} / \text{eV}$ $= 1/2 k_{\text{B}}T$	$\varepsilon_{\text{coll},\tau} / \text{eV}$ $= -1/2 k_{\text{B}}T \cdot \text{Lam}(-100^{-2}e^{-1})^b$
50	0.0065	0.0022	0.0275
100	0.0129	0.0043	0.0551
200	0.0259	0.0086	0.1100
300	0.0388	0.0129	0.1647
500	0.0647	0.0215	0.2752

^aThe integrand corresponds to the *Langevin* model, i. e., $\sigma_{\text{R}} \propto \varepsilon_{\text{coll}}^{-1/2}$

^bLam defines the negative real branch of the Lambert \mathcal{W} function (\mathcal{W}_{-1}) which is the solution to the relation $(-\varepsilon_{\text{coll},\tau}/ak_{\text{B}}T) e^{(-\varepsilon_{\text{coll},\tau}/ak_{\text{B}}T)} = -(1/100)^{1/a} e^{-1}$ with $a=1/2$.

on the results given in Table B.1, a 99% approximation of the exact $k_{\text{MD}}(T)$ for temperatures up to 200 K requires an interval of $\varepsilon_{\text{coll}}$ between 0 and 0.11 eV.

Due to high computational demands, the statistical framework was limited to a few $\varepsilon_{\text{coll}}$

values. A set of nine collisional energies $\varepsilon_{\text{coll},i}$ was chosen. The first set contains:

$$\varepsilon_{\text{coll},i}/\text{eV} = \{0.001, 0.005, 0.01, 0.025, 0.05, 0.075, 0.10, 0.25, 0.50\}. \quad (\text{B.13})$$

A second set was defined later due to discrepancy between microcanonical and canonical capture cross section at low collision energies (compare results of Sections 4.3.1.3 and 4.4.1.4). Between 0.001 and 0.005 eV the value 0.003 eV was introduced. Additionally, the high energy values, 0.25 and 0.50 eV, were removed resulting in:

$$\varepsilon_{\text{coll},i}/\text{eV} = \{0.001, 0.003, 0.005, 0.01, 0.025, 0.05, 0.075, 0.10\}. \quad (\text{B.14})$$

B.2 Determination of k_f and σ_R based on the MD simulations

The determination of $k_{\text{MD}}(\varepsilon)$, $k_{\text{MD}}(T)$ and σ_R is based on the scheme depicted in Figure B.3. While $k_{\text{MD}}(\varepsilon)$ is defined as the product of σ_R and its corresponding collision velocity (Eq. (2.15)), σ_R and $k_{\text{MD}}(T)$ were computed by numerical integration of the data sets via cubic spline interpolation [190].

In the case of the cross sections σ_R follows:

$$\sigma_R = 2\pi \cdot \sum_{k=0}^{m-1} \left(\int_{b_k}^{b_{k+1}} P(b) db \right), \quad \text{with } P_m(b_m) = P_m(b_{\text{max}}) \text{ and } P_0(b_0) = 0, \quad (\text{B.15})$$

where the summation of the integrated intervals is completed when the probability at large b_k drops to zero. Note that the integration of cubic splines leads for Eq. (B.15) to a sum of 4th order polynomials.

On the other hand, $k_{\text{MD}}(T)$ is determined by the following relation:

$$k_{\text{MD}}(T) = \mathcal{A}(T) \cdot \sum_{k=0}^{m-1} \left(\int_{\varepsilon_{\text{coll},k}}^{\varepsilon_{\text{coll},k+1}} \sigma_R(\varepsilon_{\text{coll}}) \cdot \varepsilon_{\text{coll}} \cdot e^{-\varepsilon_{\text{coll}}/k_{\text{B}}T} d\varepsilon_{\text{coll}} \right), \quad (\text{B.16})$$

where $\mathcal{A}(T)$ represents the prefactor and $\varepsilon_{\text{coll},m}$ is defined as the highest value in the List (B.13).

B.3 Analysis of reaction channels by bond criteria and topology

In this work, the determination of the j -th reaction channel probability $P_j(b)$ was based on statistics by counting trajectory ‘‘snapshots’’, i. e., structural configuration, that fit to predefined j -th reaction channel configurations. This counting procedure was divided into the following steps:

1. manual identification of the reaction channels and manual setup of predefined parameters of the reaction channels, and
2. identifying the structural configuration of the snapshots and assignment to the predefined reaction channels.

The complete scheme of the analysis is depicted in Figure B.5.

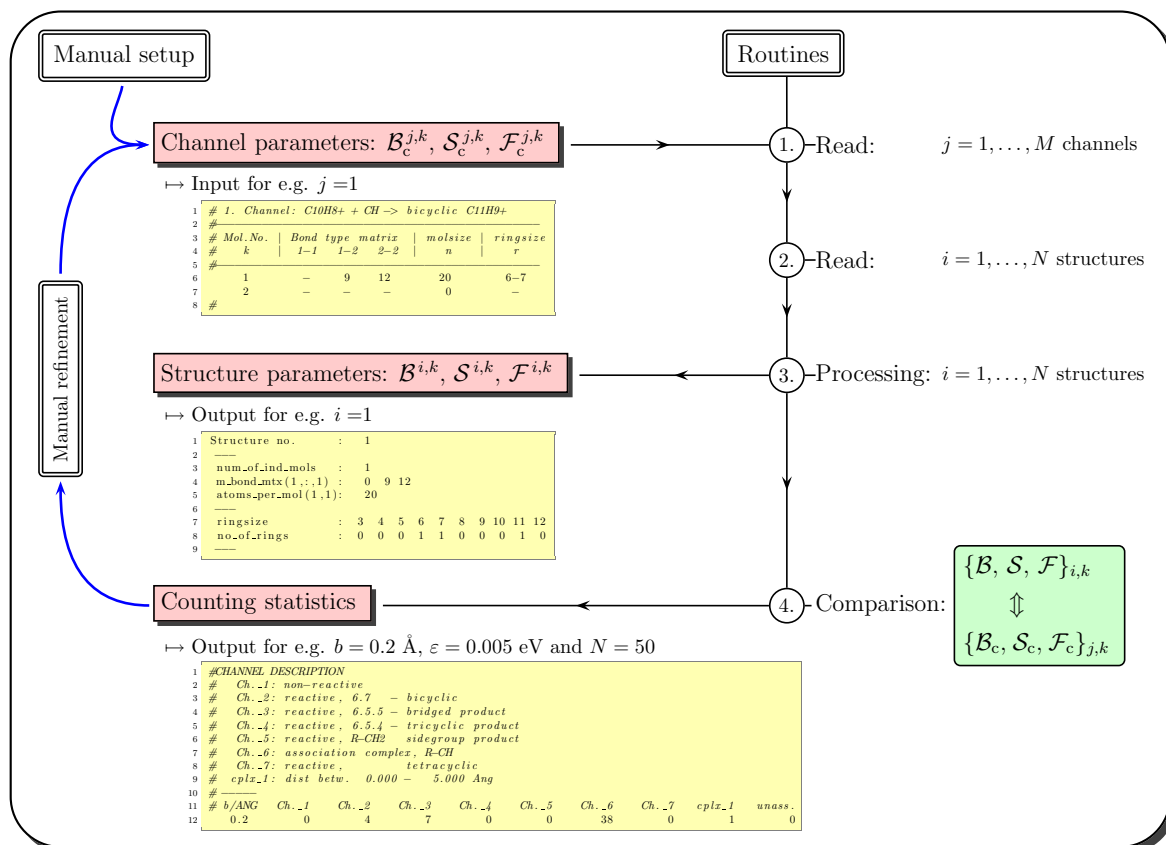


Figure B.5: Schematic structure of the reaction channel analysis based on the cartesian coordinates and channel parameter setup. Matrices \mathcal{B}^i and \mathcal{B}_c^j represent the bond matrix of the i -th cartesian structure and of the j -th product channel, while \mathcal{S}^i and \mathcal{F}^i are the molecular sizes and ring sizes of the i -th cartesian structure. \mathcal{S}_c^j and \mathcal{F}_c^j are the defined molecular sizes and ring sizes of the j -th product channel.

B.3.1 Definition of channel parameters

The channels were defined by four parameters. One defines the product channel by the number of independent molecules / fragments; it is denoted by the index k in Figure B.5 Other parameters were defined for:

1. The molecular size in terms of number of atoms denoted by the index j . The corresponding matrix is $\mathcal{S}_c(j, k)$.
2. The bond type matrix $\mathcal{B}_c(j, k, l)$, where the index l defines bond types and their amount, and
3. The ring size matrix $\mathcal{F}_c(j, k)$.

The index c is the given abbreviation for the term “channel”.

B.3.2 Definition of structure parameters

The structures, i.e., the cartesian coordinates, of the trajectory snapshots were analysed only concerning the channel parameters. This means that the structural informations were determined according the number of atoms, i.e., $\mathcal{S}(j, k)$, the amount of bond types, i.e., $\mathcal{B}(j, k)$, and ring sizes, i.e., $\mathcal{F}(j, k)$.

B.3.3 Determination of structure parameters $\mathcal{B}(j, k)$ and $\mathcal{F}(j, k)$

The bond type matrix was determined by the adjacency matrix which stores all connectivities of a single atom to any one atom based on bond length definitions. The bond length between two atoms were approximated by scaled Van-der-Waals radii. The scaling of radii was introduced in order to correct vibrational distortion of the bonds. The amount of each bond type per product molecule was computed by the summation of all corresponding connectivities but omitting redundancy.

The ring size was determined by a quasi-topology analysis based on the connectivities given by the the adjacency matrix. The corresponding algorithm follows the connectivities from atom to atom and determines connections that sketch cycles, i. e., rings. The distribution of ring sizes was determined by a redundance-free summation of all identified rings.

B.3.4 Counting

The counting was based on the sequential comparison between the structural parameters and the channel parameter. The complete agreements with one channel is counted as a positive result. Any unassigned or multiple assigned structure was registered as failure and was displayed by a diagnostic routine in order to allow a fast refinement of the given channel parameters.

B.4 NEB setup

This section describes the technical setup of the NEB method (Section 2.5.1) used in this work. The principal scheme of the setup is depicted in Figure B.6.

Generation of the elastic band

The elastic band consists of n structures \vec{R}_i which are generated by m input structures \vec{R}'_j . In the case the amount of input structures is less than that of the desired band, the input structures are positioned on the band (pos_i) by the formula:

$$\text{pos}_{i+1} = \text{pos}_i + \text{integer} \left(\frac{n - \text{pos}_i}{m - i + 1} \right), \quad \text{with } \text{pos}_1 = 1. \quad (\text{B.17})$$

while the unassigned positions are generated by linear interpolation.

Additionally, the structures \vec{R}_i are adjusted by rotation until the spatial deviations between adjacent structures are minimal in order to reduce rotational artefacts in the reaction path analysis.

B.4.1 Improved transition state search

Two different improvements were reported in the references [157, 158] and used in this work in order to enhance the transition state search based on the NEB method.

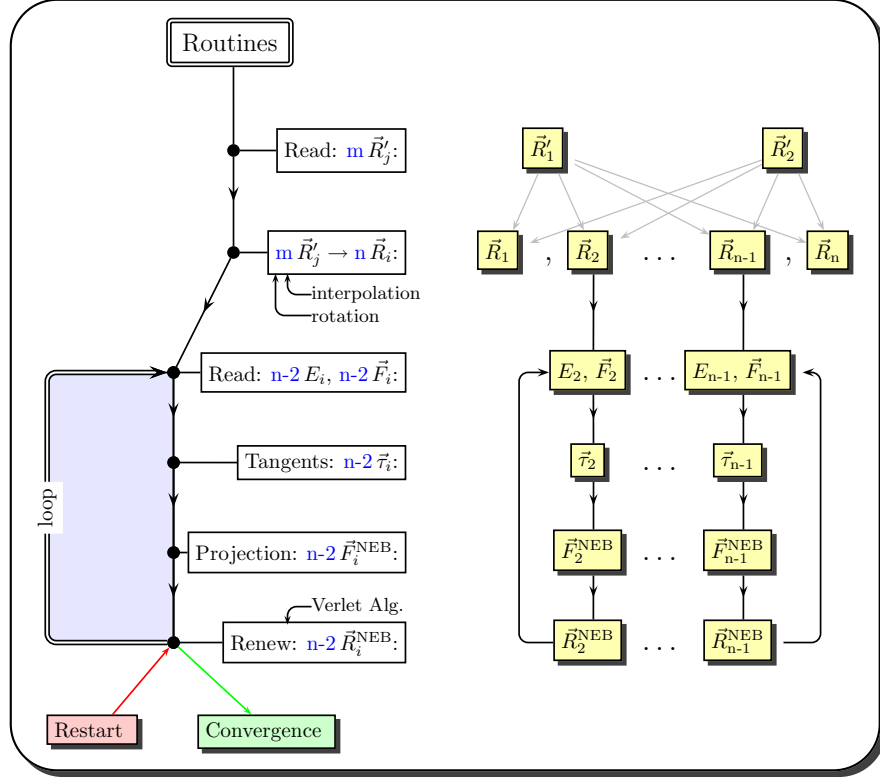


Figure B.6: Technical schematics of the NEB method. The structures \vec{R}_i are either generated by interpolation or passed from previous cycle or form a restart. The forces F_i^{NEB} acting on the structures are determined by the “read-in” energies E_i and gradients \vec{F}_i as well as the computed relative position on the elastic band. These forces are used to calculate the new coordinates \vec{R}_{i+1} .

Higher density around the transition state

By default, the spring constant K_i was set constant. In order to increase the density of structures around the transition state, the stiffness of the spring constant K has been suggested to be changed linearly with the total energy of the structures on the elastic band [157]. This leads for K to:

$$K_i^{\text{VSC}} = \begin{cases} K_{\text{max}} - \Delta K \cdot \left(\frac{E_{\text{max}} - \max\{E_i, E_{i-1}\}}{E_{\text{max}} - E_{\text{ref}}} \right) & \text{if } \max\{E_i, E_{i-1}\} > E_{\text{ref}} \\ K_{\text{max}} - \Delta K & \text{if } \max\{E_i, E_{i-1}\} < E_{\text{ref}}. \end{cases} \quad (\text{B.18})$$

This variation of K is referred as the variable spring constant (VSC) method. Within this work, E_{max} represents the maximum value of all E_i of the elastic band, and E_{ref} is a reference value which is the maximum value of both ends of the elastic band. The amount of change in the spring constant ΔK was adjusted manually.

Decoupling of $\vec{R}_{i,\text{max}}$

The spring constant and the spacing between the structures on the elastic band determine the deviation of the real transition state to the closed structure on the elastic band. In the worst case, the deviation becomes half the spacing between the structures on the elastic band.

Following the proposed enhancement by *Henkelman et al.* [157], each locally highest structure $\vec{R}_{i,\max}$ was decoupled from the elastic band and was moved between the two adjacent structures independent of the applied stiffness of the spring constant. However, the two adjacent structures are still coupled to $\vec{R}_{i,\max}$ by defining the one degree of freedom for which the energy maximisation is applied. The determination of $\vec{R}_{i,\max}$ deviates from the other structures since its forces are derived by:

$$F_{i,\max}^{\text{CI-NEB}} = -\nabla E(\vec{R}_{i,\max}) + 2\nabla E(\vec{R}_{i,\max})|_{\parallel} \quad (\text{B.19})$$

This method is referred as the “climbing image” (CI).

Table C.2: Abundances of molecular species in the *Taurus Molecular Cloud 1* (TMC-1) and the dark cloud L134N^a after Tielens [5].

species	fractional abundance ^b	
	TMC-1	L134N
CO	8×10^{-5}	8×10^{-5}
CH	2×10^{-8}	-
OH	3×10^{-7}	8×10^{-8}
HCO ⁺	8×10^{-9}	8×10^{-9}
C ₂ H	5×10^{-8}	5×10^{-8}
C ₃ H	5×10^{-10}	3×10^{-10}
C ₂	5×10^{-8}	-

^aLynds's catalogue of dark clouds [191]

^bwith respect to H₂



Figure C.1: A schematic picture of the Horsehead nebula, also known as Barnard 33 in the nebula IC 434. The pink schemes hydrogen gas that predominantly lies behind the nebula and has been ionized by the nearby star Sigma Orionis. It makes the pillar (horsehead shape) and areas of gas and thick dust visible. The propagation of the ionisation front leading to the evaporation of the MC is responsible for the streams of matter leaving the nebula.

C.2 Spectroscopical data of interstellar molecules and particles

Table C.3: Mid-IR emission features and their possible assignments to hydrocarbonaceous materials after [5, 18, 60]

band/ μm	mode	assignment
3.3	CH stretch	aromatic, sp^2
3.4	CH stretch	aliphatic – in methyl groups hydrogenated PAHs
6.2	CC stretch NH ₂ deformation	aromatic, sp^2
7.6	CC stretch	
7.8	CC stretch	
8.6	CH bend (in-plane)	
11.0	CH bend (out-of-plane)	isolated C-H (solo), cationic molecule
11.3	CH bend (out-of-plane)	isolated C-H (solo), neutral molecule

Appendix D Properties of the ISM

The interstellar medium is defined as the space between the stars. The interstellar medium is pervaded by matter that consists of gas and grain in a mass ratio of 99 to 1 [192], but is so highly diluted that the galactic density averages to only a few $10^{-21}\text{kg}\cdot\text{cm}^{-3}$ [5]. On the other side, star and associated planetary systems fill such a tiny fraction of the space – only $3\cdot 10^{-10}$ [5] – that the total mass of interstellar matter corresponds to 1% of the total star mass in our galaxy.

In terms of stellar evolution, the ISM represents a repository. It is filled by the “remains” of old star generations, redistributed by stellar winds and (super-)novae, and is continuously compacted to star-forming regions by gravitational collapse [193]. The nucleosynthesis of stars continuously enriches the ISM with heavy elements at the cost of primordial H and He. Present fractions of H and He constitute about 90% and 10%. Heavy elements are evaluated with ppm relative to hydrogen, e. g. carbon with 140 ppm relative to hydrogen [69].

D.1 Phases of the ISM

The ISM is highly inhomogeneous in terms of temperature, pressure and composition. The mass injections, stellar and cosmic radiation fields as well as mechanical energy injections (e. g. explosions by novae and supernovae) alter the physical and chemical composition of the ISM. The ISM is on scale of 10 parsecs (pc) and below not in thermodynamic equilibrium; it is composed of phases. Based on extensions of the three-phase model [194, 195], the phases are organised by physical and chemical properties as given in Table D.1.

D.2 Molecular clouds - the habitat of interstellar molecules

Molecular clouds (MC) frame the densest part and also one of the smallest parts of the ISM. In the field of astrochemistry, the study is focused on these clouds since MCs are the origin of distinctive spectral bands and lines which are commonly assigned to molecules. MCs are characterised to be in an self-gravitating and turbulent state [196].

MCs are categorised based on visible extinction characterised by A_v given in magnitude^{†1} into diffuse clouds with $A_v < 2$, translucent clouds with $A_v = 3-5$, and dark clouds with

^{†1}Magnitude is an logarithmic scale of the brightness I of celestial objects.

$A_v = 10$. Giant molecular clouds (GMCs) reach 10^5 – 10^6 solar masses and possess distinctive substructures including diffuse and dark clouds.

D.3 Diffuse and dark clouds

The diffuse clouds constitute a state between atomic and molecular particles and represent often the edges of MCs and GMCs as depicted in Fig C.1.

The dark clouds are related with the coldest and the highest UV-radiation shielded part of the MC, and appear therefore opaque at UV/VIS wavelengths. The radiation shielding and opacity is originated from molecules and grains as indicated by absorption and emission band.

D.4 Bok globules and clumps

Small dark clouds with a diameter \varnothing between 0.1 and 1 lightyears (ly) are often categorised as Bok globules [197, 198, 199] and clumps [196]. They appear isolated in HII regions, such as the Barnard 68 object, or inside of molecular clouds. The inner parts show increasing densities with decreasing distance from the centre, $\rho \sim \varnothing^{-1\pm 0.2}$ [200], and gravitational instabilities [201]. The subsequent gravitational collapse of such instabilities leads to hot cores with a diameter of about 0.1 ly, densities ρ between 10^6 and 10^8 cm^{-3} , and temperatures T between 100 and 300 K [91]. These hot cores are supposed to be highly chemically active [91, 202] and the centres of star formation.

D.5 Composition of a molecular cloud

MCs consist mainly of molecular hydrogen. The total fraction of residual molecules is below 1%. About 1% of the cloud mass belongs to tiny dust particles, with a size distribution maximum at a radius of 10^{-7} m. The elements carbon, nitrogen, and oxygen have fractional abundances with respect to hydrogen of 4×10^{-4} , 9×10^{-5} , and 7×10^{-4} , respectively [81]. Fractional abundance of other elements such as N, Mg, Si, Fe, S, Al, Ca, Na, and Ni is below 10^{-6} .

Table D.1: Phases of the ISM adapted from [5, 203, 204]

Phase	T/K	n_0/cm^{-3}	$\phi/\%$ ^a	$M/10^9 M_\odot$ ^b	State
Molecular clouds	10–50	10^3 – 10^6	0.05	1.3	molecules (> 99.9% H ₂)
Cold HI medium	50–100	1 – 10^3	1.0	2.2	neutral atoms
Warm HI medium	8000	0.5	30	2.8	neutral atoms
Warm ionised medium	8000	0.1	25	1.0	mostly ionised
HII regions	10^4	1 – 10^5	<1	0.05	mostly ionised
Coronal gas	10^5 – 10^6	10^{-4} – 10^{-3}	~ 50	–	fully ionised

^aVolume filling factor relative to the total ISM

^bTotal mass in units of sun mass

Appendix E Theoretical background

E.1 Reaction kinetics and statistical rate theories

E.1.1 Basics of the ion-molecule reactions [82, 184, 205]

E.1.1.1 Definition of the effective potential

The potential energy surfaces of ion-molecule reactions are determined by long-range attractive forces $V(R)$ and are mostly barrier-free at the collision point but the dynamics on them also generate a repelling potential due to the angular momentum conservation.

$$V_{\text{eff}}(R) = V(R) + \frac{L^2}{2\mu R^2} \quad (\text{E.1})$$

This repelling potential (2nd term in Eq. (E.1)) is also referred as centrifugal barrier or centrifugal energy. Due to the angular momentum conservation, translational energy is transformed into centrifugal energy. At very low temperatures which also correlate to low collisional energies, the transfer into centrifugal energy might be complete. As a result the collision between the ion and the neutral is prevented.

The attractive long-range potentials are described in the case of phenomenological models by asymptotic potentials:

$$V(R) = -\frac{C_s}{R^s}, \quad (\text{E.2})$$

where C_s is defined as a constant depending on the exponent s . Considering *London* dispersion forces, s is equal to 6, while $s = 4$ represents the charge-induced dipole forces between ions and molecules.

E.1.1.2 Definition of reaction probability and steric factor

The relation between the reaction probability P and the steric factor p is often given by a step function which is based on the relation between the translational energy ε_{tr} and the repulsive potential $V_j(R)$ as follows:

$$P = \begin{cases} p & \text{if } \varepsilon_{\text{tr}} \geq V_j(R) \\ 0 & \text{if } \varepsilon_{\text{tr}} < V_j(R) \end{cases} \quad (\text{E.3})$$

In the case of the ion-molecule reaction, the reaction probability P of collisions with translational energy below the centrifugal energy is set to zero, otherwise P is equal to the steric

factor p . In the most simple models p is unity. Structure of complex particles, i. e., molecules, and their reactivity effects on the orientation are considered by the introduction of complex functions of p [184].

E.1.2 Counting statistics [184, 206]

E.1.2.1 State-specific reaction probability

In the case of the ion-molecule reaction, the reaction probability P of the reactant pair i in a specific vibrational-rotation state α forming the product j in another specific vibrational-rotational state ω is defined by counting statistics as follows:

$$P_{i\alpha \rightarrow j\omega}(\varepsilon_{\text{coll}}, b) = \lim_{N \rightarrow \infty} \frac{N_{\text{R}, i\alpha \rightarrow j\omega}}{N_{i\alpha \rightarrow j\omega}}, \quad (\text{E.4})$$

where N_{R} is the amount of reactions resulting from N initiated collisions within the defined state, but different orientations. $P_{i\alpha \rightarrow j\omega}(\varepsilon_{\text{coll}}, b)$ already represents the orientation averaged reaction probability $P_{i\alpha \rightarrow j\omega}(\varepsilon_{\text{coll}}, b; \vartheta, \varphi)$ as follows:

$$P_{i\alpha \rightarrow j\omega}(\varepsilon_{\text{coll}}, b) = \int_{\vartheta} \int_{\varphi} P_{i\alpha \rightarrow j\omega}(\varepsilon_{\text{coll}}, b; \vartheta, \varphi). \quad (\text{E.5})$$

In this work a sufficient number of pseudo-randomised initial orientations was used to approximate the integral as described by *Karplus et al.* [206].

E.1.2.2 State-specific reaction cross sections

The state-specific reaction cross section $\sigma_{\text{R}, i\alpha \rightarrow j\omega}(\varepsilon_{\text{coll}})$ is given by the integration of the reaction probability over the collision parameter b as follows:

$$\sigma_{\text{R}, i\alpha \rightarrow j\omega}(\varepsilon_{\text{coll}}) = 2\pi \int_0^{b_{\text{max}}(\varepsilon)} P_{i\alpha \rightarrow j\omega}(\varepsilon_{\text{coll}}, b) b \, db, \quad (\text{E.6})$$

where b_{crit} represents the maximal b at which P turns to zero.

E.1.2.3 State-specific microcanonical rate coefficient

The relation between the state-specific rate coefficient and the state-specific reaction cross section corresponds to:

$$k_{i\alpha \rightarrow j\omega}(v_{\text{coll}}) = v_{\text{coll}} \times \sigma_{\text{R}, i\alpha \rightarrow j\omega}(v_{\text{coll}}), \quad (\text{E.7})$$

where v_{coll} is defined by $(2\varepsilon_{\text{coll}}/\mu)^{1/2}$.

E.1.2.4 State-specific canonical rate coefficient

The transition from microcanonical rate coefficients to the canonical rate coefficients is achieved by the thermal averaging of the initial velocities v_{coll} based on the *Maxwell-Boltzmann* distribution:

$$k_{i\alpha \rightarrow j\omega}(T) = \langle v_{\text{coll}} \times \sigma_{\text{R}, i\alpha \rightarrow j\omega}(v_{\text{coll}}) \rangle. \quad (\text{E.8})$$

Note that the cross sections are to be included in the averaging process.

E.1.2.5 Transition to non-state correlating rate coefficient

The transition of state-specific rate coefficients to non-state correlating (or so-called global) rate coefficients, $k(T) \equiv k_{\bar{i} \rightarrow \{j\}}(T)$, is achieved by the summation of all possible states ω of the product j , labelled hereafter $\{j\}$, and the averaging of all possible initial states α of the reactant pair i , labelled hereafter \bar{i} :

$$k_{\bar{i} \rightarrow \{j\}}(T) = \sum_{\alpha} p_{\alpha} \sum_{\omega} k_{i_{\alpha} \rightarrow j_{\omega}}(T) \quad (\text{E.9})$$

$$= \langle v_{\text{coll}} \times \sigma_{\text{R}, \bar{i} \rightarrow \{j\}}(v_{\text{coll}}) \rangle, \quad (\text{E.10})$$

where p_{α} represents the weight of each α state.

E.1.3 Basics of the RRKM theory [110]

The RRKM theory is a statistical reaction rate theory that allows the evaluation of complex unimolecular rate coefficients such as the recombination of radicals [113, 207]. This theory is an extension of the *Rice-Ramsperger-Kassel* (RRK) theory [208, 209] that includes the transition state (TS) concept. The complex process was considered to follow the path:



where the total unimolecular rate is evaluated in terms of the rate coefficients of the energisation (k_1), the de-energisation (k_2), the transition rate of the energised molecule into the transition state (k_a), and the crossing of the barrier to the products (k_3).

However, since the energisation of the molecule (k_1) is part of the association process during the ion-molecule collisions (Section 2.2.2), and the de-energisation (k_2) was restricted to radiative emission processes (Section 2.2.5), both quantities were omitted for the calculations of the isomerisation rate coefficients. The evaluation was, therefore, restricted to the RRKM-based k_a and k_3 in this work.

E.1.3.1 Expression for k_a and k_3

A relation between k_a and k_3 is achieved by considering a quasi-equilibrium which defines the energised molecules, that become the transition state, to enter the critical section on the reaction coordinate at the same rate as they would be in a true equilibrium (eqm). Based on this assumption, the relation between k_a and k_3 is given by the equation:

$$k_a(E_{\text{vr}}^*) = \frac{1}{2} k_3 \left(\frac{[\text{A}^{\ddagger,*}]}{[\text{A}^*]} \right)_{\text{eqm}}. \quad (\text{E.12})$$

Based on further assumptions such as (1st) a rapid and free intramolecular energy transfer, (2nd) a random lifetime of A^* , and (3rd) a continuous density of states distribution function $\rho(E)$ of A^* , k_a can be expressed as follows [110]:

$$k_a(E_{\text{vr}}^*) \equiv \mathcal{L} \frac{\mathcal{W}(E^{\ddagger,*})}{h \rho(E_{\text{vr}}^*)} \quad (\text{E.13})$$

where $\mathcal{W}(E^{\ddagger,*})$ is the sum of all quantum states available to the non-fixed energy $E^{\ddagger,*}$ of the transition state, $\rho(E_{\text{vr}}^*)$ is the density of states at the non-fixed energy level E_{vr}^* of the energised molecule, and \mathcal{L} represents the degeneracy of the reaction path. The non-fixed energy E_{vr}^* corresponds to the vibrational and rotational energy above the zero-point energy level of the molecule and the non-fixed energy $E^{\ddagger,*}$ to the vibrational, rotational and translational energy above the zero-point energy level of the transition state. A translation of $A^{\ddagger,*}$ is referred to the motion in the direction of the reaction coordinate. The relation between the non-fixed energy in a molecule E_{vr}^* and its transition state $E^{\ddagger,*}$ corresponds to the enthalpy of the barrier height at 0 K:

$$\begin{aligned} E_{\text{vr}}^* - E^{\ddagger,*} &= \Delta H_{0K}^{\ddagger}, & \text{with} \\ E_{\text{vr}}^* &= E_{\text{vib}}^* + E_{\text{rot}}^*, \\ E^{\ddagger,*} &= E_{\text{vib}}^{\ddagger,*} + E_{\text{rot}}^{\ddagger,*} + E_{\text{trans}}^{\ddagger,*}. \end{aligned} \quad (\text{E.14})$$

E.1.3.2 Expression for \mathcal{L}

The reaction path degeneracy \mathcal{L} (Eq. (E.13)) was approximated as in the CTST treatment by the ratio of the rotational symmetry numbers corresponding to the energised molecule ς and the transition state ς^{\ddagger} :

$$\mathcal{L} = \frac{\varsigma}{\varsigma^{\ddagger}}. \quad (\text{E.15})$$

E.2 Basis sets

For quantum chemical calculations spatial orbital functions are typically substituted by a set of basis functions which are atomic orbitals in the case of calculations involving molecules. Technically, the radial function $R(r)$ of atomic orbitals (AOs)

$$\phi(r) = R(r)Y_{lm}(\theta, \vartheta) \quad (\text{E.16})$$

are described by either *Slater*-type [210] or *Gaussian*-type functions [211] as follows:

$$R^{\text{Slater}}(r) = N r^a e^{-\xi r} \quad (\text{E.17})$$

$$R^{\text{Gaussian}}(r) = N r^b e^{-\alpha r^2} \quad (\text{E.18})$$

where N represent a normalisation constant, a and b are coefficients determined by quantum numbers, and $Y_{lm}(\theta, \vartheta)$ are the spherical harmonic functions. While *Slater*-type orbitals

(STO) mimic better eigenfunctions of the hydrogen atom, e.g. correct cusp behaviour at $r \rightarrow 0$ and exponential decay in the tail region $r \rightarrow \infty$), *Gaussian*-type orbitals (GTO) exhibit deficiencies, e.g. they have a zero slope at $r \rightarrow 0$ and decay too fast in the tail region. However, GTOs possess mainly computational advantages since the product of two GTOs gives a new GTO with the centre in between. For a self-consistent field calculation which scales with $\mathcal{O}(n^4/8)$ two-electron integrals, i.e., four-centre integrals, can be reduced to two-centre integrals using GTOs.

In modern quantum chemical calculations, STOs and GTOs are resembled by a fixed linear combination of normalised *Gaussian* primitive functions $g(\alpha, r)$ which only differ regarding the quantum number l :

$$\phi_{\mu}(r) = \sum_{p=1}^L \mathcal{D}_{p\mu} g_p(\alpha_{p\mu}, r) \quad (\text{E.19})$$

where L is the length of the contraction and $\mathcal{D}_{p\mu}$ are the contraction coefficients. Such a set of primitive functions $g(\alpha, r)$ is also referred to as a contracted *Gaussian*-type orbital (CGTO), $\phi_{\mu}^{\text{CGTO}}(r)$. To achieve a good fitting of one STO, $\phi_{\mu}^{\text{STO}}(r)$, with one CGTO, at least a contraction length of $L = 3$ is required; this fitting is commonly referred to as STO-3G [212].

To improve the variational flexibility and the approximation accuracy of the molecular wave functions, multiple CGTOs are used for each atomic orbital. The use of multiple CGTOs is notated as follows (the so-called zeta notation): two CGTOs per AO is called double-zeta, three CGTOs per AO triple-zeta and so forth. The restriction of multiple CGTOs per AO to the valence shell is commonly applied to basis set generation and referred to as *split-valence* or *valence* basis sets. While the augmentation of polarisation function considerably improve energies of polarised molecules, diffuse functions are mainly added to improve the description of the tail region ($r \rightarrow \infty$) which are important for anions and electronically diffuse molecular systems.

E.3 Reaction minimum energy path and transition state search

E.3.1 Basics of reaction path methods

E.3.1.1 The definition of the minimum energy path

The minimum energy path represents the energetically lowest one-dimensional connection between two local minima on the potential energy surface (PES). Any connection between two local minima contains at least one saddle point. The order of the saddle point is defined by the number of negative eigenvalues of the Hessian matrix (2nd derivatives of the reaction coordinates). The determination and characterisation of these saddle points, which are commonly referred as transition states, allow the evaluation of reaction kinetics based on statistical rate theories. This means that the structural and energetic properties of the transition states give information about the stability of the connected local minimum structures that can be quantised in form of formation and depletion rates.

E.3.1.2 Single-state methods

Single-state methods are normally initialised by the structure of a local minimum on the PES. In this work, this method is required to improve the path optimisation results which give only approximative transition states. It means that the starting point is the structure of the nudged elastic band method closest to the transition state. This structure is already within the region of the transition state, i. e., where the force constant matrix contains one negative eigenvalue.

The transition state is found by tracing stepwise the path of the slowest ascent, i. e., it follows its negative eigenvalues. Starting from the local minimum, this method may be undetermined, but successful if starting in region close to the transition state. However, it is computationally demanding since it involves the evaluation and diagonalisation of the 2nd derivative matrix [213, 214].

E.3.1.3 Berny algorithm [125]

This algorithm requires a starting geometry in a region close to the transition state and an initial guess of the *Hessian* matrix with an appropriate negative eigenvalue. Both conditions are fulfilled by transition state structure given by the NEB optimisation (Section 2.5.1).

E.3.1.4 Double-states methods

The most common developments of the double-state methods are the linear synchronous transit (LST) and the quadratic synchronous transit (QST) algorithms [215, 216]. Each algorithm linearly or quadratically interpolates between the two states by incrementing or decrementing a selected internal coordinate e. g. bond length or angle. The remaining degrees of freedom are reoptimised at each step.

Each interpolation method gives good results for very simple reaction, but may fail in the case of complex molecular rearrangements. A failure would be indicated by a resulting discontinuous pathway.

E.3.1.5 Chain-of-states methods

Based on the concept of the double-state (i. e., double-ending), the path between the two local minima is discretised into a chain of structures either generated by interpolation or taken from a trajectory. Based on the chain-of-state methods, each structure is then coupled with the adjacent structures by a spring; the object function \mathcal{S} is, therefore, defined:

$$\mathcal{S}(\vec{R}_1, \dots, \vec{R}_M) = \sum_{j=1}^M V(\vec{R}_j) + \sum_{j=1}^{M-1} \frac{K}{2} (\vec{R}_{j+1} - \vec{R}_j)^2, \quad (\text{E.20})$$

where K represents the spring constant. Due to the introduced “elasticity” the path is referred as an elastic band. The chain-of-state method mainly differs by the way the initialised path, i. e., the object function \mathcal{S} (Eq. (E.20)), is refined. Common optimisation approaches for the object function \mathcal{S} are based on, e. g., a Monte Carlo algorithm [217], a line integral optimisation [218], or the LUP algorithm [154, 155]. Note that the LUP algorithm avoids 2nd derivatives since the minimising of the energy at each point j is based on a hyperplane

which is defined by the normal τ_j . Again, this normal is estimated by the local tangent or secant $\hat{\tau}_j$.

Bibliography

- [1] C. Joblin, A. Leger, and P. Martin. *Contribution of Polycyclic Aromatic Hydrocarbon Molecules to the Interstellar Extinction Curve*. *Astrophysical Journal* **393**(2), L79–L82 (1992).
- [2] L. Verstraete and A. Leger. *The visible and ultraviolet absorption of large polycyclic aromatic hydrocarbons*. *Astronomy & Astrophysics* **266**(1), 513–519 (1992).
- [3] I. Cherchneff, J. R. Barker, and A. G. G. M. Tielens. *Polycyclic Aromatic Hydrocarbon Formation In Carbon-Rich Stellar Envelopes*. *Astrophysical Journal* **401**(1), 269–287 (1992).
- [4] S. R. Langhoff. *Theoretical infrared spectra for polycyclic aromatic hydrocarbon neutrals, cations, and anions*. *Journal of Physical Chemistry* **100**(8), 2819–2841 (1996).
- [5] A. G. G. M. Tielens. *The Physics and Chemistry of the Interstellar Medium* (Cambridge University Press, Cambridge, UK, 2005).
- [6] D. A. Beintema, M. E. van den Ancker, F. J. Molster, L. B. F. M. Waters, A. G. G. M. Tielens, C. Waelkens, T. de Jong, T. de Graauw, K. Justtanont, I. Yamamura, A. Heras, F. Lahuis, and A. Salama. *The rich spectrum of circumstellar PAHs*. *Astronomy & Astrophysics* **315**(2), L369–L372 (1996).
- [7] A. G. G. M. Tielens. *Circumstellar PAHs and carbon stardust*. *Astrophysics and Space Science* **251**(1-2), 1–13 (1997).
- [8] P. Ehrenfreund. *From Molecular Clouds to the Origin of life* (Springer, 2001).
- [9] A. Leger, L. d’Hendecourt, and D. Defourneau. *Physics of IR Emission by Interstellar PAH Molecules*. *Astronomy & Astrophysics* **216**(1-2), 148–164 (1989).
- [10] L. J. Allamandola, A. G. G. M. Tielens, and J. R. Barker. *Interstellar polycyclic aromatic hydrocarbons: The infrared emission bands, the excitation emission mechanism, and the astrophysical implications*. *Astrophysical Journal Supplement Series* **71**(4), 733–775 (1989).
- [11] C. Joblin, L. d’Hendecourt, A. Leger, and D. Defourneau. *Infrared spectroscopy of gas-phase PAH molecules. I. Role of the physical environment*. *Astronomy & Astrophysics* **281**(3), 923–936 (1994).
- [12] C. Joblin, P. Boissel, A. Leger, L. d’Hendecourt, and D. Defourneau. *Infrared spectroscopy of gas-phase PAH molecules. II. Role of the temperature*. *Astronomy & Astrophysics* **299**(3), 835–846 (1995).
- [13] A. D. McFadzean, D. C. B. Whittet, A. J. Longmore, M. F. Bode, and A. J. Adamson. *Infrared studies of dust and gas towards the Galactic Centre - 3-5 μm spectroscopy*. *Monthly Notices of the Royal Astronomical Society* **241**(4), 873–882 (1989).
- [14] S. A. Sandford, Y. J. Pendleton, and L. J. Allamandola. *The galactic distribution of aliphatic hydrocarbons in the diffuse interstellar medium*. *Astrophysical Journal* **440**(2), 697–705 (1995).
- [15] Y. J. Pendleton and L. J. Allamandola. *The organic refractory material in the diffuse interstellar medium: Mid-infrared spectroscopic constraints*. *Astrophysical Journal Supplement Series* **138**(1), 75–98 (2002).

- [16] T. J. Millar, J. M. C. Rawlings, A. Bennett, P. D. Brown, and S. B. Charnley. *Gas-Phase Reactions And Rate Coefficients For Use In Astrochemistry - The UMIST Ratefile*. Astronomy & Astrophysics Supplement Series **87**(3), 585–619 (1991).
- [17] H. H. Lee, R. P. A. Bettens, and E. Herbst. *Fractional abundances of molecules in dense interstellar clouds: A compendium of recent model results*. Astronomy & Astrophysics Supplement Series **119**(1), 111–114 (1996).
- [18] W. W. Duley. *Chemical evolution of carbonaceous material in interstellar clouds*. Astrophysical Journal **528**(2), 841–848 (2000).
- [19] E. Herbst and W. Klemperer. *Formation and Depletion of Molecules in Dense Interstellar Clouds*. Astrophysical Journal **185**(2), 505–533 (1973).
- [20] A. Dalgarno and J. H. Black. *Molecule formation in interstellar gas*. Reports on Progress in Physics **39**(6), 573–612 (1976).
- [21] M. Frenklach and E. D. Feigelson. *Formation of Polycyclic Aromatic Hydrocarbons in Circumstellar Envelopes*. Astrophysical Journal **341**(1), 372–384 (1989).
- [22] E. Herbst and C. M. Leung. *Gas-Phase Production of Complex Hydrocarbons, Cyanopolyynes, and Related Compounds in Dense Interstellar Clouds*. Astrophysical Journal Supplement Series **69**(2), 271–300 (1989).
- [23] M. Frenklach and E. D. Feigelson. . In: *From Stardust To Planetesimals*, edited by Y. Pendleton and A. G. G. M. Tielens (1997), ASP, p. 109.
- [24] E. Herbst and C. M. Leung. *The gas phase production of CH₂CN and other organonitrogen species in dense interstellar clouds*. Astronomy & Astrophysics **233**(1), 177–180 (1990).
- [25] E. Herbst. *The in situ formation of large molecules in dense interstellar clouds*. Astrophysical Journal **366**(1), 133–140 (1991).
- [26] G. Seifert, D. Porezag, and T. Frauenheim. *Calculations of molecules, clusters, and solids with a simplified LCAO-DFT-LDA scheme*. International Journal of Quantum Chemistry **58**(2), 185–192 (1996).
- [27] D. Porezag, T. Frauenheim, T. Kohler, G. Seifert, and R. Kaschner. *Construction of tight-binding-like potentials on the basis of density-functional theory: Application to carbon*. Physical Review B **51**(19), 12947–12957 (1995).
- [28] R. O. Jones and G. Seifert. *Structure of Phosphorus Clusters Using Simulated Annealing. II. P₉, P₁₀, P₁₁, Anions P₄²⁻, P₁₀²⁻, P₁₁³⁻, and Cations P_n⁺ To N = 11*. Journal of Chemical Physics **96**(10), 7564–7572 (1992).
- [29] G. Fischer, R. Barthel, and G. Seifert. *Molecular dynamics study of the reaction C₃ + H₃⁺*. European Physical Journal D **35**, 479–481 (2005).
- [30] J. Schulte and G. Seifert. *DFT-LDA Molecular Dynamics of Molecular Collision Processes*. Chemical Physics Letters **221**(3-4), 230–236 (1994).
- [31] P. Blaudeck, T. Frauenheim, D. Porezag, G. Seifert, and E. Fromm. *A method and results for realistic molecular dynamic simulation of hydrogenated amorphous carbon structures using a scheme consisting of a linear combination of atomic orbitals with the local-density approximation*. Journal of Physics - Condensed Matter **4**(30), 6389–6400 (1992).
- [32] G. Winnewisser and E. Herbst. *Interstellar Molecules*. Reports on Progress in Physics **56**(10), 1209–1273 (1993).
- [33] R. P. Lindstedt and G. Skevis. *Chemistry of acetylene flames*. Combustion Science and Technology **125**(1-6), 73–137 (1997).

-
- [34] Z. X. Wang and M. B. Huang. *Insertions of methylidyne and silylidyne into methane and silane*. Journal of the Chemical Society - Faraday Transactions **94**(5), 635–640 (1998).
- [35] J. Benedikt, S. Agarwal, D. Eijkman, W. Vandamme, M. Creatore, and M. C. M. van de Sanden. *Threshold ionization mass spectrometry of reactive species in remote Ar/C₂H₂ expanding thermal plasma*. Journal of Vacuum Science & Technology A **23**(5), 1400–1412 (2005).
- [36] M. C. McCarthy, C. A. Gottlieb, H. Gupta, and P. Thaddeus. *Laboratory and astronomical identification of the negative molecular ion C₆H⁻*. Astrophysical Journal **652**(2), L141–L144 (2006).
- [37] P. Botschwina. *Spectroscopic properties of interstellar molecules: Theory and experiment*. Physical Chemistry Chemical Physics **5**(16), 3337–3348 (2003).
- [38] M. C. McCarthy, W. Chen, M. J. Travers, and P. Thaddeus. *Microwave spectra of 11 polyynic carbon chains*. Astrophysical Journal Supplement Series **129**(2), 611–623 (2000).
- [39] J. Cernicharo, C. A. Gottlieb, M. Guelin, T. C. Killian, G. Paubert, P. Thaddeus, and J. M. Vrtilik. *Astronomical detection of H₂CCC*. Astrophysical Journal **368**(2), L39–L41 (1991).
- [40] P. W. Merrill. *Stationary lines in the spectrum of the binary star Boss 6142*. Astrophysical Journal **83**(2), 126–128 (1936).
- [41] G. H. Herbig. *The Diffuse Interstellar Bands*. Annual Review of Astronomy & Astrophysics **33**, 19–73 (1995).
- [42] J. Krelowski, G. A. Galazutdinov, F. A. Musaev, and J. Nirski. *Identification of the naphthalene cation in space?* Monthly Notices of the Royal Astronomical Society **328**(3), 810–814 (2001).
- [43] G. Mallocci, G. Mulas, and C. Joblin. *Electronic absorption spectra of PAHs up to vacuum UV - Towards a detailed model of interstellar PAH photophysics*. Astronomy & Astrophysics **426**(1), 105–117 (2004).
- [44] G. Mallocci, G. Mulas, G. Cappellini, V. Fiorentini, and I. Porceddu. *Theoretical electron affinities of PAHs and electronic absorption spectra of their mono-anions*. Astronomy & Astrophysics **432**(2), 585–594 (2005).
- [45] G. F. Mitchell and W. T. Huntress. *Long chain carbon molecules and diffuse interstellar lines*. Nature **278**(5706), 722–723 (1979).
- [46] A. E. Douglas. *Origin of diffuse interstellar lines*. Nature **269**(5624), 130–132 (1977).
- [47] W. Krätschmer, N. Sorg, and D. R. Huffman. *Spectroscopy of matrix-isolated carbon cluster molecules between 200 nm and 850 nm wavelength*. Surface Science **156**, 814–821 (1985).
- [48] P. F. Bernath, K. H. Hinkle, and J. J. Keady. *Detection of C₅ in the circumstellar shell of IRC+10216*. Science **244**(4904), 562–564 (1989).
- [49] E. L. Fitzpatrick and D. Massa. *An Analysis of the Shapes of Ultraviolet Extinction Curves. I. The 2175 Å Bump*. Astrophysical Journal **307**(1), 286–294 (1986).
- [50] J. H. Hecht. *The nature of the dust around R-Coronae-Borealis stars - Isolated amorphous carbon or graphite fractals*. Astrophysical Journal **367**(2), 635–640 (1991).
- [51] H. W. Kroto, J. R. Heath, S. C. O'Brien, R. F. Curl, and R. E. Smalley. *C₆₀ buckminsterfullerene*. Nature **318**(6042), 162–163 (1985).
- [52] A. Leger, L. d'Hendecourt, L. Verstraete, and W. Schmidt. *Remarkable Candidates for the Carrier of the Diffuse Interstellar Bands: C₆₀⁺ and Other Polyhedral Carbon Ions*. Astronomy & Astrophysics **203**(1), 145–148 (1988).
- [53] J. Fulara, M. Jakobi, and J. P. Maier. *Electronic and infrared spectra of C₆₀⁺ and C₆₀⁻ in neon and argon matrices*. Chemical Physics Letters **211**(2-3), 227–234 (1993).

- [54] D. C. B. Whittet, A. J. Adamson, W. W. Duley, T. R. Geballe, and A. D. Mcfadzean. *Infrared spectroscopy of dust In the Taurus dark clouds: solid carbon monoxide*. Monthly Notices of the Royal Astronomical Society **241**(4), 707–720 (1989).
- [55] A. P. Jones, W. W. Duley, and D. A. Williams. *Interstellar Extinction Correlations*. Monthly Notices of the Royal Astronomical Society **229**(2), 213–221 (1987).
- [56] Y. J. Pendleton, S. A. Sandford, L. J. Allamandola, A. G. G. M. Tielens, and K. Sellgren. *Near-Infrared Absorption Spectroscopy of Interstellar Hydrocarbon Grains*. Astrophysical Journal **437**(2), 683–696 (1994).
- [57] F. C. Gillett, W. J. Forrest, and K. M. Merrill. *8-13-Micron Spectra of NGC 7027, Bd+30° 3639, and NGC 6572*. Astrophysical Journal **183**(1), 87–93 (1973).
- [58] K. Sellgren. *The Near-Infrared Continuum Emission Of Visual Reflection Nebulae*. Astrophysical Journal **277**(2), 623–633 (1984).
- [59] A. Leger and J. L. Puget. *Identification Of The Unidentified IR Emission Features Of Interstellar Dust*. Astronomy & Astrophysics **137**(1), L5–L8 (1984).
- [60] W. W. Duley and D. A. Williams. *The infrared spectrum of interstellar dustsurface functional groups on carbon*. Monthly Notices of the Royal Astronomical Society **196**(1), 269–274 (1981).
- [61] L. J. Allamandola. In: *Galactic and Extragalactic IR Spectroscopy*, edited by M. F. Kessler and J. P. Phillips (Reidel, Dordrecht, Netherlands, 1984).
- [62] D. Cesarsky, J. Lequeux, A. Abergel, M. Perault, E. Palazzi, S. Madden, and D. Tran. *Infrared spectrophotometry of NGC 7023 with ISOCAM*. Astronomy & Astrophysics **315**(2), L305–L308 (1996).
- [63] D. Cesarsky, J. Lequeux, A. Abergel, M. Perault, E. Palazzi, S. Madden, and D. Tran. *Infrared spectrophotometry of M17 with ISOCAM*. Astronomy & Astrophysics **315**(2), L309–L312 (1996).
- [64] M. Jura, C. J. Bohac, B. Sargent, W. J. Forrest, J. Green, D. M. Watson, G. C. Sloan, F. Markwick-Kemper, C. H. Chen, and J. Najita. *Polycyclic aromatic hydrocarbons orbiting HD 233517, an evolved oxygen-rich red giant*. Astrophysical Journal **637**(1), L45–L48 (2006).
- [65] F. J. Molster, M. E. van den Ancker, A. G. G. M. Tielens, L. B. F. M. Waters, D. A. Beintema, C. Waelkens, T. de Jong, T. de Graauw, K. Justtanont, L. Yamamura, B. Vandenbussche, and A. Heras. *The shape and strength of circumstellar PAH emission bands*. Astronomy & Astrophysics **315**(2), L373–L376 (1996).
- [66] L. Verstraete, C. Pech, C. Moutou, K. Sellgren, C. M. Wright, M. Giard, A. Leger, R. Timmermann, and S. Drapatz. *The aromatic infrared bands as seen by ISO-SWS: Probing the PAH model*. Astronomy & Astrophysics **372**(3), 981–997 (2001).
- [67] L. J. Allamandola, A. G. G. M. Tielens, and J. R. Barker. *Polycyclic aromatic hydrocarbons and the unidentified infrared emission bands: Auto exhaust along the milky way!* Astrophysical Journal **290**(1), L25–L28 (1985).
- [68] J. L. Puget, A. Leger, and F. Boulanger. *Contribution of Large Polycyclic Aromatic Molecules to the Infrared Emission of the Interstellar Medium*. Astronomy & Astrophysics **142**(2), L19–L22 (1985).
- [69] J. A. Cardelli, D. M. Meyer, M. Jura, and B. D. Savage. *The abundance of interstellar carbon*. Astrophysical Journal **467**(1), 334–340 (1996).
- [70] T. Henning and F. Salama. *Carbon in the Universe*. Science **282**(5397), 2204–2210 (1998).

-
- [71] W. A. Schutte, A. G. G. M. Tielens, and L. J. Allamandola. *Theoretical Modeling of the Infrared Fluorescence from Interstellar Polycyclic Aromatic Hydrocarbons*. *Astrophysical Journal* **415**(1), 397–414 (1993).
- [72] D. J. Cook, S. Schlemmer, N. Balucani, D. R. Wagner, B. Steiner, and R. J. Saykally. *Infrared emission spectra of candidate interstellar aromatic molecules*. *Nature* **380**(6571), 227–229 (1996).
- [73] D. J. Cook and R. J. Saykally. *Simulated infrared emission spectra of highly excited polyatomic molecules: A detailed model of the PAH-UIR hypothesis*. *Astrophysical Journal* **493**(2), 793–802 (1998).
- [74] D. M. Hudgins and L. J. Allamandola. *The spacing of the interstellar 6.2 and 7.7 micron emission features as an indicator of polycyclic aromatic hydrocarbon size*. *Astrophysical Journal* **513**(1), L69–L73 (1999).
- [75] L. J. Allamandola, D. M. Hudgins, and S. A. Sandford. *Modeling the unidentified infrared emission with combinations of polycyclic aromatic hydrocarbons*. *Astrophysical Journal* **511**(2), L115–L119 (1999).
- [76] L. Verstraete, A. Leger, L. d’Hendecourt, O. Dutuit, and D. Defourneau. *Ionization cross-section measurements for 2 PAH molecules: Implications for the heating of diffuse interstellar gas*. *Astronomy & Astrophysics* **237**(2), 436–444 (1990).
- [77] G. C. Clayton, K. D. Gordon, F. Salama, L. J. Allamandola, P. G. Martin, T. P. Snow, D. C. B. Whittet, A. N. Witt, and M. J. Wolff. *The role of polycyclic aromatic hydrocarbons in ultraviolet extinction. I. Probing small molecular polycyclic aromatic hydrocarbons*. *Astrophysical Journal* **592**(2), 947–952 (2003).
- [78] J. Bergeat, A. Knapik, and B. Rutily. *Carbon-rich giants in the HR diagram and their luminosity function*. *Astronomy & Astrophysics* **390**, 967–986 (2002).
- [79] D. D. Clayton, E. A. N. Deneault, and B. S. Meyer. *Condensation of carbon in radioactive supernova gas*. *Astrophysical Journal* **562**(1), 480–493 (2001).
- [80] A. P. Jones, A. G. G. M. Tielens, and D. J. Hollenbach. *Grain shattering in shocks: The interstellar grain size distribution*. *Astrophysical Journal* **469**(2), 740–764 (1996).
- [81] E. Herbst. *Chemistry In The Interstellar Medium*. *Annual Review of Physical Chemistry* **46**, 27–53 (1995).
- [82] G. Gioumouzis and D. P. Stevenson. *Reactions of Gaseous Molecule Ions with Gaseous Molecules. V. Theory*. *Journal of Chemical Physics* **29**(2), 294–299 (1958).
- [83] S. S. Prasad and W. T. Huntress. *A Model for Gas-Phase Chemistry in Interstellar Clouds: I. The Basic Model, Library of Chemical Reactions, and Chemistry Among C, N, and O Compounds*. *Astrophysical Journal Supplement Series* **43**(1), 1 (1980).
- [84] S. S. Prasad and W. T. Huntress. *A Model for Gas-Phase Chemistry in Interstellar Clouds: II. Nonequilibrium Effects and Effects of Temperature and Activation Energies*. *Astrophysical Journal* **239**(1), 151–165 (1980).
- [85] E. Herbst. *Chemistry of star-forming regions*. *Journal of Physical Chemistry A* **109**(18), 4017–4029 (2005).
- [86] W. D. Watson. *Gas-Phase Reactions in Astrophysics*. *Annual Review of Astronomy and Astrophysics* **16**, 585–615 (1978).
- [87] E. Herbst. *A Model For Competitive Binary And Ternary Ion Molecule Reactions*. *Journal of Chemical Physics* **82**(9), 4017–4021 (1985).

- [88] S. J. Klippenstein, Y. C. Yang, V. Ryzhov, and R. C. Dunbar. *Theory and modeling of ion-molecule radiative association kinetics*. Journal of Chemical Physics **104**(12), 4502–4516 (1996).
- [89] E. Herbst and R. C. Dunbar. *A global view of radiative association as a function of product size: Interstellar implications*. Monthly Notices of the Royal Astronomical Society **253**(2), 341–349 (1991).
- [90] E. A. Bergin, W. D. Langer, and P. F. Goldsmith. *Gas-phase chemistry in dense interstellar clouds including grain surface molecular depletion and desorption*. Astrophysical Journal **441**(1), 222–243 (1995).
- [91] T. J. Millar and J. Hatchell. *Chemical models of hot molecular cores*. Faraday Discussions pp. 15–30 (1998).
- [92] S. B. Charnley, A. G. G. M. Tielens, and T. J. Millar. *On the Molecular Complexity of the Hot Cores in Orion A: Grain Surface Chemistry as "The Last Refuge of the Scoundrel"*. Astrophysical Journal **399**(1), L71–L74 (1992).
- [93] T. J. Millar, P. R. A. Farquhar, and K. Willacy. *The UMIST database for astrochemistry 1995*. Astronomy & Astrophysics Supplement Series **121**(1), 139–185 (1997).
- [94] Y. H. Le Teuff, T. J. Millar, and A. J. Markwick. *The UMIST database for astrochemistry 1999*. Astronomy & Astrophysics Supplement Series **146**(1), 157–168 (2000).
- [95] V. Wakelam, E. Herbst, and F. Selsis. *The effect of uncertainties on chemical models of dark clouds*. Astronomy & Astrophysics **451**(2), 551–562 (2006).
- [96] I. Cherchneff and J. R. Barker. *Polycyclic Aromatic Hydrocarbons and Molecular Equilibria in Carbon-Rich Stars*. Astrophysical Journal **394**(2), 703–716 (1992).
- [97] G. Pascoli and A. Polleux. *Condensation and growth of hydrogenated carbon clusters in carbon-rich stars*. Astronomy & Astrophysics **359**(2), 799–810 (2000).
- [98] J. Cernicharo. *The polymerization of acetylene, hydrogen cyanide, and carbon chains in the neutral layers of carbon-rich proto-planetary nebulae*. Astrophysical Journal **608**(1), L41–L44 (2004).
- [99] R. P. A. Bettens and E. Herbst. *The abundance of very large hydrocarbons and carbon clusters in the diffuse interstellar medium*. Astrophysical Journal **468**(2), 686–693 (1996).
- [100] S. E. Stein. *On the High Temperature Chemical Equilibria of Polycyclic Aromatic Hydrocarbons*. Journal of Physical Chemistry **82**(5), 566–571 (1978).
- [101] V. V. Kislov, N. I. Islamova, A. M. Kolker, S. H. Lin, and A. M. Mebel. *Hydrogen abstraction acetylene addition and Diels-Alder mechanisms of PAH formation: A detailed study using first principles calculations*. Journal of Chemical Theory and Computation **1**(5), 908–924 (2005).
- [102] P. Langevin. *A fundamental formula of kinetic theory*. Annales de Chimie et de Physique **5**, 245–288 (1905).
- [103] L. P. Theard and W. H. Hamill. *Energy Dependence of Cross Sections of Some Ion-Molecule Reactions*. Journal of the American Chemical Society **84**(7), 1134–1139 (1962).
- [104] S. K. Gupta, E. G. Jones, A. G. Harrison, and J. J. Myher. *Reactions Of thermal energy ions. VI. Hydrogen-transfer ion-molecule reactions involving polar molecules*. Canadian Journal of Chemistry **45**(24), 3107–3117 (1967).
- [105] T. Su and M. T. Bowers. *Ion-Polar Molecule Collisions . The effect of Molecular Size on Ion-Polar Molecule Rate Constants*. Journal of the American Chemical Society **95**(23), 7609–7610 (1973).

-
- [106] T. Su and M. T. Bowers. *Theory of ion-polar molecule collisions. Comparison with experimental charge transfer reactions of rare gas ions to geometric isomers of difluorobenzene and dichloroethylene*. Journal of Chemical Physics **58**(7), 3027–3037 (1973).
- [107] T. Su and M. T. Bowers. *Parameterization of Average Dipole Orientation Theory: Temperature Dependence*. International Journal of Mass Spectrometry and Ion Processes **17**(2), 211–212 (1975).
- [108] T. Beyer and D. F Swinehart. *Number Of Multiply-Restricted Partitions*. Communications of the ACM **16**(6), 379–379 (1973).
- [109] S. E. Stein and B. S. Rabinovitch. *Accurate evaluation of internal energy-level sums and densities including anharmonic oscillators and hindered rotors*. Journal of Chemical Physics **58**(6), 2438–2445 (1973).
- [110] K. A. Holbrook, M. J. Pilling, and S. H. Robertson. *Unimolecular reactions* (John Wiley & Sons Ltd, Chichester, UK, 1996), 2nd edn.
- [111] G. Z. Whitten and B. S. Rabinovitch. *Accurate and Facile Approximation for Vibrational Energy-Level Sums*. Journal of Chemical Physics **38**(10), 2466–2473 (1963).
- [112] D. C. Tardy, B. S. Rabinovitch, and G. Z. Whitten. *Vibration-Rotation Energy-Level Density Calculations*. Journal of Chemical Physics **48**(3), 1427–1429 (1968).
- [113] R. A. Marcus and O. K. Rice. *The kinetics of the recombination of methyl radicals and iodine atoms*. Journal of Physical and Colloid Chemistry **55**(6), 894–908 (1951).
- [114] G. Z. Whitten and B. S. Rabinovitch. *Approximation for Rotation-Vibration Energy Level Sums*. Journal of Chemical Physics **41**, 1883 (1964).
- [115] H. Eyring. *The Activated Complex in Chemical Reactions*. Journal of Chemical Physics **3**(2), 107–115 (1935).
- [116] M. G. Evans and M. Polanyi. *Some applications of the transition state method to the calculation of reaction velocities, especially in solution*. Transactions of the Faraday Society **31**(1), 875–893 (1935).
- [117] P. W. Atkins. *Physical chemistry* (Oxford University Press, Oxford, UK, 1998), 6th edn.
- [118] E. Herbst. *An Approach to the Estimation of Polyatomic Vibrational Radiative Relaxation Rates*. Chemical Physics **65**(2), 185–195 (1982).
- [119] M. J. Frisch, G. W. Trucks, H. B. Schlegel, G. E. Scuseria, M. A. Robb, J. R. Cheeseman, J. A. Montgomery, Jr., T. Vreven, K. N. Kudin, J. C. Burant, J. M. Millam, S. S. Iyengar, J. Tomasi, V. Barone, B. Mennucci, M. Cossi, G. Scalmani, N. Rega, G. A. Petersson, H. Nakatsuji, M. Hada, M. Ehara, K. Toyota, R. Fukuda, J. Hasegawa, M. Ishida, T. Nakajima, Y. Honda, O. Kitao, H. Nakai, M. Klene, X. Li, J. E. Knox, H. P. Hratchian, J. B. Cross, V. Bakken, C. Adamo, J. Jaramillo, R. Gomperts, R. E. Stratmann, O. Yazyev, A. J. Austin, R. Cammi, C. Pomelli, J. W. Ochterski, P. Y. Ayala, K. Morokuma, G. A. Voth, P. Salvador, J. J. Dannenberg, V. G. Zakrzewski, S. Dapprich, A. D. Daniels, M. C. Strain, O. Farkas, D. K. Malick, A. D. Rabuck, K. Raghavachari, J. B. Foresman, J. V. Ortiz, Q. Cui, A. G. Baboul, S. Clifford, J. Cioslowski, B. B. Stefanov, G. Liu, A. Liashenko, P. Piskorz, I. Komaromi, R. L. Martin, D. J. Fox, T. Keith, M. A. Al-Laham, C. Y. Peng, A. Nanayakkara, M. Challacombe, P. M. W. Gill, B. Johnson, W. Chen, M. W. Wong, C. Gonzalez, and J. A. Pople. *Gaussian 03, Revision C.02*. Gaussian, Inc., Wallingford, CT, 2004.
- [120] A. Komornicki and J. W. Mciver. *Efficient ab initio method for computing infrared and Raman intensities: Application to ethylene*. Journal of Chemical Physics **70**(4), 2014–2016 (1979).

- [121] J. F. Durana and J. D. McDonald. *Infrared chemiluminescence studies of chlorine substitution reactions with brominated unsaturated hydrocarbons*. *Journal of Chemical Physics* **64**(6), 2518–2527 (1976).
- [122] Z. Slanina. *Potential-hypersurface local minima and temperature*. *Theoretica Chimica Acta* **83**(3-4), 257–261 (1992).
- [123] Z. Slanina, K. Kobayashi, and S. Nagase. *Temperature development in a set of C₆₀H₃₆ isomers*. *Chemical Physics Letters* **382**(1-2), 211–215 (2003).
- [124] Z. Slanina, X. Zhao, F. Uhlik, S. L. Lee, and L. Adamowicz. *Computing Enthalpy-Entropy Interplay for Isomeric Fullerenes*. *International Journal of Quantum Chemistry* **99**(5), 640–653 (2004).
- [125] H. B. Schlegel. *Optimization of equilibrium geometries and transition structures*. *Journal of Computational Chemistry* **3**(2), 214–218 (1982).
- [126] C. Møller and M. S. Plesset. *Note on an approximation treatment for many-electron systems*. *Physical Review* **46**(7), 0618–0622 (1934).
- [127] R. Krishnan and J. A. Pople. *Approximate 4th-order perturbation theory of electron correlation energy*. *International Journal of Quantum Chemistry* **14**(1), 91–100 (1978).
- [128] W. J. Hehre, L. Radom, P. v. R. Schleyer, and J. A. Pople. *Ab Initio Molecular Orbital Theory* (Wiley, New York, U.S.A., 1986).
- [129] M. Head-Gordon, J. A. Pople, and M. J. Frisch. *MP2 energy evaluation by direct methods*. *Chemical Physics Letters* **153**(6), 503–506 (1988).
- [130] M. J. Frisch, M. Head-Gordon, and J. A. Pople. *A direct MP2 gradient method*. *Chemical Physics Letters* **166**(3), 275–280 (1990).
- [131] A. Szabo and N. S. Ostlund. *Modern Quantum Chemistry - Introduction to Advanced Electronic Structure Theory* (Dover Publications, Inc., Mineola, N.Y., USA, 1996), 1st edn.
- [132] W. J. Hehre, R. Ditchfield, and J. A. Pople. *Self-Consistent Molecular Orbital Methods. XII. Further Extensions of Gaussian-Type Basis Sets for Use in Molecular Orbital Studies of Organic Molecules*. *Journal of Chemical Physics* **56**(5), 2257–2261 (1972).
- [133] T. H. Dunning. *Gaussian basis sets for use in correlated molecular calculations. I. The atoms boron through neon and hydrogen*. *Journal of Chemical Physics* **90**(2), 1007–1023 (1989).
- [134] J. A. Pople, M. Head-Gordon, D. J. Fox, K. Raghavachari, and L. A. Curtiss. *Gaussian-1 theory: A general procedure for prediction of molecular-energies*. *Journal of Chemical Physics* **90**(10), 5622–5629 (1989).
- [135] J. A. Pople, M. Headgordon, and K. Raghavachari. *Quadratic configuration interaction. A general technique for determining electron correlation energies*. *Journal of Chemical Physics* **87**(10), 5968–5975 (1987).
- [136] L. A. Curtiss, K. Raghavachari, P. C. Redfern, V. Rassolov, and J. A. Pople. *Gaussian-3 (G3) theory for molecules containing first and second-row atoms*. *Journal of Chemical Physics* **109**(18), 7764–7776 (1998).
- [137] W. Koch and M. C. Holthausen. *A Chemist's Guide to Density Functional Theory* (Wiley-VCH, Weinheim, Germany, 2001), 2nd edn.
- [138] J. P. Perdew and Y. Wang. *Accurate and simple analytic representation of the electron-gas correlation energy*. *Physical Review B* **45**(23), 13244–13249 (1992).
- [139] J. P. Perdew, J. A. Chevary, S. H. Vosko, K. A. Jackson, M. R. Pederson, D. J. Singh, and C. Fiolhais. *Atoms, Molecules, Solids, And Surfaces applications Of The Generalized Gradient Approximation For Exchange And Correlation*. *Physical Review B* **46**(11), 6671–6687 (1992).

-
- [140] J. P. Perdew, K. Burke, and M. Ernzerhof. *Generalized gradient approximation made simple*. Physical Review Letters **77**(18), 3865–3868 (1996).
- [141] N. Godbout, D. R. Salahub, J. Andzelm, and E. Wimmer. *Optimization of Gaussian-type basis-sets for local spin density functional calculations. Part I. Boron through neon, optimization technique and validation*. Canadian Journal of Chemistry **70**(2), 560–571 (1992).
- [142] A. D. Becke. *Density-functional thermochemistry. III. The role of exact exchange*. Journal of Chemical Physics **98**(7), 5648–5652 (1993).
- [143] P. J. Stephens, F. J. Devlin, C. F. Chabalowski, and M. J. Frisch. *Ab initio calculation of vibrational absorption and circular dichroism spectra using density functional force fields*. Journal of Physical Chemistry **98**(45), 11623–11627 (1994).
- [144] G. Seifert, H. Eschrig, and W. Bieger. *An approximation variant of LCAO- X_α methods*. Zeitschrift für physikalische Chemie (Leipzig) **267**(3), 529–539 (1986).
- [145] A. Köster, R. Flores-Moreno, G. Geudtner, A. Goursot, T. Heine, J. Reveles, A. Vela, S. Patchkovskii, and D. R. Salahub. *deMon 2004*. NRC, Canada.
- [146] D. Tomanek and M. A. Schluter. *Structure and bonding of small semiconductor clusters*. Physical Review B **36**(2), 1208–1217 (1987).
- [147] W. Matthew, C. Foulkes, and R. Haydock. *Tight-binding models and density-functional theory*. Physical Review B **39**(17), 12520–12536 (1989).
- [148] M. Elstner, T. Frauenheim, E. Kaxiras, G. Seifert, and S. Suhai. *A self-consistent charge density-functional based tight-binding scheme for large biomolecules*. Physica Status Solidi B - Basic Research **217**(1), 357–376 (2000).
- [149] M. Elstner. *The SCC-DFTB method and its application to biological systems*. Theoretical Chemistry Accounts **116**(1-3), 316–325 (2006).
- [150] R. G. Parr and R. G. Pearson. *Absolute hardness - companion parameter to absolute electronegativity*. Journal of the American Chemical Society **105**(26), 7512–7516 (1983).
- [151] L. Verlet. *Computer "Experiments" on Classical Fluids. I. Thermodynamical Properties of Lennard-Jones Molecules*. Physical Review **159**(1), 98–& (1967).
- [152] G. Mills and H. Jónsson. *Quantum and thermal effects in H_2 dissociative adsorption: Evaluation of free energy barriers in multidimensional quantum systems*. Physical Review Letters **72**(7), 1124–1127 (1994).
- [153] G. Mills, H. Jónsson, and G. K. Schenter. *Reversible work transition state theory: application to dissociative adsorption of hydrogen*. Surface Science **324**(2-3), 305–337 (1995).
- [154] A. Ulitsky and R. Elber. *A new technique to calculate steepest descent paths in flexible polyatomic systems*. Journal of Chemical Physics **92**(2), 1510–1511 (1990).
- [155] C. Choi and R. Elber. *Reaction path study of helix formation in tetrapeptides: Effect of side chains*. Journal of Chemical Physics **94**(1), 751–760 (1991).
- [156] H. Jónsson, G. Mills, and W. Jacobsen. *Nudged elastic band method for finding minimum energy paths of transitions*. In: *Classical and Quantum Dynamics in Condensed Phase Simulations*, edited by B. J. Berne, G. Ciccotti, and D. F. Coker (World Scientific, Singapore, 1998), chap. 16, p. 385.
- [157] G. Henkelman, B. P. Uberuaga, and H. Jónsson. *A climbing image nudged elastic band method for finding saddle points and minimum energy paths*. Journal of Chemical Physics **113**(22), 9901–9904 (2000).

- [158] G. Henkelman and H. Jónsson. *Improved tangent estimate in the nudged elastic band method for finding minimum energy paths and saddle points*. Journal of Chemical Physics **113**(22), 9978–9985 (2000).
- [159] M. P. Allen and D. J. Tildesley. *Computer Simulation of Liquids* (Clarendon, Oxford, UK, 1989).
- [160] O. R. Inderwildi, S. J. Jenkins, and D. A. King. *An Unexpected Pathway for the Catalytic Oxidation of Methylidyne on Rh{111} as a Route to Syngas*. Journal of the American Chemical Society **129**(6), 1751–1759 (2007).
- [161] J. Peeters, I. Langhans, W. Boullart, M. T. Nguyen, and K. Devriendt. *Formation of CH($A^4\Sigma^-$ and/or $X^2\Pi$) in the Reaction of Ketenyl Radicals with Oxygen atoms. Determination of the Methylidyne Yield at 290 K and ab initio Calculations*. Journal of Physical Chemistry **98**(46), 11988–11996 (1994).
- [162] M. R. Berman, J. W. Fleming, A. B. Harvey, and M. C. Lin. *Temperature Dependence of the Reactions of CH Radicals with Unsaturated Hydrocarbons*. Chemical Physics **73**(1-2), 27–33 (1982).
- [163] J. E. Butler, J. W. Fleming, L. P. Goss, and M. C. Lin. *Kinetics of CH Radical Reactions with Selected Molecules at Room Temperature*. Chemical Physics **56**(3), 355–365 (1981).
- [164] J. Benedikt, K. G. Y. Letourneur, M. Wisse, D. C. Schram, and M. C. M. de Sanden. *Plasma chemistry during deposition of a-C:H*. Diamond and Related Materials **11**(3-6), 989–993 (2002).
- [165] R. Engeln, K. G. Y. Letourneur, M. G. H. Boogaarts, M. C. M. van de Sanden, and D. C. Schram. *Detection of CH in an expanding argon/acetylene plasma using cavity ring down absorption spectroscopy*. Chemical Physics Letters **310**(5-6), 405–410 (1999).
- [166] E. F. van Dishoeck, R. A. Beärda, and M. C. van Hemert. *The photodissociation of interstellar and cometary CH₂*. Astronomy & Astrophysics **307**(2), 645–652 (1996).
- [167] A. Kasdan, E. Herbst, and W. C. Lineberger. *Laser Photoelectron Spectrometry of CH⁻*. Chemical Physics Letters **31**(1), 78–82 (1975).
- [168] D. H. Phelps and F. W. Dalby. *Experimental determination of electric dipole moment of ground electronic state of CH*. Physical Review Letters **16**(1), 3–4 (1966).
- [169] K. L. Baluja and A. Z. Msezane. *Electron collisions with methylidyne (CH) radical using the R-matrix method*. Journal of Physics B - Atomic Molecular and Optical Physics **34**(15), 3157–3170 (2001).
- [170] T. Weselak, G. Galazutdinov, F. Musaev, and J. Krelowski. *Relation between CH cation and neutral/molecular hydrogen*. Astronomy & Astrophysics **479**(1), 149–154 (2008).
- [171] G. Herzberg and J. W. C. Johns. *New spectra of the CH molecule*. Astrophysical Journal **158**(1P1), 399 (1969).
- [172] C.E. Moore. *Ionization potentials and ionization limits derived from the analyses of optical spectra*. Natl. Stand. Ref. Data Ser., (U.S. Natl. Bur. Stand.) **34**, 1 (1970).
- [173] M. Scheer, R. C. Bilodeau, C. A. Brodie, and H. K. Haugen. *Systematic study of the stable states of C⁻, Si⁻, Ge⁻, and Sn⁻ via infrared laser spectroscopy*. Physical Review A **58**(4), 2844–2856 (1998).
- [174] D. Shiner, J. M. Gilligan, B. M. Cook, and W. Lichten. *H₂, D₂, and HD ionization potentials by accurate calibration of several iodine lines*. Physical Review A **47**(5), 4042–4045 (1993).
- [175] C. E. Mortimer. *Chemistry: A conceptual approach* (Wadsworth Inc., Belmont, California, U.S.A., 1986), 6th edn.

- [176] P. Rosmus, P. Botschwina, and J. P. Maier. *On the ionic states of vinylidene and acetylene*. Chemical Physics Letters **84**(1), 71–76 (1981).
- [177] P. Plessis and P. Marmet. *Electroionization study of acetylene and fragment ions*. International Journal of Mass Spectrometry and Ion Processes **70**(1), 23–44 (1986).
- [178] T. L. Nguyen, A. M. Mebel, S. H. Lin, and R. I. Kaiser. *Product Branching Ratios of the $C(^3P) + C_2H_3(^2A')$ and $CH(^2\Pi) + C_2H_2(^1\Sigma_g^+)$ Reactions and Photodissociation of $H_2CC\equiv CH(^2B_1)$ at 193 and 242 nm: an ab initio/RRKM Study*. Journal of Physical Chemistry A **105**(51), 11549–11559 (2001).
- [179] S. A. Maluendes, A. D. Mclean, K. Yamashita, and E. Herbst. *Calculations on the competition between association and reaction for $C_3H^+ + H_2$* . Journal of Chemical Physics **99**(4), 2812–2820 (1993).
- [180] O. Dopfer, D. Roth, and J. P. Maier. *Interaction of $C_3H_3^+$ isomers with molecular nitrogen: IR spectra of $C_3H_3^+-(N_2)_n$ clusters ($n=1-6$)*. International Journal of Mass Spectrometry **218**(3), 281–297 (2002).
- [181] P. Thaddeus, C. A. Gottlieb, A. Hjalmarsen, L. E. B. Johansson, W. M. Irvine, P. Friberg, and R. A. Linke. *Astronomical identification of the C_3H radical*. Astrophysical Journal **294**(1), L49–L53 (1985).
- [182] L. M. Ziurys. *The chemistry in circumstellar envelopes of evolved stars: Following the origin of the elements to the origin of life*. Proceedings of the National Academy of Sciences of the United States of America **103**(33), 12274–12279 (2006).
- [183] D. Fosse, J. Cernicharo, M. Gerin, and P. Cox. *Molecular carbon chains and rings in TMC-1*. Astrophysical Journal **552**(1), 168–174 (2001).
- [184] R. D. Levine and R. B. Bernstein. *Molecular Reaction Dynamics and Chemical Reactivity* (Oxford University Press, Oxford, UK, 1987).
- [185] A. Leger, P. Boissel, F. X. Desert, and L. d’Hendecourt. *Photo-Thermo-Dissociation: A General Mechanism For Destroying Molecules*. Astronomy & Astrophysics **213**(1-2), 351–359 (1989).
- [186] F. J. Lovas, R. J. McMahon, J. U. Grabow, M. Schnell, J. Mack, L. T. Scott, and R. L. Kuczkowski. *Interstellar chemistry: A strategy for detecting polycyclic aromatic hydrocarbons in space*. Journal of the American Chemical Society **127**(12), 4345–4349 (2005).
- [187] P. Thaddeus. *The prebiotic molecules observed in the interstellar gas*. Philosophical Transactions of the Royal Society B - Biological Sciences **361**(1474), 1681–1687 (2006).
- [188] A. Scott and W. W. Duley. *The decomposition of hydrogenated amorphous carbon: A connection with polycyclic aromatic hydrocarbon molecules*. Astrophysical Journal **472**(2), L123–& (1996).
- [189] L. T. Scott. *Fragments of fullerenes: Novel syntheses, structures and reactions*. Pure and Applied Chemistry **68**(2), 291–300 (1996).
- [190] C. A. Hall. *Natural cubic and bicubic spline interpolation*. SIAM Journal on Numerical Analysis **10**(6), 1055–1060 (1973).
- [191] B. T. Lynds. *Catalogue of Dark Nebulae*. Astrophysical Journal Supplement **7**, 1 (1962).
- [192] S. L. Thorndike. *Interstellar Matter*. Astronomical Society of the Pacific **42**, 99–104 (1930).
- [193] D. C. Black and P. Bodenheimer. *Evolution of rotating interstellar clouds. II. The collapse of protostars of 1, 2, and $5M_\odot$* . Astrophysical Journal **206**(1), 138–149 (1976).
- [194] C. F. McKee and J. P. Ostriker. *A theory of the interstellar medium: Three components regulated by supernova explosions in an inhomogeneous substrate*. Astrophysical Journal **218**(1), 148–169 (1977).

- [195] D. P. Cox. *The three-phase interstellar medium revisited*. Annual Review of Astronomy and Astrophysics **43**, 337–385 (2005).
- [196] J. P. Williams, L. Blitz, and C. F. McKee. *Protostars and Planets IV* (University of Arizona Press, Tucson, U.S.A., 2000), chap. The Structure and Evolution of Molecular Clouds: from Clumps to Cores to the IMF, p. 97.
- [197] B. J. Bok and E. F. Reilly. *Small Dark Nebulae*. Astrophysical Journal **105**(2), 255–257 (1947).
- [198] D. P. Clemens, J. L. Yun, and M. H. Heyer. *Bok Globules and Small Molecular Clouds: Deep IRAS Photometry and ^{12}CO Spectroscopy*. Astrophysical Journal Supplement Series **75**(3), 877–904 (1991).
- [199] J. F. Alves, C. J. Lada, and E. A. Lada. *Internal structure of a cold dark molecular cloud inferred from the extinction of background starlight*. Nature **409**(6817), 159–161 (2001).
- [200] J. P. Vallee. *Interstellar clump behavior and magnetic effects in small clumps*. Astrophysical Journal **538**(1), 226–232 (2000).
- [201] J. H. Jeans. *The stability of a spherical nebula*. Philosophical Transactions of the Royal Society of London Series: A Containing Papers of a Mathematical or Physical Character **199**, 1–53 (1902).
- [202] P. D. Brown, S. B. Charnley, and T. J. Millar. *A model of the chemistry in hot molecular cores*. Monthly Notices of the Royal Astronomical Society **231**(2), 409–417 (1988).
- [203] A. Weigert, H. J. Wendker, and L. Wisotzki. *Astronomie und Astrophysik* (Wiley-VCH, Weinheim, Germany, 2005), 4th edn.
- [204] A. Unsöld and B. Baschek. *The new cosmos, an introduction to astronomy and astrophysics* (Springer, Berlin, Germany, 2004), 5th edn.
- [205] A. K. Shukla and J. H. Futrell. *Encyclopedia of Spectroscopy and Spektrometry* (Academic Press, San Diego, U.S.A., 1999), chap. Ion Collision Theory, p. 954.
- [206] M. Karplus and R. D. Sharma. *Exchange Reactions with Activation Energy. I. Simple Barrier Potential for (H, H_2)* . Journal of Chemical Physics **43**(9), 3259–3287 (1965).
- [207] R. A. Marcus. *Unimolecular dissociations and free radical recombination reactions*. Journal of Chemical Physics **20**(3), 359–364 (1952).
- [208] O. K. Rice and H. C. Ramsperger. *Theories of unimolecular gas reactions at low pressures*. Journal of the American Chemical Society **49**, 1617–1629 (1927).
- [209] L. S. Kassel. *Studies in homogeneous gas reactions*. Journal of Physical Chemistry **32**(2), 225–242 (1928).
- [210] J. C. Slater. *Atomic shielding constants*. Physical Review **36**(1), 0057–0064 (1930).
- [211] S. F. Boys. *Electronic wave functions. I. A general method of calculation for the stationary states of any molecular system*. Proceedings of the Royal Society of London Series A - Mathematical and Physical Sciences **200**(1063), 542–554 (1950).
- [212] W. J. Hehre, R. F. Stewart, and J. A. Pople. *Self-consistent molecular orbital methods. I. Use of gaussian expansions of slater-type atomic orbitals*. Journal of Chemical Physics **51**(6), 2657–2664 (1969).
- [213] H. Taylor and J. Simons. *Imposition of geometrical constraints on potential energy surface walking procedures*. Journal of Physical Chemistry **89**(4), 684–688 (1985).
- [214] J. Baker. *An algorithm for the location of transition states*. Journal of Computational Chemistry **7**(4), 385–395 (1986).

- [215] C. Y. Peng and H. B. Schlegel. *Combining Synchronous Transit and Quasi-Newton Methods to Find Transition-States*. Israel Journal of Chemistry **33**(4), 449–454 (1993).
- [216] C. Y. Peng, P. Y. Ayala, H. B. Schlegel, and M. J. Frisch. *Using Redundant Internal Coordinates to Optimize Equilibrium Geometries and Transition States*. Journal of Computational Chemistry **17**(1), 49–56 (1996).
- [217] L. R. Pratt. *A statistical method for identifying transition states in high dimensional problems*. Journal of Chemical Physics **85**(9), 5045–5048 (1986).
- [218] R. Elber and M. Karplus. *A method for determining reaction paths in large molecules: application to myoglobin*. Chemical Physics Letters **139**(5), 375–380 (1987).

Acknowledgement

This work marks an important step in my life. Without it, I would have not learned the fascinating world of astrochemistry, theoretical chemistry and computational science. With great pleasure I would like to thank all the people that supported me during this time:

At first place, my supervisor Prof. Dr. Gotthard Seifert for giving me the opportunity to study and the support to write the thesis in the field of astrochemistry;

Prof. Dr. Christine Joblin for her collaboration, enjoyable meetings and discussions;

Prof. Dr. Thomas Heine for the interesting collaborations and discussions;

the colleagues and guests of the Forschergruppe Laboratory Astrophysics especially Prof. Dr. Dieter Gerlich, Dr. Reinhard Scholz and Dr. Mathias Rapacioli for fruitful discussions during all the interesting workshops and seminars;

my colleagues in the workgroup for the pleasant and enjoyable time here in Dresden;

Dipl. Phys. Vietze for making me to understand the “bright” site of the computational world – without him I would still click myself through the world;

Dr. Johannes Frenzel for sharing some latex style templates and for his fruitfull discussions and proof-reading of this thesis;

Dr. Sergei Yurchenko for his proof-reading of this work and fruitfull discussions; and the Deutsche Forschungsgemeinschaft (DFG) – the administrative body of the Forschergruppe Laboratory Astrophysics – and the German-Israeli-Foundation (GIF) for financial support.

Finally, I deeply thank Dr. Isabel Llamas Jansa for her great support, patience and encouragement during my “long” time of writing and her comments and proof-reading of this work. Muchos Besos.

Versicherung § 5 Abs. 1 Nr. 5

Versicherung nach § 5 Abs. 1 Nr. 5 der Promotionsordnung der Fakultät Mathematik und Naturwissenschaften an der Technischen Universität Dresden in der Fassung vom 16. April 2003:

- a) Hiermit versichere ich, dass ich die vorliegende Arbeit ohne unzulässige Hilfe Dritter und ohne Benutzung anderer als der angegebenen Hilfsmittel angefertigt habe; die aus fremden Quellen direkt oder indirekt übernommenen Gedanken sind als solche kenntlich gemacht. Die Arbeit wurde bisher weder im Inland noch im Ausland in gleicher oder ähnlicher Form einer anderen Prüfungsbehörde vorgelegt.
- b) Die vorliegende Arbeit wurde in der Arbeitsgruppe Theoretische Chemie am Institut für Physikalische Chemie an der Technischen Universität Dresden unter der wissenschaftlichen Betreuung von Prof. Gotthard Seifert angefertigt.
- c) Hiermit versichere ich, dass ich keine früheren erfolglosen Promotionsverfahren bestritten habe.
- d) Hiermit erkenne ich die Promotionsordnung der Fakultät Mathematik und Naturwissenschaften an der Technischen Universität Dresden in der Fassung vom 16. April 2003 an.

Datum

Unterschrift